Time-Domain Studies in the New Eras of Multi-Messenger Astrophysics and Big Data

Time-domain Studies in the New Eras of Multi-Messenger Astrophysics and Big Data

A dissertation presented

by

Victoria Ashley Villar

to

The Department of Astronomy

in partial fulfillment of the requirements

for the degree of

Doctor of Philosophy

in the subject of

Astronomy & Astrophysics

Harvard University

Cambridge, Massachusetts

April 2020

Dissertation Advisor: Professor Edo Berger Victoria Ashley Villar

Time-domain Studies in the New Eras of Multi-Messenger Astrophysics and Big Data

Abstract

Time-domain astrophysics probes high-energy phenomena, the end-lives of massive stars and the creation of new elements which enrich the cosmos. Wide-field, untargeted photometric surveys have drastically increased the quantity and variety of known extragalactic transients, continuously challenging our understanding of late-stage stellar evolution. At the same time, gravitational wave detectors have ushered in a new era of multi-messenger astrophysics. This thesis presents a series of theoretical and observational studies which address the questions associated with a new era of data-driven, multi-messenger time-domain astrophysics.

First, we explore the breadth of engines and progenitor systems which lead to extragalactic transients. Through a systematic census of optical light curves, we explore the spread of stellar eruptions, explosions and collisions in simple feature spaces. We then take a detailed look into the eruption of a massive star with a neutron star companion.

Second, we focus on the collisions of compact objects: neutron star mergers and black hole-neutron star mergers. We present a detailed analysis of the complete photometric dataset covering the first two months of the kilonova associated with the gravitational event GW1701817, resulting in the strongest constraints on the kilonova properties. We then present the first *Spitzer Space Telescope* infrared observations of the kilonova. Our results highlight the discrepancy between theory and the observed

late-time behavior of kilonovae.

Finally, we focus on the upcoming age of large data streams. In late 2022, the Vera C. Rubin Observatory will begin its Legacy Survey of Space and Time (LSST), which will increase our annual discovery rate of extragalactic transients by two orders of magnitude. Transients which are currently rare will become commonplace. In this context, we first present a case study of the rare class of superluminous supernovae (SLSNe) in the new era of LSST. We find that the number of LSST SLSN discoveries will rival the current literature sample in less than a week, and we will be able to recover physical parameters for most events without multi-wavelength follow up. However, no population studies of transients will be possible without classification of LSST light curves. We present two data-driven machine learning methods, one supervised and one semi-supervised, which classify supernovae from the Pan-STARRs Medium Deep Survey.

Contents

Acknowledgments

This thesis – and the years of work leading up to it – would not have been possible without the encouragement and support of others.

First, I would like to thank my advisor Edo Berger, who has mentored me throughout my six years at Harvard. Edo has prepared me with the toolset to pursue my own research interests, to continuously challenge myself, and to otherwise survive the world of academia. Edo's advice and guidance have shaped the scientist I have become, and I will always be grateful to him.

Faculty and staff at Harvard and beyond have also guided my path throughout graduate school. Thank you to the members of my research exam and thesis committees: Charlie Conroy, Josh Grindlay, Selma de Mink, Ramesh Narayan and Rosanne Di Stefano. Thank you as well to my external reader, Renee Hlozek. My graduate career would have been notably more hectic without the endless work of Lisa Catella, Peg Herlihy and Robb Scholten – thank you all for everything you do. I truly appreciate the financial support in part by the National Science Foundation, Harvard University, and the Ford Foundation through fellowships.

I am grateful to the remarkable collaborators and co-workers I have been fortunate enough to meet over the years. In particular, a special thanks to Paul Duffell, James Guillochon, David Jones, Atish Kamble, Brian Metzger, Michelle Ntampaka, Or Graur and Armin Rest for advice, mentorship and friendship. I am lucky to be in a group – the Berger Time Domain Group – whose current and former members support one another in and out of the workplace. I am so thankful to have made lifelong friends in our group

and the Berger Block.

Thank you to my friends in the broader graduate student community and beyond. You all motivate (and entertain) me daily. Thank you for the laughs, the coffee, and the questing. To the members of Astrobites, especially Chris Faesi, Susanna Kohler, Nathan Sanders and Mike Zevin: thank you for your hard work and companionship during AAS meetings.

Before coming to Harvard, I had the opportunity to work with a number of wonderful research mentors: Christoph Baranec, Chris Britt, Andrew Collazzi, Nestor Espinoza, Rob Hynes, John Johnson, Andres Jordan, Danny Milisavljevic, Raffaella Margutti, Reed Riddle, Alicia Soderberg, Nevin Weinberg, and Josh Winn. These advisors spent numerous hours passing on their knowledge, which I still use and am grateful for today. I am additionally grateful to the organizers of these programs: Carol Casey, Stafanie Garcia, Kip Matthews, Marie Machacek, Jonathan McDowell, Elsie Otero, Christin Roberson and many others behind the scenes, who believed in me enough to give me a chance to do research.

Any success in my life is thanks to the people who believed in me, which led me on a path to where I am today. Thank you to Aunt Betsy Harrison and my teacher Barbara Hett who encouraged my interest in mathematics at an early age. To Neil deGrasse Tyson who inspired me to become an astronomer through his book *Death By Black Hole* and who personally wished me good luck on my endeavors. To Uncle Doug Simons, who took me to my first observatory. To Ed Bertschinger, who encouraged me to apply to the APS Minority Scholarship, found my first research experience and helped me join MIT's Laureates and Leaders Program. To the countless volunteers of programs I directly or

indirectly benefited from throughout my life. I will forever be indebted to the people who believed in me, and I am committed to paying it forward.

Thank you to my brother Alex, for years of love and friendship. To my mother Barbara, for teaching me the value of giving your time, talent and treasure to others. To my father Alex, for teaching me the value of perseverance. Thank you to my second family, Karen, Brian and Brian McCarthy, for your love and support over the last seven years. A special thanks to Apollo, my constant lap companion.

Finally, I want to thank my husband, Alex McCarthy, for making me the luckiest person in the universe.

To the giants in us all.

Chapter 1

Introduction

Time-domain astrophysics, the study of astrophysical events evolving on human timescales, impacts almost every other branch of astrophysics. In addition to being unique cosmic laboratories for high-energy physics, transient events drive the chemical evolution of the universe; lead to the formation of compact objects like black neutron stars and black holes; and unveil the end-stages of stellar evolution.

This thesis comes at the dawn of two revolutions in time-domain astrophysics. The first is one of multi-messenger astrophysics, in which a single astrophysical event can be detected in electromagnetic radiation and gravitational waves. The second is one of big data quantities, with an exponentially increasing number of extragalactic transients being detected annually. This Chapter introduces the three pillars of this thesis: the "zoo" of astrophysics that drives the diversity of extragalactic transients; the birth of a new era of multi-messenger astrophysics due to gravitational wave detectors; and the start of a new age of "big data" in time-domain astrophysics thanks to wide-field surveys.

1.1 A Zoo of Extragalactic Transients

In 1938, Walter Baade and Fritz Zwicky noted that "*there exist two well-defined types of new stars or novae which might be distinguished as common novae and super-novae*" (Baade & Zwicky 1934). Amongst this new class of so-called supernovae, Minkowski (1941) noted that two spectroscopic subclasses appeared to exist: an "*extremely homogenous*" group of hydrogen-less "Type I" SNe and the more heterogenous class of "Type II" SNe. Today, the number of known astrophysical transients has drastically increased; however, we still largely classify these events with similar phenomenological reasoning and labels. The "zoo" of transients which we see today arise from a combination of unique progenitor scenarios, environments and stellar configurations (e.g., binarity).

This thesis will focus on transients arising from three general scenarios: the eruptions, explosions and collisions of stars. While this Section will provide a general background on stellar eruptions and explosions, Section 1.2 will give the introduction to the collisions of stars and their multi-messenger signals. The wide-range of underlying physics found in extragalactic transients will be the focus of Chapters 2-3.

In particular, Chapter 3 will present a theoretical census of optical light curves for a wide variety of extragalactic transients, including supernovae (SNe), kilonovae (KNe) and gamma-ray bursts (GRBs). A key contribution of this Chapter is uncovering transients which are intrinsically (vs. observationally) rare from a theoretical perspective. We conclude that both fast-rising and intermediate-luminosity transients are intrinsically rare due to a lack of plausible physical engines to produce them. This work also resulted

in the creation of a large number of open-source[1] models and modules in the Modular Open-Source Fitter for Transients (`MOSFiT`).

1.1.1 Stellar Eruptions

We define stellar eruptions as non-terminal bursts of stars, typically arising from mass-loss events and/or accretion onto a companion star. The most famous example of such events are classical novae, in which a non-degenerate star accretes matter onto a white dwarf. In this work, we focus on the more unusual eruptions of massive stars, seen in both the Milky Way and beyond.

Eruptive transients typically peak in luminosity between novae ($M_V \sim -9$ mag) and the dimmest supernovae ($M_V \sim -14$), and are referred to as "intermediate luminosity optical transients" (ILOTs) for this reason. Exceptionally bright eruptions may be confused for dim SNe, leading to a class of objects known as SN-impostors (see, e.g., Kochanek et al. 2012).

What drives these eruptive events? There are a number of suggested theories. For single massive stars, a sudden increase in bolometric luminosity may launch radiation-driven, super-Eddington winds (Quataert et al. 2016). Larger outbursts may result from intense mass-transfer events via Roche-lobe overflow in close binary systems (Smith 2014). Finally, massive eruptions occurring months to years before core-collapse SNe (e.g., Margutti et al. 2013) hint that mass-loss events may be related to late-stage, unstable nucleosynthetic processes. Regardless of origin, the objects resulting from these

[1] `https://github.com/villrv/MOSFiT`

eruptive mass-loss events span a wide range of observational properties and probe the late-stage evolution of massive stars.

In Chapter 2, we present a case study of a particular interesting ILOT and SN-imposter, dubbed SN 2010da. With more than a decade of spectroscopic and photometric, multi-wavelength followup, we show that SN 2010da is the result of the eruption of a massive star with a neutron star companion. We are the first to note that this object is a ultra-luminous X-ray source (in which the X-ray luminosity is greater than the Eddington limit of a neutron star.) Our conclusions were later confirmed through *NuSTAR* and *XMM-Newton* X-ray observations (Carpano et al. 2018).

1.1.2 Stellar Explosions (Supernovae)

As with stellar eruptions, the *explosions* of stars also exhibit a wide range of observational properties. Following historic precedent, SNe are classified largely by spectroscopic and other observational properties. In Figure 1.1, we show an example classification tree for SN subtypes. There are, generally speaking, two progenitor systems of SNe: the thermonuclear explosions of white dwarfs as Type Ia (and Type Ia-like) SNe and core-collapse SNe (CCSNe) resulting from the collapse of massive stars. There is a greater diversity, both in physical origins and observational properties, in CCSNe compares to thermonuclear SNe.

Amongst the many classes of CCSNe, we will focus on four: Type II SNe; Type IIn SNe, Type Ibc SNe and Type I superluminous supernovae (SLSNe). Type II SNe are the most common (volumetrically and observationally) CCSNe. They arise from the collapse of red supergiants. They have a distinct "plateau" stage in their light curves,

caused by a wave of Hydrogen recombination passing through their outflowing ejecta. In contrast, Type IIn SNe arise from massive stars which experience substantial mass loss during their final decades. Narrow Hydrogen lines in their spectra suggest that they are powered by shock-heating from the interaction of the SN ejecta and pre-existing circumstellar material. In contrast, Type Ibc SNe have lost substantial mass, given their *lack* of Hydrogen and Helium in their SN ejecta. However, the SN ejecta does not interact with the lost mass, making their main power source the radioactive decay of ^{56}Ni. Finally, Type I superluminous supernovae (SLSNe) are a rare class of objects that are believed to originate from the birth of highly magnetized neutron stars (magnetars). As their name suggests, they are distinguished by their brightness with peak magnitudes brighter than $M < -20$ mag.

1.2 The Birth of Multi-messenger Astrophysics

The Laser Interferometer Gravitational-Wave Observatory (LIGO) began its hunt for gravitational waves in 2002, a century after their prediction (Einstein 1918; Abbott et al. 2009). In addition to searching for binary black hole binaries, LIGO and other gravitational wave detectors search for the mergers of binary neutron stars (BNs) or neutron star-black hole (NSBH) pairs. Stellar collisions involving at least one neutron star are expected to synthesize heavy elements via the rapid neutron-capture process (r-process; Li & Paczyński 1998. The decay of the newly synthesized material results in a so-called *kilonova* (Li & Paczyński 1998; Rosswog et al. 1999; Metzger & Berger 2012). Although not the sole site of r-process nucleosynthesis, it is believed that kilonovae and BNS mergers are the dominate producer of the universe's heaviest elements.

Unfortunately due to the small ejecta masses and large opacities of kilonovae (see, e.g. Metzger 2017), kilonovae were not detected prior to 2017.

On August 17, 2017, the advanced LIGO/Virgo network detected the first gravitational wave signal from a BNS merger (Abbott et al. 2017). This detection was followed by the joint discovery of an associated gamma-ray burst and kilonova (Abbott et al. 2017; Coulter et al. 2017a; Soares-Santos et al. 2017). This event, dubbed GW170817, led to a number of significant discoveries, including the first joint detection of GWs and EM radiation from a single event; proof that short gamma-ray bursts arise from BNS mergers; and evidence that kilonovae are the dominate site r-process nucleosynthesis. Our team led a number of initial studies related to the discovery (Soares-Santos et al. 2017), ultraviolet/optical/infrared emission (Chornock et al. 2017; Nicholl et al. 2017b; Cowperthwaite et al. 2017), X-ray/radio/gamma-ray emission (Alexander et al. 2016; Margutti et al. 2017a; Fong et al. 2017) and host properties (Blanchard et al. 2017) of the event.

Chapter 4 and Chapter 5 present results following the initial follow-up efforts, including studies of the kilonova associated with GW170817 and of continued followup efforts of new BNS and NSBH mergers discovered by the advanced LIGO network.

In Chapter 4, we present the complete set of ultraviolet, optical and near-infrared light curves published within two months of GW170817. We analyze the complete dataset using a multi-component, semi-analytical kilonova model, finding clear evidence for second- and third-peak (the heaviest) r-process elements.

In Chapter 5, we present the first infrared Spitzer Space Telescope observations of the kilonova associated with GW170817. We find that the observation lie significantly

below our model predictions, following a similar trend to the higher wavelength photometry. We comment on the physical implications of these observations and the observability of future events with the James Webb Space Telescope.

1.3 A New Era of Big Data

We turn again to the work of Baade & Zwicky (1934). The authors note that the newly discovered class of SNe must be exceptionally rare, with an observational frequency of approximately one per galaxy ("*nebula*") per "*several centuries*". One would therefore need to observe hundreds of galaxies each year for any hope of discovering just one SN.

The discovery rate of SNe and other extragalactic transients has grown exponentially since the 1980s. The exponential growth is driven by both technological developments, including the shift from photometric plates to charged-coupling devices (CCDs) and changing survey strategies. The first transient surveys (e.g. the Lick Observatory Supernova Search; Filippenko et al. 2001) made targeted observations of hundreds of galaxies to search for new transients. Thanks to improved CCDs and increased computational power, modern surveys such as Panoramic Survey Telescope and Rapid Response System (Pan-STARRS; Kaiser et al. 2002), the Palomar Transient Factory (PTF; Law et al. 2009) and the Zwicky Transient Facility (ZTF; Kulkarni 2018) adopt an *untargeted* approach in which large patches of the sky are observed every few nights. Through untargeted surveys, we now discover nearly ten-thousand SNe annually (see Figure 1.2).

While discovery rates have exponentially increased, spectroscopic follow up has

lagged behind. As shown in Figure 1.2, we spectroscopically identify roughly 10% of the SNe we discover each year. Because our current method of classification relies on spectra, the vast majority of all discovered SNe are not utilized in scientific efforts.

This mismatch of SN classification/follow up and discovery will only worsen. In 2022, a new observatory, the Vera C. Rubin Observatory (VRO), will begin a ten-year survey of the southern hemisphere known as the Legacy Survey of Space and Time (LSST). In its current main survey strategy, LSST will observe 18,000 square degrees in six broadband optical filters (*ugrizy*), with a typical cadence of several days. The VRO wide field-of-view (9.6 square degrees) coupled with its 8.4-meter mirror will allow LSST to reach an unprecedented discovery rate of transient phenomena. LSST will push up our discovery rate of extragalactic transients by over two orders of magnitude (see Figure 1.2)–an unparalleled surge and the beginning of a new era of big data in time-domain astrophysics. In contrast, spectroscopic resources will likely remain constant, meaning that an extremely small fraction of events (likely $\sim 0.1\%$) will receive a spectroscopic classification.

The expected deluge of discoveries has driven the need for new methods of classifying and studying extragalactic transients, which is the subject of Chapters 8-9. In particular, this thesis will focus on two questions: (1) How do we label extragalactic transients by their spectroscopic subtypes using only their broadband light curves?; and (2) What science can we do with *only* broadband light curve data?

We address the latter question in Chapter 6. We present a case study for the currently rare class of hydrogen-free (Type I) SLSNe. SLSNe are thought to be powered by the birth of magnetars (Nicholl et al. 2017). We present a unified set of 58 SLSNe

light curves, the largest set in the literature. We then use this set to realistically model a population of SLSNe in a LSST simulation. We find that, like many known classes, SLSNe will switch from one of the rarest known SN types to a commonplace event, with more than 10,000 SLSNe being discovered annually. We find that roughly half of these events do not need any followup to sufficiently constrain magnetar and SN properties.

In Chapters 7 and 8, we address the question of classifying SNe into their spectroscopic classes using light curves from Pan-STARRs Medium Deep Survey (PS1-MDS). In Chapter 7, we present the first supervised machine learning algorithm to classify thermonuclear and core-collapse SNe subclasses which is trained on a real (rather than simulated) dataset. Our algorithm achieves classification accuracies which rival methodologies based on simulated datasets. In Chapter 8, we extend on the work of Chapter 7 and present a novel semi-supervised machine learning method to classify the *complete* set of 3,000 PS1-MDS SN-like light curves. We comment on the ability of this algorithm to both classify objects in real time and be used as an anomaly detection mechanism.

We will conclude with future directions in Chapter 9.

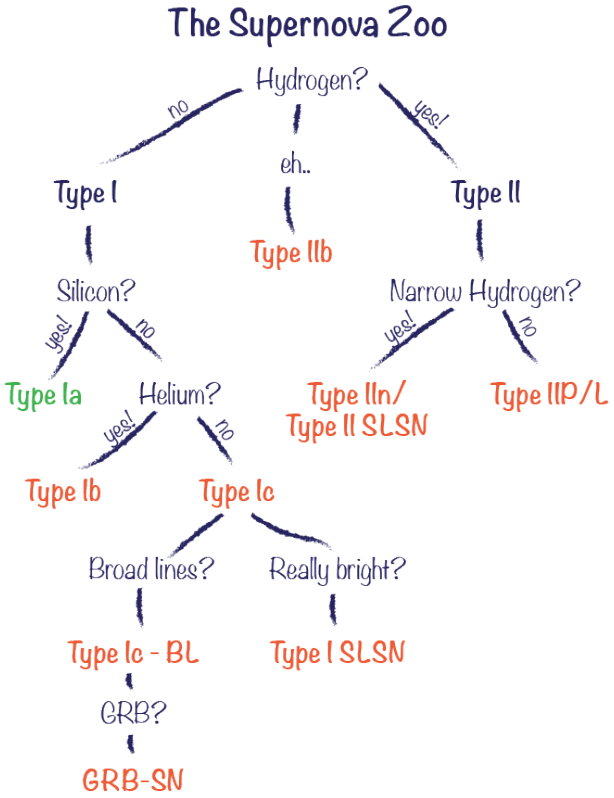

Figure 1.1: Diagram showing a subset of spectroscopic subclasses of SNe. SNe types are colored based on whether they arise from thermonuclear explosions (green) or core-collapse of massive stars (orange). SNe are classified largely by the presence/absence of elemental lines in their spectra, rather than their physical origin. This Figure was originally published by Villar 2016 for Astrobites.

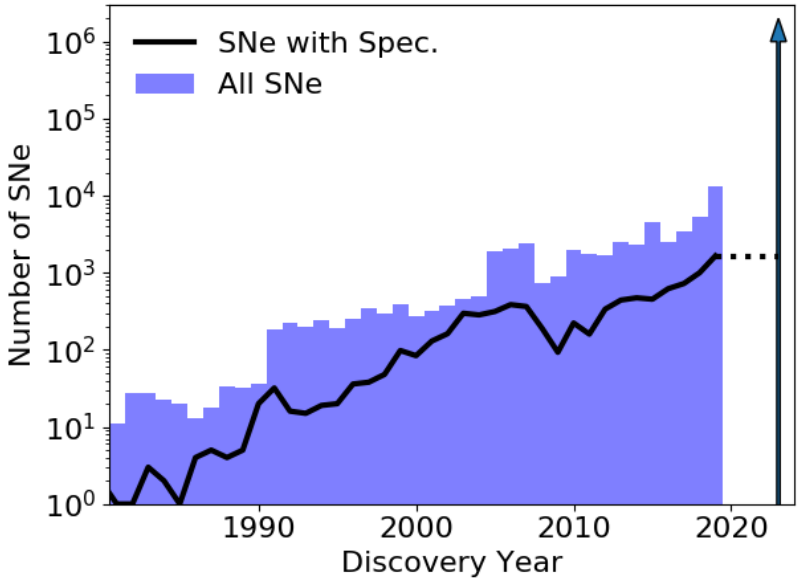

Figure 1.2: Discovery rate of SNe as a function of year (blue) and the number of SNe which received a spectroscopic classification (black line). The exponential increase in annual discoveries is driven by technological and computational developments. The upward arrow reflects the expected discovery rate of the Vera C. Rubin Observatory (VRO), which will begin scientific observations in late 2022.

Chapter 2

The Intermediate Luminosity Optical Transient SN 2010da: The Progenitor, Eruption and Aftermath of a Peculiar Supergiant High-mass X-ray Binary

This thesis chapter originally appeared in the literature as

V. A. Villar, E. Berger, R. Chornock et al., *The Astrophysical Journal* 830, 11

Abstract

We present optical spectroscopy, ultraviolet to infrared imaging and X-ray observations of the intermediate luminosity optical transient (ILOT) SN 2010da in NGC 300 ($d = 1.86$ Mpc) spanning from -6 to $+6$ years relative to the time of outburst in 2010. Based on the light curve and multi-epoch SEDs of SN 2010da, we conclude that the progenitor of SN 2010da is a $\approx 10 - 12$ $M_\odot$ yellow supergiant possibly transitioning into a blue loop phase. During outburst, SN 2010da had a peak absolute magnitude of $M_{bol} \lesssim -10.4$ mag, dimmer than other ILOTs and supernova impostors. We detect multi-component hydrogen Balmer, Paschen, and Ca II emission lines in our high-resolution spectra, which indicate a dusty and complex circumstellar environment. Since the 2010 eruption, the star has brightened by a factor of ≈ 5 and remains highly variable in the optical. Furthermore, we detect SN 2010da in archival *Swift* and *Chandra* observations as an ultraluminous X-ray source ($L_X \approx 6 \times 10^{39}$ erg s^{-1}). We additionally attribute He II 4686Å and coronal Fe emission lines in addition to a steady X-ray luminosity of $\approx 10^{37}$ erg s^{-1} to the presence of a compact companion.

2.1 Introduction

Between the luminosities of the brightest novae ($M_V \approx -10$; Hachisu & Kato 2014) and the dimmest supernovae ($M_V \approx -14$; Zampieri et al. 2003), there is a dearth of well-studied optical transients (see Kasliwal 2012a). In the last decade, we have begun to fill in this gap with a number of exotic events such as luminous red novae (Kulkarni et al. 2007), luminous blue variable (LBV) outbursts and other "supernova impostors" (e.g.

Van Dyk et al. 2000; Pastorello et al. 2007; Berger et al. 2009; Tartaglia et al. 2015). Additionally, there are expected events which have not been definitively observed, such as "failed" supernovae (Kochanek et al. 2008). Following Berger et al. (2009), we will collectively refer to these events as intermediate luminosity optical transients (ILOTs).

The link between ILOTs and their progenitors remains elusive, especially for ILOTs surrounded by dense circumstellar media (CSM). Brighter dusty ILOTs, such as the great eruption of Eta Carinae (Davidson & Humphreys 1997) or SN 1954J (Van Dyk et al. 2005), are attributed to LBV outbursts; however, the progenitors of dimmer events are under debate with a larger pool of viable origins. For example, theorized progenitors of the famous dusty ILOTs, such as NGC 300 OT2008-1 and SN 2008S have ranged from mass loss events of yellow hypergiants (Berger et al. 2009), to mass transfer from an extreme AGB star to a main sequence companion (Kashi et al. 2010), to low luminosity electron-capture supernovae (Thompson et al. 2009; Adams et al. 2016). Each of these interpretations shares the common theme of marking an important point in the evolution of relatively massive stars ($\gtrsim 9M_{\odot}$).

Adding to the diversity of ILOTs is the possibility of optical transients within X-ray binary systems. High mass X-ray binaries (HMXBs) consist of a massive star and a compact object (e.g. a neutron star or a black hole) and produce X-rays as material accretes onto the compact object through a variety of channels (Lewin et al. 1997; Reig 2011). A relatively new subclass of HMXBs known as obscured HMXBs are cloaked in a high density of local material ($N_{\rm H} \sim 10^{23} - 10^{24}$ cm^{-2}; Chaty & Rahoui 2007; Tomsick et al. 2009). While the primary stars of these systems are largely unknown, several have been shown to be supergiants exhibiting B[e] phenomena (Clark et al. 1999; Chaty & Filliatre 2005; Kaplan et al. 2006). These systems likely produce their dense

circumstellar material through either a continuous wind or periodic outbursts which have not yet been observed.

In this work we report data from a five-year, multiwavelength (X-ray, ultraviolet, optical and infrared) observational campaign of the dusty ILOT SN 2010da which was discovered in the nearby galaxy NGC 300 (Monard 2010). We show that SN 2010da exhibits many features shared amongst dusty ILOTs, such as striking Balmer emission and optical variability on the order of months, but it is the only ILOT to sit in an intermediate range between extremely dusty red transients such as SN 2008S and the bluer, brighter LBV outbursts. Additionally, SN 2010da is the first ILOT to be a member of a high mass X-ray binary which undergoes an ultraluminous X-ray outburst ($\sim 10^{40}$ erg s^{-1}). Previous work on SN 2010da (Binder et al. 2011, 2016) concluded that the progenitor is a massive ($\gtrsim 25$ M$_\odot$) luminous blue variable using limited *HST* photometry. However, from our broadband photometry and spectroscopy we infer that SN 2010da originated from an intermediate mass ($\sim 10 - 12$M$_\odot$), variable yellow supergiant progenitor which is now transitioning into a blue loop phase of its evolution. We discuss these conflicting interpretations and the importance of comprehensive, multi-wavelength coverage of ILOTs.

2.2 Observations

SN 2010da was discovered in NGC 300 on 2010 May 23.169 UT by Monard (2010) with an unfiltered magnitude of 16.0 ± 0.2, corresponding to $M \approx -10.3$ assuming a distance of 1.86 Mpc (Rizzi et al. 2006) and a foreground extinction of E(B-V)= 0.011 (Schlafly & Finkbeiner 2011). We neglect addition extinction from NGC 300 based on

our observed *Swift* colors (Section 2.3.1). Throughout this Chapter, Epoch 0 will refer to the discovery date, 2010 May 23. Prior to discovery, NGC 300 was behind the Sun, although Monard (2010) reported an upper limit of $\lesssim 15.5$ mag on May 6. Archival *Spitzer* data indicated that the source began brightening in the infrared at least 150 days before the optical discovery (Laskar et al. 2010). Multi-wavelength follow-up, spanning from the radio to X-rays, revealed that despite its supernova designation, SN 2010da was likely an outburst of a massive star enshrouded by dust (Elias-Rosa et al. 2010; Chornock & Berger 2010; Prieto et al. 2010). This conclusion was reaffirmed by archival *Spitzer*/IRAC observations of the dusty progenitor (Khan et al. 2010; Berger & Chornock 2010), but the lack of extinction in the spectral energy distribution (SED) suggested that some dust had been destroyed during the outburst (Brown 2010; Bond 2010). Early spectroscopic followup revealed narrow emission features (FWHM ≈ 1000 km s^{-1}) with no signs of P-Cygni profiles (Elias-Rosa et al. 2010). Hydrogen Balmer, Fe II and He I emission lines provided further support for interaction with a dense CSM surrounding the progenitor.

The transient was also detected in the X-rays and UV with the *Swift* X-ray Telescope (XRT) and Ultraviolet/Optical Telescope (UVOT), respectively (Immler et al. 2010; Brown 2010). Additionally, 3σ upper limits of $F_\nu \lesssim 87$ (4.9 GHz), $\lesssim 75$ (8.5 GHz), and $\lesssim 225$ (22.5 GHz) μJy were obtained with the Karl G. Jansky Very Large Array (Chomiuk & Soderberg 2010). Following the event, we monitored SN 2010da in the near-infrared (NIR) and optical using Gemini and Magellan. We report below our ground-based imaging and spectroscopy, as well as an analysis of archival *Spitzer, Hubble, Swift* and *Chandra* observations.

2.2.1 *Spitzer* Infrared Imaging

We obtained publicly available *Spitzer* images spanning from 2003 November 21 to 2016 March 19 (see Table 2.1 for program IDs; Lau et al. 2016). This data set extends several years before and after the event, but no data are available within a four month window surrounding the optical discovery. We used data from the InfraRed Array Camera (IRAC) in the 3.6 and 4.5 μm bands through both the original and "warm" *Spitzer* missions, and we use IRAC data in the 5.8 and 8.0 μm bands available prior to the 2010 eruption. Additionally, we used photometry from the Multiband Imagine Photometer (MIPS) in the 24 μm band prior to the discovery of the transient. We processed the *Spitzer* data with the `Mopex` package, which creates a mosaic of the dithered *Spitzer* images. For the IRAC images, we used a drizzling parameter of 0.7 and an output pixel scale of $0.4''$. For the MIPS images, we used the same drizzling parameter but with an output pixel scale of $1.8''$. Images of the field in the *Spitzer* bands are shown in Figure 2.1.

We performed aperture photometry using DS9's `Funtools`. For the IRAC photometry, we used an aperture of 3 native IRAC pixels (corresponding to 3.66") with an inner and outer background annulus radii of 3 (3.66") and 7 (8.54") native pixels, respectively. These radii have calculated aperture correction factors for point sources in the IRAC Instrument Handbook. For the MIPS 24 μm photometry we used an aperture size of 3.5" with no background annulus, following the MIPS Instrument Handbook. We calculated the flux uncertainties following Equation 1 in Laskar et al. (2011). The observations are summarized in Table 2.1, and the *Spitzer*/IRAC light curves at 3.6 and 4.5 μm are shown in Figure 2.2. Our photometric results are consistent with those

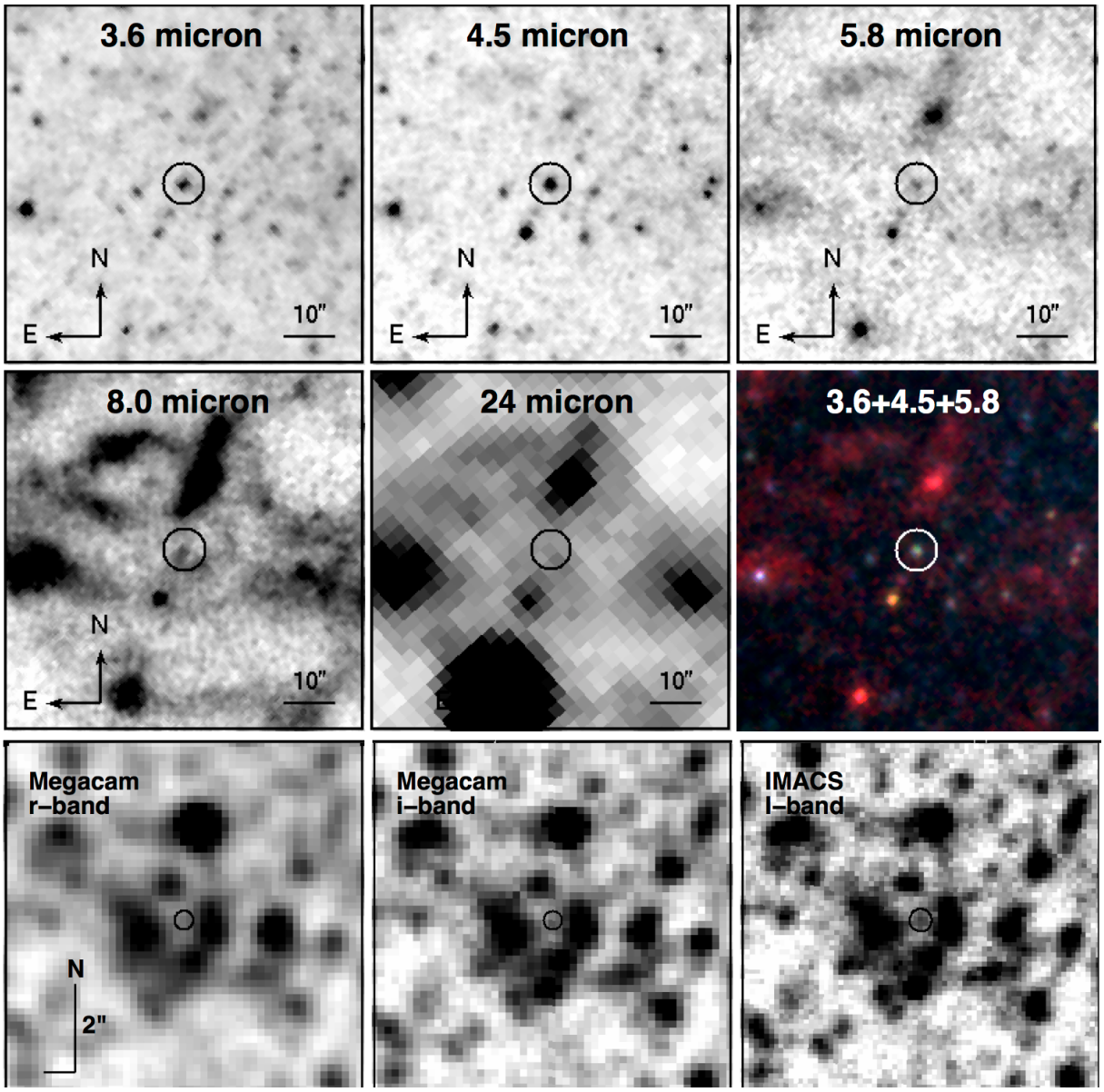

Figure 2.1: Top rows: *Spitzer* images of the SN 2010da progenitor. The right panel of the middle row shows a false color image combining the 3.6 (blue), 4.5 (green) and 5.8 (red) μm images. Bottom row: Archival MegaCam and IMACS images. The progenitor is only detected in the IMACS I-band image.

presented in Lau et al. (2016).

2.2.2 Ground-based Near-Infrared Imaging

We obtained near-infrared imaging observations with the FourStar Infrared Camera (Persson et al. 2013) on the Magellan/Baade 6.5m telescope at the Las Campanas Observatory in Chile on three epochs: 2011 December 7 (J, H, K_s), 2015 July 31 (H, K_s) and 2015 August 18 (J, H, K_s). We calibrated, aligned and co-added each of these observations using the `FSRED` package[1]. Each image was calibrated using the 2MASS Point Source Catalog, and the magnitude of the transient was measured using aperture photometry. The results are summarized in Table 2.2.

2.2.3 Ground-based Optical Imaging

We obtained optical imaging observations with the Low Dispersion Survey Spectrograph 3 (LDSS-3, upgraded from LDSS-2 Allington-Smith et al. 1994) and the Inamori-Magellan Areal Camera & Spectrograph (IMACS; Dressler et al. 2006) on the Magellan Clay and Baade 6.5m telescopes at the Las Campanas Observatory, respectively, in the *gri* filters spanning from $\approx$ 610 days before to $\approx$ 1900 days after the optical discovery. In our earliest IMACS I-band image (at Epoch -609), we detect the object with 24.2 ± 0.2 mag (see Figure 2.1). However, we do not detect a source at the location of SN 2010da in pre-transient *gri* images taken with the Magellan/Clay wide field imager

[1]http://instrumentation.obs.carnegiescience.edu/FourStar/SOFTWARE/reduction.html

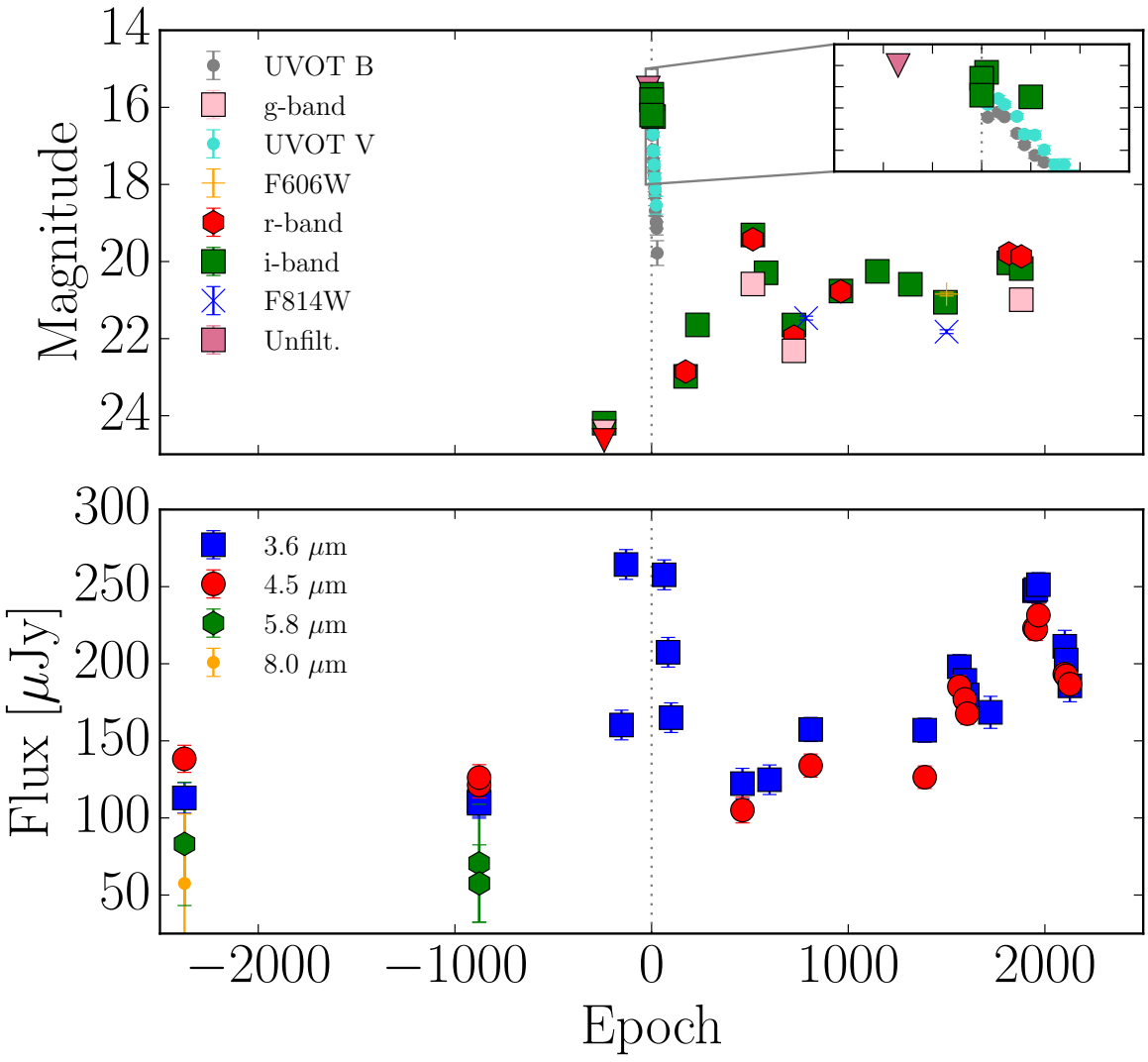

Figure 2.2: The *Spitzer*, ground-based optical, *HST* and *UVOT* light curves of SN 2010da, spanning 6 years before to 6 years after the 2010 eruption. Epoch 0 refers to 2010 May 23.169 UT, the date of discovery. Downward facing triangles are 3σ upper limits.

MegaCam (at Epoch −183; McLeod et al. 2015). We use the MegaCam images in each filter as templates for image subtraction. For all other ground-based optical imaging observations, we performed image subtraction using the `ISIS` package (Alard 2000). We then performed aperture photometry on the subtracted images and calibrated to southern standard stars listed in Smith et al. (2007). The photometry is summarized in Table 2.3.

2.2.4 *HST* Optical Imaging

SN 2010da was observed by the *Hubble Space Telescope* Advanced Camera for Surveys (ACS) on 2012 July 18 (Program 12450) and 2014 July 9 (Program 13515). The object was observed in the F814W filter in both programs (2224 s and 2548 s exposure times, respectively) and in the F606W filter with program 13515 (2400 s). We processed the data using the standard `PyDrizzle` pipeline in `PyRAF` which supplies geometric distortion corrections to combine undersampled, dithered images from *HST*. We scaled the pixel size by 0.8 for a final pixel scale of $0.032''$. We detected a source coincident with the position of SN 2010da, and using five objects detected in the field from the 2MASS Point Source Catalog, we determined a position of $\alpha = 00^h55^m04.86^s$, $\delta = -37^o41'43.8''$ (J2000) with $0.3''$ uncertainty in both coordinates. This is in good agreement (within 1σ) with previous results (Monard 2010; Binder et al. 2011). With the high resolution of *HST*, SN 2010da appears isolated, and we used aperture photometry to measure its magnitude. These magnitudes are listed in Table 2.4 and are in good agreement with those reported by Binder et al. (2016).

2.2.5 Optical Spectroscopy

We obtained medium- and high-resolution spectra of SN 2010da using: the Gemini South Multi-Object Spectrograph (GMOS;Davies et al. 1997) located in the southern Gemini Observatory in Chile; IMACS, the Magellan Inamori Kyocera Echelle (MIKE; Bernstein et al. 2003) spectrograph on the 6.5m Magellan/Clay telescope; and the Magellan Echellette Spectrograph (MagE; Marshall et al. 2008) also mounted on the Magellan/Clay telescope. Table 2.5 summarizes these observations. We used standard `IRAF` routines to process the spectra and applied wavelength calibrations using HeNeAr arc lamps. The MIKE spectra were processed using a custom pipeline and calibrated using ThAr arc lamps. We used our own IDL routines to apply flux calibrations from observations of standard stars (archival in the case of Gemini) and correct for telluric absorption. We estimate the resolution of each spectrum (see Table 2.5) using their associated arc lamp spectra. All spectra are corrected for air-to-vacuum and heliocentric shifts.

2.2.6 *Swift*/UVOT Imaging

The Swift/UVOT data was processed using the method of the Swift Optical/Ultraviolet Supernova Archive (SOUSA; Brown et al. 2014). We combined pre-outburst observations from December 2006 and January 2007 into templates from which the underlying host galaxy count rate was measured. A 3″ aperture was used with aperture corrections based on an average PSF. A time-dependent sensitivity correction was used (updated in 2015) and AB zeropoints from Breeveld et al. (2011). The photometry is summarized in Table 2.6.

2.2.7 X-ray Spectral Imaging

We aggregated archival X-ray observations from the *Swift*/XRT, the *Chandra* X-ray Observatory and *XMM-Newton*. These X-ray observations span from 2000 December 26 to 2014 November 17, including the outburst period. The source was undetected with *XMM-Newton*, and we use the 3σ upper limits obtained by Binder et al. (2011).

The XRT observations were made before, during and after the 2010 outburst, and an X-ray source coincident with SN 2010da is detected in all three regimes. These observations are publicly available from the *Swift* Archive (Evans et al. 2009), and the XRT photometry and spectra are automatically generated through this database.

We used three archival *Chandra* observations from 2010 September 24 (Obs. ID: 12238; PI: Williams), 2014 June 16 (Obs. ID: 16028; PI: Binder) and 2014 November 17 (Obs. ID: 16029; PI: Binder). All observations were made using the Advanced CCD Imaging Spectrometer (ACIS-I) with similar exposure times (63.0 ks, 64.24 ks and 61.27 ks, respectively). We analyzed the observations using `CIAO` version 4.7 and `CALDB` version 4.6.7 using standard extraction procedures. We performed photometry with `WAVDETECT` using an annular background region with an inner radius of $24.6''$ and a width of $4.9''$ centered on the source. The results are summarized in Table 2.7. We extracted spectra of the source using the built-in function `specextract`.

2.3 The Multi-wavelength Properties of SN 2010da, its Progenitor, and its Progeny

2.3.1 Light Curve and Spectral Evolution

The Progenitor

We are able to constrain the progenitor properties using the *Spitzer* (3.6, 4.5, 5.8, 8 and 24 μm) and MegaCam/IMACS (*gri*) observations. We note that the location of SN 2010da was observed in the i'-band on both 2008 September 09 and 2009 November 25 by IMACS and MegaCam, respectively. The MegaCam/IMACS observations are summarized in Table 2.3. The progenitor IMACS detection and MegaCam upper limit are consistent with a magnitude ~ 24.2. The *gr* upper limits were both obtained with MegaCam on 2009 November 25. The location of SN 2010da was observed five times by *Spitzer* before the transient, ranging between 2003 November 21 and 2010 January 14. These observations are summarized in Table 2.1 We find no significant change in the color and brightness between the pre-eruption observations.

To create a progenitor SED, we average the two pre-eruption *Spitzer* observations in the 3.6 and 4.5 μm filters and compiled the other detections. The SED of the progenitor is well fit by an unabsorbed blackbody spectrum with $T = 1500 \pm 40$ K and $R = 9.4 \pm 0.5$ AU ($\chi^2_r = 1.2$ for d.f. $= 3$). These parameters correspond to a bolometric luminosity of $L = (1.92 \pm 0.26) \times 10^4$ $L_\odot$, suggesting a ~ 15 $M_\odot$ main sequence progenitor if we assume solar metallicity (Meynet & Maeder 2000). The large radius and cool temperature of this fit imply that the progenitor is surrounded by dust. The progenitor SED is shown

in Figure 2.3 along with several red supergiants (RSGs) and the progenitor of a previous ILOT in NGC 300 (NGC 300 OT2008-1; Berger et al. 2009). Also shown is the SED of an obscured HMXB (IGR J16207-5129; Tomsick et al. 2006). The progenitor SED peaks between the typically bluer obscured HMXBs and the redder ILOTs such as NGC 300 OT2008-1. The SEDs of RSGs seem to bridge this gap, owing their SED variability to diverse geometries (e.g. WOH G64 has notable IR excess possibly due to a dusty torus along the line of sight; Ohnaka et al. 2008), although neither RSG fits the observed SED.

The 2010 Outburst

SN 2010da was discovered at its brightest known magnitude of $m_{\rm unfiltered} = 16.0 \pm 0.2$. It is unclear if SN 2010da was caught at its true peak brightness, but the optical 15.5 mag upper limit 18 days prior and a slight rise in the *Swift*/UVOT light curve hints that SN 2010da was discovered near its peak luminosity. An increase in IR flux is seen in the IRAC data as early as ≈ 130 days before the optical discovery. The full rise and fall caught by *Spitzer* spans ≈ 250 days, as shown in Figure 2.2.

During the 2010 outburst, the SED of SN 2010da is well fit by two unabsorbed blackbodies at $\sim 0.2 - 1.7$ μm: a hotter blackbody with $T_{H,1} = 9440 \pm 280$ K and $R_{H,1} = 1.59 \pm 0.14$ AU and a cooler blackbody with $T_{C,1} = 3230 \pm 490$ K and $R_{C,1} = 9.5 \pm 2.9$ AU ($\chi^2_r \approx 0.8$ for d.f. $= 6$), as shown in Figure 2.4. These black bodies have a combined bolometric luminosity of $L = (1.3 \pm 0.4) \times 10^6$ L$_\odot$, about 60 times more luminous than the progenitor. Nine days later, the SED is consistent with similar blackbodies, although the larger one has cooled ($T_{C,2} = 2760 \pm 250$ K, $R_{C,2} = 10.5 \pm 1.6$ AU), while the hotter one remains at roughly the same temperature ($T_{H,2} = 9080 \pm 330$

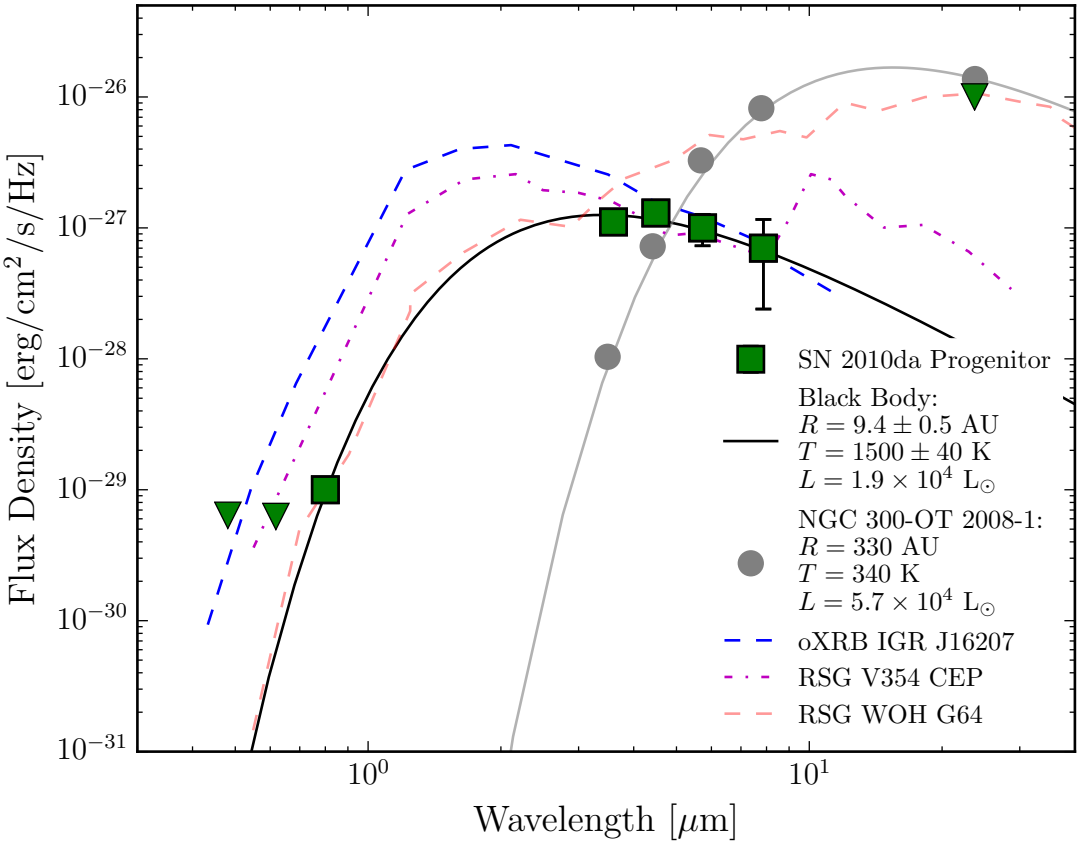

Figure 2.3: Spectral energy distribution of the progenitor of SN 2010da (green squares) with a blackbody fit (black). Also shown are an obscured HMXB (blue dashed line, IGR J16207-5129; Tomsick et al. 2006) and two RSGs (purple and pink lines, see Section 2.3.1 for a discussion of these objects; van Loon et al. 1999; Mauron & Josselin 2011). The latter three objects have been arbitrarily scaled to match the luminosity of the progenitor of SN 2010da. NGC 300's other well-known impostor, NGC 300 OT2008-1, as well as its best-fit blackbody, are shown in grey for comparison. Although NGC 300 OT2008-1 and SN 2010da are spectroscopically similar, the progenitor of SN 2010da is obscured by significantly warmer dust. Downward facing triangles are 3σ upper limits.

K, $R_{H,2} = 1.25 \pm 0.13$ AU). The radius of the cooler, larger blackbody component is consistent with the estimated pre-eruption radius ($R_{C,2} \approx R_{C,1} \approx R_{C,0}$) but has a temperature that is twice as high ($T_{C,2} \approx 2T_{C,0}$). These relations are summarized in Table 2.8. This indicates that at least some dust in the original shell survived the outburst and has heated up.

The UVOT data trace the evolution of the hotter blackbody detected in the initial outburst. The blackbody radius decreases from about 1.7 to 0.55 AU over the ten days of observations while remaining at a steady temperature of ≈ 9200 K, as shown in Figure 2.5. This is consistent with a receding photosphere of the initial outburst. We can use this observation to constrain the radius of the progenitor/surviving star to $\lesssim 0.55$ AU, since we expect the photosphere of the eruption to exceed the radius of the star at all times.

The Progeny

About 200 days after its discovery, SN 2010da dips to $m_i \approx 23$ mag in the optical but returns to $m_i \approx 20$ mag after 500 days. In the same time frame, the IR flux declines by about one magnitude to $m_{3.6} \approx 18.7$ mag at 460 days. The optical light curve then appears to settle into an aperiodic, variable state that oscillates between $m_{r,i} \approx 20$ mag and $m_i \approx 22$ mag every $500-1000$ days. The IR light curve remains roughly at its pre-eruption brightness, but the color becomes much bluer (from $m_{3.6} - m_{4.5} \approx 0.2$ to ≈ -0.2). Beginning around ≈ 1500 days after discovery, the IR light curve begins to rise to magnitudes comparable to the initial outburst. We refer to the surviving star as the *progeny* of SN 2010da.

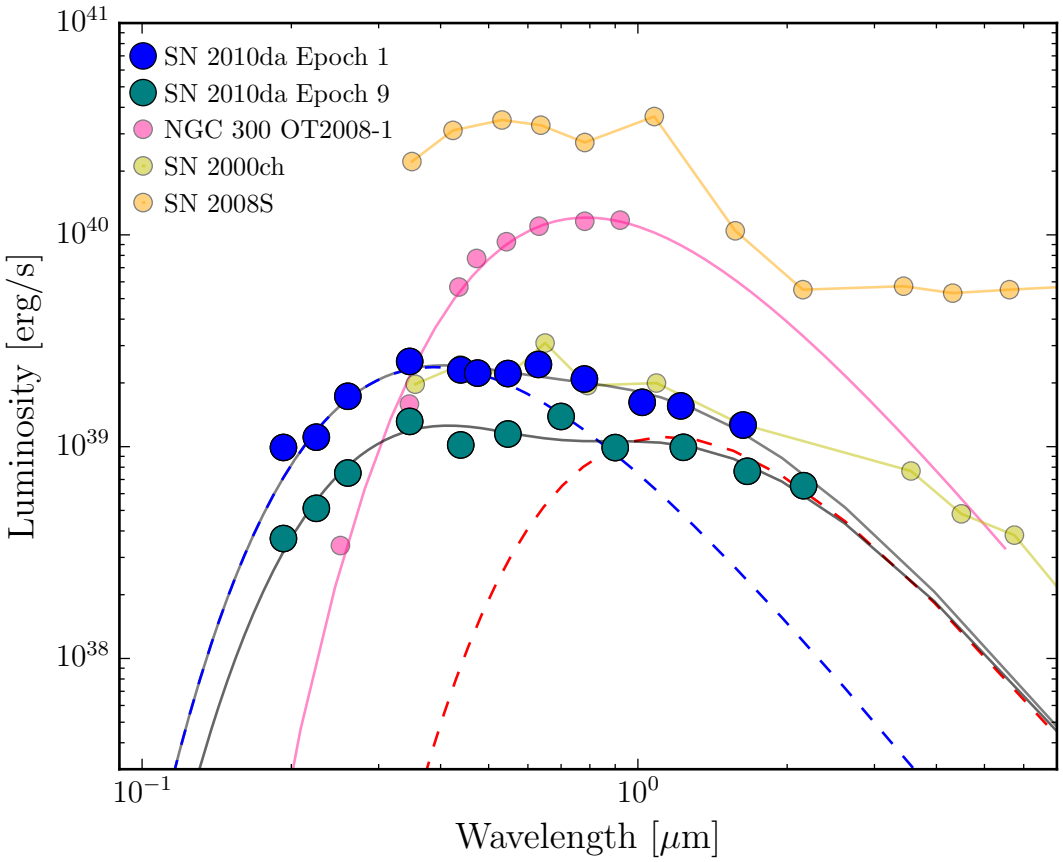

Figure 2.4: The spectral energy distribution of SN 2010da 1 day (dark blue points) and 9 days (dark cyan points) after discovery. Both SEDs are fit with a two-component blackbody model. The total fit is shown in black, while the components of the outburst SED model are shown in blue and red for the first epoch. Also shown are the SEDs of a three similar ILOTs during outburst, NGC 300 OT2008-1 (pink), SN 2000ch (yellow) and SN 2008S (orange). NGC 300 OT2008-1 and SN 2008S are ILOTs with very red progenitors, while SN 2000ch is an LBV-like star.

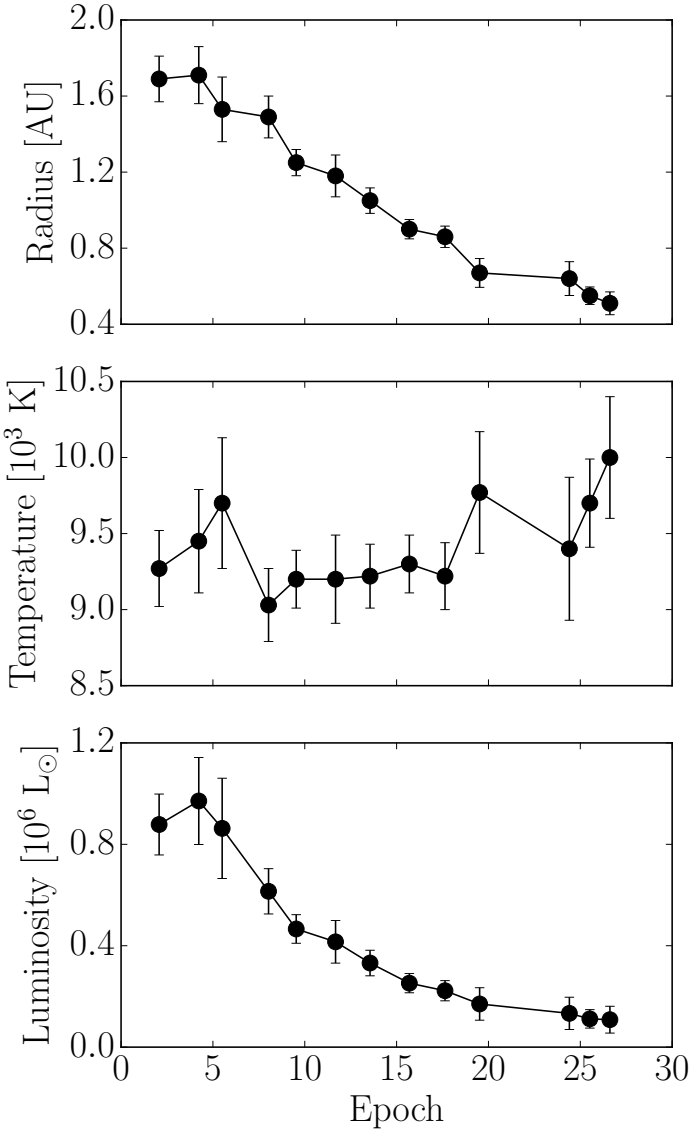

Figure 2.5: We fit the *UVOT* dataset to a blackbody as a function of time. We find that the blackbody radius recedes (top), while the temperature remains roughly constant (middle). The estimated luminosity decreases with the receding radius (bottom)

The progeny's optical/IR SED can be roughly described by a single blackbody with variable excess flux in the optical. After 500 days, the NIR and IR fluxes are fit by a blackbody with a radius of ≈ 6 AU and a temperature of ≈ 2000 K. The derived radius is smaller than the progenitor radius at ≈ 10 AU, and the temperature is higher than the blackbody temperature of the pre-eruption SED ($T = 1500$ K), consistent with the color shift seen in the IR. The optical flux, however, varies by ≈ 2 mag even two years after the initial outburst. Fitting our NIR/IR measurements to blackbodies, we track the bolometric luminosity of the system over time, as shown in Figure 2.6. The luminosity of the progeny and its surrounding environment is about $2 - 5$ times larger than the progenitor of SN 2010da excluding contribution from the UV/optical, which supplies $\sim 10 - 20\%$ of the total luminosity.

We compare the SEDs taken more than 800 days after the initial outburst to a variety of SEDs of massive stars in the LMC analyzed by Bonanos et al. (2009). We group these massive stars by their spectroscopic classification reported by Bonanos et al. (2009), and we construct "typical" SED ranges for each class using the 10^{th} and 90^{th} percentile magnitude of each filter within each group. The SEDs for red, yellow and blue supergiants (RSGs, YSGs, BSGs), luminous blue variables (LBVs) and B[e] stars compared to the SED of the progeny of SN 2010da are shown in Figure 2.7. Here, we are defining B[e] stars as any star with B[e] emission lines (e.g. Hydrogen Balmer, iron, etc.), regardless of luminosity class. The progeny's SED most closely matches the SED of a typical RSG. As a test, we also convert our SDSS bandpasses into Johnson magnitudes and search for the nearest neighbor of the progeny SED within the space of the magnitudes used by Bonanos et al. (2009); the nearest neighbor is [SP77]46-31-999, an M2 Iab star. The fact that the SED of the progeny most closely resembles that of

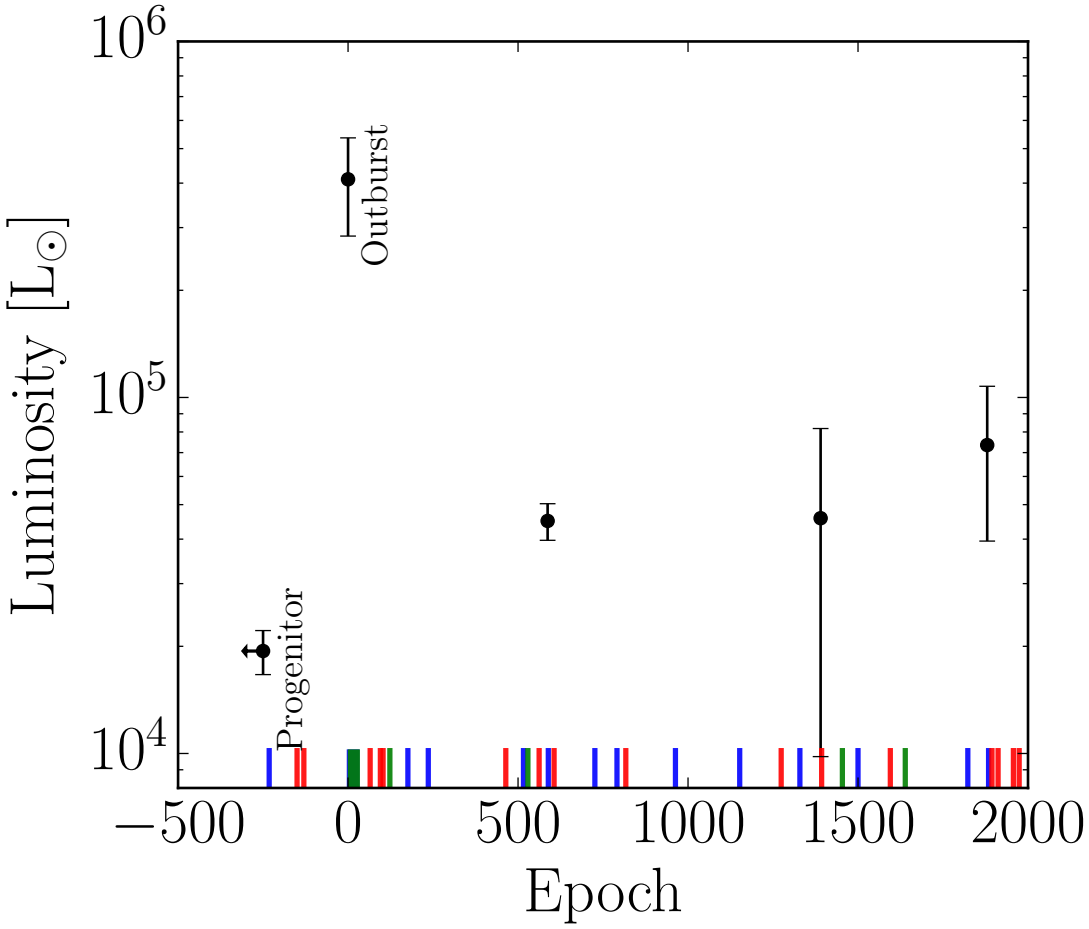

Figure 2.6: Bolometric luminosity of SN 2010da as derived from the NIR/IR flux as a function of time (black). The colored lines at the bottom of the plot indicate our photometric X-ray (green), optical (blue), and infrared (red) coverage for reference. The progeny of SN 2010da system has a consistently higher bolometric luminosity than its progenitor.

a RSG does not necessarily imply that the progenitor or progeny is a RSG. In fact, the small radius we infer from the *Swift*/UVOT data ($\lesssim 0.5AU$) rules out most RSG candidates. Both broadband photometry and spectroscopy are necessary when classifying obscured, massive stars.

2.3.2 Spectroscopic Properties of SN 2010da

Throughout our observations, spanning from 2 to 1881 days after the optical discovery, the spectra of SN 2010da exhibit strong hydrogen Balmer and Paschen, He I and II, Fe II and Ca II emission lines. Early spectra reveal P-Cygni profiles in the Balmer, Paschen and helium lines, while later spectra develop strong nebular emission lines. A full list of these lines with a 3σ detection in at least one epoch and their properties is provided in Table 2.9. The low-resolution spectra are shown in Figure 2.8, and the high-resolution spectra are shown in Figure 2.9. The high-resolution spectra have been normalized by fitting a low-order polynomial to the smoothed spectra. The strong Balmer lines, low excitation emission lines (especially Fe II), the forbidden lines and the IR excess all indicate that the progeny of SN 2010da exhibits B[e] phenomena by the criteria enumerated in Lamers et al. 1998. This classification scheme is purely observational but is linked to a complex CSM surrounding the star (see Lamers et al. 1998 Section 2.2). We observe the development of high ionization emission lines of iron at later epochs and continuous He II 4686Å emission. Both of these observations are due to the presence of a hard radiation field (UV/X-ray emission) associated with the HMXB nature of the object (see Section 2.4.3).

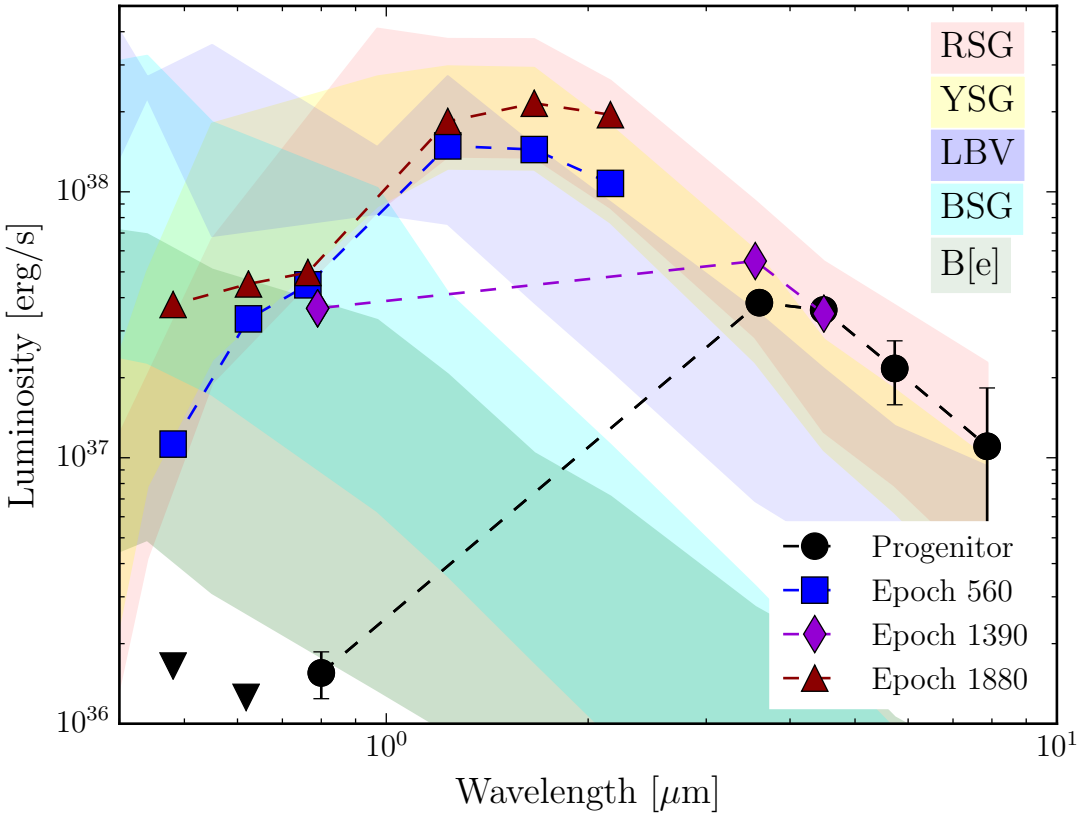

Figure 2.7: Spectral energy distributions of SN 2010da compared to SEDs calculated using massive stars in the LMC (Bonanos et al. 2010). The red region is the typical range for a RSG (M-type), yellow for a YSG (K-type), cyan for a BSG (B-type), dark blue for a LBV and dark green for a B[e] star. Although SN 2010da displays B[e] properties in its spectrum, its SED seems to follow that of a RSG or YSG. Downward facing triangles are 3σ upper limits.

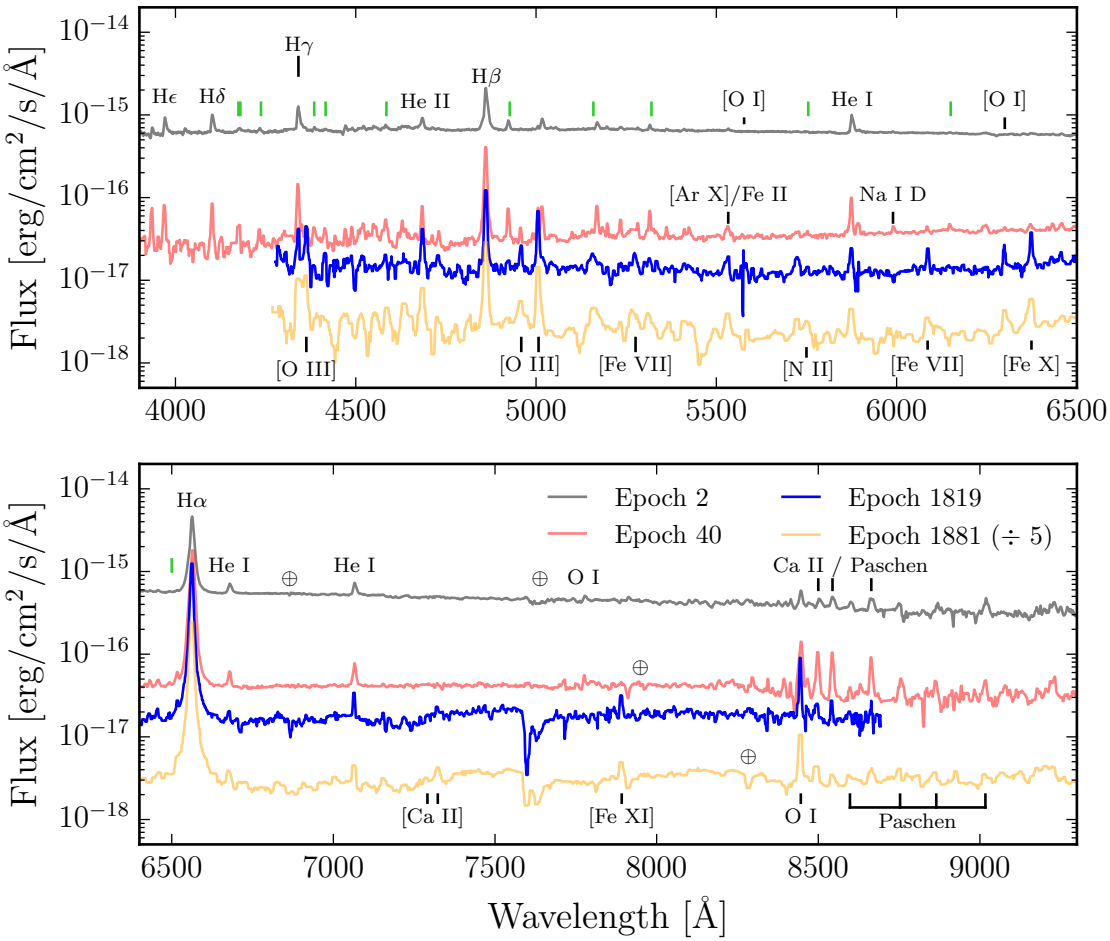

Figure 2.8: Low-/medium-resolution optical spectra of SN 2010da. All spectra have been smoothed to a $\approx$ 10Å resolution, and the 1881-day spectrum has been shifted downward by a factor of 5 for clarity. Unlabeled green lines refer to Fe II emission lines with a 3σ detection in at least one epoch.

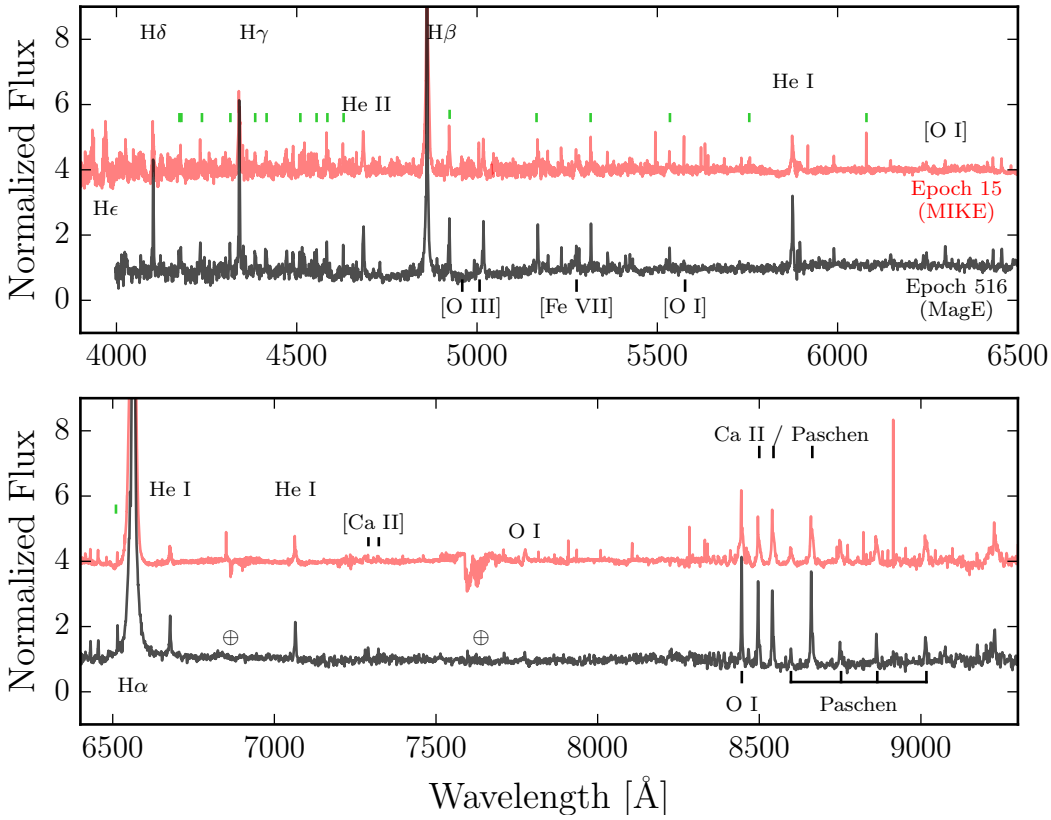

Figure 2.9: High-resolution optical spectra of SN 2010da from MIKE and MagE. Both spectra have been smoothed to ≈ 4Å resolution for display purposes. Unlabeled green lines refer to Fe II emission lines with a 3σ detection in at least one epoch.

Hydrogen Balmer Lines

The Balmer lines exhibit some of the most drastic changes of the spectrum over the span of our observations. Their equivalent widths roughly follow the optical/IR flux variations and appear to be significantly increasing in the most recent observations. A time sequence of the Balmer lines is shown in Figure 2.10.

The spectra are marked by large Hα luminosity, contributing up to $\approx 30\%$ of the r-band flux at later times. Following the initial outburst, Hα is well described by a Lorentzian profile with a full width at half maximum of ≈ 560 km s^{-1}. The full-width at continuum intensity is ≈ 3600 km s^{-1}. The Hα flux immediately following the discovery is $\approx 6.6 \times 10^{-13}$ erg s^{-1} cm^{-2}Å^{-1} and approximately halves 40 days later. As the object cools, the continuum flux decreases while the Hα flux remains relatively constant at $\approx (2-3) \times 10^{-13}$ erg s^{-1} cm^{-2} . At the same time, $F_{\mathrm{H}_\alpha}/F_{\mathrm{H}_\beta}$ increases from ≈ 4 to ≈ 8 in the first 40 days. This is far greater than the expected value of $F_{\mathrm{H}_\alpha}/F_{\mathrm{H}_\beta} \approx 2.8$ for Case B recombination at $\sim 10^4$ K, the approximate temperature of the hotter blackbody component in the SED during outburst. While dust extinction may account for this excess, the continuum is unabsorbed. An alternative possibility is that a high-density CSM affects the Balmer decrement via a self absorption and collisions (Drake & Ulrich 1980). Using the static slab model at 10^4 K from Drake & Ulrich (1980), we find that the observed $F_{\mathrm{H}_\alpha}/F_{\mathrm{H}_\beta}$ ratio roughly corresponds to a density of $n_e \sim 10^{10} - 10^{12}$ cm^{-3}. At these densities, $F_{\mathrm{H}_\gamma}/F_{\mathrm{H}_\beta}$ is suppressed to ≈ 0.3, $F_{\mathrm{H}_\delta}/F_{\mathrm{H}_\beta}$ to ≈ 0.2, and $F_{\mathrm{H}_\epsilon}/F_{\mathrm{H}_\beta}$ to ≈ 0.15. The observed line fluxes roughly match these predictions during the initial outburst. At 40 days later, the $F_{\mathrm{H}_\alpha}/F_{\mathrm{H}_\beta}$ ratio remains consistent with $n_e \sim 10^{10} - 10^{12}$ cm^{-3}.

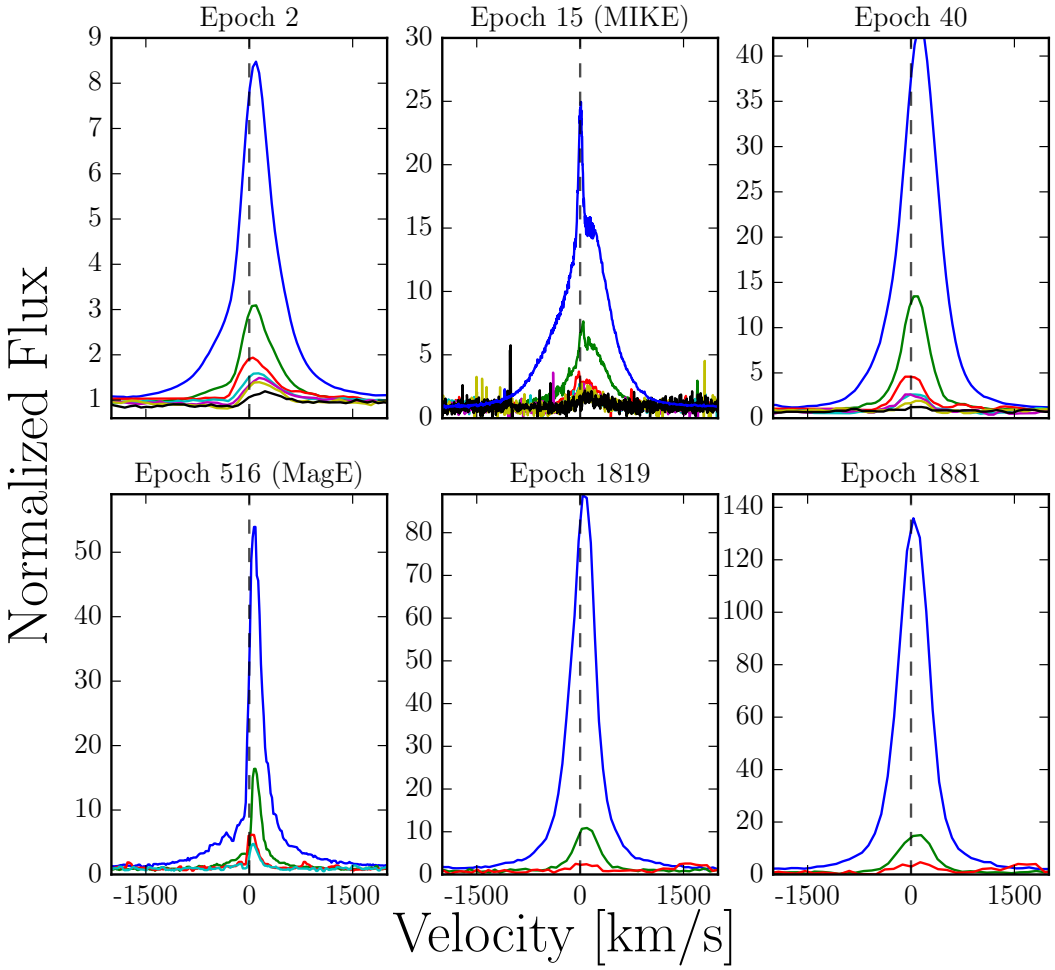

Figure 2.10: Evolution of Balmer lines in the optical spectra. Each epoch is listed above its corresponding subplot. Hα, Hβ, Hγ, Hδ, Hϵ,Hζ and Hη are shown in blue, green, red, teal, pink, yellow and black, respectively. Note that the y-axis are all on independent scales for clarity. The local continuum has been normalized to one by fitting a first order polynomial.

In our high-resolution MIKE spectrum taken 14 days after discovery, the Hα line includes multiple components. We fit the Hα profile with three Gaussian components: a narrow component (FWHM $\approx$ 70 km s^{-1}), an intermediate component (FWHM $\approx$ 500 km s^{-1}) and a broad component (FWHM $\approx$ 1060 km s^{-1}) with $\chi^2_r \approx 1.9$ (see Figure 2.11). Multi-component (specifically three-component) lines are common in dusty ILOTs (Berger et al. 2009; Van Dyk & Matheson 2012; Tartaglia et al. 2015; Turatto et al. 1993). The narrow component is broader than the other detected narrow emission lines (e.g. other Balmer lines with FWHM $\sim 40 - 60$ km s^{-1}) possibly due to electron scattering. These narrow components are consistent with a pre-existing wind, possibly from an earlier red supergiant phase. As with SNe IIn emission lines, the intermediate component is ascribed to the shockwave-CSM interaction (see Chevalier & Fransson 1994), although the velocity is nearly an order of magnitude slower than in SNe. The intermediate component is significantly red-shifted (by $\approx$ 140 km s^{-1}) relative to the narrow component. The apparent redshift may be an artifact of electron-scattering through high optical depths and is often seen in other dusty ILOTs, giants, Wolf-Rayet stars and other stars experiencing significant mass loss (Humphreys et al. 2011; Hillier 1991). The broadest component is only identified in Hα, which may be due to lower signal-to-noise in the other lines or additional scattering. The central wavelength of this component is consistent with that of the intermediate component, also suggesting a common physical origin.

At later times, the Hα emission line can be described as roughly Gaussian or Lorentzian with an extended red wing and a FWHM $\sim 300 - 600$ km s^{-1}. This red wing is especially apparent in the high-resolution MagE spectrum at 516 days. The FWHM of the late-time Hα emission is consistent with the intermediate component of the Hα line

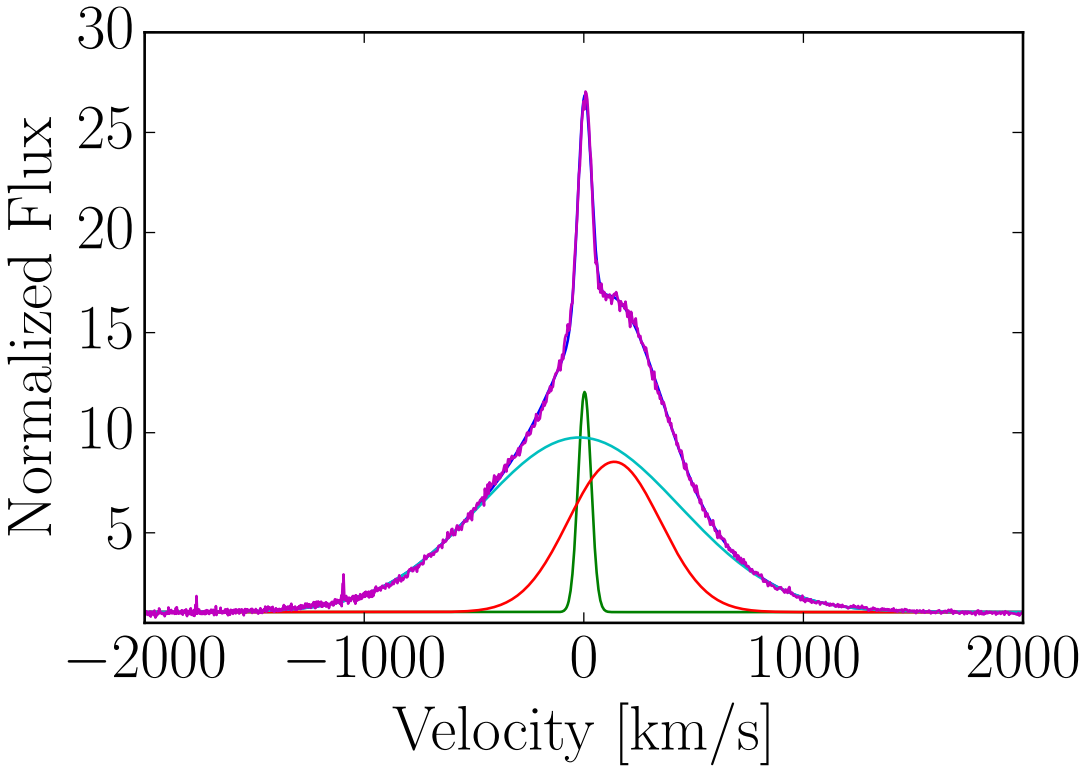

Figure 2.11: The Hα emission line 14 days after the outburst. The line is well described by three Gaussian components (shown in cyan, red and green). The local continuum has been normalized to one by fitting a first order polynomial.

during the initial eruption, while the narrow component remains unresolved in all other spectra. This suggests that the late-time emission is powered by a persistent wind or mass loss consistent with that of a blue or yellow supergiant.

Ca II Lines

Narrow [Ca II] lines (FWHM $\lesssim$50 km s^{-1}) are detected in our highest resolution (MIKE) spectrum 15 days after discovery and possibly again in the MagE spectrum (Figure 2.12). Similar forbidden calcium emission was observed in NGC 300 OT2008-1 (Berger et al. 2009) and SN 2008S (Botticella et al. 2009), as well as in several warm hypergiants (Humphreys et al. 2013), and its presence is typically associated with a dusty environment. Because collisional de-excitation normally drives calcium to its ground state, the [Ca II] doublet is associated with cooler, low density regions. Forbidden calcium lines are additionally suppressed by UV radiation due to the low ionization potential of calcium. Highly ionized iron and He II lines indicate a strong UV radiation field. We can conclude from this fact and the narrow line shape that the [Ca II] forbidden lines are from excited calcium located in the outer CSM, likely in the original dust shell at $\approx$ 10 AU.

The presence of the calcium triplet also supports the existence of a cool, low density circumstellar environment (Polidan & Peters 1976). However, the calcium triplet is significantly blended with hydrogen Paschen emission, so we cannot make a definitive statement about the line shape or strength. The Ca H & K doublet, typically associated with the calcium triplet, are also blended with Hη and an iron line.

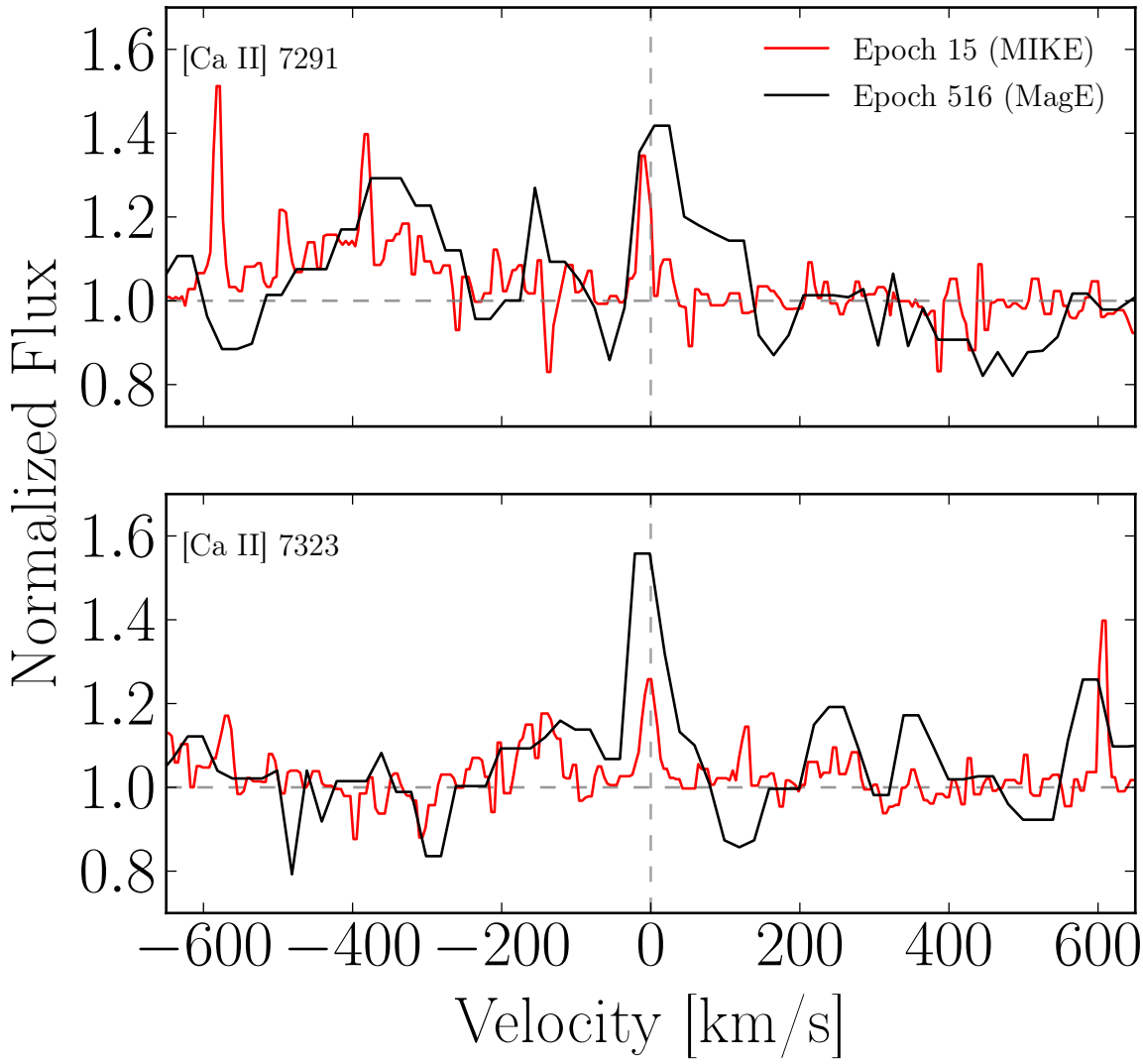

Figure 2.12: Narrow, [Ca II] lines detected in our high-resolution spectra. The local continuum has been normalized to one by fitting a first order polynomial.

Fe Lines

We detect strong Fe II emission lines in all spectra. The Fe II features roughly match the hydrogen Balmer series in shape, FWHM and line offset, indicating that these features also arise from material within the ejecta and CSM. Fe II emission is seen in NGC300 OT2008-1 and M85 OT2006-1 (Berger et al. 2009; Bond et al. 2009), although the lines seen in SN 2010da are notably stronger.

In addition to Fe II, we detect emission from high ionization, forbidden iron lines, including [Fe VII], [Fe X] and [Fe XI] in the last two epochs of spectroscopy (Epochs 1819 and 1881; see Figure 2.13). These forbidden iron lines are not typically seen in ILOTs due to their weakly ionizing radiation. High ionization iron lines are occasionally found in SNe IIn such as SN 1997eg (Hoffman et al. 2008) and SN 2005ip (Smith et al. 2009) due to shock heating of the surrounding CSM. Unlike SNe IIn, the iron lines seen in SN 2010da do *not* arise from continual shock heating over hundreds of days. Instead, these lines arise in regions of diffuse gas surrounding the progeny which are heated to temperatures of about 2×10^6 K, the approximate ionization temperature for lines such as [Fe XII] and [Fe XIV] (Corliss & Sugar 1982), by X-rays from the compact companion (see Section 4.3).

He Lines

He I and II emission lines are seen throughout our observations, as shown in Figure 2.14. The widths (FWHM $\sim 200 - 400$ km s^{-1}) and profiles of the He I lines largely follow the Balmer series with a double-peaked structure in our high-resolution spectra. We additionally detect single-peaked He II 4686Å emission during each epoch. The

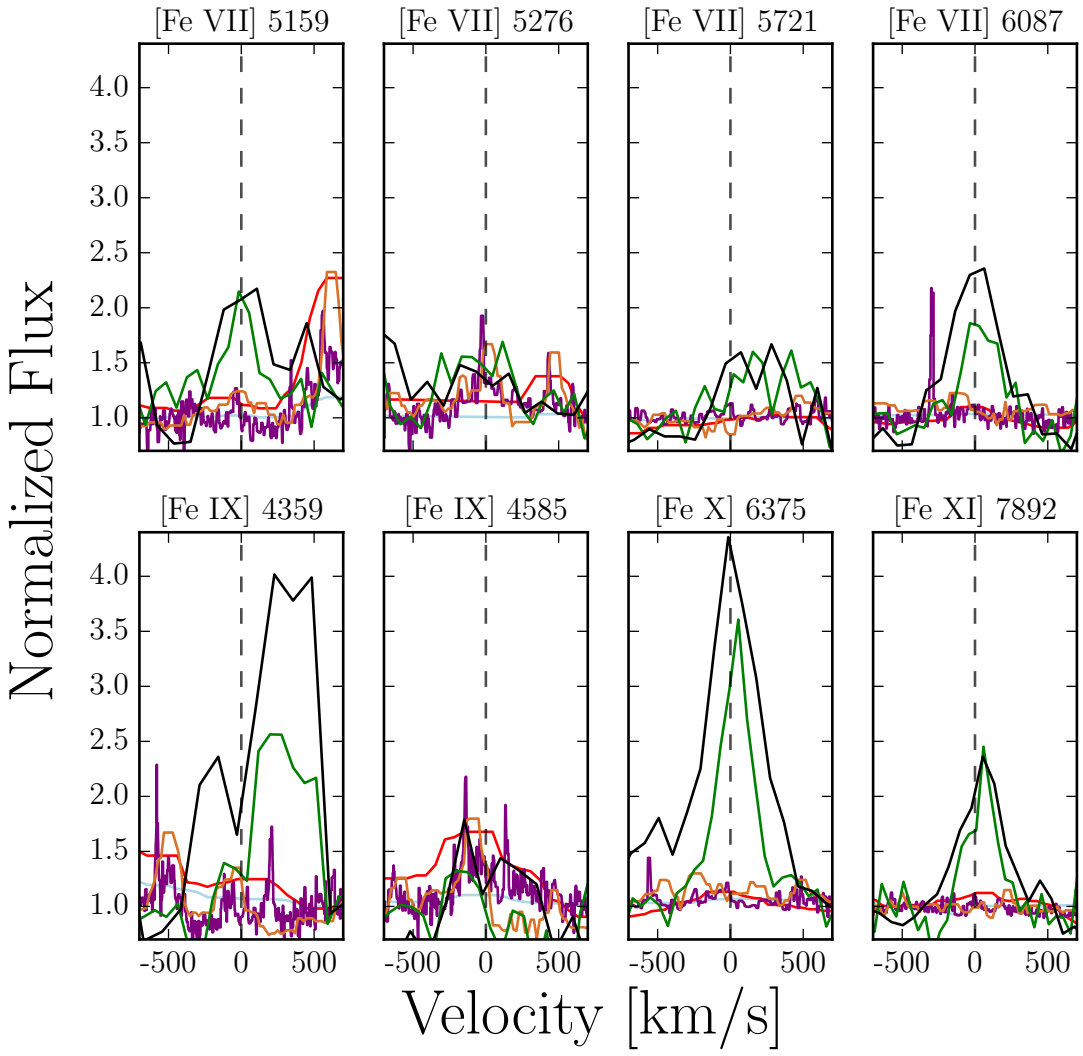

Figure 2.13: Evolution of the coronal iron lines. Spectra taken on days 2, 15, 40, 516, 1819 and 1881 are shown in light blue, purple, red, orange, green, and black, respectively. The local continuum has been normalized to one by fitting a first order polynomial.

low-resolution spectra are unable to resolve the He II 4686Å line, but our MIKE spectrum reveals a FWHM ≈ 270 km s^{-1}. He II 4686Å has a relatively high ionization potential and is sensitive to the EUV flux of the system. For this reason, it is often linked to the accretion onto a compact object (Lewin et al. 1997). The continual presence of He II 4686Å emission in each of our observations is due to the compact companion and indicates consistent mass transfer onto this compact object.

Additional Absorption and Emission Features

Hydrogen Paschen emission lines extending to approximately Pa30 are observed within the first 15 days of the outburst. The high-resolution MIKE spectrum reveals double-peaked emission with narrow and broad components, similar to the Balmer lines. These profiles are not resolved in our lower-resolution spectra. Within the first 40 days, the ratio $F(\mathrm{P}_\delta)/(\mathrm{H}_\beta)$ decreases from ≈ 0.2 to ≈ 0.08. The latter value is roughly consistent with that expected from Case B recombination (≈ 0.07), although the effect of high electron density on this line is unclear.

At early times, we detect O I at 7774Å and 8446Å in emission. The O I 8446Å line shows the same double-peaked profile as the Balmer series, while O I 7774Å maintains a P-Cygni profile until 40 days after the initial eruption. After 1800 days, O I 7774Å becomes undetectable while O I 8446Å strengthens. The expected ratio between these lines is $F(\text{O I } 8446\text{Å})/F(\text{O I } 7774\text{Å}) = 0.6$, implying that O I 7774Å should be detectable. The independent strengthening of O I 8446Å can be attributed to Lyβ emission which is outside of our observed spectral range. Lyβ photons pump O I from the ground state to an unstable state whose decay produces O I 8446Å emission (Mathew

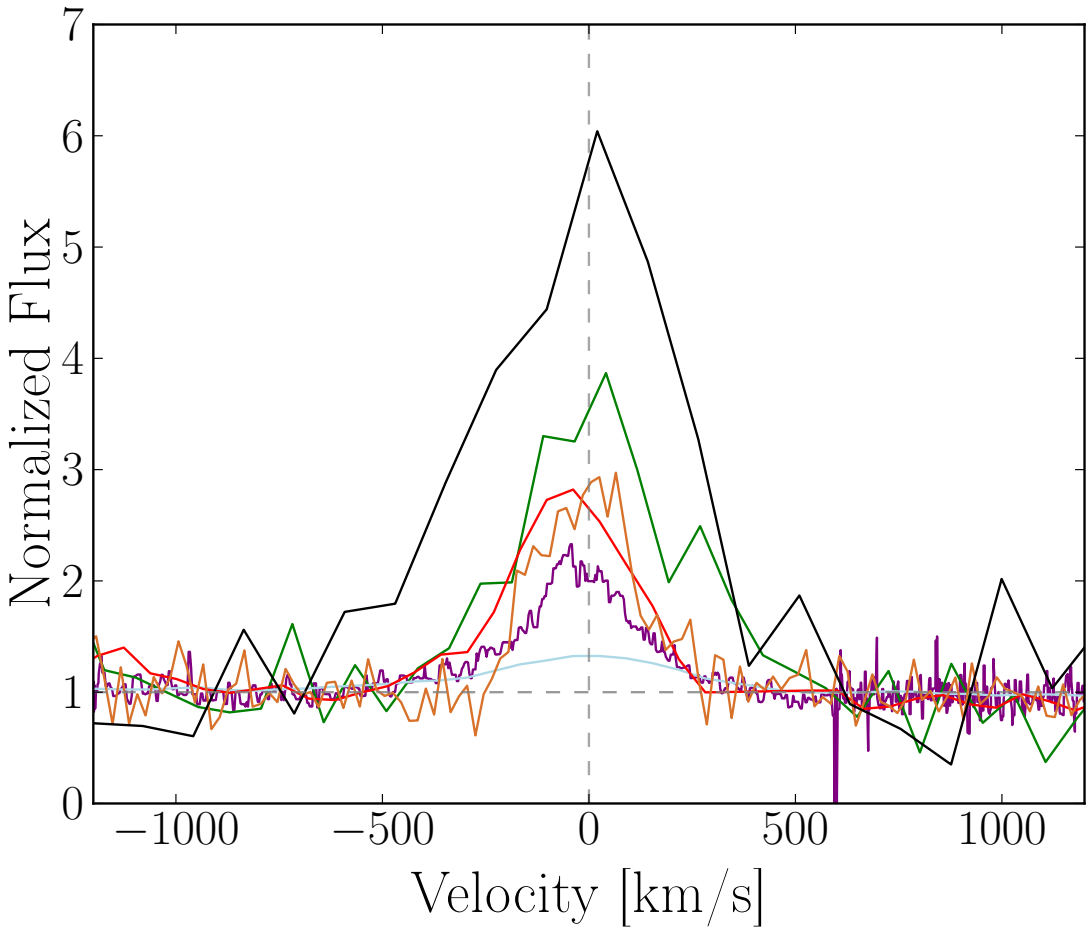

Figure 2.14: Evolution of the He II 4686Å emission. Spectra taken on days 2, 15, 40, 516, 1819 and 1881 are shown in light blue, purple, red, orange, green and black, respectively. The local continuum has been normalized to one by fitting a first order polynomial.

et al. 2012). This is consistent with the increased Balmer emission and UV flux at later times. In addition to O I, we detect [O I] and [O III] features. Unfortunately, the [O III] 4363Å feature appears blended with either [Fe IX] or an Fe II emission line, making it difficult to use the [O III] ratios to calculate the electron temperature.

Unresolved Na I D lines are observed in the two latest epochs (517 and 1817 days) as emission and absorption respectively. The variability of these lines indicates that they are associated with the CSM rather than interstellar medium.

2.3.3 X-ray Spectral Modeling

We model the X-ray emission from SN 2010da and its progeny using XSPEC version 12.8.2n (Arnaud 1996). We use the Cash statistic, a derivative of the Poisson likelihood, as our fit statistic. To test our fits, we use the XSPEC built-in command `goodness` to perform 10^4 Monte Carlo simulations of the spectral data. For each simulation, the program calculates the Cramér von Mises (CVM) test statistic, which is shown to be a good fit statistic for the data derived from a Poisson distribution (Spinelli & Stephens 1997). If about 50% of these simulations have a CVM statistic less than that of our model, the best-fit model is a good representation of the data. A percentage much lower than 50% implies that our model is over parametrized, and a percentage much greater than 50% implies that our model is inconsistent with the data. All reported errors correspond to 1σ error bars (the 68% confidence interval).

We combine all of the *Swift*/XRT $0.5 - 8$ keV data taken within 40 days of the outburst and fit it to a power law with Galactic absorption (`tbabs * pow`) with $N_{\rm H,MW} = 4 \times 10^{20}$ cm^{-2}. We find that additional absorption over-parametrizes the

model (`goodness` = 15%), but an excess column density as large as $N_H \approx 5 \times 10^{21}$ cm^{-2} is consistent with the data. Our best fit model is described by $\Gamma = -0.05^{+0.11}_{-0.10}$ with an unabsorbed $0.3 - 10.0$ keV flux of $9.62^{+0.87}_{-0.85} \times 10^{-16}$ erg s^{-1} cm^{-2} (assuming $N_{\rm H} = 0$). This corresponds to a luminosity of $3.98^{+0.36}_{-0.35} \times 10^{38}$ erg s^{-1}. Similarly, we fit the first *Chandra* observation (Epoch 123) to an absorbed power law. We find the best fit model is described by $\Gamma = 0.26^{+0.20}_{-0.21}$ with an unabsorbed $0.3 - 8.0$ keV luminosity of $1.95^{+0.17}_{-0.48} \times 10^{37}$ erg s^{-1}. We find an absorption upper limit beyond the Galactic column of $N_H \lesssim 4 \times 10^{21}$ cm^{-2}. The estimated column density and the photon index are degenerate such that a higher column density implies a softer power law.

Due to limited statistics, we are unable to fit a spectrum to the second *Chandra* observation (Epoch 1453). In the third *Chandra* observation (Epoch 1638), there is a significant decrease in counts between $\approx 2 - 3$ keV. We are unable to fit this spectrum to a single power law or blackbody component and instead combine a power law with either a soft Bremsstrahlung (`bremss`) or blackbody disk (`diskbb`) model, with no statistical preference for either model based on the CVM statistic. For both models we obtain a similar power law with index $\Gamma = -2.2^{+0.3}_{-0.5}$ for the Bremsstrahlung model and $\Gamma = -2.3^{+0.4}_{-0.4}$ for the disk model. The Bremmstralung component has a temperature of $0.6^{+0.3}_{-0.2}$ keV, while the disk model has an inner-disk temperature of $0.33^{+0.08}_{-0.06}$ keV. While these fits were performed by fixing the hydrogen column density to the Galactic value, fixing N_H to values as high as 4×10^{21} cm^{-2} also gives reasonable (although statistically less favorable) fits with softer power laws. This hard power law differs from the recent results of Binder et al. (2016), who find $\Gamma \approx 0$. Specifically, we are unable to reconcile the double peak in the spectrum with softer power laws (see Figure 2.15). The extremely hard power law in our models indicates that additional and detailed modelling

is necessary to explain this unusual *Chandra* spectrum. All X-ray spectra and models are shown in Figure 2.16.

2.3.4 The X-ray and UV Light Curves

Using archival observations of SN 2010da (Section 2.2.7), we are able to construct the X-ray and UV light curves of SN 2010da. The full X-ray light curve is shown in Figure 2.17. We build the *Swift*/XRT light curve by converting the light curve produced automatically by the UK *Swift* Science Data Center from a count rate to a flux using the conversion factor found for the XRT spectrum. This light curve was dynamically binned using a rate factor of 10 and a bin factor of 5.

Binder et al. (2011) estimate a 3σ upper limit on the unabsorbed $0.3 - 10$ keV luminosity of the progenitor to be $\approx 3 \times 10^{36}$ erg s^{-1} using archival *XMM-Newton* data. However, about 1300 days before the optical outburst, we find a weak *Swift*/XRT detection at 2.6σ with a luminosity of $1.8^{+0.7}_{-0.7} \times 10^{37}$ erg s^{-1}, indicating X-ray variability even before the 2010 optical outburst.

During the transient, the X-ray luminosity increases to a peak of $\approx 6 \times 10^{39}$ erg s^{-1}, making SN 2010da an ultraluminous X-ray source well above the Eddington limit of a 1.4 $M_\odot$ neutron star. (We note that this luminosity is larger than the luminosity reported from the spectral fit in Section 2.3.3 and Binder et al. 2011, because the spectral fit averaged the luminosity over 40 days following the initial outburst.) In the week following discovery, the X-ray luminosity fluctuates between 2×10^{39} erg s^{-1} and 6×10^{39} erg s^{-1} before decaying with an e-folding time of ≈ 3.5 days. This decay rate is slightly longer that of the UVOT light curves (≈ 10 days, shown in Figure 2.18) and

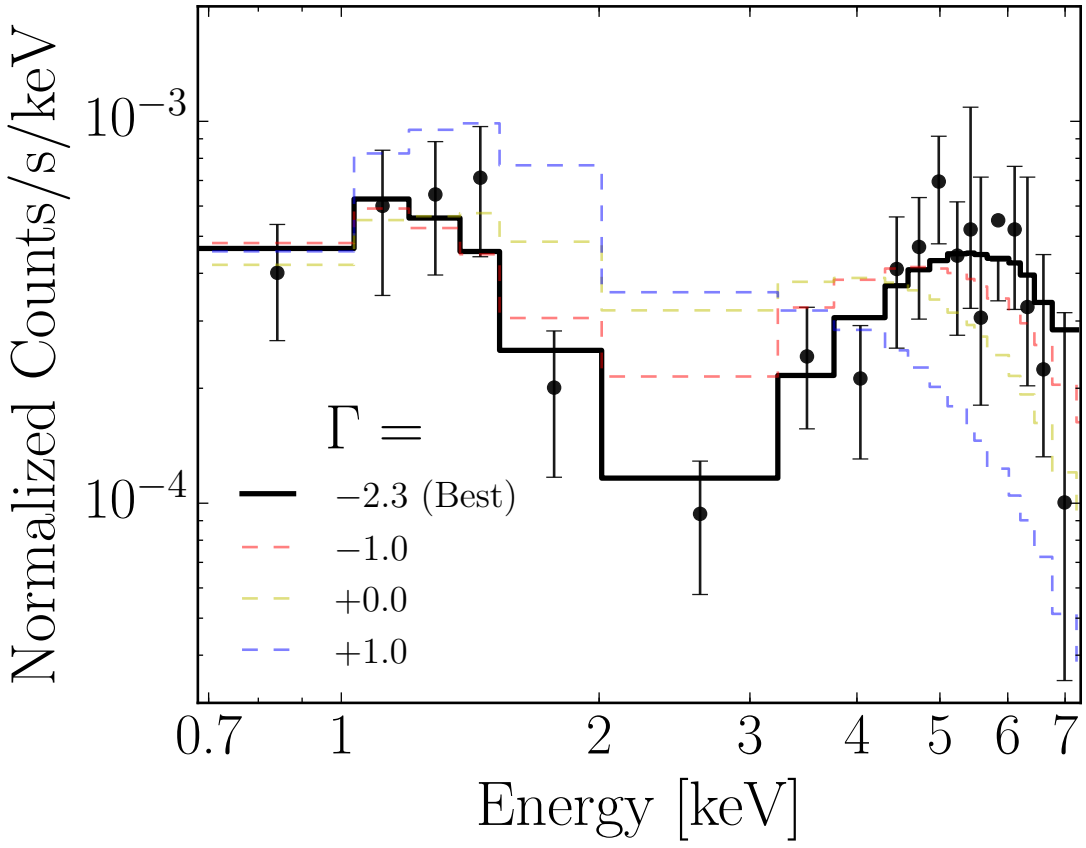

Figure 2.15: The latest X-ray spectrum of SN 2010da from *Chandra* Observation 16029, normalized by the detector's effective area. Shown are four models with a Bremsstrahlung and power law component. We fix the photon index, Γ, to -1.0 (red), 0.0 (yellow) and +1.0 (blue) and compare to the best fit model with $\Gamma = -2.3$. We are unable to recover the bimodal structure of the spectrum with softer power laws.

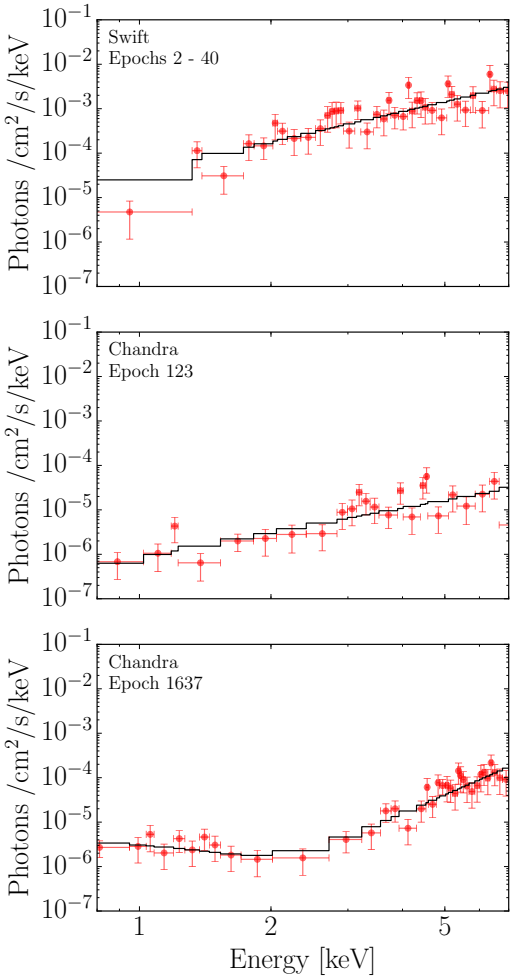

Figure 2.16: Top: The *Swift* X-ray spectrum created using data taken within 40 days of the transient. The best fit power law model is overlaid. Middle/Bottom: The *Chandra* X-ray spectra (Obs. ID 12238 and 16029) with best fit power law and disc models (see text for details).

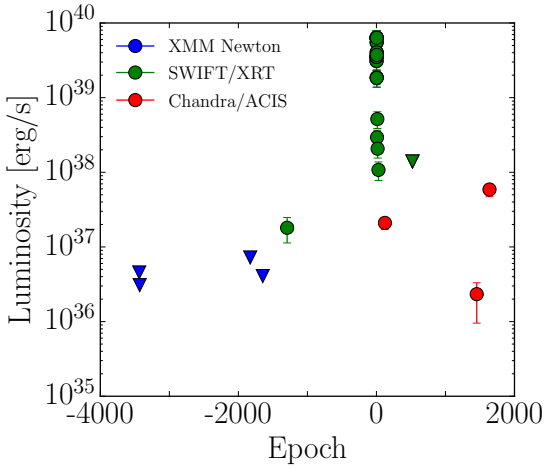

Figure 2.17: X-ray light curve of SN 2010da. Triangles indicate 3σ upper limits. Downward facing triangles are 3σ upper limits.

is much shorter than the decay rates found in the eruptions of η Car (≈ 200 days, from Binder et al. 2011). About 1450 days after the transient, we find an X-ray luminosity of $\approx 2.4 \times 10^{36}$ erg s^{-1} which increases to $\approx 5.9 \times 10^{37}$ erg s^{-1} at about 1640 days. This increase in X-ray luminosity occurs at roughly the same time as the increase in optical/IR luminosity.

2.4 Discussion

Taken together, the X-ray, optical and IR light curves and spectra consistently describe an HMXB undergoing an episode of active accretion which is fueled by persistent eruptions of the primary star, with SN 2010da representing the largest observed eruption in nearly a decade of observations. The optical and IR light curves are powered by mass loss of the supergiant. This mass accretes onto the compact object, giving rise to

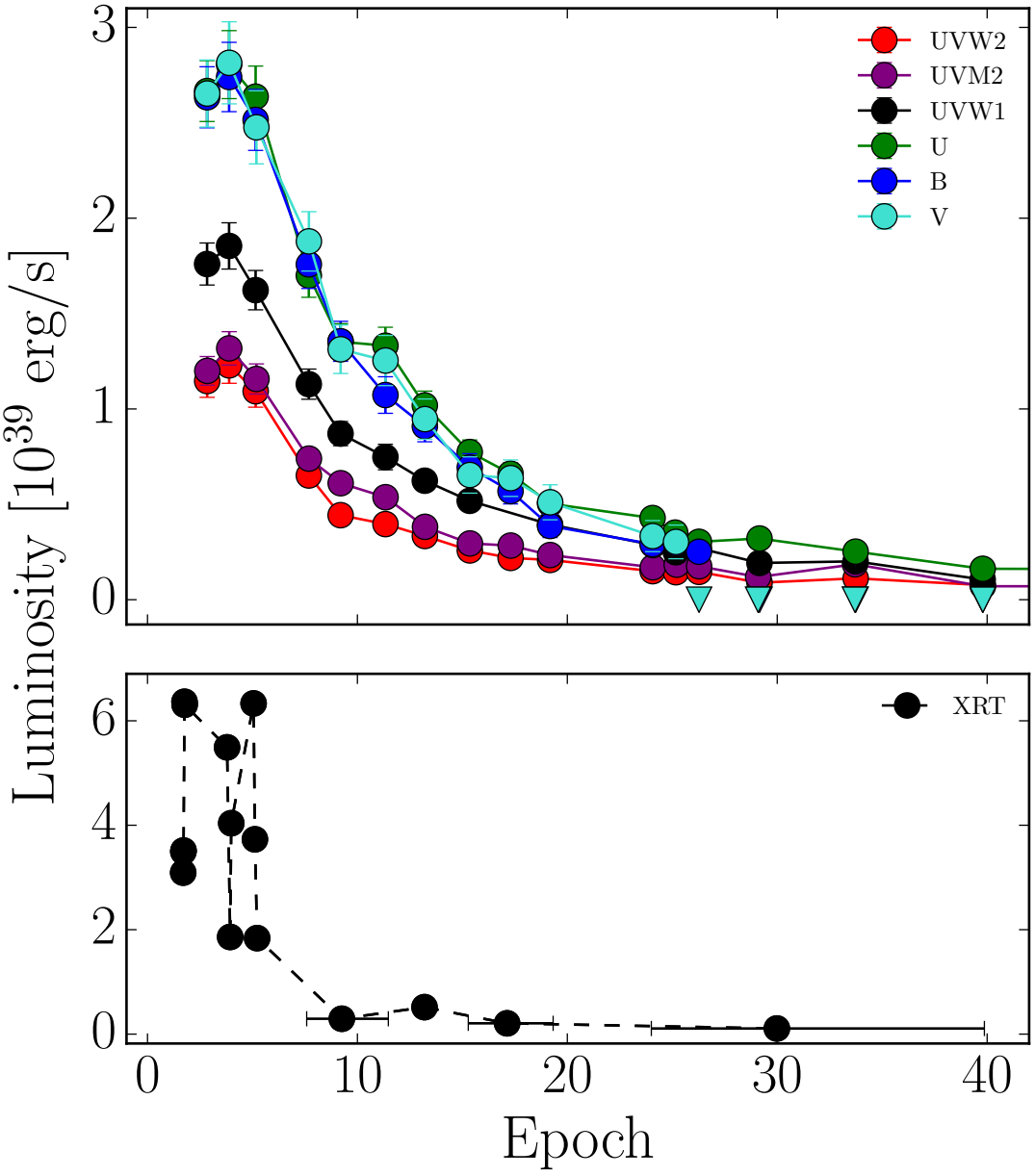

Figure 2.18: XRT (top) and UVOT light curves near the time of discovery. Downward facing triangles are 3σ upper limits.

X-ray emission. The X-rays in turn excite the high ionization He II and coronal iron lines seen in the optical spectra. In this section, we summarize the properties of the progenitor and the surviving progeny of the 2010 eruption, and we discuss potential compact companions.

2.4.1 The Progenitor of SN 2010da

Ignoring any contribution from a compact companion or accretion disk, our blackbody fit of the progenitor SED (with a temperature of 1500 K and a radius of 9.6 AU) reveals a stellar bolometric luminosity of about 2×10^4 $L_\odot$. This luminosity is consistent with a 15 $M_\odot$ main sequence star (Meynet & Maeder 2000) or a supergiant with a $10-12$ $M_\odot$ ZAMS mass (Ekstrom et al. 2012). The low temperature suggests that this blackbody is not the photosphere of the progenitor. Instead, we interpret this SED as a dusty shell surrounding the star.

To further investigate progenitor candidates, we model the dusty environment of the progenitor and its SED using the radiative transfer code `DUSTY` (Ivezic et al. 1999). `DUSTY` is able to model the density profiles of spherically symmetric, radiatively driven winds, requiring as input the central source SED, the dust composition, the optical depth and the inner dust temperature. Since we do not see silicate features around 8 μm in our pre-eruption *Spitzer* observations, we choose a pure graphite environment (Drake & Ulrich 1980). The carbon-rich dust is consistent with the stability of the dust shell at a relatively high temperature ($\approx$ 1500 K), which has a higher sublimation temperature than silicate (Kobayashi et al. 2011). We assume that the shell has a thickness of $R_{\rm out}/R_{\rm in} = 2$ and use a power law density model which falls off as $\rho \propto r^{-2}$, typical of a

wind. We additionally assume that the central source is a blackbody, and we leave its temperature as a free parameter. The final luminosity of the model is calculated using the normalized flux and radius computed by DUSTY. The UVOT observations during the 2010 outburst constrain the progenitor radius to be ≈ 120 $R_\odot$. This limits the progenitor temperature to $T \gtrsim 6200$ K. We are additionally unable to find satisfactory fits ($\chi^2_r < 2$) of the progenitor SED for temperatures above $\approx 18,000$ K. The temperature of a 15 $M_\odot$ main sequence star is about 30,000 K, meaning that we can rule out such a progenitor. Due to the low luminosity, we can also rule out an LBV progenitor, which was previously suggested by others (Binder et al. 2016). The only remaining viable option at this luminosity is an evolved yellow or blue supergiant progenitor.

We can additionally use the DUSTY models to estimate the mass loss rate of the progenitor. Following Kochanek et al. (2012), the mass loss is approximately equal to:

$$\dot{M} \approx \frac{\kappa_V}{8\pi v_w R_{\rm in}}$$

where the opacity is $\kappa_V \approx 120$ cm^2 g^{-1}, we assume a wind velocity $v_w \approx 40$ km s^{-1} (the approximate line width of the narrow Balmer/He lines from the high resolution MIKE spectrum), and $R_{\rm in}$ is the inner radius of the dusty shell as calculated by DUSTY. For the range of plausible models, the estimated mass loss rates are $(4-5) \times 10^{-7}$ $M_\odot$ yr^{-1}. This is in agreement with typical mass loss rates of RSGs of this luminosity, significantly smaller than in super-AGB stars (Mauron & Josselin 2011; Poelarends et al. 2008) and greater than in BSGs (Martins et al. 2015). However, asymmetry and inhomogeneity (e.g. clumpiness) in the CSM can greatly affect our estimated optical depth. A more extensive review of these effects can be found in Kochanek et al. (2012).

2.4.2 The Progeny of SN 2010da and Its Environment

Our extensive photometric and spectroscopic datasets indicate that the source of SN 2010da is still active and underwent a dramatic transition to a bluer and hotter SED with a smaller radius of ≈ 6 AU after the 2010 eruption. Additionally, the progeny is significantly more luminous than the progenitor by a factor of $\sim 2-5$. Although it is possible that the bolometric luminosity of the progenitor was larger than we predict with a significant fraction of light contributed at longer wavelengths from cool dust which was heated during the transient, it is most likely that the ongoing mass ejections and their interaction with a compact companion/CSM are injecting additional energy into the system.

In addition to being brighter, the source is also undergoing significant variability in the optical of $\approx 1-2$ mags within a few hundred days. The variability and bolometric magnitude of the progeny ($M_{bol} \approx -7$) are reminiscent of supergiant long-period variables (Wood et al. 1983), although these do not typically show B[e]-like emission lines in their spectra nor are they often surrounded by a thick CSM.

To constrain the progeny properties, we use `DUSTY` to model the SEDs around 560 and 1880 days. Again using the constraint from the UVOT light curve, we find that the progeny is hotter than ≈ 8900 K. Additionally, at temperatures higher than ≈ 25000 K, the estimated radius becomes atypically small for a supergiant (i.e. $\lesssim 15$ $R_\odot$), although we can find acceptable fits beyond this temperature. To reiterate, we have previously ruled out a main sequence star as the progenitor of SN 2010da, meaning that the progeny must also be an evolved supergiant. These temperature and luminosity constraints are shown in an HR diagram in Figure 2.19. We can again calculate the mass loss rates

at these different epochs, this time assuming that a new wind of $v_w \approx 200$ km s^{-1} has formed. We find a mass loss rate of $\dot{M} \approx 3 \times 10^{-7}$ M$_\odot$ yr^{-1} at 560 days and a slightly larger rate of $\dot{M} \approx 6 \times 10^{-7}$ M$_\odot$ yr^{-1} at 1880 days. These numbers are consistent with the mass loss rate before the outburst.

The low luminosity, B[e] features and bluer SED are all consistent with a RSG transitioning into a blue loop phase of its evolution (Langer & Heger 1998). Additionally, the widths and shapes of the multi-component emission lines are consistent with a newly formed wind interacting with existing mass loss seen in the early stages of a blue-loop phase of a RSG (Chita et al. 2008). The blue loop occurs when RSGs evolve off the Hayashi-line towards the BSG regime as their envelope structure shifts from convective to radiative. During this transition, the envelope of the RSG will spin up and the radius will drastically decrease (Heger & Langer 1998). During this evolution, the star can reach its critical rotation rate and develop a slow equatorial outflow, leading to B[e]-like emission lines.

The environment surrounding the progenitor/progeny is extremely complex, as indicated by the varying estimated electron densities from the Balmer decrement and the existence of forbidden calcium and iron lines. Like many supergiants, SN 2010da might be surrounded by a clumpy wind, which can explain the low- and high-density regions necessary to excite the various emission lines detected in our spectra. The progenitor's dust shell at ≈ 10 AU seems to have been at least partially destroyed by the initial transient based on the strong initial UV and X-ray detections. However, the continued infrared excess and SED shape suggests that either some of this dust survived or new dust has since formed at ≈ 6 AU. The surrounding CSM is carbon rich and irradiated by X-ray/UV emission from the compact binary companion, meaning some dust must be

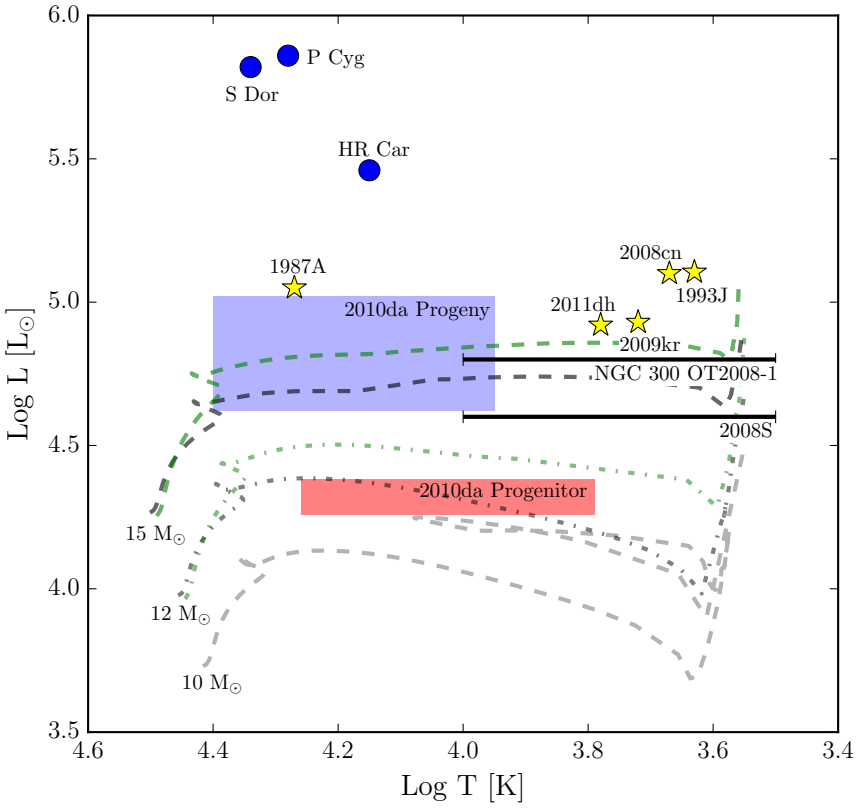

Figure 2.19: Stellar evolutionary tracks of 10 $M_\odot$, 12 $M_\odot$ and 15 $M_\odot$ RSG models with (green) and without (black) rotation from Ekstrom et al. (2012) compared to the estimated temperatures and luminosities of progenitor (red) and progeny (blue) of SN 2010da. For comparison, we also show the progenitors of NGC 300 OT2008-1 (Prieto et al. 2008), SN 2008S (Prieto 2008), several supernovae and three well-studied LBVs: S Doradus, P Cygni, and HR Carinae (Humphreys et al. 2011).

continuously destroyed and formed. During periods of eruptions and enhanced accretion, the UV emission excites coronal iron lines in the CSM, which we observe in the most recent optical spectra taken at 1819 and 1881 days.

2.4.3 SN 2010da as a High Mass X-ray Binary

Based on the strong X-ray luminosity ($\sim 10^{37}$ erg s^{-1}) detected well before and after the optical transient, the strong He II 4686Å emission, the coronal iron lines, and the hard X-ray spectrum, we conclude that SN 2010da is in a supergiant X-ray binary system exhibiting B[e] phenomena. A similar conclusion was reached by Binder et al. (2011) and Lau et al. (2016). However, it is difficult to make a definitive statement about the nature of the compact object itself. The ultraluminous X-ray transient is far above the Eddington limit of a 1.4 $M_\odot$ neutron star, but the hard spectrum ($\Gamma \approx 0$) and the high X-ray luminosity are consistent with other SGXBs with neutron star companions, such as Vela X-1 (Wang 2014; Binder et al. 2011; Lewin et al. 1997). It is possible to explain the super-Eddington luminosity of the initial outburst by invoking beaming along the line of sight or large magnetic fields (Mushtukov et al. 2015). In fact, a ULX powered by a neutron star was recently discovered with an X-ray luminosity greater than the peak luminosity of SN 2010da (Bachetti et al. 2014).

SN 2010da also exhibits B[e] phenomena, consistent with a B[e] X-ray binary. Such binaries typically undergo two types of transients: dimmer ($L_X \sim 10^{36-37}$ erg s^{-1}), shorter ($\tau \sim$ days) Type I outbursts which are associated with the orbital period of the binary, and brighter ($L_X \gtrsim 10^{37}$ erg s^{-1}), longer ($\tau \gtrsim$ weeks) Type II outbursts which are possibly associated with the disruption of the B[e] disk (Reig 2011). The disk-disruption

theory has undergone recent criticism following the discovery of several disks that have remained intact after a Type II outburst (Reig & Fabregat 2015). The duration (~ 50 days) and hard spectral index ($\Gamma \sim 0$) of the progeny of SN 2010da are consistent with a Type II outburst (Reig & Nespoli 2013). However, the X-ray luminosity during the transient ($L_X \approx 6 \times 10^{39}$ erg s^{-1}) is much more luminous than typical Type II outbursts ($L_X \approx 10^{37} - 10^{38}$ erg s^{-1}). Because little is known about the physical origin of Type II outbursts, we cannot definitely say if SN 2010da is an unusual Type II outburst or a new type of X-ray transient associated with eruptive stellar mass loss.

2.4.4 Comparison to Other Dusty ILOTs and Impostors

Although the canonical model of dusty ILOTs are massive LBVs ejecting dense shells of mass, it has become clear in recent years that these events arise from a variety of progenitors (Berger et al. 2009; Smith et al. 2011; Kochanek et al. 2012). Most of the well-studied ILOTs and their progenitors lie in one of two observational classes. The first class is made up of objects with blue and luminous progenitors, such as LBVs or yellow hypergiants (e.g. SN 2009ip, SN 1954J). ILOTs in the "blue" class survive their transients and can undergo multiple eruptions. Objects in this class include rare η Carinae analogs such as the recent UGC 2773-OT (Smith et al. 2016b) and several ILOTs associated with yellow hypergiants undergoing LBV-like outbursts, like SN Hunt 248 (Mauerhan et al. 2015) and PSN J09132750+7627410 (Tartaglia et al. 2016). The second class of ILOTs is made up of objects with red and extremely cool (T $\sim$ 100s K) progenitor SEDs. These ILOTs appear to be terminal explosions which are potentially electron capture SNe from massive AGB stars (e.g. SN 2008S, NGC 300 OT2008-1),

although other theories exist to explain these events (Smith et al. 2011; Kochanek et al. 2012; Adams et al. 2016).

Does the system hosting SN 2010da fit into one of these two classes? We directly compare the progenitor, transient and progeny associated with SN 2010da to two red dusty ILOTs (SN 2008S and NGC 300 OT2008-1) and two blue ILOTs thought to be LBVs (SN 1954J, or Variable 12 in NGC 2403, and SN 2009ip).

SN 2008S and NGC 300 OT2008-1 had peak absolute magnitudes of $M_V \approx -14$ and $M_V \approx -12$, respectively. These two objects exhibited similar properties and have since faded beyond their initial progenitor luminosities in the IR (Adams et al. 2016). SN 2008S and NGC 300 OT2008-1 had progenitors whose SEDs were consistent with cool circumstellar dust ($T \approx 300 - 500$ K) and large radii ($R \approx 150 - 350$ AU) (Prieto et al. 2008; Khan et al. 2010). These temperatures are about four times cooler than the progenitor of SN 2010da (≈ 1500 K), and their estimated radii are about 10 times larger. The luminosities of these progenitors were $\sim 2 - 3$ times higher than the progenitor of SN 2010da. On the opposite end of the ILOT spectrum lie the blue ILOTs: SN 1954J, a massive star in NGC 2403 which underwent an LBV-like eruption and remains active today, and SN 2009ip, an LBV in NGC 7259 which likely exploded in 2012 (Smith et al. 2010; Margutti et al. 2013; Mauerhan et al. 2013). Prior to 1949, the progenitor of SN 1954J had a blue magnitude of $M_b \approx -6.6$ (assuming a distance modulus of 27.6; Smith et al. 2001). Similarly, the progenitor of SN 2009ip was extremely bright ($M_{Bol} \approx -10$) and variable by as much as one magnitude before its 2009 outburst. Both progenitors of these blue ILOTs are notably brighter and bluer than the progenitor of SN 2010da. The progenitor SED of SN 2010da sits between these two classes, as shown in Figure 2.20.

These objects show similar diversity during their transient light curves. Within the first month of discovery, the red ILOTs (SN 2008S and NGC 300 OT2008-1) experienced a similar decay rate of ≈ 0.03 mag d^{-1} (Berger et al. 2009) — much more slowly than SN 2010da, which decayed at ≈ 0.1 mag d^{-1}. Although NGC 300 OT2008-1's light curve steepens at later times (to ≈ 0.06 mag d^{-1}), it does not exceed the decline rate of SN 2010da. In contrast, the decline rate of SN 2009ip's 2009 outburst within the first month (≈ 0.2 mag d^{-1}) is faster than that of SN 2010da (Smith et al. 2010). In the case of SN 2009ip, such a fast decline rate was attributed by Smith et al. 2010 to the ejection of an optically thick shell, which is not ruled out as a possibility for SN 2010da.

Spectroscopically, SN 2010da shares features with both the red and blue ILOT classes. For example, the red ILOTs and SN 2010da share similar narrow Balmer and forbidden calcium lines, with Hα reaching a maximum width of ≈ 1200 km s^{-1}. Like NGC 300 OT2008-1, we detect He I emission in SN 2010da, but we additionally detect He II due to the X-ray/UV-enriched environment from the compact companion. Most notably unlike NGC 300 OT2008-1, our high resolution spectrum reveals Balmer lines which are weakly asymmetric and lacking any absorption; high-resolution spectra of NGC 300 OT2008-1 reveal Hα emission with clear absorption slightly blueward of rest wavelength (Berger et al. 2009; Bond et al. 2009). Similarly, the blue ILOTs are also dominated by hydrogen Balmer and Fe II emission (typical of hot LBVs) with FWHM ≈ 550 km s^{-1} (Smith et al. 2010; Margutti et al. 2013). Unlike SN 2010da, there was no [Ca II] emission detected in SN 2009ip, although [Ca II] emission has been detected in eruptions of cool LBVs such as UGC 2773-OT (Smith et al. 2010). Late time spectra of SN 1954J reveal broad Hα emission with ≈ 700 km s^{-1}, broader than what is observed in the progeny of SN 2010da.

One of the most notable differences between SN 2010da/the red ILOTs and the blue ILOTs is the fate of their progeny. The blue ILOTs underwent clearly non-terminal eruptions (excluding the 2012 explosion of SN 2009ip; Margutti et al. 2013; Mauerhan et al. 2013). Specifically, recent photometry shows that the progeny of SN 1954J has since faded by ≈ 2 mag in the optical and is now consistent with a blackbody with temperature of ≈ 6500 K. This has been interpreted as an η Car analog which is now shrouded in a dusty nebula similar to η Car's Homunculus (Smith et al. 2001; Van Dyk et al. 2005). The most recent SED of SN 1954J is much bluer than that of SN 2010da and suggests a notably higher bolometric luminosity ($\approx 10^5$ $L_\odot$). Based on luminosity and the SED, SN 2010da is unlikely to be an LBV outburst. In contrast, the progenies of SN 2008S and NGC 300 OT2008-1 have faded past their progenitors in the IR, leading some authors to argue that they were electron-capture supernovae from super AGB stars (Botticella et al. 2009; Thompson et al. 2009; Adams et al. 2016). The clear re-brightening of the progeny of SN 2010da several hundred days after the 2010 eruption illustrates that it is not a member of this red class of transients, but its similarities might point to a related progenitor which is entering the last phase of its life.

Thus, SN 2010da is unlike many of the previously studied ILOTs. First, the transient is not energetic enough to be a true LBV outburst. We can roughly estimate the energy radiatively emitted from SN 2010da as $\approx L_{\rm peak} t_{1.5}$, where $L_{\rm peak}$ is the peak luminosity and $t_{1.5}$ is the time it takes the transient to dim by 1.5 magnitudes (see Smith et al. 2011). We estimate $t_{1.5} \lesssim 30$ days based on the upper limit reported by Monard (2010), and we estimate the peak luminosity to be $L_{\rm peak} = 4.5 \times 10^{39}$ erg s^{-1}. The total radiative energy is thus $\lesssim 10^{46}$ erg. This is less energetic than the typical LBV outburst ($\approx 10^{47}$ erg; Smith et al. 2011). SN 2010da is also less energetic that the red

SN 2008S-like ILOTs, which radiate about $L_{\rm peak}t_{1.5} \approx 5 \times 10^{47}$ erg. Additionally, SN 2008S-like events are either terminal or produce progeny that are notably dimmer than their progenitors (Adams et al. 2016); the progeny is currently more luminous than its progenitor by a factor of ≈ 5.

2.5 Summary and Conclusions

We presented comprehensive, multi-wavelength observations (X-ray, UV, optical and IR) of the dusty ILOT SN 2010da, extending thousands of days before and after the outburst. These observations allowed us to study the progenitor, outburst and progeny in great detail. Due to its low luminosity and red SED, SN 2010da seems inconsistent with an LBV outburst as interpreted by Binder et al. (2016). From our dataset, we conclude that SN 2010da was the eruption of a massive star ($\sim 10 - 12$ $M_\odot$) exhibiting B[e] phenomena. The high-resolution spectra exhibit double-peaked Balmer and Paschen emission lines with narrow components consistent with a pre-existing RSG wind and a newly formed supergiant wind. This suggests that the star responsible for SN 2010da may be a YSG transitioning onto a blue loop. The optical variability and iron/calcium emission indicate a complicated CSM which is repeatedly disturbed by mass loss of the primary star.

The supergiant responsible for SN 2010da is likely the primary star of a HMXB. The system shows consistently high X-ray luminosity ($L_X \approx 10^{37}$ erg s^{-1}), and during the 2010 event, the system underwent an ultraluminous X-ray outburst ($L_x \approx 6 \times 10^{39}$ erg s^{-1}). Late time emission of coronal iron lines are fueled by a hot, X-ray- and UV-rich region near this binary. While we cannot make a definitive statement about the nature of

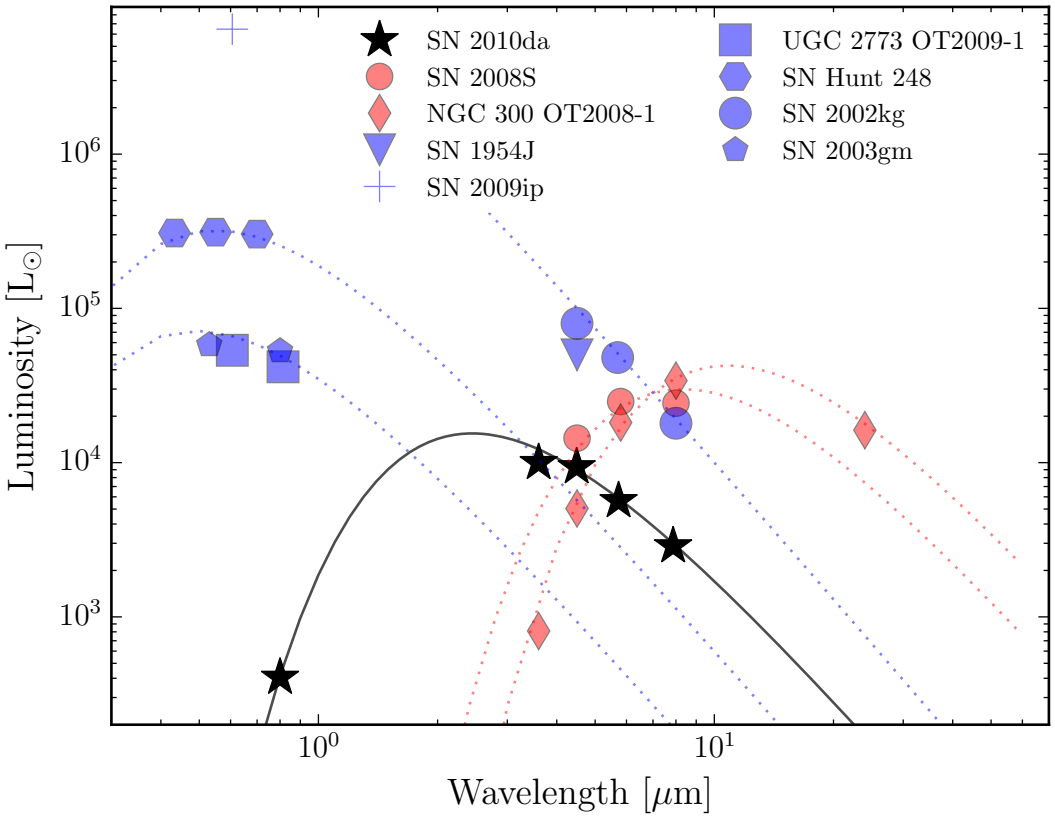

Figure 2.20: Progenitor SEDs of LBV-like (blue) and SN 2008S-like (red) ILOTs compared to the SED of the progenitor of SN 2010da (black). SN 2010da sits between these two classes. The dashed lines are black body fits for select objects to guide the eye.

the compact object, dedicated and deep X-ray observations may shed light on its nature.

SN 2010da is unique in the heterogeneous class of ILOTs. Its progenitor was dimmer and bluer than the AGB-like progenitors of dusty ILOTs NGC 300 OT2008-1 and SN 2008S; however, it is notably dimmer and redder than LBVs and yellow hypergiants experiencing similar outbursts. Also unlike other dusty ILOTs and supernova impostors, the progeny of SN 2010da is more luminous than its progenitor in both the IR and optical. The progeny is still undergoing significant outbursts, and continued followup is crucial in understanding the elusive nature of this object.

Like many ILOTs, SN 2010da marks an important point in stellar evolution of increased activity and mass loss. SN 2010da highlights the diversity of dusty ILOTs and the need for multi-wavelength photometric and high-resolution spectral followup to understand these objects. It is no doubt that future facilities such as LSST will populate the intermediate luminosity gap which currently exists. Extensive spectroscopic followup of current events will allow us to identify archetypes, like SN 2010da, of classes which will arise from these surveys.

Table 2.1:: *Spitzer* Photometry

Instrument	AOR	PI	Date (UT)	Epoch (Days)	Filter	AB Magnitude
IRAC	6069760	Helou	2003-Nov-21	−2375	3.6	18.77 ± 0.10
IRAC	6069760	Helou	2003-Nov-21	−2375	4.5	18.55 ± 0.07
IRAC	6069760	Helou	2003-Nov-21	−2375	5.8	19.10 ± 0.52
IRAC	6069760	Helou	2003-Nov-21	−2375	8	19.51 ± 0.76
MIPS	22611456	Kennicutt	2007-Jul-16	−1042	24	> 17.00
IRAC	22517504	Kennicutt	2007-Dec-29	−876	3.6	18.79 ± 0.07
IRAC	22517504	Kennicutt	2007-Dec-29	−876	4.5	18.67 ± 0.05
IRAC	22517504	Kennicutt	2007-Dec-29	−876	5.8	19.50 ± 0.51
IRAC	22517504	Kennicutt	2007-Dec-29	−876	8	>17.45
IRAC	31527680	Freedman	2009-Dec-21	−153	3.6	18.39 ± 0.07
IRAC	31527424	Freedman	2010-Jan-13	−130	3.6	17.84 ± 0.04
IRAC	31528448	Freedman	2010-Jul-27	65	3.6	17.87 ± 0.04
IRAC	31528192	Freedman	2010-Aug-16	85	3.6	18.11 ± 0.05
IRAC	31527936	Freedman	2010-Aug-31	100	3.6	18.36 ± 0.07
IRAC	42195968	Kochanek	2011-Aug-29	463	3.6	18.68 ± 0.09
IRAC	42195968	Kochanek	2011-Aug-29	463	4.5	18.85 ± 0.08
IRAC	42502912	Kasliwal	2012-Jan-14	601	3.6	18.66 ± 0.08
IRAC	42195712	Kochanek	2012-Aug-10	810	3.6	18.41 ± 0.07
IRAC	42195712	Kochanek	2012-Aug-10	810	4.5	18.58 ± 0.07
IRAC	50572032	Kasliwal	2014-Mar-13	1390	3.6	18.41 ± 0.07

Table 2.2 Continued:

IRAC	50572032	Kasliwal	2014-Mar-13	1390	4.5	18.65 ± 0.07
IRAC	50573056	Kasliwal	2014-Sep-05	1566	3.6	18.16 ± 0.05
IRAC	50573056	Kasliwal	2014-Sep-05	1566	4.5	18.23 ± 0.05
IRAC	50572544	Kasliwal	2014-Oct-03	1594	3.6	18.21 ± 0.06
IRAC	50572544	Kasliwal	2014-Oct-03	1594	4.5	18.28 ± 0.05
IRAC	50044672	Fox	2014-Oct-14	1605	3.6	18.26 ± 0.06
IRAC	50044672	Fox	2014-Oct-14	1605	4.5	18.34 ± 0.04
IRAC	53022208	Kochanek	2015-Feb-09	1723	3.6	18.33 ± 0.06
IRAC	52691712	Kasliwal	2015-Sep-22	1948	3.6	17.91 ± 0.05
IRAC	52691712	Kasliwal	2015-Sep-22	1948	4.5	18.03 ± 0.03
IRAC	52691968	Kasliwal	2015-Sep-29	1955	3.6	17.90 ± 0.04
IRAC	52691968	Kasliwal	2015-Sep-29	1955	4.5	18.03 ± 0.03
IRAC	52692224	Kasliwal	2015-Oct-12	1968	3.6	17.89 ± 0.05
IRAC	52692224	Kasliwal	2015-Oct-12	1968	4.5	17.99 ± 0.03
IRAC	52692480	Kasliwal	2016-Feb-22	2101	3.6	18.09 ± 0.06
IRAC	52692480	Kasliwal	2016-Feb-22	2101	4.5	18.18 ± 0.04
IRAC	52692736	Kasliwal	2016-Feb-29	2108	3.6	18.13 ± 0.05
IRAC	52692736	Kasliwal	2016-Feb-29	2108	4.5	18.19 ± 0.04
IRAC	52692992	Kasliwal	2016-Mar-19	2127	3.6	18.23 ± 0.06
IRAC	52692992	Kasliwal	2016-Mar-19	2127	4.5	18.22 ± 0.05

Table 2.3:: Ground-based Optical Photometry

Date (UT)	Epoch (days)	Instrument	Filter	AB Magnitude
2008-Sep-09	−609	IMACS	i'	24.19 ± 0.20
2009-Nov-25	−179	MegaCam	i'	> 24.4
2009-Nov-25	−179	MegaCam	r'	> 24.4
2009-Nov-25	−179	MegaCam	g'	> 24.4
2010-Nov-13	174	IMACS	i'	22.97 ± 0.06
2010-Nov-13	174	IMACS	r'	22.85 ± 0.04
2011-Jan-12	234	LDSS-3	i'	21.64 ± 0.03
2011-Oct-21	516	LDSS-3	i'	19.77 ± 0.06
2011-Oct-21	516	LDSS-3	r'	19.42 ± 0.04
2011-Oct-21	516	LDSS-3	g'	20.58 ± 0.03
2011-Dec-27	583	IMACS	i'	20.29 ± 0.05
2011-Dec-27	583	IMACS	r'	20.27 ± 0.09
2011-Dec-27	583	IMACS	g'	22.29 ± 0.20
2012-May-17	725	LDSS-3	i'	21.65 ± 0.04
2012-May-17	725	LDSS-3	r'	21.94 ± 0.04
2012-May-17	725	LDSS-3	g'	22.32 ± 0.03
2013-Jan-11	964	LDSS-3	i'	21.70 ± 0.04
2013-Jan-11	964	LDSS-3	r'	20.75 ± 0.06
2013-Jul-15	1149	LDSS-3	i'	20.06 ± 0.01
2013-Dec-30	1317	LDSS-3	i'	20.80 ± 0.18
2014-Jun-26	1495	LDSS-3	i'	21.03 ± 0.01

Table 2.3 Continued:

2015-May-15	1818	IMACS	i'	20.03 ± 0.02
2015-May-15	1818	IMACS	r'	18.89 ± 0.13
2015-Jul-17	1881	IMACS	i'	20.18 ± 0.02
2015-Jul-17	1881	IMACS	r'	19.87 ± 0.02
2015-Jul-17	1881	IMACS	g'	20.99 ± 0.03
2015-Aug-01	1896	IMACS	i'	19.71 ± 0.05
2015-Aug-01	1896	IMACS	r'	20.09 ± 0.05
2015-Aug-01	1896	IMACS	g'	20.74 ± 0.08

Table 2.2:: Magellan/*FourStar* Photometry

Date (UT)	Epoch	Filter	AB Magnitude
2011-Dec-07	563	J	14.47 ± 0.09
2011-Dec-07	563	H	14.17 ± 0.11
2011-Dec-07	563	K_s	14.21 ± 0.12
2015-Jul-31	1895	J	14.23 ± 0.02
2015-Jul-31	1895	H	13.76 ± 0.03
2015-Jul-31	1895	K_s	13.57 ± 0.02
2015-Aug-18	1913	H	13.97 ± 0.01
2015-Aug-18	1913	K_s	13.63 ± 0.02

Table 2.4:: *HST* Photometry

Start Date (UT)	Epoch	Proposal ID	PI	Filter	AB Magnitude
2012-Jul-18	787	12450	Kochanek	F814W	20.63 ± 0.03
2014-Jul-02	1501	13515	Binder	F606W	20.68 ± 0.02
2014-Jul-02	1501	13515	Binder	F814W	20.99 ± 0.03

Table 2.5:: Ground-based Optical Spectroscopy

Date (UT)	Epoch (days)	Instrument	Exposure (s)	Grating/Grism	Resolution (Å)
2010-May-25	2	GMOS-S	1200	R400	4
2010-May-25	2	GMOS-S	600	B600	4
2010-Jun-07	15	MIKE	1800	R2	0.3
2010-Jun-07	15	MIKE	1800	R2.4	0.4
2010-Jul-02	40	GMOS-S	1200	R400	4
2010-Jul-02	40	GMOS-S	900	B600	4
2011-Oct-21	516	MagE	1200	-	2
2011-Dec-29	585	IMACS	300	300-17.5	5
2015-May-16	1819	IMACS	1500	300-17.5	5
2015-Jul-17	1881	IMACS	1800	300-17.5	5

Table 2.6:: *Swift UVOT*/ Photometry

Date	Epoch	AB Magnitude					
(UT)		UVW2	UVM2	UVW1	U	B	V
2010-May-26	3	18.27 ± 0.08	18.06 ± 0.07	17.48 ± 0.07	16.72 ± 0.07	16.48 ± 0.07	16.23 ± 0.07
2010-May-27	4	18.20 ± 0.08	17.96 ± 0.07	17.43 ± 0.071	16.67 ± 0.07	16.43 ± 0.07	16.17 ± 0.08
2010-May-28	5	18.33 ± 0.08	18.10 ± 0.07	17.57 ± 0.07	16.73 ± 0.067	16.53 ± 0.07	16.31 ± 0.08
2010-May-31	8	18.89 ± 0.09	18.58 ± 0.08	17.97 ± 0.076	17.21 ± 0.07	16.92 ± 0.08	16.61 ± 0.09
2010-Jun-01	9	19.31 ± 0.10	18.79 ± 0.08	18.25 ± 0.08	17.46 ± 0.08	17.20 ± 0.08	17.00 ± 0.11
2010-Jun-03	11	19.43 ± 0.11	18.93 ± 0.09	18.41 ± 0.10	17.48 ± 0.08	17.45 ± 0.10	17.05 ± 0.11
2010-Jun-05	14	19.61 ± 0.11	19.30 ± 0.09	18.61 ± 0.085	17.77 ± 0.08	17.63 ± 0.10	17.35 ± 0.12
2010-Jun-07	16	19.89 ± 0.12	19.58 ± 0.10	18.81 ± 0.092	18.06 ± 0.09	17.93 ± 0.11	17.75 ± 0.16
2010-Jun-09	18	20.07 ± 0.13	19.62 ± 0.10	1.46 ± 0.0	18.24 ± 0.10	18.14 ± 0.13	17.78 ± 0.16
2010-Jun-11	20	20.13 ± 0.14	19.83 ± 0.11	19.11 ± 0.10	18.53 ± 0.11	18.56 ± 0.17	18.02 ± 0.20
2010-Jun-16	24	20.49 ± 0.16	20.18 ± 0.13	19.46 ± 0.123	18.71 ± 0.12	18.87 ± 0.21	18.48 ± 0.27
2010-Jun-17	25	20.53 ± 0.17	20.10 ± 0.15	19.61 ± 0.15	18.92 ± 0.14	18.85 ± 0.20	18.59 ± 0.32
2010-Jun-18	26	20.51 ± 0.16	20.15 ± 0.13	19.52 ± 0.12	19.08 ± 0.14	19.03 ± 0.23	> 19.01

Table 2.6 Continued:

2010-Jun-21	29	21.05 ± 0.26	20.57 ± 0.24	19.89 ± 0.148	19.02 ± 0.14	> 19.71	> 18.25
2010-Jun-26	34	20.8 ± 0.24	20.08 ± 0.22	19.84 ± 0.181	19.28 ± 0.20	> 19.42	> 17.98
2010-Jul-02	40	21.21 ± 0.25	21.13 ± 0.23	20.54 ± 0.219	19.76 ± 0.21	> 19.82	> 19.00
2011-Oct-26	521	> 21.46	> 20.86	> 20.72	20.84 ± 0.30	> 19.43	> 18.62
2011-Oct-27	522	> 22.32	> 21.02	> 20.84	> 20.30	> 19.53	> 18.72
2011-Oct-28	523	> 21.64	21.85 ± 0.33	> 20.92	> 20.39	> 19.60	> 18.80

Table 2.7:: *Chandra* Photometry

Start Date (UT)	Epoch	Proposal ID	PI	Counts	Detection Significance	0.3 - 10 keV Flux (10^{-15} erg s^{-1} cm^{-2})
2010-Sep-24	123	12238	Williams	77 ± 9	21σ	$50.7^{+8.9}_{-9.2}$
2014-May-16	1453	16028	Binder	7 ± 3	3σ	$5.6^{+2.4}_{-3.3}$
2014-Nov-17	1638	16029	Binder	140 ± 12	52σ	142^{+12}_{-28}

Table 2.8:: Summary of SN 2010da Blackbody Fits

	Progenitor	Epoch 1	Epoch 9
T_C	1500 ± 40 K	3230 ± 490 K	2760 ± 250 K
T_H	...	9440 ± 280 K	9080 ± 330 K
R_C	9.4 ± 0.5 AU	9.5 ± 2.9 AU	10.5 ± 1.6 AU
R_H	...	1.59 ± 0.14 AU	1.25 ± 0.13 AU

Table 2.9:: Catalog of Spectral Lines Identified in Spectra of SN 2010da

Line	Epoch	Profile	Line Center (Å)	EW (Å)	FWHM (km s^{-1})	Flux (10^{-16} erg s^{-1} cm^{-2})
Fe I 3752.88	2	SP	3752.4	−0.2 (0.1)	$\lesssim$ 400	7 (1)
Fe I 3774.76	2	SP	3772.1	−1.30 (0.02)	420 (40)	6.46 (0.08)
Fe I 3800.61	2	DP	3802.0, 3804.0	−2.21 (0.09)	< 400 450	10.56 (0.09)
	15	SP	3800.1	−4(1)	420 (10)	...
	40	SP	3800.0	−1.4(0.3)	$\lesssim$ 300	0.5 (0.3)
Hη	2	SP	3839.0	−1.83(0.08)	570 (60)	7 (2)
	15	SP	3838.2	−1.8 (0.8)	440 (20)	...
	40	SP	3836.9	−2.4 (0.2)	140 (50)	1.0 (0.4)
Hζ	2	P-Cyg	3885.3, 3891.9	...	...	...
	15	DP	3890.1 3891.8	−9 (3)	430 (10) 65 (9)	...

Table 2.9 Continued:

	40	SP	3891.2	−3.1 (0.2)	350 (40)	2.6 (0.2)
Fe I 3935.81	2	P-Cyg	3932.9,	...	...	...
& Ca II K			3937.9			
	15	SP	3935.77	−5 (1)	390 (10)	...
	40	SP	3936.97	−15 (2)	470 (30)	1.1 (0.3)
Hϵ	2	DP	3976.0	−3.8 (0.1)	1100 (300)	27 (1)
& Ca II H			3973.13		490 (40)	
	15	DP	3971.8	−10 (2)	490 (20)	...
			3972.8		130 (20)	
	40	SP	3971.36	−18 (1)	< 300	5.2 (0.3)
Hδ	2	SP	4104.72	−5.52 (0.07)	560 (20)	32 (1)
	15	DP	4102.9	−6 (1)	42 (2)	...
			4104.1		449 (8)	...
	40	SP	4103.76	−12 (1)	480 (30)	2.2 (0.5)
	516	SP	4014.11	−12 (4)	110 (10)	...
Fe II 4174.62	2	ND	...	...	...	...

Table 2.9 Continued:

	15	SP	4174.86	−0.23 (0.05)	100 (10)	...
	40	SP	4174.81	−5.2 (0.2)	220 (30)	2.5 (0.3)
	516	SP	4175.29	−5.0 (0.7)	150 (20)	...
Fe II 4180.03	2	ND	...	...	...	...
	15	SP	4180.15	−0.7 (0.1)	220 (30)	...
	40	SP	4179.66	−15 (3)	590 (70)	1.3 (0.3)
	516	SP	4180.15	−6 (2)	900 (200)	...
Fe I 4237.12	2	SP	4236.24	−0.75 (0.02)	500 (50)	4.3 (0.7)
	15	SP	4234.9	−2.2 (0.2)	109 (6)	...
	40	SP	4234.6	−7.8 (0.6)	350 (50)	1.6 (0.2)
	516	SP	4235.0	−8 (1)	450 (60)	...
Hγ	2	SP	4342.9	−8.8 (0.1)	590 (20)	53 (1)
	15	DP	4342.2	−11 (2)	458 (9)	...
			4342.8		56 (2)	
	40	SP	4342.0	−29 (4)	180 (10)	8.6 (0.2)
	516	DP	4341.4	−19 (3)	510 (200)	...

Table 2.9 Continued:

			4342.9		120 (10)	
	1819	SP	4343.2	−9 (3)	400 (60)	2.2 (0.3)
	1881	SP	4343.2	−20 (20)	630 (140)	7 (1)
[O III] 4363	2	ND	...	...	...	...
& [Fe IX] 4359	15	SP	4364.3	−0.027 (0.008)	40 (4)	...
& Fe II	40	ND	...	...	...	...
	516	ND	...	...	...	...
	1819	SP	4365.8	−5 (1)	260 (50)	2.2 (0.1)
	1881	SP	4365.9	−30 (20)	500 (100)	7.2 (0.2)
Fe I 4384.77	2	P-Cyg	4382.0	...	...	...
			4388.3			
	15	SP	4387.1	−0.8 (0.1)	280 (20)	...
	40	SP	4387.0	−2.8 (0.2)	460 (80)	1.4 (0.1)
	516	SP	4388.0	−3.3 (0.4)	360 (40)	...
	1819	ND	...	...	...	...
Fe I 4416.36	2	SP	4418.6	−0.27 (0.01)	340 (80)	3.1 (0.5)

Table 2.9 Continued:

	15	SP	4418.5	−2.0 (0.2)	280 (10)	...
	40	SP	4417.3	−3.1 (0.3)	450 (70)	0.8 (0.3)
	516	SP	4418.0	−3.8 (0.4)	390 (40)	...
	1819	ND	...	...	...	...
	1881	ND	...	...	...	...
He I 4471.5	2	P-Cyg	4467.0	...	...	...
	2		4474.5			
	15	SP	4473.4	−2.7 (0.3)	370 (10)	...
	40	SP	4473.3	−3.7 (0.3)	340 (50)	0.8 (0.1)
	516	SP	4474.6	−2.9 (0.6)	250 (40)	...
	1819	ND	...	...	...	...
	1881	ND	...	...	...	...
Fe I 4585	2	SP	4586.0	−1.30 (0.03)	340 (80)	6 (1)
	15	SP	4586.0	−7 (1)	330 (50)	...
	40	SP	4585.9	−2.4 (0.7)	440 (50)	1.6 (0.7)
	516	SP	4585.9	−1.4 (0.3)	130 (20)	...

Table 2.9 Continued:

	1819	SP	4584.8	>-6	$\lesssim$ 230	< 0.9
	1881	SP	4587.8	>-6	600 (100)	< 1.0
He II 4686	2	SP	4683.0	−3.2 (0.6)	550 (30)	23 (1)
	15	SP	4687.2	−3.0 (0.2)	270 (10)	...
	40	SP	4686.7	−7.5 (0.5)	330 (20)	2.7 (0.2)
	516	SP	4687.6	−7 (2)	270 (20)	...
	1819	SP	4687.5	−12 (4)	480 (60)	1.6 (0.3)
	1881	SP	4687.6	−30 (10)	560 (70)	4.5 (0.7)
Hβ	2	SP	4863.6	−20.9 (0.4)	530 (20)	160.8 (0.7)
	15	DP	4862.9	−16 (1)	66 (3)	...
			4864.6		499 (7)	
	40	SP	4863.4	−110 (10)	360 (10)	36.3 (0.2)
	516	DP	4863.7	−70 (10)	106 (4)	...
			4861.7		540 (60)	...
	1819	SP	4863.8	−80 (20)	450 (10)	12.5 (0.2)
	1881	SP	4864.0	−170 (4)	620 (10)	24.7 (0.3)

Table 2.9 Continued:

[O III] 4959	2	ND	...	...	...	...
	15	SP	4960.3	> -0.4	50 (10)	...
	40	SP	4960.0	-2.3 (0.1)	280 (30)	0.4 (0.1)
	516	ND	...	...	...	...
	1819	SP	4960.9	-8 (1)	300 (40)	1.8 (0.3)
	1881	SP	4958.0	-20 (7)	530 (80)	3.1 (0.3)
[O III] 5007	2	SP	5007.9	-0.22 (0.03)	< 240	2.1 (0.5)
	15	SP	5008.0	-1.4 (0.1)	63 (2)	...
	40	SP	5008.0	-4.4 (0.5)	$\lesssim 240$	1.7 (0.3)
	516	ND	...	...	...	...
	1819	SP	5009.1	-25 (7)	350 (20)	5.6 (0.3)
	1881	DP	5008.3	-80 (10)	$\lesssim 300$	9.4 (0.3)
			5012.3		500 (20)	
Fe I 5017.87	2	SP	5020.15	-2.36 (0.02)	440 (20)	17.6 (0.2)
	15	DP	5021.1	-5.1 (0.8)	430 (20)	2.9 (0.2)
			5020.0		37 (3)	

Table 2.9 Continued:

	40	SP	5019.8	−7 (1)	350 (50)	3.2 (0.1)
	516	DP	5019.7	−7 (1)	420 (50)	...
			5020.7		$\lesssim$ 90	
	1819	ND	...	...	...	...
	1881	ND	...	...	...	...
[Fe VII] 5159	2	SP	5159.8	> 0.07	170 (50)	1.1 (0.1)
& Fe II	15	SP	5160.2	−1.2 (0.4)	< 80	...
	40	ND	...	...	...	...
	516	SP	5160.6	< 0.6	130 (30)	...
	1819	SP	5161.0	−6 (1)	< 290	0.4 (0.1)
	1881	SP	5161.0	−5 (2)	400 (100)	1.0 (0.2)
[Fe VII] 5276	2	–	...	...	...	Note: on chip
	15	SP	5277.4	−0.4 (0.1)	300 (30)	...
	40	–	...	...	...	Note: on chip
	516	SP	5276.6	−2.9 (0.4)	60 (10)	...
	1819	SP	5277.7	> -4	< 400	< 0.7

Table 2.9 Continued:

	1881	SP	5274.0	> -4	< 600	< 2
[O I] 5577	2	ND	...	...	...	...
	15	ND	...	...	...	...
	40	ND	...	...	...	...
	516	SP	5576.5	-0.08 (0.04)	60 (20)	...
	1819	SP	5577.2	-11 (2)	180 (20)	0.20 (0.08)
	1881	SP	5577.3	$+4$ (1)	300 (50)	-1.0 (0.1)
[N II] 5755	2	ND	...	...	...	...
& Fe II	15	SP	5756.3	-1.2 (0.1)	200 (100)	0.4 (0.1)
	40	ND	...	...	...	...
	516	ND	...	...	...	...
	1819	SP	5756.5	-0.9 (0.5)	200 (100)	0.29 (0.03)
	1881	SP	5753.6	-6 (2)	800 (200)	1.5 (0.4)
He I 5877	2	SP	5890.0	-5.1 (0.1)	450 (20)	36.6 (0.7)
	15	DP (LG)	5877.3	-6.2 (0.8)	30 (4)	...
			5878.7		370 (10)	

Table 2.9 Continued:

	40	SP	5878.2	−7.6 (0.7)	290 (20)	6.7 (0.3)
	516	SP	5877.5	−8 (2)	170 (20)	…
	1819	SP	5878.0	−11 (9)	360 (80)	0.4 (0.3)
	1881	SP	5878.5	−32 (7)	500 (40)	4.3 (0.5)
[Fe VII] 6086	2	SP	6088.4	−0.07 (0.01)	260 (60)	0.2 (0.1)
	15	SP	6088.3	> -0.3	240 (30)	…
	40	SP	6087.6	0.83 (0.03)	230 (30)	0.60 (0.06)
	516	ND	…	…	…	…
	1819	SP	6090.0	−3.3 (0.8)	280 (40)	0.7 (0.2)
	1881	SP	6088.8	−13 (4)	400 (50)	1.81 (0.3)
?	2	SP (L)	6280.5	+0.3 (0.1)	280 (50)	1.4 (0.4)
	15	ND	…	…	…	…
	40	ND	…	…	…	…
	516	ND	…	…	…	…
	1819	ND	…	…	…	…
	1881	ND	…	…	…	…

Table 2.9 Continued:

[O I] 6300	2	ND	...	...	...	...
	15	SP	6302.1	−0.53 (0.02)	270 (20)	...
	40	SP	6303.8	−0.73 (0.05)	240 (60)	0.28 (0.05)
	516	SP	6302.5	−1.4 (0.1)	150 (20)	...
	1819	SP	6302.2	−7.6 (0.7)	260 (50)	0.84 (0.04)
	1881	SP	6303.2	−9 (2)	400 (70)	1.0 (0.3)
[Fe X] 6374	2	SP	6380.8	−0.7 (0.1)	700 (100)	1.2 (0.2)
	15	SP	6375.5	−0.8 (0.1)	230 (20)	...
	40	P-Cyg	6360.4	...	...	...
			6374.9			
	516	ND	...	...	...	...
	1819	SP	6377.3	−18 (3)	270 (20)	2.7 (0.1)
	1881	SP	6377.8	−26 (4)	430 (40)	3.9 (0.2)
Hα	2	SP	6566.9	−105 (3)	556 (6)	660 (1)
	15	TP	6564.9,	−302 (2)	69.6 (0.4),	...
			6565.0,		494 (3),	

Table 2.9 Continued:

			6568.4		1074 (4)	
	40	SP (L)	6567.7	−680 (30)	490 (10)	292.7 (0.2)
	516	DP	6566.7	−260 (50)	140 (4),	...
			6570.4		280 (20)	
	585	SP	6566.7	−150 (30)	470 (20)	9.5 (0.3)
	1819	SP	6566.4	−980 (50)	360 (8)	164.0 (0.3)
	1881	DP	0 6563.3,	−1300 (100)	1700 (200),	256.7 (0.5)
			0 6565.8		570 (10)	
He I 6678	2	SP	6684.0	−3.98 (0.02)	580 (10)	17.4(0.9)
	15	SP	6681.2	−4.5 (0.2)	350 (10)	...
	40	SP	6682.7	−5.9 (0.2)	440 (20)	1.5 (0.2)
	516	SP	6681.3	−7.2 (0.7)	210 (10)	...
	1819	SP	6681.0	−5 (1)	260 (50)	0.8 (0.1)
	1881	SP	6680.3	−1.2 (0.7)	440 (90)	1.3 (0.2)
He I 7065	2	SP	7070.5	−5.44 (0.05)	500 (10)	30.4 (0.4)
	15	DP (LG)	7067.2,	−5.4 (0.8)	28 (3),	...

Table 2.9 Continued:

			7068.4		40 (20)	
	40	SP	7070.0	−9.8 (0.2)	428 (9)	4.46 (0.07)
	516	SP	7069.0	−6.6 (0.5)	200 (10)	...
	1819	SP	7067.7	−10 (1)	250 (20)	0.8 (0.1)
	1881	SP	7068.1	−18 (2)	280 (20)	1.5 (0.3)
He I 7281	2	ND	...	...	...	...
	15	SP	7284.8	−1.0 (0.1)	270 (40)	...
	40	ND	...	...	...	...
	516	ND	...	...	...	...
	1819	ND	...	...	...	...
	1881	ND	...	...	...	...
[CaII] 7291	2	ND	...	...	...	...
	15	SP	7293.7	> -0.2	$\lesssim 16$	...
	40	ND	...	...	...	...
	516	SP	7293.3	−0.5 (0.1)	$\lesssim 40$	...
	1819	ND	...	...	...	...

Table 2.9 Continued:

	1881	ND	...	...	...	...
[CaII] 7323	2	ND	...	...	...	...
	15	SP	7326.1	−0.123 (0.003)	$\lesssim$ 20	...
	40	ND	...	...	...	...
	516	SP	7326.0	−0.9 (0.1)	$\lesssim$ 60	...
	1819	ND	...	...	...	...
	1881	ND	...	...	...	...
O I 7774	2	P-Cyg	7765.4, 7783.1	...	...	...
	15	P-Cyg	7769.8, 7780.4	...	...	...
	40	P-Cyg	7771.7, 7781.0	...	...	...
	516	SP	7779.4	−1.9 (0.2)	90 (30)	...
	1819	ND	...	...	...	...
	1881	ND	...	...	...	...

Table 2.9 Continued:

[Fe XI] 7892	2	ND	...	...	...	...
	15	ND	...	...	...	...
	40	ND	...	...	...	...
	516	ND	...	...	...	...
	1819	SP	7895.3	−6 (2)	230 (40)	1.0 (0.2)
	1881	SP	7895.0	−17 (2)	400 (40)	1.9 (0.5)
O I 8446	2	SP (L)	8451.4	−5.6 (0.2)	160 (10)	6 (1)
	15	DP	8449.1, 8451.3	−10.3 (0.9)	35 (2), 470 (20)	...
	40	SP (L)	8452.1	−30 (10)	190 (20)	1.3 (0.2)
	516	SP	8450.0	−7 (2)	270 (20)	...
	585	SP	8450.3	−7 (1)	270 (60)	0.4 (0.1)
	1819	SP	8449.8	−6 (1)	270 (60)	6.3 (0.7)
	1881	SP	8449.4	−24 (4)	190 (10)	6.5 (0.8)
Ca II	2	P-Cyg	8495.6,	...	...	...
& Pa 8500			8509.1			

Table 2.9 Continued:

	15	DP	8500.6,	−11.1 (0.6)	36 (1),	...
			8503.7		418 (7)	
	40	SP	8503.6	−26 (1)	346 (9)	9.0 (0.1)
	516	DP	8504.3,	−16 (1)	60 (5),	...
			8500.8		30 (2)	
	585	SP	8502.3	−9 (3)	180 (30)	1.0 (0.2)
	1819	SP	8501.4	−7 (1)	620 (140)	1.4 (0.1)
	1881	SP	8498.5	−12 (2)	510 (60)	2.03 (0.09)
Ca II	2	SP	8549.0	−2.30 (0.06)	420 (20)	19.0 (0.9)
& Pa 8544	15	DP	8544.7,	−9 (2)	39 (1),	...
			8547.7		520 (70)	
	40	SP	8547.7	−20 (2)	320 (8)	7.56 (0.05)
	516	DP	8545.6,	−16 (1)	43 (3),	...
			8546.6		270 (20)	
	585	SP	8547.7	−7 (3)	240 (50)	0.7 (0.1)
	1819	SP	8547.3	−7 (1)	190 (40)	0.6 (0.1)

Table 2.9 Continued:

	1881	SP	8545.7	−7 (1)	250 (40)	1.21 (0.06)
Ca II	2	SP − flat	8669.9	−4.8 (0.1)	540 (20)	22.6 (0.5)
& Pa 8664	15	DP	8664.9,	−9.3 (0.9)	37 (4),	...
			8668.0		460 (40)	
	40	SP	8668.2	−16.7 (0.8)	301 (9)	5.30 (0.08)
	516	DP	8665.5,	−18 (3)	58 (4),	...
			8668.2		340 (30)	
	585	SP	8667.0	−8 (2)	190 (30)	< 0.4
	1819	SP	8666.0	−7 (2)	130 (40)	1.3 (0.3)
	1881	DP	8666.7,	−11 (1)	380 (70),	1.4 (0.1)
			8672.2		400 (300)	
Pa 8753	2	SP	8755.0	−1.88 (0.06)	410 (60)	5 (1)
	15	DP	8753.1,	−2.7 (0.2)	32 (5),	...
			8755.9		160 (10)	
	40	SP	8760.0	−13.1 (0.8)	550 (20)	3.6 (0.1)
	516	SP	8754.8	−3.7 (0.3)	150 (20)	...

Table 2.9 Continued:

	1819	ND	...	...	...	...
	1881	SP	8755.0	−6 (2)	180 (60)	1.0 (0.2)
Pa 8865	2	P-Cyg	8851.9, 8871.7	...	...	...
	15	DP	8865.4, 8867.8	−4.7 (0.6)	100 (10), 400 (30)	...
	40	SP	8868.0	−6 (1)	360 (50)	3.0 (0.3)
	516	SP	8867.4	−4.0 (0.5)	100 (10)	...
	1819	SP	8866.5	−1.1 (0.9)	100 (50)	2.0 (0.3)
	1881	SP	8865.6	−7.2 (0.9)	600 (100)	1.3 (0.2)
Pa 9017	2	SP	9024.3	−6.5 (0.5)	840 (70)	26.7 (0.9)
	15	SP	9020.5	−4.9 (0.5)	410 (50)	...
	40	SP	9021.6	−11 (1)	430 (30)	2.3 (0.1)
	516	SP	9019.0	−4.6 (0.5)	180 (20)	...
	1819	ND	...	...	...	...
	1881	SP	9018.3	−7 (1)	290 (50)	0.3 (0.1)

Table 2.9 Continued:

Pa 9232	2	SP	9234.1	−2.4 (0.2)	820 (240)	8 (1)
	15	DP	9231.7,	−2.4 (0.2)	49 (3),	...
			9235.2		110 (10)	
	40	DP	9227.1,	−7 (1)	180 (20),	2.8 (0.2)
			9236.3		630 (80)	
	516	SP	9233.0	−5.0 (0.7)	150 (20)	...
	1819	SP	9233.0	−8 (1)	150 (30)	0.40 (0.09)
	1881	SP	9232.1	−5 (1)	290 (50)	0.7 (0.3)
Paϵ 9548	2	SP	9557.1	−0.77 (0.02)	180 (40)	50 (1)
	40	SP	9553.1	−19 (4)	500 (60)	5.4 (0.2)
	1881	SP	9548.8	−9 (2)	280 (60)	4.2 (0.5)
Paδ 10052	2	SP	10057.1	−7.2 (0.2)	152 (7)	32 (2)
	40	SP	10051.7	−0.7 (0.9)	430 (70)	3 (1)
	1881	SP	10052.6	−10 (3)	230 (40)	3.7 (0.5)

Acknowledgments

We thank Rosanne Di Stefano, Sebastian Gomez, Josh Grindlay, Jeffrey McClintock, and Ramesh Narayan for helpful discussions. We also wish to thank Ian Thompson for obtaining the MIKE spectrum. This Chapter includes data gathered with the 6.5 meter Magellan Telescopes located at Las Campanas Observatory, Chile. This work is based in part on archival data obtained with the Spitzer Space Telescope, which is operated by the Jet Propulsion Laboratory, California Institute of Technology under a contract with NASA and based on observations obtained at the Gemini Observatory under the Program ID GS-2010A-Q-19, which is operated by the Association of Universities for Research in Astronomy, Inc., under a cooperative agreement with the NSF on behalf of the Gemini partnership: the National Science Foundation (United States), the National Research Council (Canada), CONICYT (Chile), Ministerio de Ciencia, Tecnología e Innovación Productiva (Argentina), and Ministério da Ciência, Tecnologia e Inovação (Brazil). This work made use of data supplied by the UK Swift Science Data Centre at the University of Leicester. Additionally, the scientific results reported in this article are based in part on data obtained from the Chandra Data Archive. VAV and PKB acknowledge support by the National Science Foundation through a Graduate Research Fellowship.

Chapter 3

Theoretical Models of Optical Transients: A Broad Exploration of the Duration–Luminosity Phase Space

This thesis chapter originally appeared in the literature as

V. A. Villar, E. Berger, B. D. Metzger, J. Guillochon, *The Astrophysical Journal* 849, 70

Abstract

The duration-luminosity phase space of optical transients is used, mostly heuristically, to compare various classes of transient events, to explore the origin of new transients, and to influence optical survey observing strategies. For example, several observational searches have been guided by intriguing voids and gaps in this phase space. However we should ask: Do we expect to find transients in these voids given our understanding of the various heating sources operating in astrophysical transients? In this work, we explore a broad range of theoretical models and empirical relations to generate optical light curves and to populate the duration-luminosity phase space (DLPS). We explore transients powered by adiabatic expansion, radioactive decay, magnetar spin-down, and circumstellar interaction. For each heating source, we provide a concise summary of the basic physical processes, a physically motivated choice of model parameter ranges, an overall summary of the resulting light curves and their the occupied range in the DLPS, and how the various model input parameters affect the light curves. We specifically explore the key voids discussed in the literature: the intermediate luminosity gap between classical novae and supernovae, and short-duration transients ($\lesssim 10$ days). We find that few physical models lead to transients that occupy these voids. Moreover, we find that only relativistic expansion can produce fast and luminous transients, while for all other heating sources, events with durations $\lesssim 10$ days are dim ($M_{\rm R} \gtrsim -15$ mag). Finally, we explore the detection potential of optical surveys (e.g., LSST) in the DLPS and quantify the notion that short-duration and dim transients are exponentially more difficult to discover in untargeted surveys.

3.1 Introduction

The initial classification of astronomical transient sources is phenomenological by necessity. Focusing on optical light curves as an example, one can extract a number of salient features including durations, colors, peak luminosities and rise/decline times (see e.g., Richards et al. 2011). The hope is that unique physical classes will ultimately become distinguishable in this multidimensional feature space without extensive photometric and spectroscopic datasets, leading in turn to physical insight about the underlying heating sources. Furthermore, the underlying distribution of objects within this multidimensional feature space can guide the design and optimization of future optical surveys. As larger optical surveys (such as the Zwicky Transient Facility, ZTF, and the Large Synoptic Survey Telescope, LSST) come online, understanding the distribution of transients within this space is essential for classification of optical light curves. There has been a number of works devoted to the computational and algorithmic problems of discovering and classifying transients from such surveys (Bailey et al. 2007; Karpenka et al. 2012; Lochner et al. 2016a; Charnock & Moss 2017a). However, little work has been done on the *expected* distribution of astrophysical transients within this feature space utilizing well-motivated physical models.

This work focuses on a useful subspace of the full feature space of optical transients: the duration-luminosity phase space (DLPS). The DLPS is valuable to astronomers for a number of reasons. Both duration and peak magnitude are easily measured from the light curve, and optical transients span a wide range in both properties. Additionally, when coupled with survey parameters and progenitor properties, the DLPS can be used to measure expected observational rates of each transient class or to tune survey

parameters to optimize the detectability of specific classes.

To date, the DLPS has been used mainly to collate transients after they have been observed and to illuminate "voids" in the observed DLPS. Of particular interest are two known voids: objects with short duration ($\lesssim$ 10 days) durations and objects which lie in the luminosity gap between classical novae and supernovae ($M_{\rm R} \sim -10$ to -14 mag). The latter has been noted in the literature as early as the 1930s (Baade 1938) and has been the focus of some observational searches (e.g.,Kasliwal 2011). However, it also essential to explore the DLPS using theoretical models that couple various heating sources with expected ranges of physical parameters relevant for each model in order to to understand if the voids in the DLPS can, in principle, be heavily occupied (e.g., Berger et al. 2013b).

Here we aim to take the first step of exploring the full extent of the DLPS using physically-motivated models and input parameter ranges, as well as a uniform framework for generating the models and populating the DLPS. We review a broad range of heating sources for optical transients and generate R-band light curves for each physical class. We then use these light curves to produce the DLPS, and we explore the overlap of classes with observed transients. We address the question of whether these voids appear to be occupied by theoretical models with reasonable ranges of physical parameters.

The layout of the Chapter is as follows. In Section 3.2, we introduce the mathematical framework for our one-zone models. In Section 3.3, we systematically explore a wide range of heating sources, their resulting light curves, and the ranges and trends that they follow in the DLPS. We discuss the resulting distributions and the broad discovery potential of untargeted surveys like LSST throughout the DLPS in

Section 3.4. We draw our primary conclusions about the DLPS, the observed voids, and the design of optical transient surveys in Section 3.5.

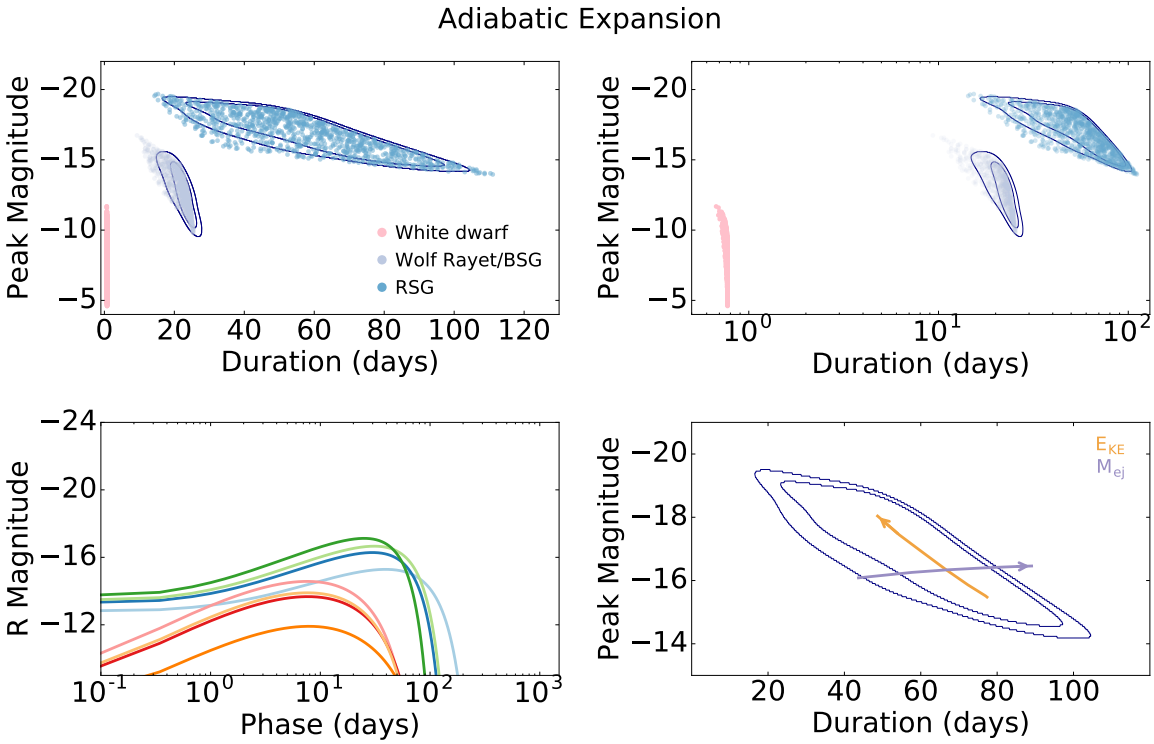

Figure 3.1: *Top Row*: DLPS for adiabatically expanding explosions for white dwarf progenitors (pink), Wolf Rayet/BSG progenitors (purple) and RSG progenitors (blue). Also shown are 68th and 90th percentile contours for the realizations, estimated using a kernel density estimate (KDE). The WD contours are omitted for clarity. *Bottom left*: Representative simulated light curves. *Bottom right*: Effect of $E_{\rm KE}$ (orange) and $M_{\rm ej}$ (purple) on adiabatically expanding light curves. Arrows point towards increasing values of each parameter, with all other parameters held constant. Also shown are the contours of the simulated light curve realizations for the RSG case.

3.2 One-Zone Models and Mathematical Framework

Throughout this Chapter we use simple one-zone models of transients within the framework laid out by Arnett (1980) for Type I SN light curves. For heating source we assume the following:

1. The ejecta are spherically symmetric and undergo homologous expansion, unless otherwise stated.
2. Radiation pressure dominates over electron and gas pressure in the equation of state.
3. The heating source is located in the center of the ejecta, unless otherwise stated.
4. The optical opacity is a constant $\kappa = 0.1$ cm^2 g^{-1}, unless otherwise stated. This is a typical value for stripped SNe (see e.g., Wheeler et al. 2015).
5. The initial radius is small, unless otherwise stated.

We can write the first law of thermodynamics as

$$\dot{E} = -P\dot{V} - \frac{\partial L}{\partial m} + \epsilon \tag{3.1}$$

where $E = aT^4V$ is the specific internal energy, $P = aT^4V/3$ is the pressure, $V = 1/\rho$ is the specific volume, L is the radiated bolometric luminosity, ϵ is the energy generation rate of the heating source, T is the temperature and ρ is the density (e.g., Arnett 1980; Chatzopoulos et al. 2012). In this framework, all available energy from the heating source supplies either the expansion of the ejecta or observable radiation, and we ignore

neutrino losses. Following our assumption of homologous expansion, the radius grows as $R(t) = vt$ (assuming a negligible initial radius), where we approximate v as the photospheric velocity, $v = v_{\rm ph}$. This assumption also means that no significant additional kinetic energy is added to the ejecta during the duration of the transient (i.e., the ejecta does not accelerate).

The sink terms in Equation 1 control the diffusion timescale of the system, which acts as a smoothing filter to the input luminosity function. During the photospheric phase at early times (i.e., the phase explored in this study), the luminosity and duration of the resulting transient depend heavily on the diffusion properties of the system. During the nebular phase at later times, the light curve of the transient should converge on the input luminosity of the heating source, assuming that the heating source is a smooth function.

The solution for generic input heat sources has been outlined in a number of works (e.g., Arnett 1980; Kasen & Bildsten 2010; Chatzopoulos et al. 2012). We cite the solutions derived by Chatzopoulos et al. (2012). For the case of a homologously expanding photosphere, the output luminosity is given by:

$$L_{\rm obs}(t) = \frac{2E_0}{t_{\rm d}} e^{-\left(\frac{t^2}{t_{\rm d}^2}+\frac{2R_0 t}{v t_{\rm d}^2}\right)} \times \int_0^t e^{-\left(\frac{t'^2}{t_{\rm d}^2}+\frac{2R_0 t'}{v t_{\rm d}^2}\right)} \left(\frac{R_0}{v t_{\rm d}} + \frac{t'}{t_{\rm d}}\right) L_{\rm in}(t') dt' + HS \quad (3.2)$$

where $L_{\rm in}$ is the input luminosity from the central heating source, $E_0 \sim M_{\rm ej} v_{\rm ph}^2/4$ is the initial energy of the transient, R_0 is the initial radius of the source, $t_{\rm d} = \sqrt{2\kappa M_{\rm ej}/\beta c v}$ is the diffusion timescale, and HS is the homogeneous solution to Equation 3.1 (the

solution with no source term), which will only be considered in the case of no internal sources of heating (Section 3.3.1). In most cases we consider $R_0 = 0$ (i.e., a small initial radius) and $\beta = \frac{4\pi^3}{9} \approx 13.7$, a geometric correction factor (Arnett 1982).

In the case of transients powered by interaction of the shock wave and circumstellar material (CSM), we consider diffusion through a fixed photospheric radius. The luminosity is then described by:

$$L_{\rm obs}(t) = \frac{2R_0}{vt_{\rm d}^2} e^{-\frac{2R_0}{vt_{\rm d}^2}t} \int_0^t e^{-\frac{2R_0}{vt_{\rm d}^2}t'} L_{\rm in}(t')dt' + HS' \tag{3.3}$$

where HS' is the homogeneous solution to Equation 1 for the fixed photosphere conditions. Again, we will neglect this term for the case of transients powered by ejecta-CSM interaction.

To generate light curves from these models, we use the open-source program `MOSFiT`[1] (Modular Open-Source Fitter for Transients v0.7.1). `MOSFiT` is a Python-based package that generates and fits semi-analytical models of various transients using modular scripts for different input heating sources, diffusion methods, template spectral energy distributions (SEDs), fitting routines, etc. (Guillochon et al. in prep.). We generate thousands of model light curves by sampling uniformly over reasonable parameter spaces for the various models (see Table 3.1 and Section 3). The `MOSFiT` modules used to generate the models are listed in Table 3.2. In all cases we assume a blackbody SED, and we report the properties of the R-band light curves at redshift $z = 0$ with no reddening. Our blackbody assumption is a reasonable approximation when broadly exploring the DLPS rather than detailed modeling for individual sources. We are specifically interested

[1] https://github.com/guillochon/mosfit

in the "first-order" properties of the optical light curves: the peak absolute magnitude and the duration. We define the duration as the timescale for the light curve to rise and decline by one magnitude relative to the peak. If the light curve is multi-peaked, with secondary peaks within 1 mag of the maximum luminosity, we include the secondary peak in the duration. We select R-band because it samples the mid-range of the optical wavelength regime. We stress that the choice of filter does not have a significant effect on our results, although in general the durations may be slightly shorter in bluer filters, and slightly longer in redder filters due to cooling of the blackbody SED as a function of time. We also note that at substantial redshifts the duration will be stretched by a factor of $1 + z$. However, given the resulting peak luminosities, most transients are expected to be detected at modest redshifts, and therefore time dilation will not be a significant factor compared to the ranges of physical parameters we consider in this work.

3.3 Specific Engine Sources

In this section we investigate various heating sources for optical transients and systematically explore the resulting light curves and the regions they occupy in the DLPS. In most cases, the free parameters of each class can be divided into two categories: those which contribute to the sink terms of Equation 1 (e.g., v, $M_{\rm ej}$) and those which contribute to the source term (e.g., $M_{\rm Ni}$, $P_{\rm spin}$, B). The parameters explored for each class, their ranges, and their sampling method (linearly or logarithmically spaced) are listed in Table 3.1.

In each subsection, we introduce the basic physics and free parameters of each heating source. We describe our choice of parameter ranges and the effect of each

parameter on the light curves. We then present the simulated DLPS, specifically highlighting boundaries or interesting features. Finally, we compare our simulated DLPS with observed objects when possible.

3.3.1 Adiabatic Expansion (No Central Heating Source)

Without a heating source, the light curves are entirely defined by the homogeneous solution to Equation 2 for an expanding photosphere:

$$L(t) = L_0 e^{-\left(\frac{t^2}{t_{\rm d}^2} + \frac{2R_0 t}{v_{\rm ej} t_{\rm d}}\right)} \tag{3.4}$$

where R_0 is the progenitor radius and $L_0 \approx E_{\rm KE}/2t_{\rm d}$ is the initial luminosity from the explosion. Although the bolometric luminosity is monotonically decreasing, the R-band light curve rises and then declines as the photosphere expands, and the peak of the blackbody SED evolves from shorter to longer wavelengths through the optical regime.

Rather than varying the progenitor radius across several orders of magnitude, we focus on three specific regimes that sample the full range of reasonable scenarios: white dwarfs ($R_0 \sim 0.01$ R$_\odot$, $M_{\rm ej} \sim 0.1 - 1$ M$_\odot$), Wolf-Rayet/blue supergiant (BSG)-like stars ($R_0 \sim 10$ R$_\odot$, $M_{\rm ej} \sim 1 - 10$ M$_\odot$) and red supergiant (RSG)-like stars ($R_0 \sim 500$ R$_\odot$, $M_{\rm ej} \sim 1 - 10$ M$_\odot$). Luminous blue variables (LBVs), known for their eruptive mass loss events, have radii intermediate between the BSG and RSG progenitors, $R_0 \sim 10 - 100$ R$_\odot$.

In Figure 3.1, we plot a sample of simulated light curves and the DLPS of each progenitor type, randomly sampling from uniform distributions of ejecta mass and

logarithmically in kinetic energy ($E_{\rm KE} \sim 10^{49} - 10^{51}$ erg). As expected, we find the general trend that larger progenitors produce longer-duration and more luminous transients. The upper and lower bounds to the quadrilateral-like areas each of these models occupy are defined by our chosen energy limits, while the vertical (duration) boundaries are set by our chosen ejecta mass limits. Only compact (WD) progenitors produce transients with durations $t_{\rm dur} \lesssim 1$ day all of which have a low luminosity ($M_{\rm R} \gtrsim -12$ mag). In contrast, the larger progenitors (BSG/RSG) only produce transients with longer durations ($t_{\rm dur} \gtrsim 10$ days) which are brighter ($M_{\rm R} \gtrsim -10$ mag). Thus, there is an overall clear positive correlation between luminosity and duration for this type of explosions.

The effects of the main parameters ($E_{\rm KE}$ and $M_{\rm ej}$) are explicitly shown in Figure 3.1. For a constant $E_{\rm KE}$, the transients become longer and somewhat brighter with increasing $M_{\rm ej}$. On the other hand, transients become shorter and brighter for increasing values of $E_{\rm KE}$ given a constant value of $M_{\rm ej}$. Therefore, the brightest (dimmest) transients with no central heating have large (small) kinetic energies and small (large) ejecta masses for a fixed value of R_0. We find that these trends are generally true in all other heating sources as well.

3.3.2 Radioactive Heating from Decay of ^{56}Ni

One of the most important and well-studied heating sources, responsible for the bulk of thermonuclear and stripped-envelope core-collapse SNe, is the radioactive decay of ^{56}Ni (and ^{56}Co) synthesized in the explosion (see Arnett 1979, 1980, 1982; Chatzopoulos et al. 2012, etc). The input luminosity is given by

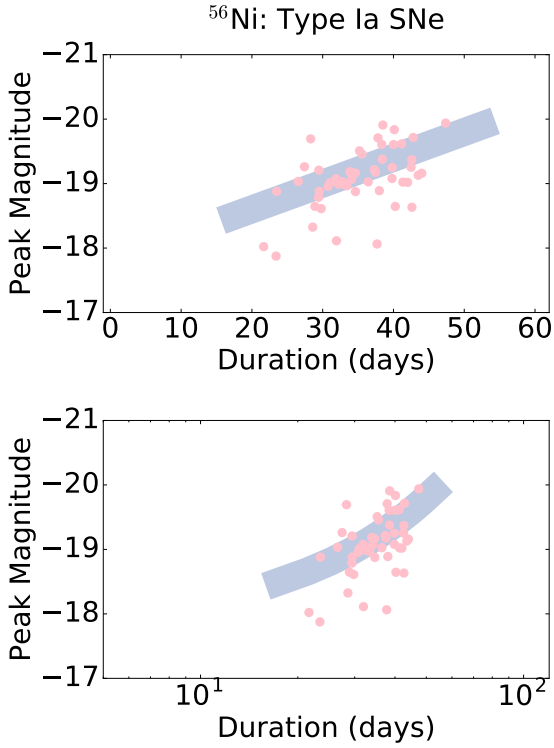

Figure 3.2: Derived duration-luminosity relation for Type Ia SNe using Equations 6 and 7, assuming a luminosity scatter of ≈ 0.2 mag (purple) with a sample of 50 well-sampled Type Ia SNe from the OSC after correcting for reddening and time dilation. This sample contains the 50 objects with redshifts $z \geq 0.1$ (to avoid distance-dominated errors in nearby SNe) with the greatest number of data points on the OSC at the time of writing. Objects from Riess et al. (1999); Stritzinger et al. (2002); Vinkó et al. (2003); Jha et al. (2006); Pastorello et al. (2007); Hicken et al. (2009); Contreras et al. (2010); Ganeshalingam et al. (2010); Silverman et al. (2011); Hicken et al. (2012); Silverman et al. (2012); Walker et al. (2015); Firth et al. (2015); Ferretti et al. (2016).

$$L_{\rm in}(t) = M_{\rm Ni}\left[\epsilon_{\rm Co}e^{-t/\tau_{\rm Co}} + (\epsilon_{\rm Ni} - \epsilon_{\rm Co})\,e^{-t/\tau_{\rm Ni}}\right] \tag{3.5}$$

where $M_{\rm Ni}$ (the initial nickel mass) is the only free parameter of this heating source. The energy generation rates of ^{56}Ni and ^{56}Co ($\epsilon_{\rm Ni} = 3.9 \times 10^{10}$ erg s^{-1} g^{-1} and $\epsilon_{\rm Co} = 6.8 \times 10^{9}$ erg s^{-1} g^{-1}) and the decay rates ($\tau_{\rm Ni} = 8.8$ days and $\tau_{\rm Co} = 111$ days) are known constants.

The radioactive decay of ^{56}Ni powers objects spanning a broad range of properties. We explore four regimes in this work: Type Ia SNe, Type Ib/c SNe, pair-instability SNe and Iax-like SNe.

Type Ia SNe

White dwarfs can explode as Type Ia SNe after thermonuclear ignition (Hoyle & Fowler 1960), although there is ongoing debate about whether this ignition arises from pure deflagration, delayed detonation or other mechanisms (see e.g., Khokhlov 1991; Arnett & Livne 1994; Phillips et al. 2007). Although it is unclear whether the progenitors of Type Ia SNe are single- or double-degenerate systems, Type Ia SNe occupy a narrow range of the DLPS due to their homogeneity.

Type Ia SNe have low ejecta masses ($M_{\rm ej} \approx 1.4$ M$_\odot$) with a relatively large fraction of this ejecta being radioactive ^{56}Ni ($f_{\rm Ni} \sim 0.3 - 0.5$). Rather than modelling these light curves using simple blackbody SEDs, we use an empirical relation described by Tripp & Branch (1999) and Betoule et al. (2014):

$$t_{\rm dur} = 35s \text{ days} \tag{3.6}$$

$$M_{\rm peak} = -19.4 + 1.4(s-1) \tag{3.7}$$

where s is the stretch of the light curve, which we range from 0.6 to 1.2 (roughly matching the range explored in Guy et al. 2005). We use the canonical ($s = 1$) template from Nugent et al. (2002) to extract a template R-band light curve to stretch. As a consistency check, we find that this relation roughly agrees with that found using the R-band templates from Prieto et al. (2006).

Using this relation, we find the well-known result that brighter (dimmer) Type Ia SNe have longer (shorter) durations. Type Ia SNe are constrained to a small subset of the DLPS, with durations of $t_{\rm dur} \sim 25 - 50$ days and $M_{\rm R} \sim -18$ to -20 mag. In Figure 3.2, we plot the duration-luminosity relation and several Type Ia SNe from the Open Supernova Catalog (OSC; Guillochon et al. 2017; see caption for details). To summarize, Type Ia SNe occupy a narrow portion of the DLPS, with no sources having durations of $t_{\rm dur} \lesssim 20$ days.

Type Ib/c SNe

Type Ib/c SNe occur when stripped-envelope massive stars undergo core-collapse at the end of their lives and are identified by their hydrogen-free (and helium-free in the case of Type Ic SNe) spectra. Type Ib/c SNe contain a relatively low fraction of ^{56}Ni ($f_{\rm Ni} \sim 0.01 - 0.15$) in their ejecta ($M_{\rm ej} \sim 1 - 10$ M$_\odot$; Drout et al. 2011). In this class, we include the parameter ranges for both normal and broad-lined Type Ib/c SNe and sample uniformly across their typical kinetic energies ($E_{\rm KE} \sim 10^{51} - 10^{52}$ erg).

Our simulated light curves (Figure 3.3) span a wide range in both absolute magnitude ($M_R \sim -16$ to -19 mag) and duration ($t_{\rm dur} \sim 10 - 120$ days). The brightest (dimmest) transients have the largest (smallest) ^{56}Ni masses ($f_{\rm Ni} M_{\rm ej}$), while the longest (shortest) durations are largely set by the ejecta velocity ($v \approx [E_{\rm KE}/M_{\rm ej}]^{1/2}$). Due to this positive correlation, the shortest duration transients ($t_{\rm dur} \sim 10$) also have the lowest luminosities ($M_{\rm R} \sim -16$ mag). We find essentially no transients with $t_{\rm dur} \lesssim 10$ d. Such transients would require faster ejecta velocities than typically observed in these sources.

We compare our generated light curve properties to samples from the literature (Drout et al. 2011; Taddia et al. 2015). The observed sample generally overlaps our simulated DLPS, although our models extend to shorter durations of $t_{\rm dur} \sim 10 - 20$ days which have not been observed.

Pair-instability SNe (PISNe)

It is predicted that stars with $M \sim 140 - 260$ M$_\odot$ will reach sufficiently high core temperatures to produce electron-positron pairs leading to a loss of pressure and a resulting thermonuclear runaway and explosion that leaves no remnant (Barkat et al. 1967). Due to the large ejecta masses and kinetic energies, the optical light curves are expected to be both bright and long-duration (Kasen et al. 2011; Dessart et al. 2013). We expect PISNe to have similar (extending to slightly larger) ^{56}Ni fractions as Type Ib/c SNe ($f_{\rm Ni} \sim 1 - 30\%$) but to have much larger ejecta masses ($M_{\rm ej} \sim 50 - 250$ M$_\odot$, with the lower masses representing stripped progenitors) and kinetic energies ($E_{\rm KE} \sim 10^{51} - 10^{53}$ erg); see Kasen et al. 2011.

In Figure 3.4, we show a sample of simulated PISNe light curves and the associated

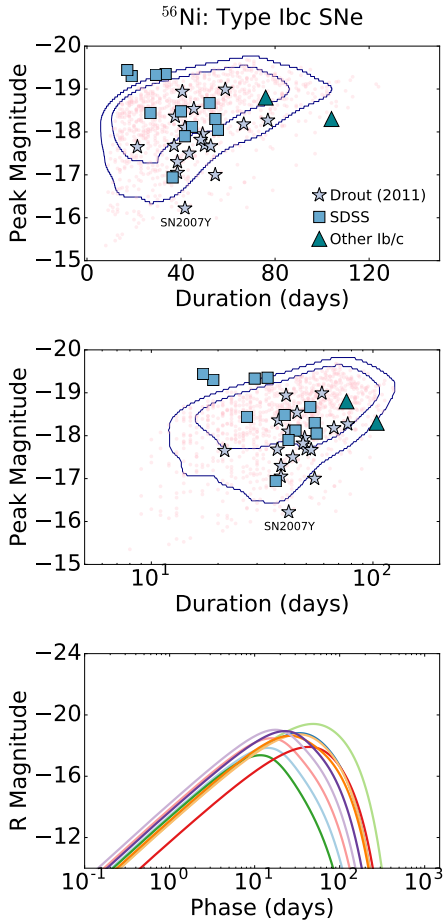

Figure 3.3: *Top & Middle*: DLPS of Type Ib/c SNe (pink) with a sample of observed objects from Drout et al. (2011) (purple stars) and Taddia et al. (2015) (blue squares). For both samples, we estimate the transient durations using the reported Δm_{15} values, assuming symmetric light curves about the peak. Exceptional long-duration events: SN 2011bm (Valenti et al. 2012) and iPTF15dtg (Taddia et al. 2016) are also plotted for comparison (green triangles). Also shown are 68th and 90th percentile contours for the realizations, estimated using a KDE. *Bottom*: Representative simulated light curves for Type Ib/c SNe.

DLPS. Compared to Type Ib/c SNe, the PISNe typically have longer durations ($t_{\rm dur} \sim 100 - 400$ days) and higher luminosities ($M_{\rm R} \sim -18$ to -22 mag). Like the other ^{56}Ni-decay powered models, the durations and luminosities are positively correlated, with the shortest duration transients ($t_{\rm dur} \sim 100$) being the least luminous ($M_{\rm R} \sim -18$ mag).

We compare our results to more detailed calculations by Kasen et al. (2011) and Dessart et al. (2013). The first order properties of the light curves are in rough agreement (Figure 3.4), although the Kasen et al. (2011) models allow for less energetic/luminous explosions. By allowing energy and ejecta mass to vary independently, our model explores a larger parameter space than comprehensive PISNe models in which the progenitor masses and kinetic energies are linked.

Ultra-stripped SNe/Iax-like SNe

Although ultra-stripped SNe and Iax SNe have some similar properties, they emerge from distinct physical scenarios and more detailed simulations predict unique spectral features. Ultra-stripped SNe are theorized to arise from helium star-neutron star binary systems which undergo significant stripping of the helium envelope (Tauris et al. 2015; Moriya et al. 2017). Iax SNe define a loose observational class which are spectroscopically similar to Type Ia SNe, although they are dimmer in optical bands (Foley et al. 2013).

Ultra-stripped SNe and Iax-like SNe have a high nickel content ($f_{\rm Ni} \sim 0.1 - 0.5$) similar to Type Ia SNe but have lower ejecta masses ($M_{\rm ej} \sim 0.01 - 1$ M$_\odot$) and kinetic energy ($E_{\rm KE} \sim 10^{49} - 10^{51}$ erg) compared to Type Ib/c SNe. In Figure 3.5 we present a sample of Iax-like SNe light curves and the associated DLPS. We find a tighter positive correlation between duration ($t_{\rm dur} \sim 10 - 50$ days) and peak magnitudes ($M_{\rm R} \sim -16$ to

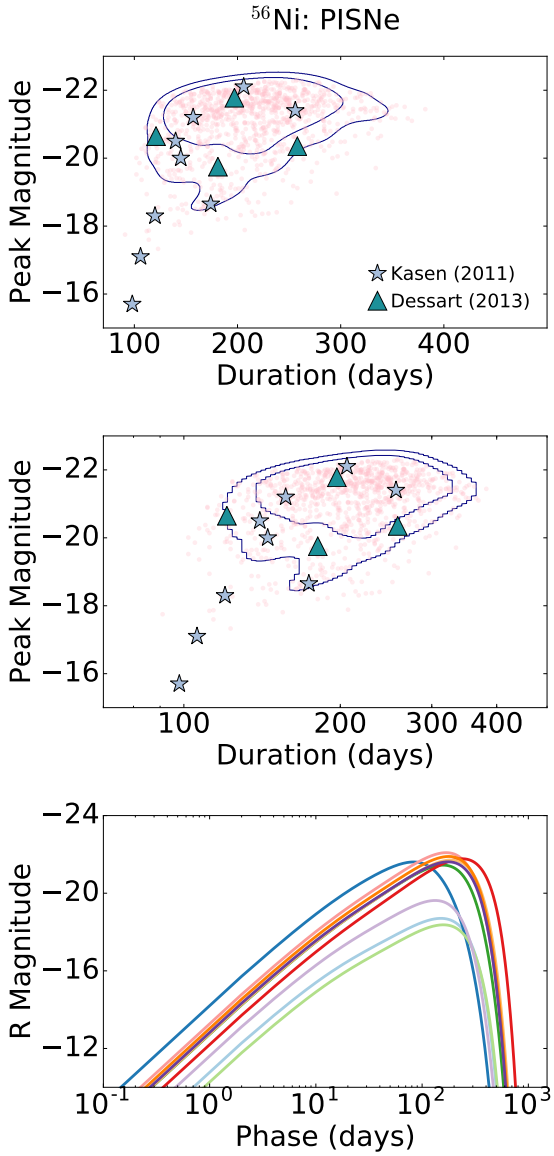

Figure 3.4: *Top & Middle*: DLPS for PISNe (pink) with a sample of models from Kasen et al. (2011) (purple stars) and Dessart et al. (2013) (green triangles). Also shown are 68th and 90th percentile contours for the realizations, estimated using a KDE. *Bottom*: Representative simulated light curves for PISNe.

-19 mag) compared to the Type Ib/c SNe due to the narrower ranges of $f_{\rm Ni}$ and $M_{\rm ej}$. Unlike the other ^{56}Ni-decay powered models, the Iax-like model can produce a small fraction of transients with durations $t_{\rm dur} \lesssim 10$ days (with a shortest duration of $t_{\rm dur} \sim 1$ week), but these transients are also the dimmest ($M_{\rm R} \sim -16.5$ mag).

We compare our models to the Iax SNe sample from Foley et al. (2013) and a sample of short-duration transients from Drout et al. (2014) in Figure 3.5. Our models do not account for the lowest luminosity observed objects, which likely have lower ^{56}Ni and ejecta masses than our model ranges. Furthermore, the realizations extend to longer durations ($t_{\rm dur} \sim 30 - 60$ days) than seen in current observations.

General Trends

The effects of the kinetic energy, ejecta mass and nickel fraction on all ^{56}Ni-powered models are explored in Figure 3.6. Unsurprisingly, the unique free parameter of this engine, $M_{\rm Ni}$, exclusively impacts the brightness of the transient with no impact on its duration. $M_{\rm ej}$ and $E_{\rm KE}$ have degenerate and opposing effects on the light curve parameters (the same effect as in the adiabatic case, Figure 3.1.). For a given kinetic energy, larger ejecta masses lead to longer and dimmer transients as the diffusion process becomes less efficient. For a given ejecta mass, larger kinetic energies lead to shorter and brighter transients due to the resulting larger velocities. Thus, the shortest duration transients have small ejecta masses and large kinetic energies and vice versa for the longest-duration transients. The brightest (dimmest) transients have large (small) nickel masses, corresponding to either large (small) nickel fractions or ejecta masses. We specifically find that ^{56}Ni heating cannot power transients with durations $t_{\rm dur} \lesssim 1$ week,

unless their peak luminosities are also small, $M_{\rm R} \gtrsim -16.5$ mag.

3.3.3 r-Process Radioactive Heating (Kilonovae)

Neutron-rich ejecta from binary neutron star or black hole-neutron star mergers are expected to undergo r-process nucleosynthesis due to the neutron-rich ejecta from either the initial merger event or a remnant disk outflow (Li & Paczyński 1998; Metzger et al. 2010). The radioactive decay of r-process products provides a heating source, while the synthesis of Lanthanides provides a high opacity (Barnes & Kasen 2013). The ejecta masses are expected to be small, $M_{\rm ej} \sim 10^{-3} - 0.1$ M$_\odot$ (Li & Paczyński 1998; Metzger 2017). The input luminosity can be parameterized by (Korobkin et al. 2012; Metzger 2017):

$$L_{\rm in}(t) = 4 \times 10^{18} \epsilon_{th}(t) M_{\rm rp} \times \left[0.5 - \pi^{-1} \arctan\left(\frac{t - t_0}{\sigma}\right)\right]^{1.3} {\rm erg\ s^{-1}} \quad (3.8)$$

where $M_{\rm rp}$ is the mass of the r-process material, $t_0 = 1.3$ s and $\sigma = 0.11$ s are constants, and $\epsilon_{\rm th}(t)$ is the thermalization efficiency (Barnes et al. 2016; Metzger 2017) parameterized as:

$$\epsilon_{\rm th}(t) = 0.36 \left[e^{-0.56t} + \frac{\ln(1 + 0.34t^{0.74})}{0.34t^{0.74}}\right] \quad (3.9)$$

Because kilonovae have not yet been conclusively observed (with the potential exception of GRB 130603B; Berger et al. 2013a; Tanvir et al. 2013), there are a number

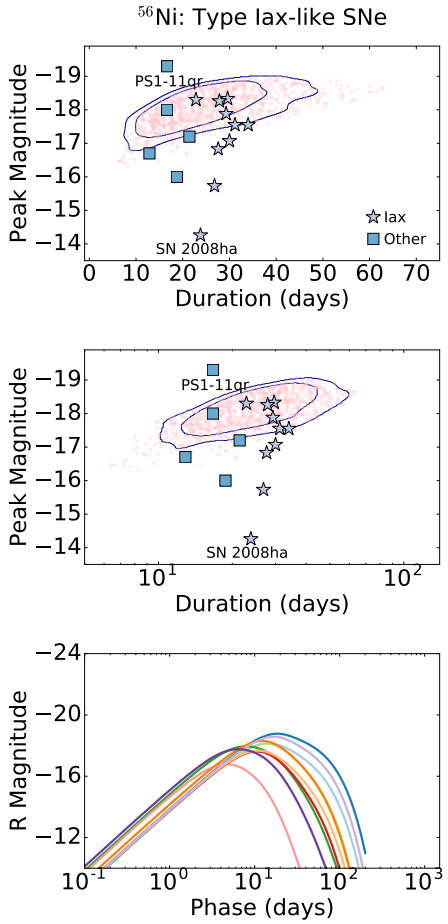

Figure 3.5: *Top & Middle*: DLPS for Iax-like SNe (pink) with a sample of Iax SNe from Foley et al. (2013) (purple stars) and rapidly evolving transients from Drout et al. (2014) (blue squares). Also shown are 68th and 90th percentile contours for the realizations, estimated using a KDE. Note that the Drout et al. (2014) objects are not necessarily powered by ^{56}Ni decay (see Section 3.4). For both samples, we estimate the transient durations using the reported Δm_{15} values, assuming symmetric light curves about the peak. We remove SN2008ge from the Foley et al. (2013) sample due to its highly uncertain duration. *Bottom*: Representative simulated light curves for Iax-like SNe.

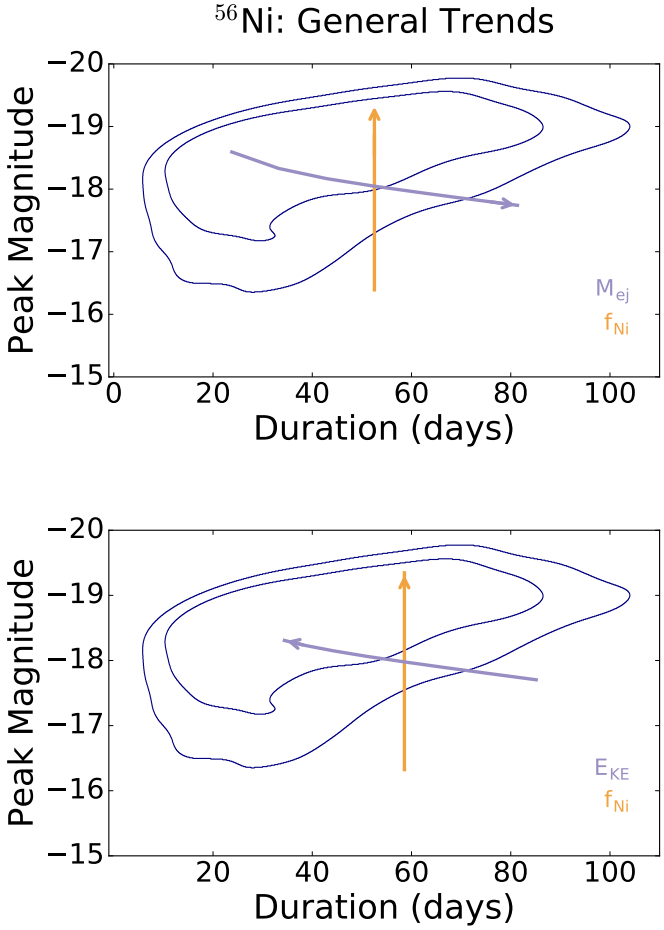

(b)

Figure 3.6: *Top*: The effects of $f_{\rm Ni}$ (orange) and $M_{\rm ej}$ (purple) on light curves powered by ^{56}Ni decay given a constant kinetic energy. Arrows points towards increasing values of each parameter. Also shown are contours of our simulated DLPS. *Bottom*: Same, but for of $f_{\rm Ni}$ (orange) and $E_{\rm KE}$ (purple).

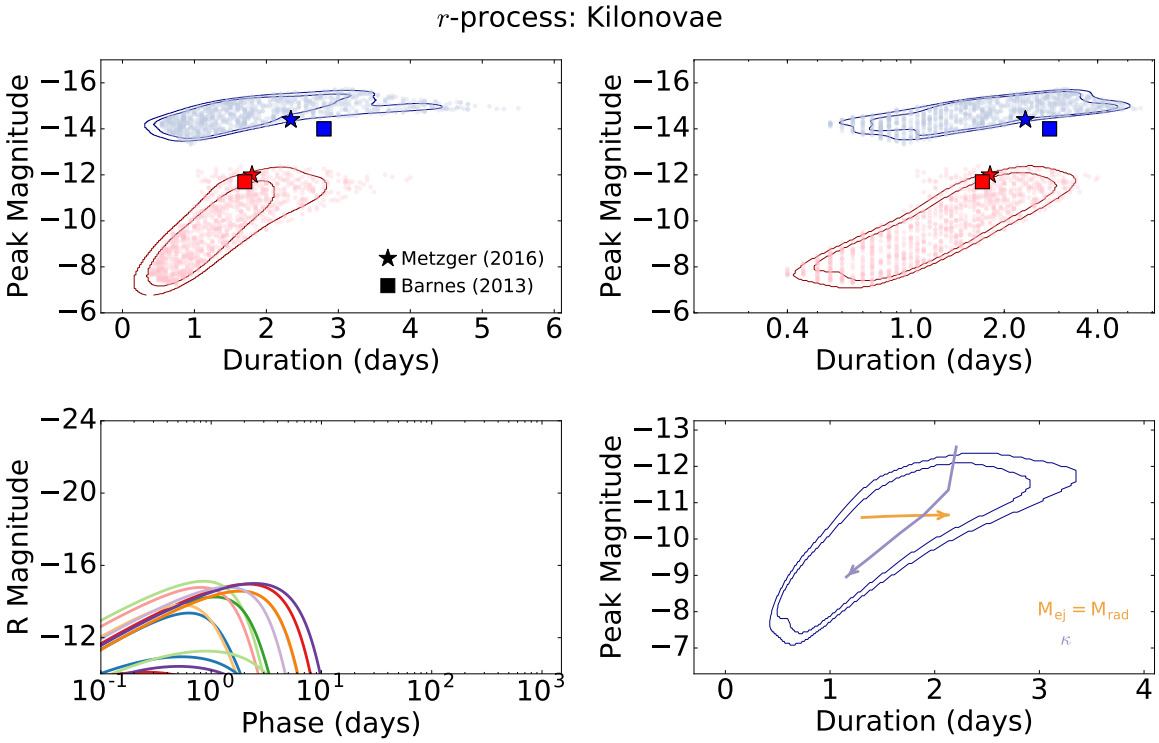

Figure 3.7: *Top Row*: Kilonova DLPS assuming Lanthanide-rich (red) and Lanthanide-free (blue) ejecta. Also shown is a sample of detailed models from Metzger (2017) (stars) and Barnes & Kasen (2013) (squares), and 68th and 90th percentile contours for the realizations, estimated using a KDE. *Bottom Left*: Representative simulated light curves for r-process explosions. *Bottom Right*: Effect of $M_{\rm ej}$ (orange) and κ (purple) on light curves powered by r-process decay assuming a constant mass fraction of r-process material. Arrows point towards increasing values of each parameter. Also shown are contours of our simulated DLPS.

of uncertainties in the light curve properties. Notably, the optical opacity of the Lanthanide-rich ejecta is unknown due to the complex structure of their valence f-shells. Early work assumed that Lanthanide-rich material had opacities similar to that of iron-peak elements, leading to bluer transients (Li & Paczyński 1998). Recent work suggests that Lanthanide-rich material will have an optical opacity $\kappa \sim 10^2 - 10^3$ times larger than that of iron-peak elements (Barnes & Kasen 2013; Barnes et al. 2016). However, it is possible that both cases exist, if binary neutron star mergers leave a NS remnant with a survival timescale of $\gtrsim 0.1$ s (Kasen et al. 2015). We consider these two possibilities in our models by generating two sets of light curves, following parameter ranges from Metzger (2017): one with a fixed $\kappa = 0.2$ cm^2 g^{-1} (a "blue" kilonova, similar to that originally explored by Li & Paczyński 1998) and one with a variable κ sampled logarithmically in the range $\kappa \sim 10 - 200$ cm^2 g^{-1} (a "red" kilonova). For each group, we logarithmically sample from ejecta masses of $M_{\rm ej} \sim 10^{-3} - 10^{-1}$ M$_\odot$, uniformly sample from ejecta velocities of $v_{\rm ej} \sim 0.1{\rm c} - 0.3{\rm c}$ and fix the r-process mass fraction $f_r = 1$ (Metzger 2017). We additionally choose the geometric factor $\beta = 3$ to calculate the diffusion timescale, following Metzger (2017).

A sample of these models and their associated DLPS are shown in Figure 3.7. Both classes are dim ($M_{\rm R} \gtrsim -15$ mag) and short-duration ($t_{\rm dur} \lesssim 5$ days). The red kilonovae are dimmer ($M_{\rm R} \sim -7$ to -13 mag) than the blue kilonovae ($M_{\rm R} \sim -13$ to -15 mag). Both subclasses have similar average durations of $t_{\rm dur} \sim 2$ days, although a large fraction of the red kilonovae have even shorter durations of $t_{\rm dur} \lesssim 1$ day. We note that although red kilonovae are expected to last ~ 1 week in the near-infrared, the transients are short-lived and dim in the R-band even if the ejecta is Lanthanide-poor. As with the ^{56}Ni-powered models, the duration and peak luminosities are positively correlated.

In Figure 3.7 we explicitly show the effects of κ and $M_{\rm ej}$ on the light curve properties. Increasing opacity makes the transient shorter and dimmer in the optical, while larger ejecta masses increase the duration and luminosity. The shortest (longest) duration transients have large (small) values of κ and small (large) values of $M_{\rm ej}$. The brightest kilonovae have small opacity values, and vice versa for the dimmest kilonovae. We find that kinetic energy has a similar effect on the light curves as seen in transients lacking a central heating source (see Section 3.3.1 and Figure 3.1); larger (smaller) kinetic energy leads to more (less) luminous transients with shorter (longer) durations.

Finally, we compare our simple model with more detailed calculations from Metzger (2017) and Barnes & Kasen (2013). Our models are in rough agreement with the detailed calculation, both in duration and luminosity. However, our models include even dimmer kilonovae ($M_{\rm R} \gtrsim -11$ mag) which have low ejecta masses. We conclude that r-process heating in the context of compact object mergers can lead to short duration transients ($\lesssim$ few days), but that these transients are invariably dim ($\gtrsim -15$ mag).

3.3.4 Magnetar Spin-down

Young magnetars, or highly magnetized neutron stars, can power optical transients as they spin down and deposit energy into the expanding ejecta (Woosley 2010; Kasen & Bildsten 2010; Metzger et al. 2015). For a dipole field configuration, the input luminosity is given by

$$L_{\rm in}(t) = \frac{E_{\rm p}}{t_{\rm p}} \frac{1}{(1+\frac{t}{t_{\rm p}})^2} \tag{3.10}$$

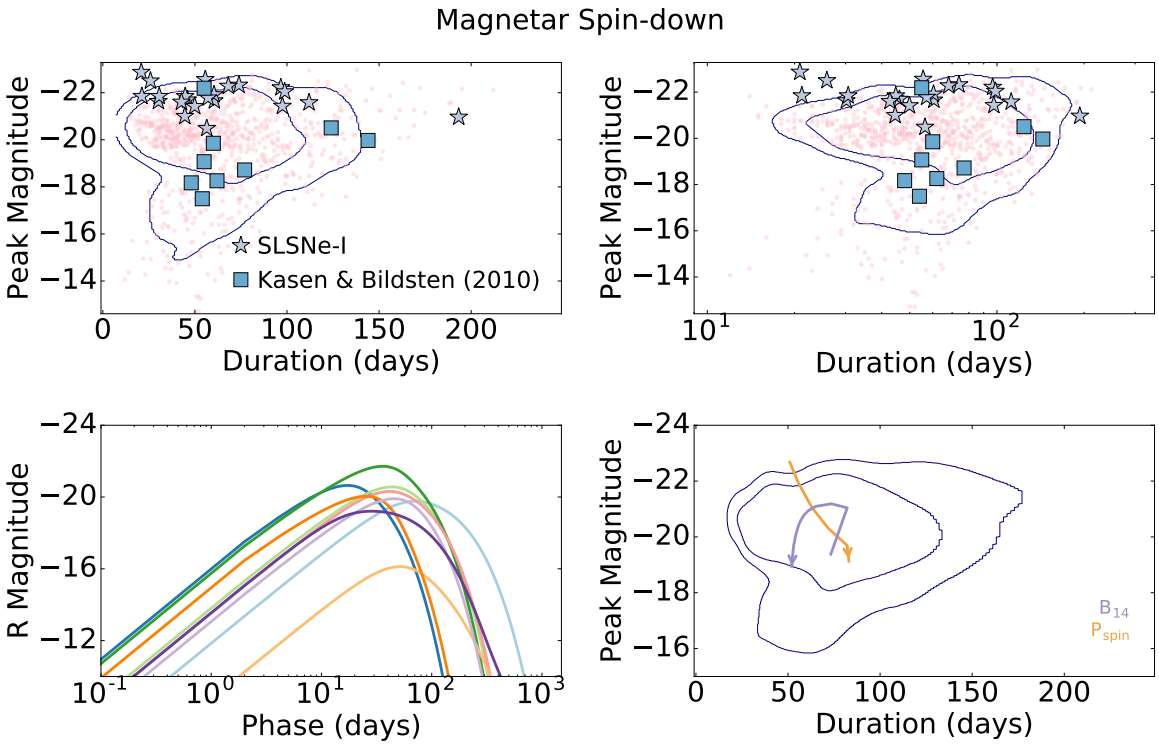

Figure 3.8: *Top row*: DLPS of magnetar powered transients (pink) along with a sample of observed Type I SLSNe from the literature (Young et al. 2010; Quimby et al. 2011; Howell et al. 2013; Inserra et al. 2013; Lunnan et al. 2013; Nicholl et al. 2013; McCrum et al. 2014; Nicholl et al. 2014; Vreeswijk et al. 2014; Nicholl et al. 2015; Papadopoulos et al. 2015; Smartt et al. 2015; Lunnan et al. 2016; Nicholl et al. 2016, 2017; purple stars) and theoretical models from Kasen & Bildsten 2010 (blue squares). Also shown are 68th and 90th percentile contours for the realizations, estimated using a KDE. *Bottom left*: Representative simulated light curves. *Bottom right*: Effect of B_{14} (purple) and $P_{\rm spin}$ (orange). Arrows point towards increasing values of each parameter, with all other parameters held constant. Also shown are contours of our simulated DLPS.

where $E_{\rm p} = I_{\rm NS}\Omega^2/2$ is the initial magnetar rotational energy, described by the moment of inertia ($I_{\rm NS}$) and angular velocity of the neutron star (Ω), and t_p is the spin-down characteristic timescale:

$$t_p = (1.3 \times 10^5)\frac{P_{\rm spin}^{-2}}{B_{14}^2}\ {\rm s} \tag{3.11}$$

where $P_{\rm spin} = 5\left(\frac{E_{\rm p}}{10^{51}{\rm erg/s}}\right)^{-0.5}$ ms is the spin period, and B_{14} is the magnetic field in units of 10^{14} G. Recently, the magnetar model has been used to explain Type I superluminous supernovae (SLSNe) (Quimby et al. 2011; Gal-Yam 2012; Dessart et al. 2012; Nicholl et al. 2013; Nicholl et al. 2017a).

In this work we explore magnetar-powered transients with spin periods $P_{\rm spin} \sim 1-10$ ms, magnetic fields $B \sim 10^{13} - 10^{15}$ G, ejecta masses $M_{\rm ej} \sim 1 - 10$ M$_\odot$ and kinetic energies $E_{\rm KE} \sim 10^{51} - 10^{52}$ erg. These parameter ranges are designed to span realistic values where magnetar spin-down can be the dominant power source. Large spin periods of $\gtrsim 10$ ms, and low magnetic fields of $B \lesssim 10^{13}$ will result in low input power, and the transients will likely be dominated by ^{56}Ni-decay (see Section 3.3.10). We additionally eliminate unphysical models with $E_{\rm KE} - E_{\rm SN,min} > E_{\rm p}$, where $E_{\rm SN,min} = 10^{51}$ erg is the minimum energy required to leave a NS remnant. This condition removes models in which most of the rotational energy feeds into ejecta expansion rather than radiation. The magnetar-powered models and the associated DLPS are shown in Figure 3.8. While increasing spin periods lead to dimmer transients, the transient luminosity is actually optimized at intermediate values of B_{14} which depend on $P_{\rm spin}$ when the spin-down timescale roughly matches the diffusion timescale.

There are several notable features caused by these dependencies in the magnetar DLPS. First, the paucity of long duration and low luminosity transients reflects the

lower bound of our magnetic field range. In contrast, the luminosity upper limit is set by the lower bound on the spin period, which we set at the maximal NS spin (1 ms). There is also an absence of shorter duration transients with $M_{\rm R} \sim -18$ to -20 mag. The upper boundary of this void is set by our magnetic field lower limit, while the lower boundary is set by the lower ejecta mass limit; all of the transients below this void have low magnetic field strengths. The effects of $P_{\rm spin}$ and B on the magnetar light curves are shown explicitly in Figure 3.8. We conclude that magnetar-powered transients are typically luminous ($M_{\rm R} \lesssim -19$ mag) with long durations ($t_{\rm dur} \gtrsim 30$ days).

Finally, we compare our DLPS with a sample of Type I SLSNe from the literature and with detailed models by Kasen & Bildsten (2010). We find that the majority of our realizations agree with the observed population ($M_{\rm R} \sim -19$ to -23 mag and $t_{\rm dur} \sim 20 - 200$ days). Additionally, we also reproduce the lower luminosity models ($M_{\rm R} \sim -17$ to -19 mag) explored by Kasen & Bildsten (2010).

3.3.5 Ejecta-CSM Interaction

Several types of optical transients, including Type IIn SNe and Luminous Blue Variable (LBV) outbursts, display clear signs of interaction between their ejecta and dense surrounding circumstellar material (CSM). Properties such as narrow hydrogen and metal emission lines, bright Hα luminosities, and considerable X-ray/radio luminosities can be explained by a shock propagating through a CSM (Chevalier & Fransson 1994; Matzner & McKee 1999). Similarly, bright, blue and short-duration transients have been linked to shock breakout from dense CSM "cocoons" (Chevalier & Irwin 2011; Drout et al. 2014; Arcavi et al. 2016). Because CSM interaction can describe an expansive

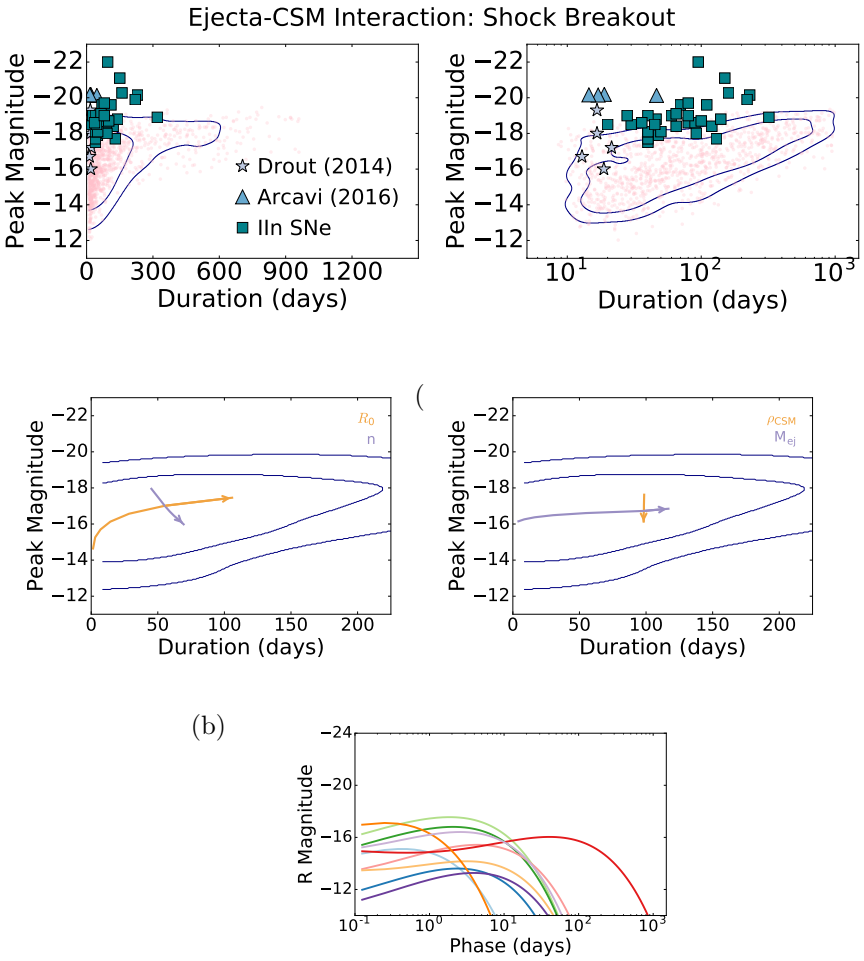

Figure 3.9: *Top row*: DLPS of CSM shock breakout transients with a complete sample of V,R or I Type IIn SNe and SLSNe-II with well-sampled light curves (> 20 data points) from the OSC, a sample of short-duration transients from Drout et al. (2014) and a sample of short-duration and bright transients from Arcavi et al. (2016). Also shown are 68th and 90th percentile contours for the realizations, estimated using a KDE. *Middle left*: Effect of R_0 (orange) and n (purple) on light curves. *Middle right*: Effect of $\rho_{\rm CSM}$ (orange) and $M_{\rm ej}$ (purple) on light curves. Arrows points towards increasing values of each parameter. *Bottom*: Representative simulated light curves.

range of transients, we consider two primary regimes: SN-like with ejecta masses ($M_{\rm ej} \sim 1 - 10$ M$_\odot$) and kinetic energies ($E_{\rm KE} \sim 10^{51} - 10^{52}$ erg) typical of Type IIn SNe; and outburst-like, with low ejecta masses ($M_{\rm ej} \sim 10^{-3} - 1$ M$_\odot$) and wind-like velocities ($v \sim 10^2 - 10^3$ km s^{-1}), typical of intermediate luminosity optical transients (ILOTs; including LBV outbursts and Type IIn precursors).

Many semi-analytical models have been created to describe optical light curves powered by shock heating (Chatzopoulos et al. 2012; Smith 2013; Moriya et al. 2013; Ofek et al. 2014). Most of these models follow the same formalism presented by Chevalier (1982) and Chevalier & Fransson (1994) and track a shock through the CSM as it thermalizes the large kinetic energy reservoir (Chevalier 1982; Chevalier & Irwin 2011; Dessart et al. 2015). Due to the current uncertainty in the analytical models available, we explore two interaction models described by Chatzopoulos et al. (2012) and Ofek et al. (2014) and discuss their key differences. We specifically use the Ofek et al. (2014) model for CSM shock breakout transients, and an altered Chatzopoulos et al. (2012) model for both SN-like and outburst-like transients. The details of these models are presented in the Appendix. In the subsections below, we discuss the input luminosities and model parameters.

Shock Breakout from a Dense CSM

Shock breakouts (SBO) from dense CSM winds surrounding massive stars have been used to describe Type IIn SNe and other bright, blue transients (e.g. see Ofek et al. 2014; Margutti et al. 2013). This model assumes that the forward shock from the ejecta-CSM interaction radiates efficiently ($t_{\rm d} = 0$) such that:

$$L_{\rm in} = L_{\rm obs} = 2\pi\epsilon\rho_{\rm CSM}(r_{\rm sh})r_{\rm sh}^2 v_{\rm sh}^3 \tag{3.12}$$

where $\epsilon = 0.5$ is an efficiency factor, $\rho_{\rm CSM}(r_{\rm sh})$ is the density of the CSM as a function of the shock radius $r_{\rm sh}$, and $v_{\rm sh} = dr_{\rm sh}/dt$ is the shock velocity. The shock radius and velocity depend on the geometry of the explosion ejecta and CSM. Here we assume that the CSM is distributed as a wind-like profile, $\rho_{\rm CSM}(r) \propto r^{-2}$. The ejecta density profile is described as a broken-power law, with an outer profile of $\rho_{\rm ej}(r) \propto r^{-n}$ where n is a free parameter. We find that the inner profile has little effect on the light curves, and thus we assume a flat inner profile. (See the Appendix for details.)

Thus, the free parameters are the ejecta density index (n), the kinetic energy of the explosion ($E_{\rm KE}$), the ejecta mass ($M_{\rm ej}$), the inner radius of the CSM (R_0), and the CSM density at R_0 ($\rho_{\rm CSM}$). We sample over the following ranges: $n \sim 7 - 12$, $E_{\rm KE} \sim 10^{51} - 10^{52}$ erg, $M_{\rm ej} \sim 1 - 10$ M$_\odot$, $R_0 \sim 1 - 10^2$ AU and $\rho_{\rm CSM} \sim 10^{-17} - 10^{-14}$ g cm^{-3}. We then eliminate realizations with mass-loss rates $\dot{M} \equiv 4\pi R_0^2 \rho_{\rm CSM} v_{\rm w} < 10^{-6}$ M$_\odot$ yr^{-1}, assuming a wind velocity of $v_{\rm w} \sim 10^2$ km s^{-1}. This cut corresponds to the lower end of expected RSG mass-loss rates (Smith 2014). Our parameters therefore correspond to mass-loss rates of $\dot{M} \sim 10^{-6} - 10^{-2}$ M$_\odot$ yr^{-1}, roughly matching the range of mass-loss rates of RSGs, YSGs and LBVs (Smith 2014).

We note that our range of R_0 values extends beyond the radii of most progenitor stars. However, it is possible that R_0 is the location of a so-called cool dense shell formed by an earlier eruption and not always representative of the progenitor radius (Smith 2017).

Finally, we note that our range of n is representative of ejecta density profiles

inferred for degenerate progenitors ($n \sim 7$; Colgate & McKee 1969) and RSG progenitors ($n \sim 12$; Matzner & McKee 1999). Although previous work has typically set $n \sim 12$, Chevalier & Irwin (2011) suggest that the shallower portions of density profiles may play larger roles in the ejecta-CSM interaction, so we leave n as a free parameter. Finally, we remove events with $v > 15000$ km s^{-1}.

We show sample light curves and the associated DLPS in Figure 3.9. Our models span a wide range in both luminosity ($M_{\rm R} \sim -13$ to -19 mag) and duration ($t_{\rm dur} \sim 10 - 10^3$ days). Like most of our models, luminosity and duration are positively correlated. The shortest duration transients have $t_{\rm dur} \approx 10$ days, and peak brightness of $M_{\rm R} \gtrsim -17$ mag. The duration is largely determined by the mass-loss rate, with higher (lower) mass-loss rates leading to the longest (shortest) duration transients. The luminosities of the brightest transients are set by our minimum value of n and maximum velocities, while the luminosities of the dimmest transients are set by the minimum velocities ($\sim 4 \times 10^3$ km s^{-1}) of our parameter ranges. We explicitly show the effects of each free parameter in Figure 3.9. As shown in the figure, larger values of $\rho_{\rm CSM}$ actually lead to *less* luminous transients in the optical. This is due to the fact that large values of $\rho_{\rm CSM}$ lead to hotter effective temperatures that actually decrease the visible luminosity assuming a blackbody SED.

In Figure 3.9 we also compare our simulated distribution to the distribution of all well-sampled Type IIn SN listed on the OSC at the time of writing, a sample of short-duration transients from Pan-STARRs (Drout et al. 2014) and a sample of rapidly-rising, bright transients from Arcavi et al. (2016). We note that neither of the latter two samples are claimed to be from CSM SBO models; however, the CSM model is able to roughly reproduce the peak luminosities and durations of the rapid transients

from Drout et al. (2014). The simulated shock breakout models generally produce dimmer transients than observed and allow for longer duration transients ($t_{\rm dur} \gtrsim 400$ days).

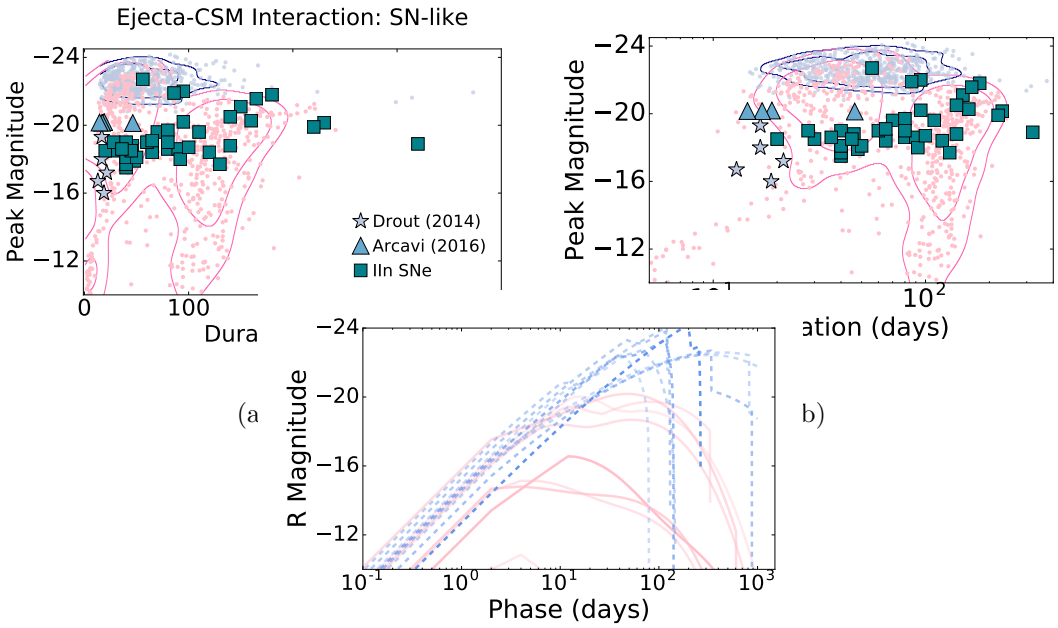

Figure 3.10: *Top & Middle*: Ejecta-CSM interaction DLPS for SN-like transients assuming $s = 0$ (blue) and $s = 2$ (pink) and the 68th and 90th percentile contours for the realizations, estimated using a KDE. Also shown is the same sample of Type IIn SNe and SLSNe-II light curves from Figure 3.9. *Bottom*: Simulated light curves for shell-like $s = 0$ (blue, dashed) and wind-like $s = 2$ (pink) mass-loss.

Ejecta-CSM Interaction with Diffusion

We now explore the generalized problem of ejecta-CSM interaction with diffusion assuming a stationary photosphere (Chatzopoulos et al. 2012). This model is similar to

that in Section 3.3.5, but in this case we consider the reverse shock contribution and a stationary photosphere (see Appendix). The input luminosity is given by:

$$L_{\rm in} = \epsilon(\rho_{\rm CSM}R_0^s)^{\frac{n-5}{n-s}}t^{\frac{2n+6s-ns-15}{n-s}} \times \left[C_1\theta\left(t_{\rm FS}-t\right) + C_2\theta\left(t_{\rm RS}-t\right)\right] \quad (3.13)$$

where s, C_1 and C_2 are geometric parameters of the CSM, and $\theta(t)$ is the heaviside function which controls the input times for the forward ($t_{\rm FS}$) and reverse ($t_{\rm RS}$) shocks. There are seven free parameters of the model: s, n, R_0, $E_{\rm KE}$, $M_{\rm ej}$, $\rho_{\rm CSM}$, and the total CSM mass ($M_{\rm CSM}$). We set $s = 0$ for "shell-like" CSM models and $s = 2$ for "wind-like" CSM models.

We place a number of additional physical constraints on these models:

1. We require the photospheric radius to be within the CSM shell: $R_0 \leq R_{\rm ph} \leq R_{\rm CSM}$

2. We require the CSM mass to be less than the ejecta mass: $M_{\rm CSM} \leq M_{\rm ej}$

3. We require the velocity of the ejecta $v_{\rm min} \leq v_{\rm ph} \equiv \sqrt{10E_{\rm KE}/3M_{\rm ej}} \leq v_{\rm max}$, where $v_{\rm min} = 5000$ km s^{-1} and $v_{\rm max} = 15000$ km s^{-1} for SN-like sources and $v_{\rm min} = 100$ km s^{-1} and $v_{\rm max} = 1000$ km s^{-1} for outburst-like sources.

4. We require the diffusion time ($t_{\rm d}$) through the CSM to be less than the shock crossing time through the CSM ($t_{\rm FS}$). If this were *not* the case, the light curve would exponentially decline as in the case of adiabatic expansion (Section 3.3.1; see the shell-shocked model described by Smith & McCray 2007). Moriya et al. (2013) and Dessart et al. (2015) argue that the optical depths in typical CSMs are significantly lower than the regime of a shell-shocked model, implying that $t_{\rm d} < t_{\rm FS}$.

Finally, we choose reasonable parameter ranges for SN- and outburst-like sources. For both subclasses, we sample logarithmically from $R_0 \sim 1 - 100$ AU and $\rho_{\rm CSM} \sim 10^{-17} - 10^{-14}$ g cm^{-3}, typical ranges in Type IIn SNe studies (Moriya et al. 2013; Dessart et al. 2015). For the SN-like models, we explore both shell-like ($s = 0$) and wind-like ($s = 2$) CSM profiles. For the outburst-like models, we only explore wind-like CSM profiles.

For SN-like transients, we sample logarithmically from $E_{\rm KE} \sim 10^{51} - 10^{52}$ erg and $M_{\rm CSM} \sim 0.1 - 10$ M$_\odot$, and uniformly from $M_{\rm ej} \sim 1 - 10$ M$_\odot$. Simulated light curves and the DLPS of our models are shown in Figure 3.10 for both shell-like and wind-like CSM profiles. In the shell-like case, the light curves decline rapidly following peak brightness due to our use of the heaviside function to abruptly discontinue the input luminosity once the forward and reverse shocks have traversed the CSM. In the wind-like case, these light curves are smoother due to the continuous $\rho(r) \propto r^{-2}$ CSM profile.

One notable difference between the shell-like and wind-like models is the range of peak magnitudes, with shell-like models ($M_{\rm peak} \sim -21$ to -24 mag) spreading a narrower range than the wind models ($M_{\rm peak} \gtrsim -23$ mag) for the same range of physical parameters. This is likely due to the fact that $L_{\rm in} \propto \frac{2n+6s-ns-15}{n-s}$, or $L_{\rm in} \propto t^{0.7}(t^{-0.3})$ for $s = 0$ ($s = 2$) assuming $n = 12$, a typical value for RSGs (Chevalier 1982). In other words, the input luminosity is always *decreasing* in the wind-like model, while it actually *increases* in the shell-like model for $t < t_{\rm FS}$. This leads to brighter transients in the shell-like case.

There is little correlation between duration and luminosity for both shell-like and wind-like models due to the complicated effects of the multiple parameters. In Figure

3.11 we show how the free and derived parameters affect the wind-like CSM models. We highlight several global trends. The brightest transients typically have the largest mass-loss rates, optically thick CSM masses ($M_{\rm CSM,th}$) and photospheric radii ($R_{\rm ph}$), and vice versa for the dimmest transients. The shortest duration ($t_{\rm dur} \sim 10$ days) transients with relatively high luminosities ($M_{\rm R} \lesssim -16$ mag) have small CSM masses although most of this CSM is optically thick.

There are two low luminosity ($M_{\rm R} \gtrsim -15$ mag) "branches" in the wind-like DLPS: one extending to shorter durations ($t_{\rm dur} < 20$ days) and the other at $t_{\rm dur} \sim 100$ days. The dearth of models between these branches is due to the fact that models within this area of phase space have optically thin CSM masses which are eliminated by our physical constraints. Realizations in the shorter-duration branch have larger CSM masses, mass-loss rates and inner CSM radii compared to the branch at ~ 100 days. Realizations in the shorter-duration branch have more peaked light curves due to thinner shells at larger radii, while those in the longer-duration branch have flatter light curves. We note that no transients with SN-like properties have been observed to date in either branch.

As with previous classes, we find that the transients with shortest durations and SN-like luminosities have $t_{\rm dur} \approx 15$ days. Transients with shorter durations (down to $t_{\rm dur} \approx 15$ days) all have low luminosities of $\gtrsim -14$ mag.

Finally, we compare our DLPS to the sample of Type IIn SNe and other objects as in Section 3.3.5. The wind-like DLPS largely overlaps with the sample, while the shell-like DLPS is only able to reproduce the brightest Type IIn SNe.

For outburst-like transients, we sample logarithmically from $v \sim 10^2 - 10^3$ km s^{-1} and $M_{\rm ej} \sim 0.001 - 1$ M$_\odot$ and assume $s = 2$. The corresponding kinetic energy limits are

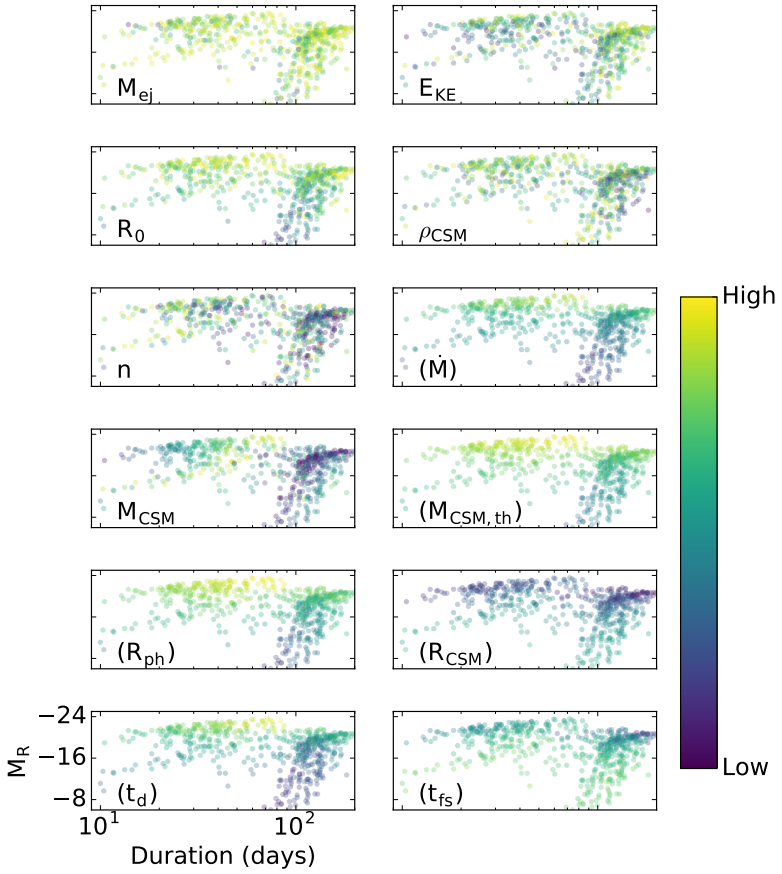

Figure 3.11: Ejecta-CSM interaction DLPS for the Type IIn SNe transients assuming $s = 2$. In each panel, the models are color coded based on the values of the inset parameters (e.g., the top left panel is color coded based on $M_{\rm ej}$). The "high" and "low" values are based on the parameter ranges listed in Table 1. The mass-loss rate ($\dot{M}$), optically thick CSM mass ($M_{\rm CSM,th}$), photospheric radius ($R_{\rm ph}$), CSM radius ($R_{\rm CSM}$) diffusion time ($t_{\rm d}$) and forward shock-crossing time ($t_{\rm fs}$) are all derived parameters. We note that many of the short-duration events are dominated by the forward shock (with the reverse shock contributing a less-luminous peak not included in the duration), while the long-duration events have durations that typically include both the forward- and reverse-shock peaks.

$E_{\rm KE} \sim 10^{44} - 10^{49}$ erg. These limits were chosen to roughly match the velocities of LBV eruptions and explore a full range of the lowest luminosity transients (Humphreys & Davidson 1994).

Sample light curves and the DLPS for outburst-like transients are shown in Figure 3.12. These models span a large range in both duration ($t_{\rm dur} \sim$ few $-$ 100 days) and luminosity ($M_{\rm R} \sim 0$ to -16 mag). The light curve properties generally follow the same trends as the Type IIn SNe models. Short-duration transients ($t_{\rm dur} \lesssim 10$ days) are less luminous ($M_{\rm R} \gtrsim -14$ mag). The parameter trends shown in Figure 3.11 also hold for ILOT-like models.

Finally, we compare the simulated DLPS to a number of events from the literature, including LBV outbursts and Type IIn precursor events (see caption for details). In general, our models cover plausible timescales and magnitudes for ILOTs with signs of CSM interaction and overlap with many known objects.

3.3.6 Hydrogen Recombination (Type IIP SNe)

Type IIP SNe are explosions of red supergiants with masses of $\approx 8 - 17$ $M_\odot$ that have retained their hydrogen envelopes (Smartt et al. 2009). Following the explosion, a shock wave ionizes the hydrogen envelope. The characteristic flat, "plateau" phase of their optical light curves is powered by hydrogen recombination as the expanding ejecta cools to ~ 5000 K at an approximately constant radius (i.e., the photosphere recedes in Lagrangian coordinates). The duration of the plateau phase is determined by the extent of the hydrogen envelope and kinematic properties of the blast wave. Following the plateau is a rapid decline in luminosity to a predominately ^{56}Co-powered tail (Arnett

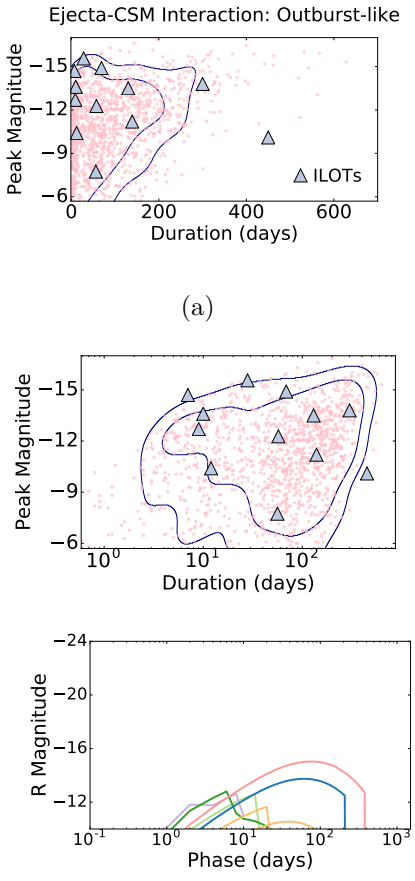

Figure 3.12: *Top & Middle*: Ejecta-CSM interaction DLPS for outburst-like transients and 68th and 90th percentile contours for the realizations, estimated using a KDE. Also shown is a sample of well-sampled ILOT light curves from the literature that are thought to be powered by CSM interaction: SN 1954J, SN 1961V, SN 2000ch, SN 2002bu, SN 2008S, SN 2009ip (Smith et al. 2011); SN 2002kg (Van Dyk et al. 2006); SN 2010da (Villar et al. 2016); PTF10fqs (Kasliwal et al. 2011); V838 Mon (Munari et al. 2002); Eta Car (Smith & Frew 2011). *Bottom*: Representative simulated light curves.

1980; Weiler 2003).

The bolometric and optical light curves of Type IIP SNe have been studied extensively (e.g., Patat et al. 1994; Hamuy 2003; Kasen & Woosley 2009; Sanders et al. 2015; Rubin et al. 2016). Multi-zone semi-analytical and numerical models generally reproduce the observed light curves (Popov 1993; Kasen & Woosley 2009) and provide scaling relations for both the plateau durations and luminosities. Here, we use these theoretical scaling relations in conjunction with empirical trends found by Sanders et al. (2015) to construct R-band light curves, neglecting contributions from both the shock breakout and ^{56}Ni radioactive decay. While shock breakout should primarily affect the early light curve, significant amounts of ^{56}Ni can extend the plateau duration. However, recent work has shown that $M_{\rm Ni}/M_{\rm ej} \lesssim 0.01$ (Müller et al. 2017), so we choose to ignore this contribution.

To construct light curves, we first assume instantaneous rise-times. In reality, Type IIP SNe have rise times which range from a few days to a week (Rubin et al. 2016). This is a minor effect given the long plateau durations. We then use the bolometric scaling relations derived in Popov (1993) to estimate both the peak R-band luminosity ($L_{\rm p}$) and duration ($t_{\rm p}$) of the plateau phase:

$$L_p = 1.64 \times 10^{42} \frac{R_{0,500}^{2/3} E_{51}^{5/6}}{M_{10}^{1/2}} \ {\rm erg\,s^{-1}} \tag{3.14}$$

$$t_{\rm p} = 99 \frac{M_{10}^{1/2} R_{0,500}^{1/6}}{E_{51}^{1/6}} {\rm days} \tag{3.15}$$

where $R_{0,500}$ is the progenitor radius in 500 $R_\odot$, E_{51} is the kinetic energy in 10^{51} erg and M_{10} is the ejecta mass in 10 $M_\odot$. Here we have assumed that the R-band bolometic

correction is negligible (approximately true during the plateau; Bersten & Hamuy 2009). Additionally, the blackbody SED has a temperature of 5054 K (the ionization temperature of neutral hydrogen) and the opacity is $\kappa = 0.34\,\mathrm{cm^2\ g^{-1}}$. Following Sanders et al. 2015, we assume that the light curve reaches a maximum and then monotonically declines during the plateau phase. The decline rate is strongly correlated to the peak luminosity and is parameterized by (Sanders et al. 2015):

$$L(t) = \frac{L_{\mathrm{p}}}{e^{(-13.1-0.47M_{\mathrm{R}})t}} \tag{3.16}$$

where M_{R} is the peak magnitude. Finally, we assume that for $t > t_{\mathrm{p}}$, the light curve drops off instantaneously. This assumption is justified by our definition of duration (within 1 mag of peak), which is minimally impacted by the late-time behaviour of the light curve. We generate light curves by sampling uniformly from ejecta mass ($M_{\mathrm{ej}} \sim 5 - 15\ \mathrm{M_\odot}$) and progenitor radii ($R_0 \sim 100 - 1000\ \mathrm{R_\odot}$), and logarithmically in kinetic energy ($10^{50} - 5 \times 10^{51}$ erg).

The simulated DLPS and sample light curves are shown in Figure 3.13. The transient durations ($t_{\mathrm{dur}} \sim 40 - 150$ days) and luminosities ($M_{\mathrm{R}} \sim -16$ to -19 mag) are negatively correlated. The upper luminosity boundary reflects our M_{ej} upper limit. In Figure 3.13 we also explore the effects of the progenitor radius and the ejecta mass on the model light curves. Larger progenitor radii lead to brighter and longer duration transients as a result of the fixed photosphere. Increasing the ejecta mass produces less luminous and longer duration transients. Thus, the brightest (dimmest) Type IIP models have large (small) radii and small (large) ejecta masses. The longest (shortest) transients have large (small) radii and ejecta masses. The shortest duration events have

$t_{\rm dur} \approx 40$ days and high luminosities of $M_{\rm R} \approx -19$ mag.

In Figure 3.13 we compare our generated light curve properties to samples from PanSTARRs (Sanders et al. 2015) and the Palomar Transient Factor (PTF; Rubin et al. 2016). It is worth noting that both samples contain so-called Type IIL SNe, which are spectroscopically similar to Type IIP SNe but decline linearly in magnitude more rapidly than most Type IIP SNe. Both Sanders et al. 2015 and Rubin et al. 2016 find no evidence that Type IIP and Type IIL SNe arise from separate progenitor populations, so we also choose to keep Type IIL SNe in the observed sample. These samples largely overlap with our generated light curves.

3.3.7 GRB Afterglows

Following a gamma-ray burst (GRB), the interaction of the relativistic jet with the CSM leads to a long-lived afterglow powered by synchrotron radiation (Sari et al. 1998). The afterglow emission can also be detected for off-axis sight lines (an "orphan" afterglow; Rhoads 1997; Rossi et al. 2002; van Eerten et al. 2010). There are two types of GRBs, long-duration (resulting from core-collapse of stripped massive stars; Woosley 1993) and short-duration (likely produced by neutron star binary mergers; Berger 2014). The energy scale of short GRBs (SGRBs) is about 20 times lower than for long GRBs (LGRBs), and their circumburst densities are at least an order of magnitude lower (Berger 2014; Fong et al. 2015).

Here we explore both LGRB and SGRB afterglow models. Rather than generating

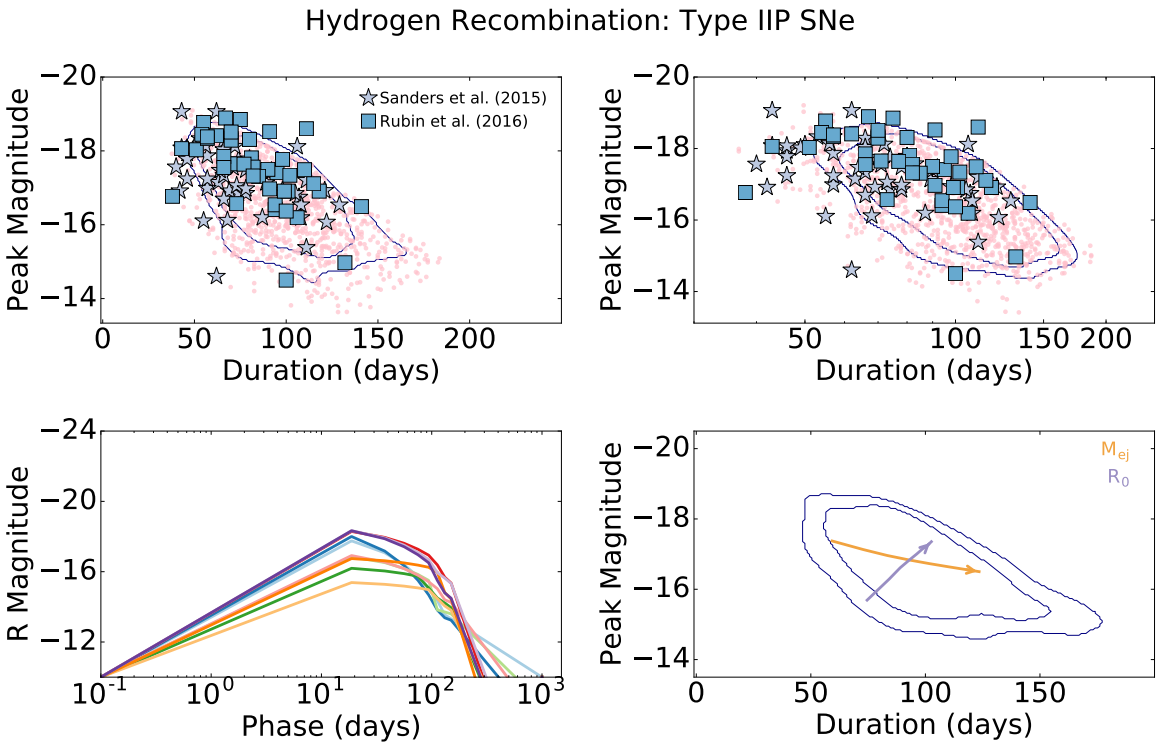

Figure 3.13: *Top row*: Simulated Type IIP SNe DLPS (pink) with a sample of objects from the PS1/MDS (Sanders et al. 2015; purple stars) and PTF (Rubin et al. 2016; blue squares). For the PS1/MDS sample, we construct light curves using the model and parameters described in Sanders et al. (2015), and we remove objects with less than 5 datapoints in the R-band. *Bottom left*: Sample light curves. *Bottom right*: Effect of $M_{\rm ej}$ (orange) and R_0 (purple) on the light curves of transients powered by hydrogen recombination given a constant kinetic energy. Arrows point towards increasing values of each parameter. Also shown are 68th and 90th percentile contours for the realizations, estimated using a KDE.

analytical models, we use the publicly available[2] broadband GRB afterglow model presented by van Eerten et al. (2010). This model calculates broadband SEDs of both on- and off-axis GRB afterglows using a high-resolution two-dimensional relativistic hydrodynamics simulation. Typical LGRB values of isotropic energy $E_{\rm iso} = 10^{53}$ erg, jet half opening angle $\theta_{\rm jet} = 11.5^o$, circumburst medium density $n_0 = 1$ cm^{-3}, accelerated particle slope $p = 2.5$, accelerated particle energy density fraction of thermal energy density $\epsilon_{\rm e} = 0.1$, and magnetic field energy density as fraction of thermal energy density $\epsilon_{\rm B} = 0.1$ are assumed. From this model, we can then generate the parameter space of long and short GRBs using scaling relation presented in Van Eerten & MacFadyen (2012):

$$\begin{aligned} L_{\nu,\rm obs} &\propto \epsilon_{\rm B}^{1/2} n_0^{-1/2} E_{\rm iso} \\ t_{\rm dur} &\propto \frac{E_{\rm iso}}{n_0}^{1/3} \end{aligned} \tag{3.17}$$

Our simulated model, using the van Eerten et al. (2010) parameters and assuming that the afterglow is first observed ≈ 0.5 days after the GRB, is shown in Figure 3.14. As the orientation becomes increasingly off-axis, the R-band transient becomes dimmer and longer duration. We also plot scaled versions of this model, assuming $n_0 \sim 1 - 10$ cm^{-1} and $E_{\rm iso} \sim (0.3 - 3) \times 10^{53}$ erg for LGRBs, and $n_0 \sim 0.01 - 0.1$ cm^{-1} and $E_{\rm iso} \sim (0.3 - 3) \times 10^{51}$ erg for SGRBs. Both the SGRB and LGRB models span a wide range of durations ($t_{\rm dur} \sim 1 - 1000$ days) and luminosity ($M_{\rm R} \sim -2$ to -21 mag for SGRBs and $M_{\rm R} \sim -12$ to -16 mag for LGRBs). The duration and luminosity are tightly negatively correlated, with the shortest duration events being the brightest. The

[2]http://cosmo.nyu.edu/afterglowlibrary/offaxis2010broadband.html

only events with $t_{\rm dur} \lesssim 10$ days are on-axis, which are known to be rare. For off-axis sight lines, the luminosity drops rapidly as the duration increases such that at $\approx 2\theta_{\rm j}$, the afterglow is comparable to SNe in terms of timescale and luminosity. For larger angles, the events are much dimmer than SNe with longer durations.

We additionally plot a region corresponding to the 1σ observed properties of a sample of rest-frame R-band afterglows of on-axis LGRBs from the BAT6 sample (after removing LGRBs with early flares; Melandri et al. 2014). The sample is in general agreement with the afterglow model, with short durations ($t_{\rm dur} \sim 0.4 - 2$ days) and bright luminosities ($M_{\rm R} \sim -22$ to -25 mag), as expected for these on-axis events.

3.3.8 Tidal Disruption Events

Tidal disruption events (TDEs) occur when a star passes near a supermassive black hole (SMBH) and becomes tidally disrupted (Frank & Rees 1976; Hills 1988). About half of the star's mass forms an accretion disk around the SMBH leading to an optically bright transient that lasts for weeks to months depending on the system's characteristics (Guillochon et al. 2009). A number of complications arise when modelling these transients, including the complex 3D geometry of the system, the hydrodynamics forming the accretion disk, the possibility of existing CSM surrounding the event and reprocessing of the disk emission by outflowing gas (Guillochon et al. 2014). We therefore present basic scaling relations for the durations and luminosities of TDEs.

Assuming that the accretion rate onto the SMBH is less than the Eddington limit, the peak bolometric luminosity of the transient scales as (Stone 2014):

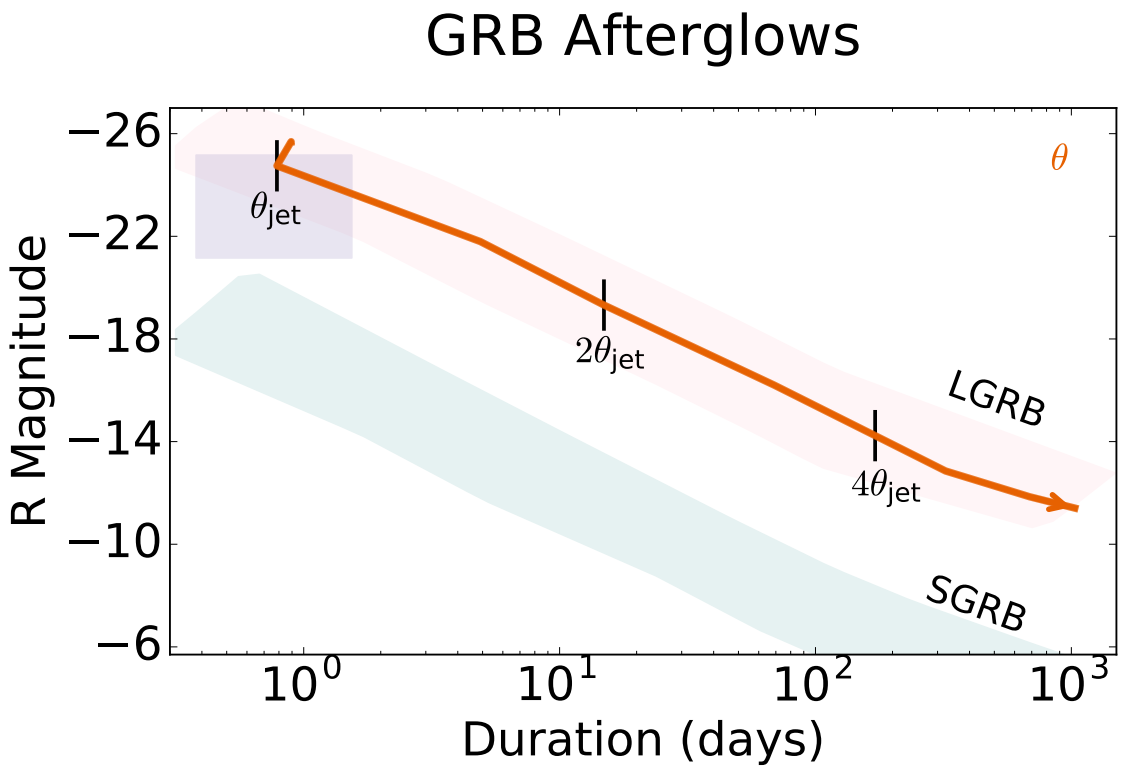

Figure 3.14: GRB optical afterglow DLPS as a function of the observer viewing angle in units of the jet opening angle. We show both LGRBs (red) and SGRBs (blue). The arrow points toward an increasing value of viewing angle θ. Black vertical lines mark models where $\theta = \theta_{\rm jet} = 0.2$ rad, $\theta = 0.4$ rad and $\theta = 0.8$ rad. Also shown is a 1σ region of on-axis LGRB afterglows observed by Melandri et al. (2014) (purple rectangle).

$$L_{\rm peak} \propto \dot{M} \propto M_{\rm BH}^{-1/2} M_*^2 R_*^{-3/2} \tag{3.18}$$

where $\dot{M}$ is the peak accretion rate of the disrupted star calculated at the tidal radius, $M_{\rm BH}$ is the black hole mass, and M_* and R_* are the star's mass and radius, respectively. The peak accretion rate is typically near the SMBH Eddington accretion rate, which leads to a plateau at the corresponding Eddington luminosity. Super-Eddington accretion will likely lead to an outflow of material (see e.g., Alexander et al. 2016).

There are three timescales which potentially affect the transient duration: the diffusion time ($t_{\rm d}$), the viscous time (t_ν) and the timescale of peak fallback accretion ($t_{\rm peak}$). In most cases, the diffusion timescale is small relative to at least one of the other two (Guillochon et al. 2009; Guillochon & Ramirez-Ruiz 2013). Assuming a low disk viscosity, the duration of the transient will be proportional to (Lodato et al. 2012):

$$t_{\rm dur} \propto t_{\rm peak} \propto M_{\rm BH}^{1/2} M_*^{-1} R_*^{3/2} \tag{3.19}$$

For canonical parameters (a sun-like star and $M_{\rm BH} = 10^6$ $\rm M_\odot$), this duration is about 40 days.

If the accretion rate is near-Eddington, the light curve will plateau for a duration roughly corresponding to (Stone 2014):

$$t_{\rm dur} \propto t_{\rm edd} \propto M_{\rm BH}^{-2/5} M_*^{1/5} R_*^{3/5} \tag{3.20}$$

For canonical parameters, this corresponds to a duration of about 750 days.

Lost in these scaling relations is the fact that more massive black holes cannot

disrupt less massive stars, because the tidal radius will be inside the horizon. The limiting SMBH mass (i.e., the Hills mass, $M_{\rm H}$) $M_{\rm H} = (1.1 \times 10^8 M_\odot) R_*^{3/2} M_*^{-1/2}$ (Hills 1988) is proportional to $M_*^{0.7}$, assuming $R_* \propto M_*^{0.8}$ for main sequence stars (Demircan & Kahraman 1991).

The scaling relations in Equations 3.18 and 3.19, along with a sample of TDEs from the literature, are shown in Figure 3.15. The majority of these transients follow the scaling relation with black hole mass, with the notable exception of extremely luminous ASASSN-15lh (Dong et al. 2016). A rapid spin rate and large black hole masses were necessary to explain the unique optical light curve of this claimed TDE (Margutti et al. 2017b; Leloudas et al. 2016; van Velzen 2018). From the sample of observed objects and the above scaling relations, it is clear that TDEs are not expected to produce short duration ($\lesssim$ 20 days) transients.

3.3.9 Other Subclasses

In this section we enumerate additional types of transients which are either observed in small numbers or only hypothesized to exist, but whose physical models we do not explore in detail.

Accretion Induced Collapse (AIC)

As an accreting white dwarf approaches the Chandrasekhar limit, it can collapse into a NS (Bailyn & Grindlay 1990; Nomoto & Kondo 1991; Fryer et al. 1999) with a rotationally-supported disk with mass $M_{\rm disk} \lesssim 0.1$ M$_\odot$ (Dessart et al. 2006). The disk will then accrete onto the NS and eventually unbind as free nucleons recombine to form

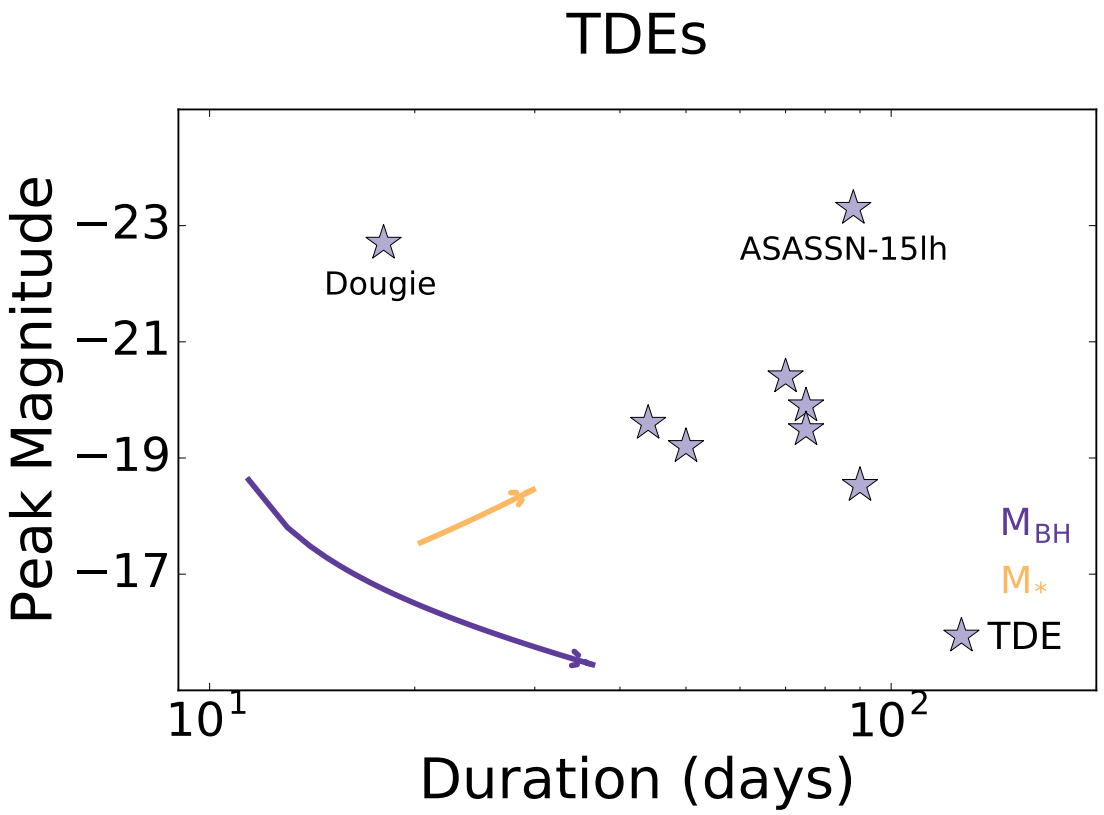

Figure 3.15: Rough effects of $M_{\rm BH}$ (purple) and M_* (orange) on TDE light curves assuming that the duration is proportional to $t_{\rm peak}$ (Equation 3.19) and that $R_* \propto M_*^{0.8}$. Arrows point towards increasing values of each parameter. Also shown is a complete sample of well-sampled R/V/I TDE light curves from which we can measure a duration from the Open TDE Catalog at the time of writing. Light curve data gathered from Dong et al. (2016); Holoien et al. (2014); Arcavi et al. (2014); Gezari et al. (2012); Chornock et al. (2014a); Gezari et al. (2006); Vinkó et al. (2015); Wyrzykowski et al. (2014).

He. The radioactive heating of this ejecta is predicted to produce a fast ($t_{\rm dur} \sim 1$ day) and dim ($M_{\rm R} \sim -13.5$ mag) optical transient (Metzger et al. 2009; Darbha et al. 2010a). These are somewhat dimmer and shorter-duration compared to those of the ^{56}Ni models explored in Section 3.3.2. We plot several models from Darbha et al. (2010a) in Figure 3.16.

Sub-Chandrasekhar Models/.Ia SNe If a WD is accreting hydrogen or helium from a companion, it can undergo unstable thermonuclear ignition, which may then lead to detonation given high enough densities of accreted material (Bildsten et al. 2007; Shen et al. 2010; Woosley & Kasen 2011). The resulting transient is specifically referred to as a ".Ia SN" if the binary companion is He-rich (Shen et al. 2010). Theoretical models of .Ia SNe peak in the optical ($M_{\rm R} \sim -17$ to -19 mag) and have intermediate durations ($t_{\rm dur} \sim 10-20$ days). More generally, these types of transients are described as sub-Chandrasekhar detonations and explosions (e.g., Sim et al. 2010; Woosley & Kasen 2011) and are powered by radioactive decay. No convincing cases of such a model have been observed to date. In Figure 3.16 we show several models from the literature (Shen et al. 2010; Sim et al. 2012; Woosley & Kasen 2011).

Ca-rich Transients

Ca-rich transients are an observational class of dim transients ($M_{\rm R} \sim -15$ to -16 mag) with intermediate durations ($t_{\rm dur} \sim 20$ days) whose nebular-phase spectra are rich in Ca and are primarily found in the outskirts of elliptical galaxies (Kasliwal et al. 2012; Lyman et al. 2014; Lunnan et al. 2017). Like many low-luminosity classes, the exact origin of these transients is uncertain, although they are likely powered by radioactive

decay. One suggested origin is a WD-NS merger (Metzger 2012). A sample of these transients (Lunnan et al. 2017) is shown in Figure 3.16.

Electron-Capture SNe

Electron-capture SNe (ECSNe) are explosions of super-asymptotic giant branch (SAGB) stars ($M_{\rm MS} \sim 7 - 9.5$ M$_\odot$) with O+Ne+Mg cores rather than Fe cores. As the density of these cores increase, the electron capture onto Mg nucei leads to a decrease in the degeneracy pressure leading to collapse (Miyaji et al. 1980; Tominaga et al. 2013). Like Type IIP SNe, ECSNe are powered by hydrogen recombination and radioactive decay. The resulting optical transients are expected to be dim ($M_{\rm R} \sim -16$ to -18 mag), due to the small ejecta masses and kinetic energies and have intermediate durations ($t_{\rm dur} \sim 40 - 100$ days). We show the theoretical light curves produced by Tominaga et al. (2013) in Figure 3.16.

Luminous Red Novae (LRNe)

LRNe are an observational class of terminal transients which are characterized by their dim ($M_{\rm R} \sim -10$ to -13 mag) and red light curves ($g - r > 1$) with durations ($t_{\rm dur} \sim 50 - 100$ days) typically longer than those of classical novae at the same brightness (Martini et al. 1999; Kulkarni et al. 2007). The class is heterogeneous, although many LRNe have double-peaked light curves, with the peaks separated by ~ 100 days. The origin of these events is unclear and theoretical explanations range from planetary capture (Retter & Marom 2003) to stellar mergers entering the common envelope phase (Soker & Tylenda 2006; Rau et al. 2007; Ivanova et al. 2013; Blagorodnova et al. 2017;

Metzger & Pejcha 2017). We show a number of observed events which were identified as LRNe in the literature in Figure 3.16.

Classical Novae

Novae have a rich observational history due to their high observed rate and utility as standardizable candles (Della Valle & Livio 1995). They occur when H-rich matter accretes onto a white dwarf from a binary companion, and the surface undergoes thermonuclear ignition (Gallagher & Starrfield 1978). We use the empirical maximum magnitude relation with decline time (MMRD) to place classical novae in the duration-luminosity phase space diagram. The MMRD relates the V-band peak magnitude with the decline time, t_2 (t_3), or the time to dim by two (three) magnitudes from peak. We approximate the duration as twice the time is takes to fall by one magnitude ($2t_1$). However, t_1 is not often reported in studies of the MMRD and can be much faster than the naive assumption of $t_2/2$ or $t_3/3$. We approximate t_1 by assuming that $t_3 - t_2 = t_2 - t_1$, or that the light curve decays linearly between t_3 and t_2. We use the relation from Capaccioli et al. (1990) to transform between t_2 and t_3 and solve our above equation for t_1:

$$t_1 = 0.31 t_2 - 1.9 \text{ days} \tag{3.21}$$

We then use the MMRD relation measured by Della Valle & Livio (1995) to estimate the peak magnitude:

$$M_{\mathrm{R}} = -7.92 - 0.81 \arctan \frac{1.32 - \log t_2}{0.23} \tag{3.22}$$

Novae R-band light curves tend to be brighter and longer-duration than V-band (Cao et al. 2012), but we do not make an explicit correction for this. The modified MMRD relation described above is shown in Figure 3.16.

Other Theoretical Merger Models

There are several other theorized merger models which might additionally occupy the short-duration regime of the DLPS, which we will not discuss in detail in this work. For example, following a WD-NS merger, both ^{56}Ni and shocks powered by wind-ejecta interaction may produce a luminous ($L \sim 10^{43}$ erg s^{-1}) and short-duration ($t_{\rm dur} \sim$ week) transient (Margalit & Metzger 2016). Similarly, WD-WD mergers which do not produce Type Ia SNe might produce less-luminous ($L \sim 10^{41} - 10^{42}$ erg s^{-1}) and shorter duration ($t_{\rm dur} \sim 1$ day) optical transients powered by the outflow of a differentially rotating merger product (Beloborodov 2014).

3.3.10 Combined Models: ^{56}Ni Decay and Magnetar Spin-down

Until now we have assumed that each transient class is powered by a single energy source. In reality, we expect SN-like explosions to have multiple heating sources. We specifically expect newly synthesized ^{56}Ni within SNe ejecta.

In this section, we consider light curves generated from a combination of two power sources: ^{56}Ni decay and magnetar spin-down. We generate these light curves by adding the input luminosities from both contributions and diffuse the input luminosity through the expanding ejecta using `MosFIT`.

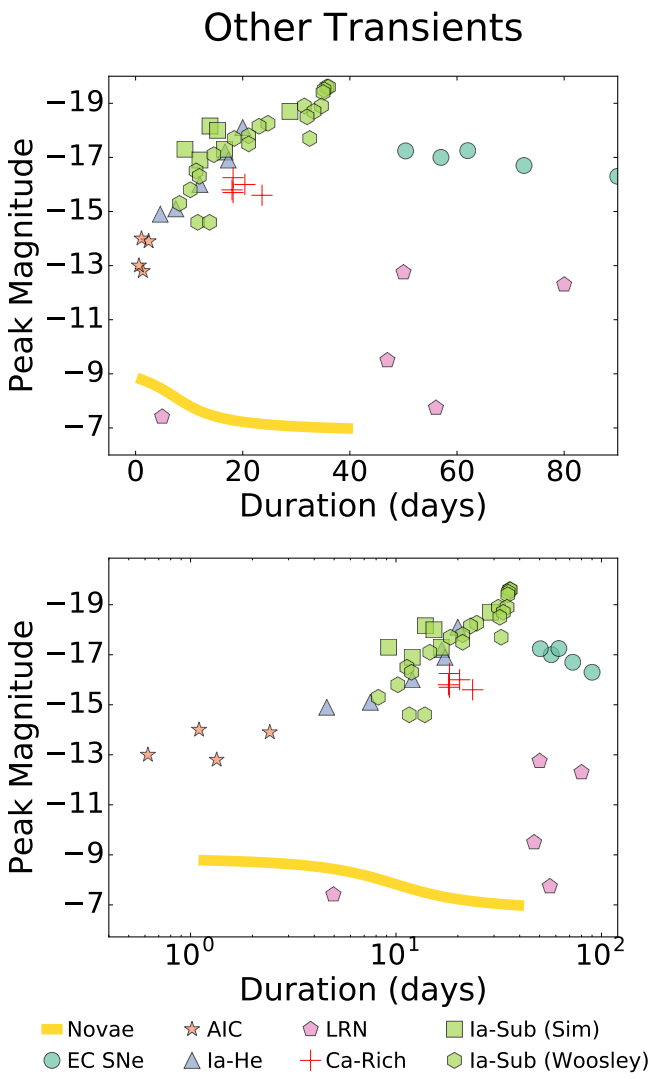

Figure 3.16: DLPS of transients described in Section 3.3.9. Specifically shown are electron-capture SNe models from Tominaga et al. (2013), accretion-induced collapse models from Darbha et al. (2010b), Ia-He models from Shen et al. (2010), and sub-Chandrasekhar Ia models from Sim et al. (2012) and Woosley & Kasen (2011). We additionally show samples of Ca-rich transients from Kasliwal et al. (2012) and Lunnan et al. (2017), and LRNe from the literature (Williams et al. 2016; Kashi & Soker 2010; Kasliwal et al. 2011; Goranskij et al. 2016).

Using the same parameter distributions as in Sections 3.3.2 and 3.3.4, we generate R-band light curves for the combined power sources, and show these distributions in Figure 3.17. The joint DLPS generally overlaps with the distribution of solely magnetar-powered transients, although the low-luminosity ($M_{\rm R} \gtrsim -16$ mag) transients are missing, since in these cases the heat input from ^{56}Ni decay dominates over the magnetar heating.

We separate the models based on the dominant (contributing $\geq 50\%$) heat source at peak (R-band) luminosity and find that almost all transients brighter than $M_{\rm R} \sim -19.5$ mag are dominated by magnetar spin-down; conversely, all transients fainter than this value are dominated by ^{56}Ni. The transition between dominating power sources is mainly controlled by the magnetic field of the magnetar. All models dominated by ^{56}Ni have $B \lesssim 5 \times 10^{13}$ G. At lower luminosities, the presence of a newly-formed magnetar will not be apparent photometrically.

3.3.11 Combined Models: ^{56}Ni Decay and Ejecta-CSM Interaction

We next explore combined ^{56}Ni decay and ejecta-CSM interaction. The diffusion processes for these two models are different: the input luminosity from the ^{56}Ni decay diffuses through the ejecta and optically thick CSM ($M_{\rm ej} + M_{\rm CSM,th}$), while the ejecta-CSM input luminosity diffuses through $M_{\rm CSM,th}$. We assume that these two components evolve independently and add together their final luminosities.

Typical light curves for the case of $s = 2$ (wind) and their distribution in the DLPS are shown in Figure 3.18. As in the case of combined ^{56}Ni-decay and magnetar

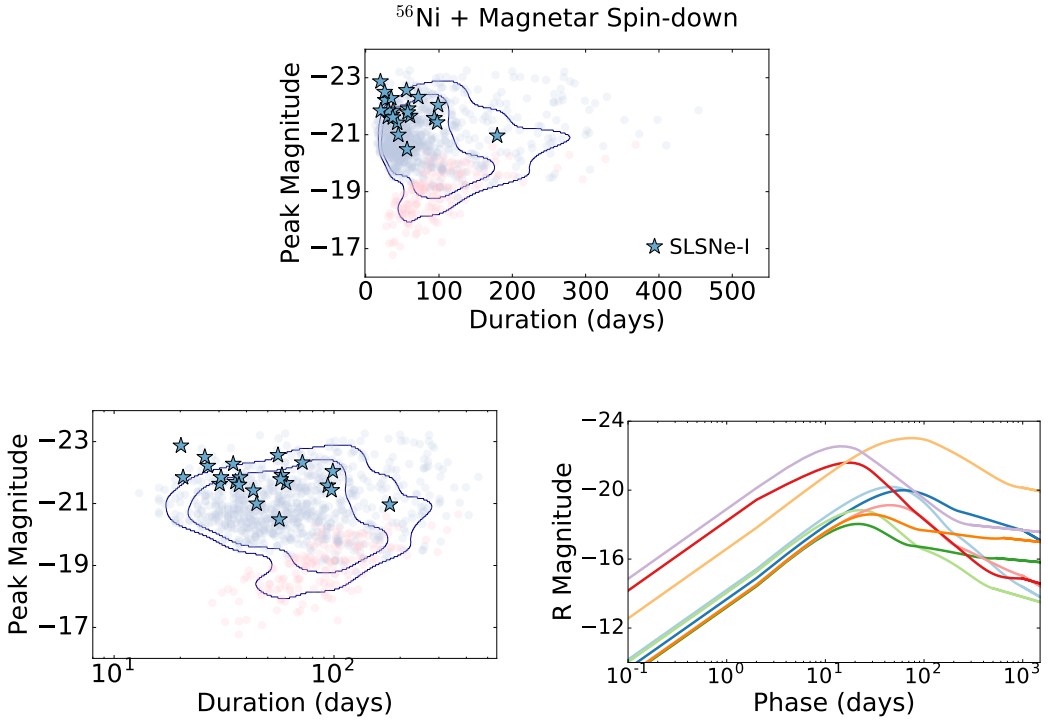

(b) (c)

Figure 3.17: *Top & Middle*: DLPS for explosions powered by magnetar spin-down and ^{56}Ni radioactive decay. The color indicates the dominated heating source at peak luminosity (blue for magnetar spin-down and red for ^{56}Ni). Also shown are 68th and 90th percentile contours for the realizations, estimated using a KDE. *Bottom*: Representative simulated light curves.

spin-down, no transients brighter than ~ -19.5 mag are dominated by the ^{56}Ni input luminosity at peak. Unlike the transients solely powered by ejecta-CSM interactions, we find no transients with durations $\lesssim 10$ days, and no transients with $M_{\rm R} \gtrsim -14$ mag, because in such cases the timescale and luminosity are determined by radioactive heating.

The dominance of CSM interaction over ^{56}Ni is mainly controlled by the mass loss rate, $\dot{M}$. Assuming $v_{\rm wind} \sim 100$ km s^{-1}, CSM interaction dominates when $\dot{M} \gtrsim 10^{-3}$ M$_\odot$ yr^{-1}. This is consistent with LBV mass loss rates (Smith 2014).

3.4 Discussion

3.4.1 Specific Engine Insights

In this section, we enumerate a number of insights which can be gained from the preceding analysis of the DLPS. We focus on the overlap of our predicted models with the observed populations and the regions of phase space that these models occupy.

We begin with the adiabatic expansion models which lack any internal heating source. The largest progenitors (RSG-like) can produce luminous (reaching $M_{\rm R} \sim -18$ mag) transients on timescales similar to those of SNe ($t_{\rm dur} \sim 20 - 100$ days). In fact, the RSG models span a similar range of peak magnitudes as the Type IIP/L models. The BSG-like subclass lie within the luminosity gap ($M_{\rm R} \sim -10$ to -15 mag) with durations similar to those of SNe ($t_{\rm dur} \sim 20$ days), and the white dwarf-like subclass have nova-like luminosities ($M_{\rm R} \sim -7$ to -11 mag) and have much shorter durations ($t_{\rm dur} \sim 1$ day). In

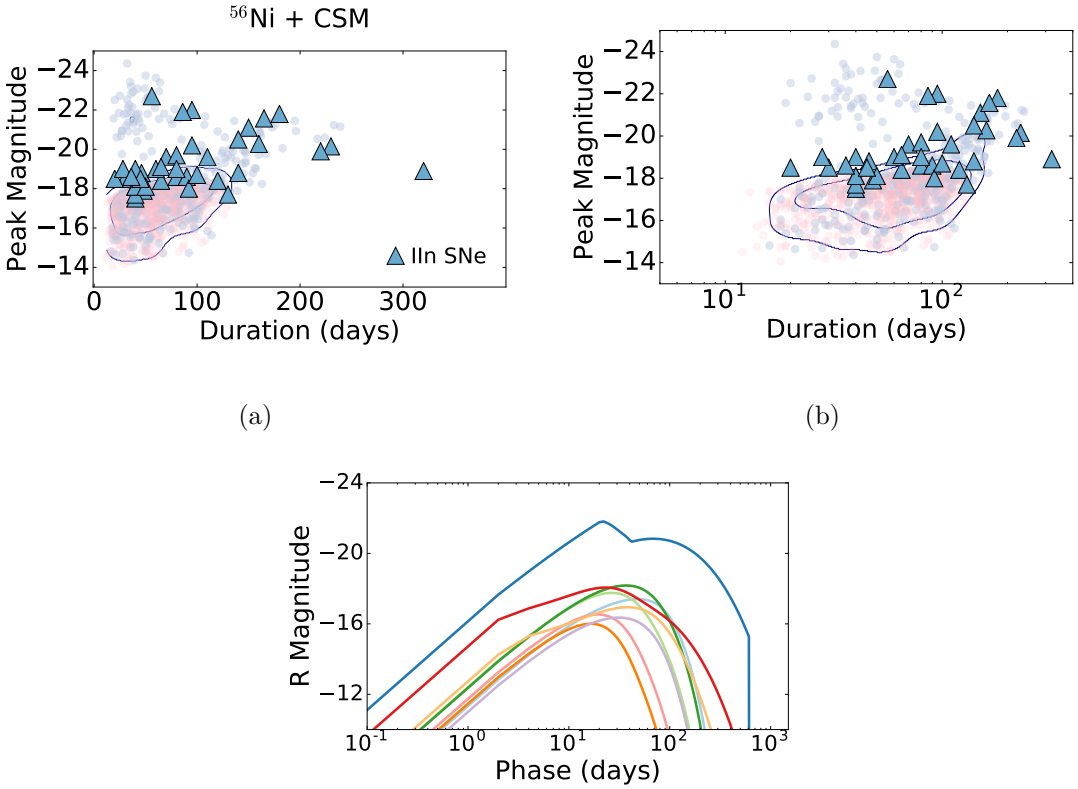

Figure 3.18: *Top & Middle*: Simulated DLPS for explosions powered by ejecta-CSM interaction and ^{56}Ni radioactive decay. The color indicates the dominated heating source at peak luminosity (blue for CSM interaction and red for ^{56}Ni). Also shown are 68th and 90th percentile contours for the realizations, estimated using a KDE. *Bottom*: Representative simulated light curves

reality, these models will likely be paired with some radioactive heating or an additional heating source and therefore represent lower limits in both duration and luminosity. We can see from these models that for massive progenitors, we expect transients which last $\gtrsim 10$ days. In contrast, compact object (or stripped) progenitors can reach the extreme limits of this phase space and generate faster transients but only at low luminosities.

Next we discuss our simulated DLPS of ^{56}Ni-powered transients. In the simulated and observed populations of Type Ib/c SNe, there is a dearth of short duration ($t_{\rm dur} \lesssim 20$ days) and long duration ($t_{\rm dur} \gtrsim 80$ days) transients. These timescales correspond to transients with small ejecta masses/high velocities and large ejecta masses/low velocities, respectively. From the literature, we find only two well-observed supernovae with durations $\gtrsim 70$ days (also shown in Figure 3.3): iPTF15dtg (Taddia et al. 2016) and SN 2011bm (Valenti et al. 2012). Both objects require large ^{56}Ni and ejecta masses to explain their extended light curves, suggesting intrinsically rare massive progenitors (Valenti et al. 2012; Taddia et al. 2016). Longer duration transients are seen in the PISNe models with larger ejecta masses and kinetic energies. However, the low-metallicity progenitors of PISNe are expected to be found at high redshift, meaning that observed PISNe are likely to be even slower (time dilated by $1 + z$) and redder. Shorter duration transients are seen in the Iax-like models due to their lower ejecta masses, although very few of these transients (observed or simulated) have $t_{\rm dur} \lesssim 10$ days.

When considering the radioactive decay of ^{56}Ni as a heating source for short-duration transients, it is important to note that it is largely the ratio of the ejecta mass to the nickel mass which limits the light curve parameters. In reasonable physical models, it is unlikely that $f_{\rm Ni} \gtrsim 0.5$ (although a few Type Ia SNe with higher nickel fractions have been observed, e.g., Childress et al. 2015). This means that, regardless of the amount of

^{56}Ni within the ejecta, the timescale of the transient will typically be set by $M_{\rm ej}$ (and other factors). This fact – the low ^{56}Ni fraction in physical models – essentially eliminates luminous, short-duration transients powered by ^{56}Ni. For example, this is why ^{56}Ni fails as the main power source for superluminous supernovae, which have relatively short durations given their high luminosities (Kasen & Bildsten 2010; Nicholl et al. 2013).

The kilonovae models, powered by r-process decay, lie in a unique area of the DLPS, with short durations ($t_{\rm dur} \sim$ few days) and low luminosities ($M_{\rm R} \sim -8$ to -16 mag). Their short durations couples with low luminosities follows the general trend seen in the stripped SNe models. Although there is currently large uncertainty in the opacity of Lanthanide-rich ejecta (Barnes et al. 2016), all of the models are below typical SNe luminosities and durations. Our red models in particular span to even dimmer events than those explored in Barnes & Kasen (2013) and Metzger (2017), consistent with the recent result by Wollaeger et al. (2018). We additionally note that a brighter and longer-lived, magnetar-powered kilonova has been recently proposed (Yu et al. 2013; Metzger & Piro 2014; Siegel & Ciolfi 2016) which was not explored in this work. Such a kilonova could peak at $\sim 10^{44} - 10^{45}$ erg s^{-1} with a duration of several days, although it would represent a small fraction of the kilonova population.

We next examine the magnetar models explored in Section 3.3.4. We find that the models span a broad range in both duration ($t_{\rm dur} \sim 20 - 250$ days) and luminosity ($M_{\rm R} \sim -16$ to -23 mag). Our models reproduce both the detailed theoretical predictions and observed light curves of SLSNe-I. However, the SLSN-I light curves span a narrower range of the DLPS, primarily at the bright end. This indicates that at least those magnetar-powered events have a narrower range of parameters than explored in this work, as suggested recently by Nicholl et al. (2017a). Transients which have weak

contributions from the magnetar's spin-down are likely dominated by ^{56}Ni-decay (as discussed in Section 3.3.10) and are classified as normal Type Ib/c SNe. We also note that several Type I SLSNe have been accompanied with early-time bumps with several day durations and SN-like luminosities (Leloudas et al. 2012; Nicholl & Smartt 2016) which were not explored in this Chapter. The origin of these bumps is currently unknown, although several theoretical explanations have been posed (e.g., Kasen et al. 2016; Margalit et al. 2018).

Our ejecta-CSM interaction models span the widest range of the DLPS of the models presented here, due to both a large number of free parameters (which may not be independent, as assumed) and the simplifying assumptions used (Chatzopoulos et al. 2012). One of the most striking features is the difference between the wind-like and shell-like CSM geometries, with shell-like models producing brighter transients with somewhat shorter durations ($t_{\rm dur} \sim 100$ days for wind-like vs $t_{\rm dur} \sim 50$ days for shell-like). Although wind-like models can reproduce both low and high luminosity Type IIn SNe, the shell-like models with SN-like ejecta masses and kinetic energies do not extend to the luminosities of normal Type IIn SNe. Focusing on the wind-like models, we find that luminosity and duration are positively correlated at shorter ($t_{\rm dur} \lesssim 20$ days) durations, with no models brighter than $M_{\rm R} \sim -14$ mag in this regime.

We note that Chatzopoulos et al. (2013) find that, when fitting SLSNe with the semi-analytical model used in this work, both $s = 0$ and $s = 2$ can generally be used to find acceptable fits, but the models lead to substantially different explosion parameters. For the normal Type IIn SNe, Moriya et al. (2014) estimated the CSM profile (s) from the post-peak light curves of 11 Type IIn SNe and found that most showed $s \sim 2$. This implies that the shell model ($s = 0$) is less physical for at least the Type IIn events.

The heterogeneous group of transients discussed in Section 3.3.9 span a broad range of the DLPS, but their phase space is not particularly unique. Many of the models with likely compact object progenitors (e.g. Ca-rich transients and sub-Chandrasekar models), are confined to a small area similar to the Iax-like models we explored in Section 3.3.2. The electron-capture SN models overlap with the Type Ib/c and Type IIP SNe, and the LRNe are broadly consistent with the CSM interaction outburst-like models. Only the AIC models and classical novae extend to novel regions of the DLPS at $t_{\rm dur} \lesssim 10$ days durations but invariably with low luminosities ($M_{\rm R} \gtrsim -14$ mag).

Finally, we focus on our combined models with radioactive decay coupled to either magnetar spin-down or ejecta-CSM interaction. In the ejecta-CSM interaction case, the addition of ^{56}Ni decay eliminates both short-duration ($t_{\rm dur} \lesssim 10$ days) and dim ($M_{\rm R} \gtrsim -14$ mag) transients that are otherwise produced by this model. The former is due to the fact that the decay of ^{56}Ni dominates the CSM interaction light curves, eliminating the artificial cutoffs to the input luminosities. Additionally, there is a clear separation of transients which are dominated by ^{56}Ni decay or CSM interaction/magnetar spin-down in the DLPS around $M_{\rm R} \sim -19.5$ mag. In the ejecta-CSM interaction case, this separation roughly coincides with where the estimated mass-loss rate of the progenitor star roughly matches typical LBV mass loss rates ($\dot{M} \sim 10^{-3}$ M$_\odot$ yr^{-1}; Smith 2014), and where many identified Type IIn SNe lie. In the case of magnetar spin-down, the separation occurs at $B \sim 5 \times 10^{13}$, about the cutoff for expected magnetar magnetic field strengths (Zhang & Harding 2000).

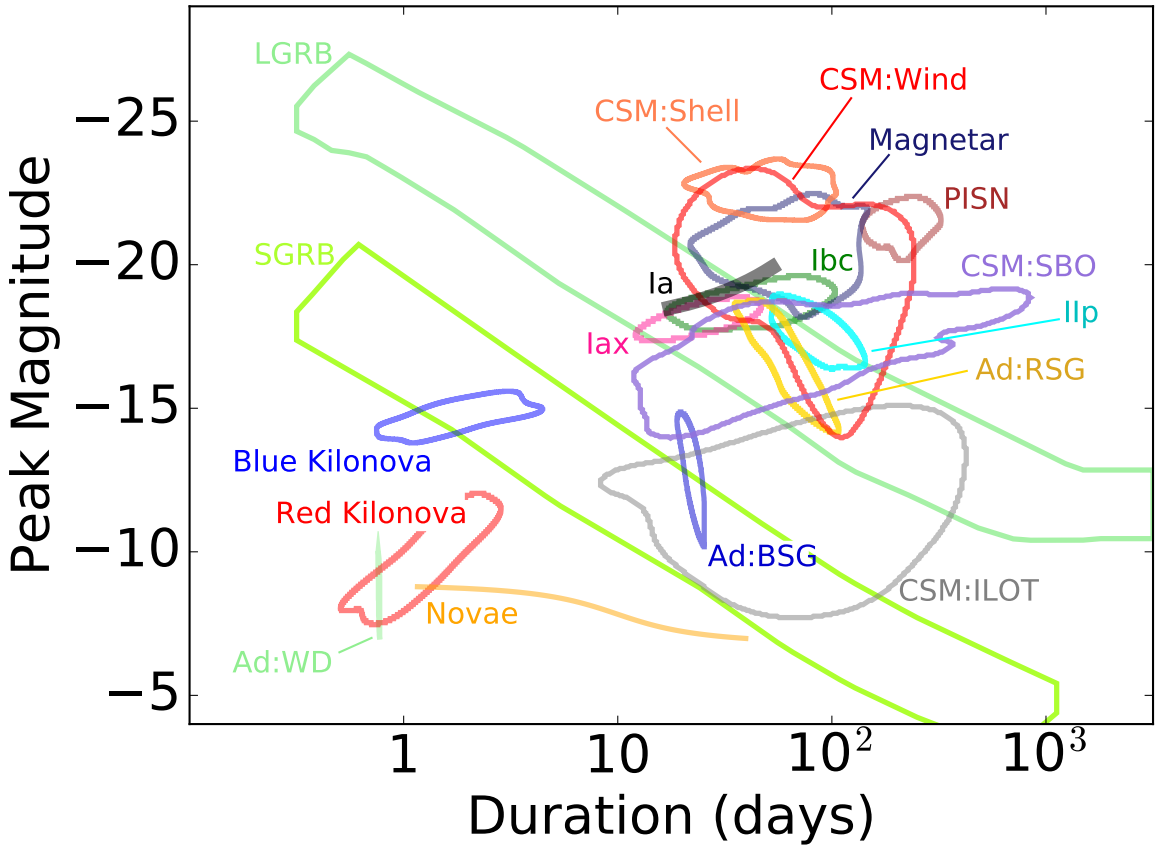

Figure 3.19: The full DLPS explored in this work. Each colored region represents a contour that contains roughly 68% of the Monte Carlo realizations for each class, estimated using a KDE. An interactive version of this plot, including 90% contours and linear-space version can be found at ashleyvillar.com/dlps.

3.4.2 The Optical Transient Landscape

In this section, we summarize the overarching results from the DLPS analysis and highlight several regions of interest. To begin, we present all of the classes simulated in this Chapter (excluding TDEs and the "other transients" in Section 3.3.9) in Figure 3.19. An interactive version of this plot, which can be used to compare user-uploaded transients to the complete DLPS, is available online[3].

There is substantial overlap among models, especially between $t_{\rm dur} \sim 10 - 100$ days and $M_{\rm R} \sim -18$ to -20 mag. Interestingly, this is also where most observed transients lie in the DLPS. A wide range of explosion physics and internal heating sources lead to similar optical light curve properties, in part due to similar kinetic energies and ejecta masses. This highly populated regime highlights the fact that the abundance of observed transients with $\sim$ month-long durations and SN-like luminosities is likely not due to observational biases but a reflection of the underlying physics. But what about the more extreme areas of the DLPS?

We begin by focusing on fast ($t_{\rm dur} \lesssim 10$ days) and bright ($M_{\rm R} \lesssim -18$ mag) transients within our explored models. We find essentially no models that can produce transients in this regime, with the exception of on-axis GRB afterglows. Luminous and fast optical transients cannot be powered by radioactivity, magnetar spin-down or CSM interaction; however, they can be powered by relativistic outflows. Relativistic sources (with $\Gamma \gtrsim$ a few) like GRBs are rare compared to other optical transients. For example, the GRB volumetric rate at $z \lesssim 0.5$ is only 0.1% of the CCSNe rate (Dahlen

[3]ashleyvillar.com/dlps. This applet allows a user to selectively plot transient classes and to add their own datapoints to the simulated DLPS.

et al. 2004; Wanderman & Piran 2010). Given this low rate and current lack of other physically-motivated models, we argue that this portion of the DLPS is, and will continue to be, sparsely populated due to intrinsically rare physics.

A number of heating sources can produce transients that are fast ($t_{\rm dur} \lesssim 10$ days) but invariably dim ($M_{\rm R} \gtrsim -14$ mag), including novae, adiabatic explosions of white dwarfs, r-process kilonovae and CSM interaction models. However, most of these models require unique combinations of parameters, mainly very low ejecta masses, and represent a small fraction of the DLPS explored. Therefore, short-duration transients seem intrinsically rare, even at lower luminosities.

At the other extreme, we find several models that can produce exceptionally luminous transients ($M_{\rm R} \lesssim -22$ mag), including ^{56}Ni decay (in the context of PISNe), magnetar spin-down, GRB afterglows and ejecta-CSM interactions. TDEs may also reach these high luminosities (as seen in the case of ASASSN-15lh; Margutti et al. 2017b). All of these models require extreme parameters to reach such bright luminosities, implying that such events are intrinsically rare. However, these luminous transients are invariably long-duration ($t_{\rm dur} \gtrsim 50$ days).

The dimmest transients ($M_{\rm R} \gtrsim -14$ mag), are generated from adiabatic explosions of white dwarfs, off-axis GRB afterglows, outburst-like ILOTs, classical novae and r-process kilonovae, with a broad range of durations ($t_{\rm dur} \sim 1 - 300$ days). Of these, few lie in the intermediate luminosity gap between the brightest classical novae and dimmest SNe ($M_{\rm R} \sim -10$ to -14 mag). Due to the low rates of GRB afterglows and kilonovae, the most commonly discovered class in this gap will likely be powered by CSM interaction in the context of massive star eruptions (rather than explosions) as inferred

for the small sample of known ILOTs (e.g., Kochanek et al. 2012).

To summarize, we find three sparse regimes of the DLPS: (i) bright and fast transients ($t_{\rm dur} \lesssim 10$ days and $M_{\rm R} \lesssim -16$ mag); (ii) intermediate luminosity transients ($M_{\rm R} \approx -10$ to -14 mag) across all durations; and (iii) luminous transients ($M_{\rm R} \lesssim -21$ mag). Of these, the most sparsely occupied by theoretical models is the first. On the other hand, the typical parameter ranges for SNe (i.e., $t_{\rm dur} \sim 10 - 100$ days and $M_{\rm R} \sim -18$ to -20 mag) contain a number of overlapping models, consistent with the fact that most observed optical transients lie within this regime.

3.4.3 Observability & Survey Considerations

Until now we have investigated theoretical models of transients that occupy the DLPS. The *observed* DLPS of transients will be modified by each class's volumetric rate and luminosity function (which we will explore in a follow-up Chapter). In this section, we will consider the effects of a given survey's parameters (cadence and area) on the observed DLPS. We perform a simple calculation to explore the effect of a transient's luminosity and duration on its survey discovery potential, or its relative discovery rate assuming a constant volumetric rate ($\mathcal{R}$) for every transient, in a flat cosmology ($\Omega_{\rm M} = 0.3$; $\Omega_\Lambda = 0.7$; $H_0 = 70$ km s^{-1} Mpc^{-1}).

The number ($\mathcal{N}$) of transients of a certain luminosity and duration discovered in a given magnitude-limited survey is proportional to:

$$\mathcal{N} \propto \int_{z=0}^{z=z_{\rm lim}} \epsilon \mathcal{R} dV \tag{3.23}$$

where $z_{\rm lim}$ is the redshift where the apparent magnitude of the transient is equal to the limiting magnitude of the survey. The parameter ϵ represents a detection efficiency of the survey, defined by our heuristic equation:

$$\epsilon = \frac{1}{1 + e^{-(t_{\rm dur}(1+z) - N_{\rm D} t_{\rm cad})}} \tag{3.24}$$

where $t_{\rm dur}$ is the transient duration in its rest frame, $t_{\rm cad}$ is the survey cadence and $N_{\rm D}$ is a penalty term to simulate the need for multiple datapoints to "detect" a transient; here we choose $N_{\rm D} = 3$ for illustrative purposes. The chosen efficiency function goes to one when $t_{\rm dur} \gg t_{\rm cad}$ and to zero when $t_{\rm dur} \ll t_{\rm cad}$. When $t_{\rm dur} = N_{\rm D} t_{\rm cad}$, the efficiency is 0.5.

In Figure 3.20, we assume a limiting R-band limiting magnitude of 24.5 (matched to LSST) and calculate $\mathcal{N}$ for a given transient's absolute magnitude and duration assuming a constant volumetric rate and ignoring any k-corrections. We find that the expected detection rates of transients drop off exponentially decreasing luminosity, as well as with shorter duration as it approaches the survey cadence. Specifically, this simple example demonstrates the fact that, even with a relatively high cadence, a wide-field survey will detect 100 – 1000 times more SN-like transients ($M_{\rm R} \lesssim -18$ mag) compared to ILOTs ($M_{\rm R} \sim -10$ to -14 mag). Similarly, a survey with a cadence of several (≈ 3) days will detect 10 – 100 times more transients with SN-like durations ($\sim 20 - 30$ days) compared to transients with short durations ($\lesssim 10$ days). To counter these facts, one could design a survey with a faster survey cadence, but there is a trade off between a survey's cadence, depth and coverage area. A high survey cadence requires a much smaller coverage area, even with a large field of view. A more efficient approach to search for dim transients

may be a targeted survey of nearby galaxies.

Bringing together the above conclusions with those of the previous section, we conclude that quickly evolving transients are invariably dim. Both characteristics lead to diminishing survey potential and therefore lower observed rates. In contrast, bright ($M_{\rm R} \lesssim -22$ mag) transients tend to have longer durations and are therefore easier to observe. However, their volumetric rates are low and have not typically been found in large numbers in untargeted surveys. Between these two regimes, SN-like transients with relatively bright luminosities and intermediate-durations typically have higher volumetric rates, allowing them to be some of the most commonly observed extragalactic phenomena in wide-field surveys.

3.5 Conclusion

We utilized semi-analytical, one-zone models to explore a wide range of heating sources that are either known to or expected to power optical transients. For each heating source we generated model light curves for a physically motivated set of parameters. We also investigated the effects of the parameters on the light curves and the locus of simulated light curves within the DLPS. Our main conclusions are as follows:

- Most model transients lie at $t_{\rm dur} \sim 20 - 100$ days and $M_{\rm R} \sim -18$ to -20 mag, consistent with the observed properties of the bulk of optical transients.
- Only sources with relativistic expansion can produce luminous ($M_{\rm R} < -18$ mag) and fast ($t_{\rm dur} < 10$ days) transients. However, such sources (i.e., GRBs) are known to be intrinsically rare.

- Luminosity and duration are positively correlated for most heating sources, implying that short-duration transients ($t_{\rm dur} \lesssim 10$ days) also have low peak luminosities ($M_R \gtrsim 15$ mag).

- There is a paucity of heating sources that produce transients in the luminosity gap between classical novae and SNe ($M_{\rm R} \sim -10$ to -14 mag) with most models in this regime powered by CSM interaction with low ejecta masses relevant to stellar eruptions rather than explosions.

- Transients with short duration and/or low luminosity are exponentially more difficult to detect in a wide field time-domain survey as the survey cadence approaches the transient duration. Since fast transients have low luminosity this implies an even more significant reduction in the survey potential for fast transients.

The rarity of fast and luminous transients seems unavoidable given our understanding of basic physical processes in optical transients; therefore fast transients will mostly be dim. In addition to this fact, the relative difficulty of detecting short and dim transients (compared to luminous and long duration) is inherent to any time-domain survey. We argue that our approach is essential for the survey designs of future missions (e.g., LSST, WFIRST, etc). Also, we argue that rapid cadence may be more relevant for capturing early phases in the evolution of "slow" transients, rather than for the discovery of intrinsically fast transients.

3.6 Detailed CSM Models

In this appendix, we outline the CSM models used in this work in greater detail. Broadly speaking, both the Chatzopoulos et al. (2012) and Ofek et al. (2014) models follow the interaction of a supernova's ejecta (whose ejecta density distribution is spherically symmetric and a described by broken power-law) and a pre-existing CSM (whose density distribution is spherically symmetric and described by a single power-law). This interaction produces forward and reverse shocks which independently power the optical transient as their kinetic energy is converted into radiation (Chatzopoulos et al. 2012):

$$L = \epsilon \frac{dE_{\rm KE}}{dt} = \epsilon \frac{d}{dt}\left(\frac{1}{2} M_{\rm sw} v_{\rm sh}^2\right) = \epsilon M_{\rm sw} v_{\rm sh} \frac{dv_{\rm sh}}{dt} + \epsilon \frac{1}{2} \frac{dM_{\rm sw}}{dt} v_{\rm sh}^2 \tag{3.25}$$

where $\epsilon = 0.5$ is an efficiency factor, $r_{\rm sh}$ is the shock (forward or reverse) radius at time t, $v_{\rm sh} = dr_{\rm sh}/dt$ is the shock's velocity at time t, $M_{\rm sw} = 4\pi \int_{R_0}^{r_{\rm fs}} \rho_{\rm CSM}(r) r^2 dr$ is the swept-up CSM mass at time t and $\rho_{\rm CSM}(r)$ is the CSM density at radius r. Dessart et al. (2015) found that the conversion efficiency (ϵ) depends on the ratio of the CSM and ejecta masses, reaching as low as $\epsilon \sim 0.3$ and as high as $\epsilon \sim 0.7$.

The progenitor star is embedded in spherically symmetric CSM shell described by a power law ($\rho_{\rm CSM}(r) = qr^{-s}$; Chevalier & Fransson 1994), where $q = \rho_{\rm CSM} R_0^s$. Note that $\rho_{\rm CSM}$ is a constant while $\rho_{\rm CSM}(r)$ is a function of r with $\rho_{\rm CSM}(R_0) = \rho_{\rm CSM}$ at $r = R_0$. The index of the CSM profile can vary from $s = 0$ (roughly corresponding to shell-like, eruptive mass-loss histories) to $s = 2$ (a wind mass-loss history). The SN ejecta's density profile profile $\rho_{SN} = g^n t^{n-3} r^{-n}$ is described by a broken power law (as described in Chevalier & Fransson 1994 and seen observationally in SN 1987A):

$$g^n = \frac{1}{4\pi(\delta - n)} \frac{\left(2(5-\delta)(n-5)E_{KE}\right)^{\frac{n-3}{2}}}{\left((3-\delta)(n-3)M_{\rm ej}\right)^{\frac{n-5}{2}}} \tag{3.26}$$

where δ is the index of the inner profile and n is the index of the outer profile. The light curves are fairly insensitive to δ, so we set its value to 0. The value of n depends on the polytropic index of the progenitor star, varying from 7– 12 for convective to degenerate cores.

The self-similar solutions for the forward and reverse shocks are, respectively (Chatzopoulos et al. 2012; Chevalier & Fransson 1994):

$$r_{\rm fs} = R_0 + \beta_F \left(\frac{Ag^n}{q}\right) t^{\frac{n-3}{n-s}} \tag{3.27}$$

and

$$r_{\rm rs} = R_0 + \beta_R \left(\frac{Ag^n}{q}\right) t^{\frac{n-3}{n-s}} \tag{3.28}$$

β_F, β_R and A are constants which depend on n and s and are order unity in most cases. We use interpolated values from those listed in Chevalier & Fransson (1994).

3.6.1 Recovering the Cacoon SBO Solution

If we assume that the shock deceleration is small $dv_{\rm sh}/dt = 0$ and the geometric factors $\beta_F = \beta_R = 1$, we can recover the bolometric luminosity solution of Ofek et al. (2014) from Equation 3.25:

$$L = \epsilon \frac{dE_{\rm KE}}{dt} = \epsilon \frac{\epsilon}{2} \frac{dM_{\rm sw}}{dt} v_{\rm sh} = 2\pi\epsilon\rho_{\rm CSM}(r_{\rm sh}) r_{\rm sh}^2 v_{\rm sh}^3 \tag{3.29}$$

Furthermore, we assume that this shock efficiently diffuses through the CSM and has an effective diffusion time $t_{\rm d} = 0$ (i.e., the input luminosity is equal to the observed luminosity; Ofek et al. 2014).

The temperature can then be estimated as (Chevalier & Irwin 2011; Ofek et al. 2014):

$$T(t) = \left(\frac{18}{7a}\rho_{\rm CSM} v_{\rm fs}^2\right)^{1/4} \tag{3.30}$$

where a is the radiation constant.

Full CSM interaction Solution

If we loosen the assumptions made to reproduce the light curve solution from Ofek et al. (2014), we will reproduce the generalized solution presented by Chatzopoulos et al. (2012). To do this, we calculate the contributions to the total luminosity from both the forward and reverse shocks and diffuse this input luminosity through the CSM.

We explore both shell-like and wind-like CSM profiles ($s = 0$ and $s = 2$, respectively) and leave the inner radius of the CSM as a free parameter (R_0). By also allowing the total mass of the CSM to be a free parameter ($M_{\rm CSM}$), we can define the total radius of the CSM as:

$$R_{\rm CSM} = \left(\frac{3M_{\rm CSM}}{4\pi q} + R_0^3\right)^{\frac{1}{3}} \tag{3.31}$$

We can further define the photospheric radius as:

$$R_{\rm ph} = \frac{2\kappa q}{3} + R_{\rm CSM} \tag{3.32}$$

where $\kappa = 0.34$ g cm^{-3}. $R_{\rm CSM}$ and $R_{\rm ph}$ will be important for setting physical constraints on our generated models.

The input luminosity arises from the conversion of the forward and reverse shocks' kinetic energy into radiation, which can be described as:

$$\begin{aligned} L_{\rm in}(t) = \frac{2\pi\epsilon}{(n-s)^3} g^n {}^{\frac{5-s}{n-s}} q^{\frac{n-5}{n-s}} (n-3)^2 (n-5) \beta_F^{5-s} A^{\frac{5-s}{n-s}} t^{\frac{2n+6s-ns-15}{n-s}} \theta(t_{\rm FS} - t) \\ + 2\pi\epsilon \left(\frac{Ag^n}{q}\right)^{\frac{5-n}{n-s}} \beta_R^{5-n} g^n \\ \times \left(\frac{3-s}{n-s}\right)^3 t^{\frac{2n+6s-ns-15}{n-s}} \theta(t_{\rm RS} - t) \end{aligned} \tag{3.33}$$

θ is the Heaviside step function, which designates which components (the forward or reverse shocks) are contributing to the total luminosity based on the shock termination times:

$$t_{\rm FS} = \left| \frac{(3-s) q^{\frac{3-n}{n-s}} (Ag^n)^{\frac{s-3}{n-s}}}{4\pi\beta_F^{3-s}} \right|^{\frac{n-s}{(n-3)(3-s)}} M_{\rm CSM}^{\frac{n-s}{(n-3)(3-s)}} \tag{3.34}$$

$$t_{\rm RS} = \left(\left(\frac{v_{\rm ph}}{\beta_R}\right) \left(\frac{q}{Ag^n}^{\frac{1}{n-s}}\right) \left(1 - \frac{(3-n)M_{\rm ej}}{4\pi v_{\rm ph}^{3-n} g^n}\right)^{\frac{1}{3-n}} \right)^{\frac{n-s}{s-3}} \tag{3.35}$$

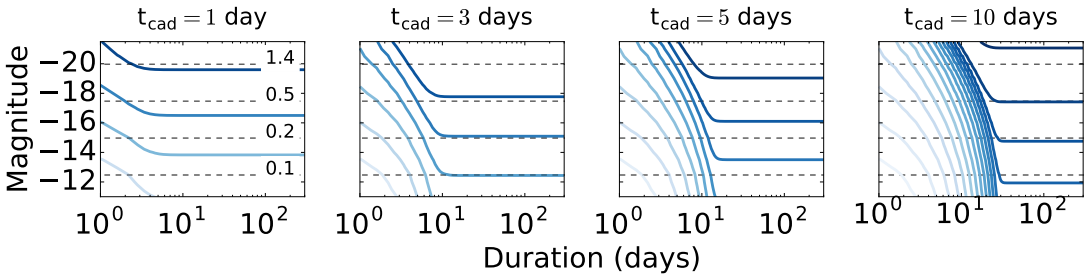

Figure 3.20: Detection rate of optical transients given a luminosity, duration, and survey cadence ($t_{\rm cad}$) and depth (24.5 mag). The lines are exponential contours, with the darkest shade of blue being the most detectable transients. The numbers (and corresponding horizontal lines) in the left panel represent $z_{\rm lim}$ for a given absolute magnitude (see text for details).

Table 3.1:: Engines and Parameters

Adiabatic Expansion (White Dwarf)		
$M_{\rm ej}/{\rm M}_\odot$	$E_{\rm KE}/10^{51}$ erg	$R_0/{\rm R}_\odot$
$0.1-1$	$0.01-1^*$	0.01
Adiabatic Expansion (BSG)		
$M_{\rm ej}/{\rm M}_\odot$	$E_{\rm KE}/10^{51}$ erg	$R_0/{\rm R}_\odot$
$1-10$	$0.01-1^*$	10
Adiabatic Expansion (RSG)		
$M_{\rm ej}/{\rm M}_\odot$	$E_{\rm KE}/10^{51}$ erg	$R_0/{\rm R}_\odot$
$1-10$	$0.01-1^*$	500
^{56}Ni (Ib/c Supernovae)		
$M_{\rm ej}/{\rm M}_\odot$	$E_{\rm KE}/10^{51}$ erg	$F_{\rm Ni}$
$1-10$	$1-10$	$0.01-0.15$
^{56}Ni (WD Eruptions, Iax Supernovae)		
$M_{\rm ej}/{\rm M}_\odot$	$E_{\rm KE}/10^{51}$ erg	$F_{\rm Ni}$
$0.01-1.0^*$	$0.01-1^*$	$0.1-0.3$
^{56}Ni (Pair Instability Supernovae)		
$M_{\rm ej}/{\rm M}_\odot$	$E_{\rm KE}/10^{51}$ erg	$F_{\rm Ni}$
$50-250$	$10-100$	$0.01-0.3$

Table 3.1 – continued from previous page

CSM Interaction (Supernova, Shell)						
$M_{\rm ej}/{\rm M}_\odot$	$E_{\rm KE}/10^{51}$ erg	$M_{\rm CSM}/{\rm M}_\odot$	$\rho/{\rm cm}^{-3}$	n	$R_0/{\rm AU}$	
$1-10$	$1-10$	$0.1-10^*$	$10^{-17}-10^{-13*}$	$7-12$	$1-100^*$	
CSM Interaction (Supernova, Wind)						
$M_{\rm ej}/{\rm M}_\odot$	$E_{\rm KE}/10^{51}$ erg	$M_{\rm CSM}/{\rm M}_\odot$	$\rho/{\rm cm}^{-3}$	n	δ	$R_0/{\rm R}_\odot$
$1-10$	$1-10$	$0.1-10^*$	$10^{-17}-10^{-13*}$	$7-12$	0	$1-100^*$
CSM Interaction (ILOT/outburst-like)						
$M_{\rm ej}/{\rm M}_\odot$	$v/{\rm km\ s}^{-1}$	$M_{\rm CSM}/{\rm M}_\odot$	$\rho/{\rm cm}^{-3}$	n	$R_0/{\rm R}_\odot$	
$0.1-10^*$	$100-1000$	$0.1-10^*$	$10^{-17}-10^{-13*}$	$7-12$	$1-100^*$	
Hydrogen Recombination (IIP/L Supernovae)						
$M_{\rm ej}/{\rm M}_\odot$	$E_{\rm KE}/10^{51}$ erg	$R_0/{\rm R}_\odot$				
$5-18$	$0.1-5$	$100-1000$				
Magnetar Spin-down						
$M_{\rm ej}/{\rm M}_\odot$	$E_{\rm KE}/10^{51}$ erg	$P/{\rm ms}$	$B/10^{14}{\rm G}$			
$1-10$	$1-10$	$1-10$	$0.1-10^*$			
r-process Decay (Red Kilonovae)						
$M_{\rm ej}/{\rm M}_\odot$	$v/1000$ km s^{-1}	$\kappa/{\rm cm}^2{\rm g}^{-1}$				
$0.001-0.1$	$30-90$	$10-100$				
r-process Decay (Blue Kilonovae)						

Table 3.1 – continued from previous page

$M_{\rm ej}/{\rm M}_\odot$	$v/1000$ km s^{-1}	$\kappa/{\rm cm}^2{\rm g}^{-1}$
$0.001 - 0.1$	$30 - 90$	0.2

Note: * Sampled log-uniformly.

Table 3.2:: `MOSFiT` Modules

Heating Source	Engine	Diffusion	Photosphere	SED	Constraints
None (Adiabatic)*	-	-	-	-	-
^{56}Ni Decay	`nickelcolbalt`	`diffusion`	`temperature_floor`	`blackbody`	-
CSM Interaction	`csm`	`diffusion_csm`	`temperature_floor`	`blackbody`	`csmconstraints`
Hydrogen Recombination*	-	-	-	-	-
Magnetar Spin-down	`magnetar`	`diffusion`	`temperature_floor`	`blackbody`	-
r-process Decay	`rprocess`	`diffusion`	`temperature_floor`	`blackbody`	-

Note: * Not implemented in `MOSFiT`

Acknowledgments

We thank Matt Nicholl and Peter Blanchard for valuable discussion and feedback on this work. The Berger Time-Domain Group at Harvard is supported in part by the NSF under grant AST-1411763 and by NASA under grant NNX15AE50G. VAV acknowledges support by the National Science Foundation through a Graduate Research Fellowship. This Chapter greatly benefited from the Open Supernova Catalog (Guillochon et al. 2017).

Chapter 4

The Combined Ultraviolet, Optical, and Near-Infrared Light Curves of the Kilonova Associated with the Binary Neutron Star Merger GW170817: Unified Data Set, Analytic Models, and Physical Implications

This thesis chapter originally appeared in the literature as

V. A. Villar, J. Guillochon, E. Berger et al., *The Astrophysical Journal* 851,

L21

Abstract

We present the first effort to aggregate, homogenize, and uniformly model the combined ultraviolet, optical, and near-infrared dataset for the electromagnetic counterpart of the binary neutron star merger GW170817. By assembling all of the available data from 17 different papers and 46 different instruments, we are able to identify and mitigate systematic offsets between individual datasets, and to identify clear outlying measurements, with the resulting pruned and adjusted dataset offering an opportunity to expand the study of the kilonova. The unified dataset includes 647 individual flux measurements, spanning 0.45 to 29.4 days post-merger, and thus has greater constraining power for physical models than any single dataset. We test a number of semi-analytical models and find that the data are well modeled with a three-component kilonova model: a "blue" lanthanide-poor component ($\kappa = 0.5$ cm^2 g^{-1}) with $M_{\rm ej} \approx 0.020$ M$_\odot$ and $v_{\rm ej} \approx 0.27c$; an intermediate opacity "purple" component ($\kappa = 3$ cm^2 g^{-1}) with $M_{\rm ej} \approx 0.047$ M$_\odot$ and $v_{\rm ej} \approx 0.15c$; and a "red" lanthanide-rich component ($\kappa = 10$ cm^2 g^{-1}) with $M_{\rm ej} \approx 0.011$ M$_\odot$ and $v_{\rm ej} \approx 0.14c$. We further explore the possibility of ejecta asymmetry and its impact on the estimated parameters. From the inferred parameters we draw conclusions about the physical mechanisms responsible for the various ejecta components, the properties of the neutron stars, and, combined with an up-to-date merger rate, the implications for r-process enrichment via this channel. To facilitate future studies of this keystone event we make the unified dataset and our modeling code public.

4.1 Introduction

The joint detection of gravitational waves and electromagnetic radiation from the binary neutron star merger GW170817 marks the beginning of a new era in observational astrophysics. The merger was detected and localized by the Advanced LIGO and Virgo detectors to a sky region of about 30 $\deg^2$ at a distance of $\approx 24 - 48$ Mpc, with inferred component masses of $\approx 1.36 - 1.60$ and $\approx 1.17 - 1.36$ $M_\odot$ (90% confidence ranges for the prior of low neutron star spins; Abbott et al. 2017). A spatially coincident short-duration gamma-ray burst (SGRB) was detected with a delay of 1.7 seconds relative to the merger time (Abbott et al. 2017; Goldstein et al. 2017; Savchenko et al. 2017). About 11 hours post-merger several groups (Abbott et al. 2017; Coulter et al. 2017b; Soares-Santos et al. 2017; Valenti et al. 2017) independently detected an optical counterpart coincident with the quiescent galaxy NGC 4993 at a distance of 39.5 Mpc (Freedman et al. 2001).

Subsequently, multiple ground- and space-based observatories followed up the optical counterpart in the UV, optical, and NIR (hereafter, UVOIR), extending to about 30 days post-merger when the location of the source near the Sun prevented further observations. These observations were published in multiple papers that appeared when the detection was publicly announced on October 16, 2017 (Andreoni et al. 2017; Arcavi et al. 2017; Coulter et al. 2017b; Cowperthwaite et al. 2017; Díaz et al. 2017; Drout et al. 2017; Evans et al. 2017; Hu et al. 2017; Kasliwal et al. 2017; Lipunov et al. 2017; Pian et al. 2017; Pozanenko et al. 2018; Smartt et al. 2017; Troja et al. 2017; Utsumi et al. 2017; Valenti et al. 2017). The various papers generally conclude that the UVOIR emission is due at least in part to a kilonova, a quasi-thermal transient powered by the radioactive decay of newly-synthesized r-process nuclei and isotopes (Li & Paczyński

1998; Metzger et al. 2010; Roberts et al. 2011; Metzger & Berger 2012; Barnes & Kasen 2013; Tanaka & Hotokezaka 2013). In particular, there is general agreement that the observed light curves require at least two distinct components: a "blue" component that dominates the emission in the first few days, followed by a transition to a "red" component. This multi-component behavior is also seen in optical and NIR spectroscopic observations of the transient (Chornock et al. 2017; Nicholl et al. 2017b; Pian et al. 2017; Shappee et al. 2017; Smartt et al. 2017). The blue emission is interpreted to be due to ejecta dominated by Fe-group and light r-process nuclei (atomic mass number $A \lesssim 140$), while the red emission is likely due to ejecta rich in lanthanides and heavy r-process material ($A \gtrsim 140$).

In Cowperthwaite et al. (2017), we modeled photometric data from the Dark Energy Camera (DECam), *Swift*/UVOT, Gemini, and the *Hubble Space Telescope* (*HST*) using the flexible light curve modeling code `MOSFiT` (Guillochon et al. 2017a). The analysis demonstrated that the UVOIR data cannot be explained by the radioactive decay of ^{56}Ni, nor with the associated opacity from Fe-peak elements alone. The data could be well matched by a kilonova model using r-process heating but required at least two distinct components (red and blue) with different opacities, masses, and velocities. A model with a third component (with a higher lanthanide fraction) fit the data equally well (Cowperthwaite et al. 2017). A similar conclusion was reached by several other groups modeling independent sets of observations (e.g., Tanaka et al. 2017a; Kilpatrick et al. 2017a). However, given our limited dataset, we were unable to break degeneracies between the two- and three-component models.

Following the publication of multiple datasets, we undertake here the first effort to aggregate, homogenize, and model all of the available UVOIR measurements. In total,

the UVOIR dataset includes 714 individual measurements from 46 different instruments. After collecting the data, we identify measurements that are clearly discrepant from the majority of similar observations, and where possible correct for systematic deviations in order to include as many photometric points as possible. The final unified dataset includes 647 measurements. With this extensive dataset we revisit the models first explored in Cowperthwaite et al. (2017) with a number of refinements to the physical setup; the model setup is available via the Open Kilonova Catalog[1] (OKC).

The layout of the Chapter is as follows: In Section 4.2 we discuss the various datasets and describe our approach to standardize the data. In Section 4.3 we present our model, including additional parameters designed to capture possible asymmetries in the ejecta geometry. We present the results of the model fits in Section 4.4 and explore their implications in Section 4.5.

[1] `https://kilonova.space/` (Guillochon et al. 2017b).

Table 4.1:: Data Summary

Reference	Bands	Instruments	Telescopes	Photometry	Comments
Andreoni et al.	g,r,i,C	SkyMapper, 2k2k CCD, 1k2k CCD, NAOS-CONICA, VISIR	SkyMapper, Zadko, VIRT, VLT	image subtraction	Additional data to be published by authors.
Arcavi et al.	V, g, r, i, z, w	Sinistro	LCO 1m/CTIO, SAAO, Siding Spring	image subtraction	Possible template contamination in V-, g-, r-, and i-band; w-band calibrated using r-band SDSS reference stars

Table 4.1 Continued:

Reference	Bands	Instruments	Telescopes	Photometry	Comments
Coulter et al.	B, V, g, r, i	E2V 4k4k CCD	Swope	PSF-fitting	
Cowperthwaite et al.	u, g, r, i, z, Y	DECam	Blanco/CTIO,	image subtraction	
Cowperthwaite et al.	$F336W$, $F475W$, $F625W$, $F775W$, $F850LP$, $F110W$, $F160W$, H, K_s	WFC3/UVIS, ACS/WFC, WFC3/IR, Flamingos-2	*HST*, Gemini-South	PSF-fitting	
Díaz et al.	g, r, i	T80Cam	T80S/CTIO	PSF-fitting	

Table 4.1 Continued:

Reference	Bands	Instruments	Telescopes	Photometry	Comments
Drout et al.	B, g, r, i, z, $J1$, J, H, K_s	IMACS, LDSS-3, FourStar, RetroCam	Magellan, du Pont	PSF-fitting	Used rotated image of galaxy as template
Drout et al.	U, V, g, I, J, H, K_s	EFOSC2, SOFI, LRIS	NTT, Keck-I	PSF-fitting	
Drout et al.	V , r, z	IMACS, LDSS-3	Magellan	synthetic photometry	Generated synthetic photometry from spectra
Evans et al.	$UVW2$, $UVM2$, U, B, V	UVOT	Swift	host count rate subtraction	

Table 4.1 Continued:

Reference	Bands	Instruments	Telescopes	Photometry	Comments
Hu et al.	i	10k10k CCD	AST3-2	image subtraction	Possible template contamination in i-band
Valenti et al.	r	Alta U47+	PROMPT5	image subtraction	Pre-existing template
Kasliwal et al.	$F225W$, $F336W$, B, g, V, r, R, i, I, z, u, J, H, K_s	Flamingos-2, GMOS, WIRC, SIRIUS, ANDICAM, NICFPS, VISIR, WFC3/UVIS	Gemini, Palomar, IRSF, CTIO 1.3m, APO 3.5m, VLT, HST	PSF-fitting, aperture photometry	Subtraction of median-filtered image to remove galaxy

Table 4.1 Continued:

Reference	Bands	Instruments	Telescopes	Photometry	Comments
Lipunov et al.	B, V, R, W	MASTER	OAFA, SAAO	image subtraction	Pre-existing template
Pian et al.	B, V, g, r, R, i, I, z	FORS2, ROS2, X-shooter, OmegaCam	VLT, VST, REM	PSF-fitting	
Pozanenko et al.	`LUM`	4k4k CCD	RC-1000	image subtraction	`LUM`-band calibrated using r-band reference stars
Smartt et al.	g, r, i, z, y, J, H, K	GFC, EFOSC2	Pan-STARRS, NTT, 1.5B	image subtraction	Pre-existing template

Table 4.1 Continued:

Reference	Bands	Instruments	Telescopes	Photometry	Comments
Smartt et al.	U, g, r, i, z, J, H, K	GROND	MPI/ESO 2.2m	image subtraction	Possible template contamination in GROND K-band
Tanvir et al.	F475W, r, F606W, i, F814W, z, Y, J, F110W, F160W, K_s	VIMOS, WFC-UVIS, FORS, DK1.5, VISTA, NOT-Cam, WFC-IR, HAWK-I	HST, VLT, HST, DK1, VISTA, NOT	aperture photometry	Local background subtraction; F110W calibrated to J-band.

Table 4.1 Continued:

Reference	Bands	Instruments	Telescopes	Photometry	Comments
Troja et al.	F275W, B,V, F475W, F606W, R, I, z, J, H, $K_{\rm s}$, F110W, F160W	WFC-IR, WFC-UVIS, GMOS	HST, KMT-Net, Gemini	image subtraction	
Utsumi et al.	V, R, g, r, i, z, J, H, K	HSC, SIR-IUS, MOA-II, MOACam, MOIRCS	B&C, IRSF, Tripol5, Subaru	PSF-fitting	MOACam R-band converted to standard R-band using empirical relationship

4.2 Ultraviolet, Optical, and Near-Infrared Data

Following the public announcement of the discovery and observations of GW170817, we aggregated the UVOIR photometry available in the literature, which we provide in this Chapter and in the OKC. The data span from 0.45 days to 29.4 days post-merger, and were collected with 46 instruments in 37 unique filters. This extensive dataset represents a departure from most transient light curves, with over twenty observations taken each night on average with fairly complete color coverage during the duration of the event. For each published set of observations, we summarize the instruments and filters used, the details of the photometry methods, and any relevant notes in Table 4.1. All photometry is reported as AB magnitudes with no correction for Milky Way extinction.

Thanks to the extensive observations from multiple telescopes there is significant redundancy of photometric measurements. This allows us to compare individual datasets to the bulk of the other observations and hence to homogenize and prune the dataset. With this approach we find that some corrections are required for three datasets: *gri*-band data from Arcavi et al. (2017), some K_s-band data from Smartt et al. 2017 and *i*-band data from Hu et al. 2017. All of these datasets utilized image subtraction to isolate the flux of the transient. However, we find that for the specific filters listed above the resulting light curves were typically dimmer, and faded more rapidly, than the rest of the data. We interpret this as being due to residual emission from the transient in the reference templates, since in each case the template was obtained after the discovery of the source. Using the dates of the template images (Arcavi, private communication, Smartt et al. 2017 and Hu et al. 2017), we estimate the kilonova brightness for each filter and add this residual flux to the reported photometry. Specifically, we use estimated

template magnitudes of: 20.8 (g), 20.9 (r), 20.3 (i) and 20.0 (z) mag to the Arcavi et al. (2017) dataset; 19.4 (K_s, GROND data only) mag to the Smartt et al. (2017) dataset; and 19.9 (i) mag to the Hu et al. (2017) dataset. With these corrections the data are in good agreement with the photometry from other sources (to $\lesssim 0.2$ mag).

We additionally exclude two datasets from our model fitting: the r-band dataset from Pozanenko et al. (2018), which was obtained in the `LUM` filter but calibrated to r-band reference stars; and the w-band from Arcavi et al. (2017), which was similarly calibrated using r-band reference stars. Because the kilonova colors differ so drastically from the comparison stars (see e.g., Cowperthwaite et al. 2017), these calibrations are unreliable.

Due to the fact that the observations conducted by the *Swift* UV/Optical Telescope (UVOT) were publicly available, three papers presented independent analyses and photometry of these data (Cowperthwaite et al. 2017; Drout et al. 2017; Evans et al. 2017). However, in our homogenized dataset we only use the photometry presented by the *Swift* team (Evans et al. 2017) without alteration. Early photometry is largely consistent among the three papers to within ≈ 0.2 mag, although the reported observation times differ by several hours due to different choices of time binning.

Similarly, several teams independently analyzed some Gemini-South FLAMINGOS-2 data (Cowperthwaite et al. 2017; Kasliwal et al. 2017; Troja et al. 2017), some NTT EFOSC2 data (Drout et al. 2017; Smartt et al. 2017), and some *HST*/WFC3 data (Tanvir et al. 2017; Troja et al. 2017). All of the measurements are listed in Table 4.3 but marked as repeated observations. The *HST*/WFC3/F110W data from Tanvir et al. (2017) are re-calibrated to ground-based J-band photometry, so we use the data for

these epochs from Troja et al. (2017). For all other epochs with multiple analyses of the same data we take a weighted average of the reported photometry for use in the model fitting, excluding outliers (see below); we report the averaged values in Table 4.3.

Finally, we identify individual outlying data points through visual inspection and comparison. In total, we find fifteen such data points. Three of these are photometry of common data analyzed by multiple teams, so we simply exclude these points from our averaged photometry. We include the twelve other outliers in our modeling, but specifically identify these outliers in Table 4.3.

The combined dataset is listed in Table 4.3. This table includes the MJD date and phase of each observation; the instrument, telescope, and filter combination; our corrected magnitudes and uncertainties; the correction applied to the original magnitudes (where applicable); a reference to the original paper; and a note indicating if the data were excluded from modeling ("X"), were included in modeling ("*"), represent a repeated reduction of the same observations ("R"), are averaged values from repeated observations ("A"), or are marked as outliers ("O").

To properly model this extensive and heterogeneous dataset we use the appropriate transmission curve (or close equivalent) for each filter, instrument, and telescope combination[2].

Photometric modeling of the host galaxy, NGC 4993, suggests that the host

[2]All transmission curves used in this work were obtained through the Spanish Virtual Observatory, `http://svo2.cab.inta-csic.es/svo/theory/fps3/` (Rodrigo et al. 2012), which aggregates official transmission curves for each instrument.

environment contributes minimal extinction (Blanchard et al. 2017)[3]. We therefore only include a correction for Milky Way extinction, with $E(B-V) = 0.105$ mag (Schlafly & Finkbeiner 2011).

4.3 Kilonova Model

In this section we outline the analytical kilonova model first introduced in Metzger (2017) and implemented in `MOSFiT` by Villar et al. (2017). This model was also used in Cowperthwaite et al. (2017) to model our own set of observations.

Following decompression from high densities, seed nuclei within the neutron-rich ejecta from a BNS merger undergo rapid neutron capture (r-process) nucleosynthesis (Li & Paczyński 1998; Metzger et al. 2010), and it is the radioactive decay of these freshly-synthesized nuclei that powers the kilonova (Metzger 2017). Unlike SNe, which are powered primarily by the radioactive decay of one species (^{56}Ni) and therefore undergo exponential decline in their bolometric light curves, kilonovae are powered by the decay of a wide range of r-process nuclei with different half-lives, leading to a power-law decay. At very early times (first few seconds), the energy generation rate is roughly constant as neutrons are consumed during the r-process, but subsequently the r-process freezes out and the energy generation rate approaches a power-law decay, $\propto t^{-\alpha}$ with $\alpha \approx 1.3$ (Metzger et al. 2010). The temporal evolution of the radioactive heating

[3]Levan et al. (2017) find evidence for more moderate extinction, $E(B-V) = 0.07$ mag, from spectroscopic observations near the explosion site.

rate can be approximated by the parameterized form (Korobkin et al. 2012):

$$L_{\rm in}(t) = 4 \times 10^{18} M_{\rm rp} \times \left[0.5 - \pi^{-1} \arctan\left(\frac{t - t_0}{\sigma}\right)\right]^{1.3} \text{erg s}^{-1}, \quad (4.1)$$

where $M_{\rm rp}$ is the mass of the r-process ejecta, and $t_0 = 1.3$ s and $\sigma = 0.11$ s are constants. Our chosen input luminosity described above neglects any contribution from fall-back accretion on the newly formed remnant. Hydrodynamical simulations suggest that disk winds prevent the fall-back material from reaching the remnant on timescales $\gtrsim 100$ ms (Fernández & Metzger 2013; Metzger 2017); however, some contribution to the bolometric light curve from fall-back accretion is possible on longer (days to weeks) timescales.

Although $L_{\rm in}$ provides the total power of radioactive decay (shared between energetic leptons, γ-rays, and neutrinos), only a fraction $\epsilon_{\rm th} < 1$ of this energy thermalizes within the plasma and is available to power the kilonova (Metzger et al. 2010). The thermalization efficiency decreases as the ejecta become more dilute with time, in a manner that can be approximated analytically as (Barnes et al. 2016):

$$\epsilon_{\rm th}(t) = 0.36 \left[e^{-at} + \frac{\ln(1 + 2bt^d)}{2bt^d}\right], \quad (4.2)$$

where a, b, and d are constants of order unity that depend on the ejecta velocity and mass. We use an interpolation of Table 1 of Barnes et al. (2016) for these values.

Assuming that the energy deposition is centrally located and the expansion is homologous, we can use the formalism originally outlined in Arnett (1982) to compute the observed bolometric luminosity (Chatzopoulos et al. 2012):

$$L_{\rm bol}(t) = \exp\left(\frac{-t^2}{t_d^2}\right) \times \int_0^t L_{\rm in}(t) \epsilon_{\rm th}(t) \exp\left(t^2/t_d^2\right) \frac{t}{t_d} {\rm d}t, \quad (4.3)$$

where $t_{\rm d} \equiv \sqrt{2\kappa M_{\rm rp}/\beta v c}$, κ is the grey opacity, and $\beta = 13.4$ is a dimensionless constant related to the ejecta mass geometric profile. We note that the assumption of a centrally concentrated power source is not necessarily true for kilonovae, as here we assume that the ejecta consists entirely of radioactive r-process material. Relaxation of this assumption should be explored in future work.

We explore multi-component models in which each component has a different opacity corresponding to theoretical expectations for different ejecta compositions. The opacity is largely determined by the fraction of lanthanides in the ejecta, with lanthanide-poor ejecta having a typical opacity of $\kappa \approx 0.5$ cm^2 g^{-1}, and lanthanide-rich ejecta having a typical opacity of $\kappa \approx 10$ cm^2 g^{-1} (Tanaka et al. 2017b). A larger opacity results in a slower light curve evolution and a shift of the spectral energy distribution peak to redder wavelengths. We specifically explore a model with two components ("blue", $\kappa = 0.5$ cm^2 g^{-1} and "red", κ left as a free parameter), and with three components ("blue", $\kappa = 0.5$ cm^2 g^{-1}; "purple", $\kappa = 3$ cm^2 g^{-1} and "red", $\kappa = 10$ cm^2 g^{-1}; Tanaka et al. 2017b). The purple component corresponds to ejecta with a low, but non-negligible, lanthanide fraction. Each component of the multi-component model is evolved independently, accounting for the unique opacities and therefore diffusion timescales.

To model the multi-band light curves, we assume that each component has a blackbody photosphere with a radius that expands at a constant velocity ($v_{\rm phot} \equiv v$, where v is the ejecta velocity). At every point in time, the temperature of each component is defined by its bolometric luminosity and radius, using the Stefan-Boltzmann law. However, when the ejecta cool to a critical temperature (T_c) the photosphere recedes into the ejecta and the temperature remains fixed. The full SED of the transient is given by the sum of the blackbodies representing each component. The blackbody approximation

and temperature floor behavior have both been seen in more sophisticated simulations (Barnes & Kasen 2013); the temperature floor may relate to the first ionization temperature in lanthanide species. The analytic form of the blackbody behavior is:

$$T_{\rm phot}(t) = \max\left[\left(\frac{L(t)}{4\pi\sigma_{\rm SB}^2 v_{\rm ej}^2 t^2}\right)^{1/4}, T_c\right], \tag{4.4}$$

and

$$R_{\rm phot}(t) = \begin{cases} v_{\rm ej} t & \left(\frac{L(t)}{4\pi\sigma_{\rm SB}^2 v_{\rm ej}^2 t^2}\right)^{1/4} > T_c \\ \left(\frac{L(t)}{4\pi\sigma_{\rm SB} T_c^4}\right)^{1/2} & \left(\frac{L(t)}{4\pi\sigma_{\rm SB}^2 v_{\rm ej}^2 t^2}\right)^{1/4} \leq T_c \end{cases} \tag{4.5}$$

4.3.1 Asymmetric Model

In addition to the spherically symmetric assumption in the previous section we also explore a simple asymmetric model in which the blue component is confined to the polar regions, while the red component (and purple component in the three-component model) are confined to an equatorial torus. Such a model is seen in numerical simulations (see e.g., Metzger & Fernández 2014; Metzger 2017). We implement this asymmetric distribution by correcting the bolometric flux of each component by a geometric factor: $(1-\cos\theta)$ for the blue component and $\cos\theta$ for the red/purple component, where θ is the half opening angle of the blue component. Although this model neglects other important contributions such as changes in diffusion timescale, effective blackbody temperature, or angle dependence, it roughly captures a first-order correction to the assumption of spherical symmetry.

4.3.2 Fitting Procedure

We model the combined dataset using the light curve fitting package `MOSFiT` (Guillochon et al. 2017a; Nicholl et al. 2017; Villar et al. 2017), which uses an ensemble-based Markov Chain Monte Carlo method to produce posterior predictions for the model parameters. The functional form of the log-likelihood is:

$$\ln \mathcal{L} = -\frac{1}{2} \sum_{i=1}^{n} \left[\frac{(O_i - M_i)^2}{\sigma_i^2 + \sigma^2} - \ln(2\pi\sigma_i^2) \right] - \frac{n}{2} \ln(2\pi\sigma^2), \tag{4.6}$$

where O_i, M_i, and σ_i, are the $i^{\rm th}$ of n observed magnitudes, model magnitudes, and observed uncertainties, respectively. The variance parameter σ is an additional scatter term, which we fit, that encompasses additional uncertainty in the models and/or data. For upper limits, we use a one-sided Gaussian penalty term.

For each component of our model there are four free parameters: ejecta mass ($M_{\rm ej}$), ejecta velocity ($v_{\rm ej}$), opacity (κ), and the temperature floor (T_c). We use flat priors for the first three parameters, and a log-uniform prior for T_c (which is the only parameter for which we consider several orders of magnitude). In the case of the asymmetric model, we assume a flat prior for the half opening angle (θ).

For each model, we ran `MOSFiT` for approximately 24 hours using 10 nodes on Harvard University's Odyssey computer cluster. We utilized 100 chains until they reached convergence (i.e., had a Gelman-Rubin statistic < 1.1; Gelman & Rubin 1992). We use the first $\simeq 80\%$ of the chain as burn-in. We compare the resulting fits utilizing the Watanabe-Akaike Information Criteria (WAIC, Watanabe 2010; Gelman et al. 2014), which accounts for both the likelihood score and number of fitted parameters for each model.

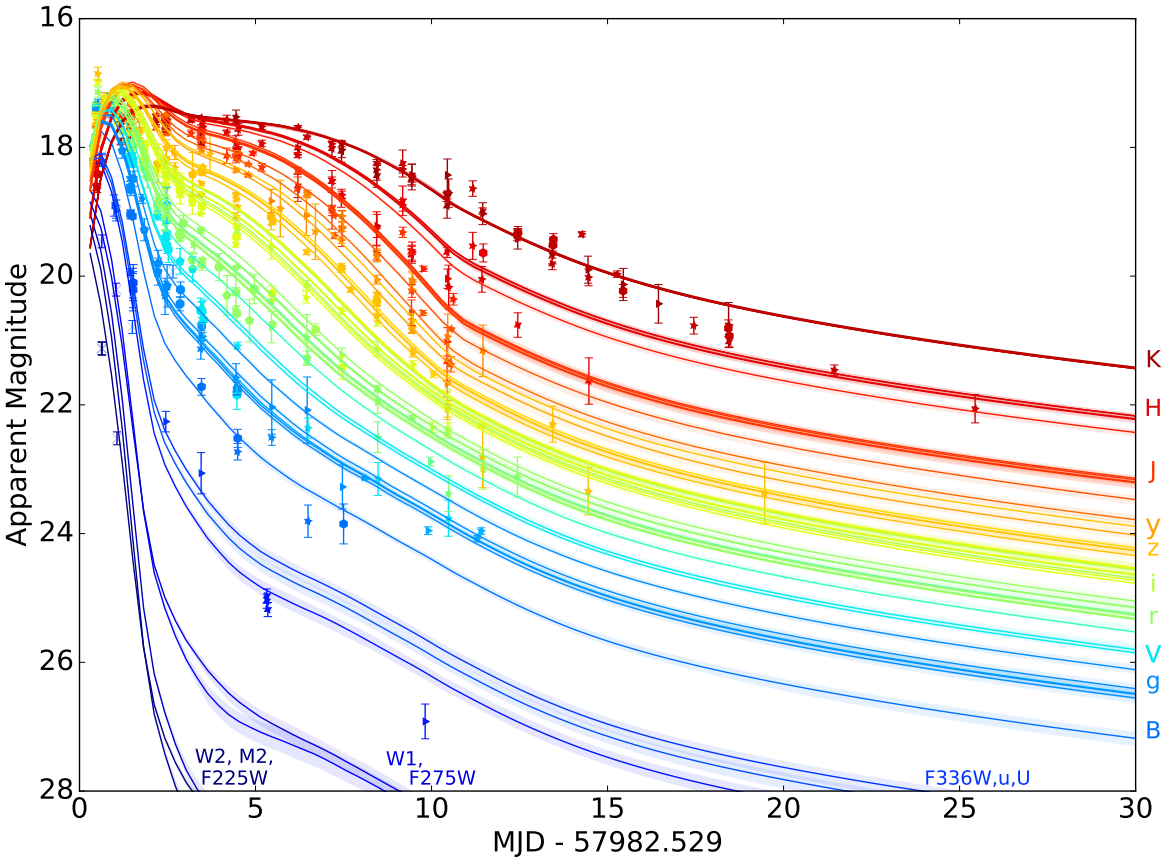

Figure 4.1: UVOIR light curves from the combined dataset (Table 4.3), along with the spherically symmetric three-component models with the highest likelihood scores. Solid lines represent the realizations of highest likelihood for each filter, while shaded regions represent the 1σ uncertainty ranges. For some bands there are multiple lines that capture subtle differences between filters. Data originally presented in Andreoni et al. 2017; Arcavi et al. 2017; Coulter et al. 2017b; Cowperthwaite et al. 2017; Díaz et al. 2017; Drout et al. 2017; Evans et al. 2017; Hu et al. 2017; Kasliwal et al. 2017; Lipunov et al. 2017; Pian et al. 2017; Pozanenko et al. 2018; Smartt et al. 2017; Troja et al. 2017; Utsumi et al. 2017; Valenti et al. 2017.

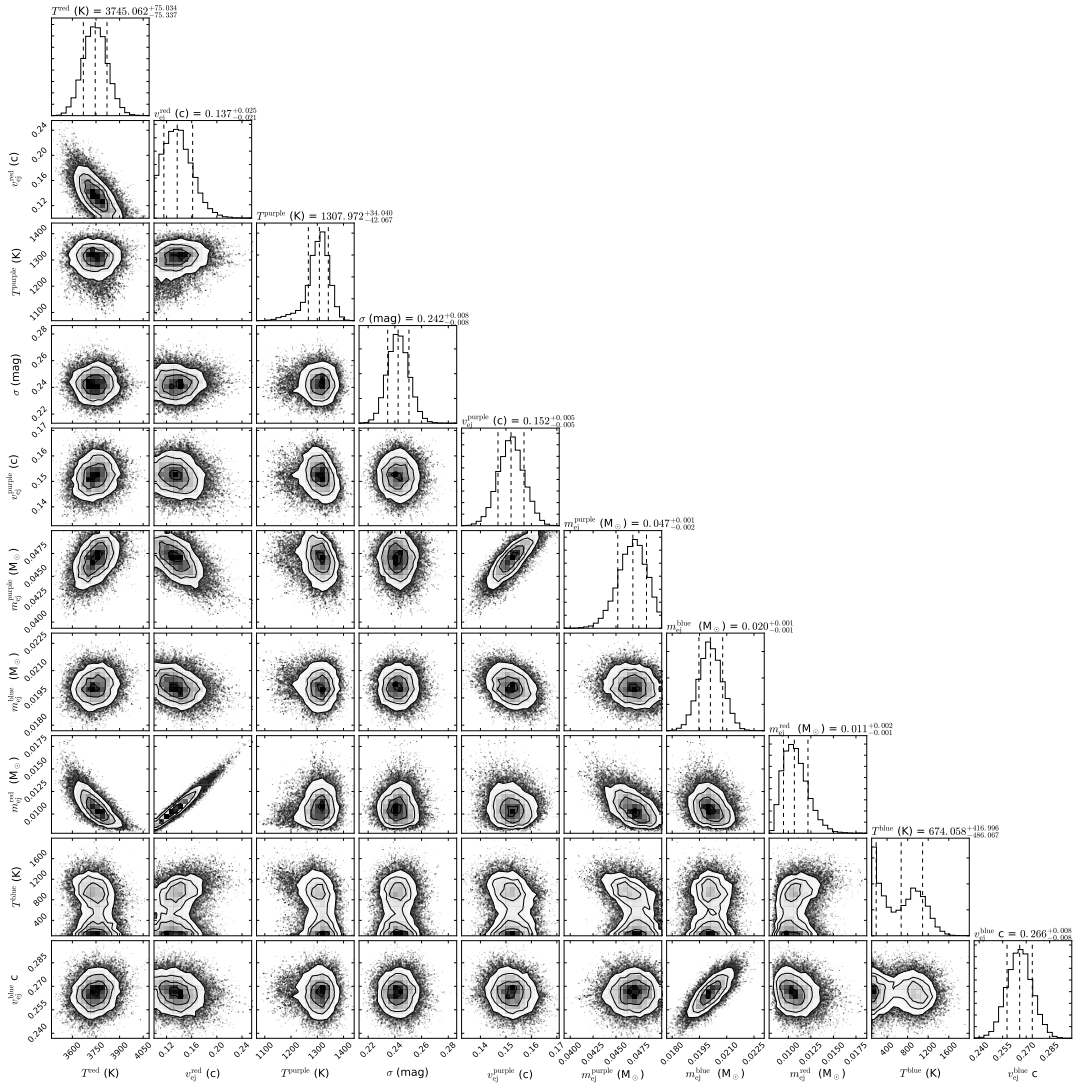

Figure 4.2: Corner plot showing the posterior distributions of parameter realizations for the three-component model (§4.3). Notable parameter degeneracies include the mass-velocity pairs of the three components, (e.g., $m_{\rm ej}^{\rm red}$ versus $v_{\rm ej}^{\rm red}$), with milder degeneracies between the temperature floors $T^{\rm red}$, $T^{\rm purple}$, and $T^{\rm blue}$ and the ejecta masses. In the former case the degeneracy is due to the ratio of the mass and velocity controlling the diffusion timescale.

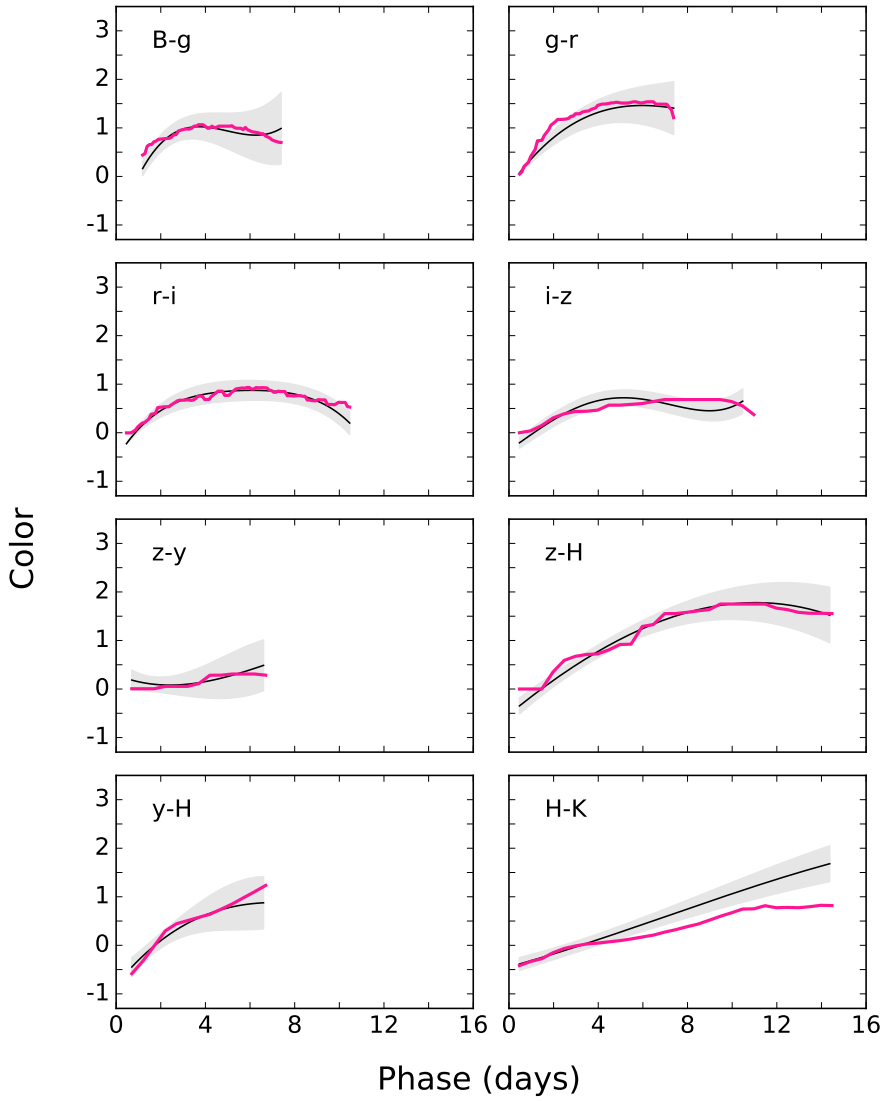

Figure 4.3: Color evolution of the kilonova from various filter pairs. The black line shows an interpolated estimate of the observed colors, while the grey region mark the 1σ uncertainty regions, each interpolated using spline interpolation. The magenta lines are the colors for the spherically symmetric three-component model with the highest likelihood score, which have been median-filtered to minimize Monte Carlo noise.

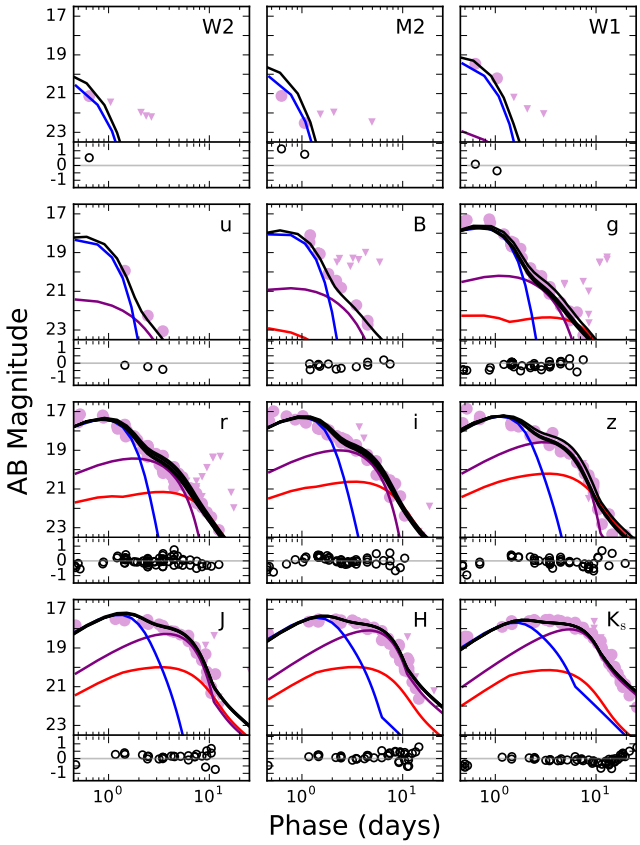

Figure 4.4: Individual band UVOIR light curves, including the data (purple circles), the three-component best-fit model (black lines), and the individual components in the model (blue, purple, and red lines). The lower section of each panel shows the residual between the data and model. Note that some panels contain multiple black lines due to unique filter transmission functions on multiple instruments. Data originally presented in Andreoni et al. 2017; Arcavi et al. 2017; Coulter et al. 2017b; Cowperthwaite et al. 2017; Díaz et al. 2017; Drout et al. 2017; Evans et al. 2017; Hu et al. 2017; Kasliwal et al. 2017; Lipunov et al. 2017; Pian et al. 2017; Pozanenko et al. 2018; Smartt et al. 2017; Troja et al. 2017; Utsumi et al. 2017; Valenti et al. 2017.

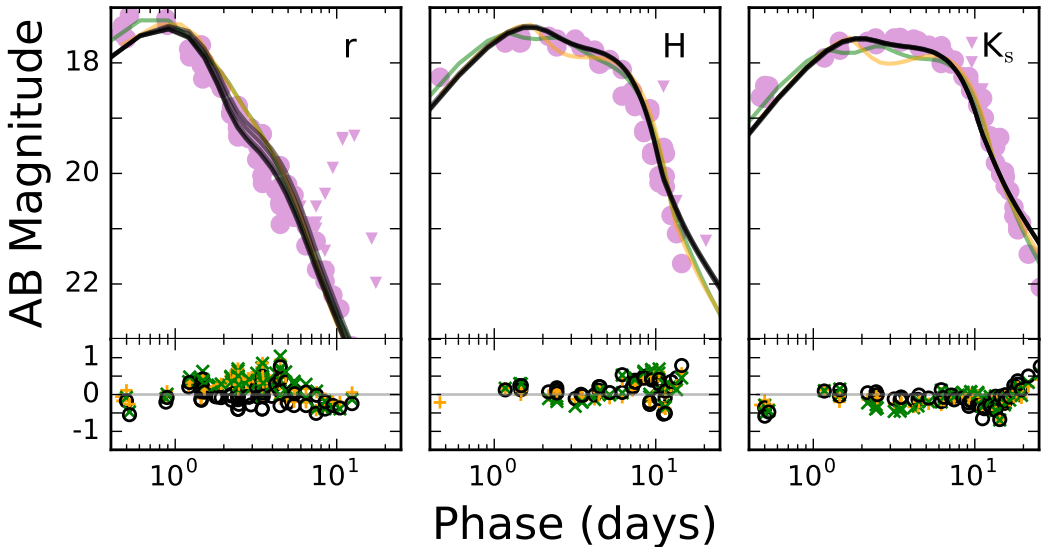

Figure 4.5: UVOIR light curves in select bands that compare the highest likelihood model realizations of the three-component model (black lines), the two-component model (orange lines), and three-component asymmetric model (green lines). The lower section of each panel shows the residual between the data and the three models. All models provide an overall adequate fit to the data, but the two-component predict a double-peaked structure in K-band that is not seen in the data. Data originally presented in Andreoni et al. 2017; Arcavi et al. 2017; Coulter et al. 2017b; Cowperthwaite et al. 2017; Díaz et al. 2017; Drout et al. 2017; Evans et al. 2017; Hu et al. 2017; Kasliwal et al. 2017; Lipunov et al. 2017; Pian et al. 2017; Pozanenko et al. 2018; Smartt et al. 2017; Troja et al. 2017; Utsumi et al. 2017; Valenti et al. 2017.

Table 4.2:: Kilonova Model Fits

Model	M_{ej}^{blue}	v_{ej}^{blue}	κ_{ej}^{blue}	T^{blue}	M_{ej}^{purple}	v_{ej}^{purple}	κ_{ej}^{purple}	T^{purple}	M_{ej}^{red}	v_{ej}^{red}	κ_{ej}^{red}	T^{red}	σ	θ	WAIC
2-Comp	$0.023^{0.005}_{0.001}$	$0.256^{0.005}_{0.002}$	(0.5)	398^{66}_{70}	-	-	-	-	$0.050^{0.001}_{0.001}$	$0.149^{0.001}_{0.002}$	$3.65^{0.09}_{0.28}$	115^{45}_{72}	$0.256^{0.006}_{0.004}$		-1030
3-Comp	$0.020^{0.001}_{0.001}$	$0.266^{0.008}_{0.008}$	(0.5)	674^{486}_{417}	$0.047^{0.001}_{0.002}$	$0.152^{0.005}_{0.005}$	(3)	130^{42}_{34}	$0.011^{0.002}_{0.001}$	$0.137^{0.025}_{0.021}$	(10)	374^{75}_{75}	$0.242^{0.008}_{0.008}$		-1064
Asym. 3-Comp	$0.009^{0.001}_{0.001}$	$0.256^{0.009}_{0.004}$	(0.5)	3259^{302}_{306}	$0.007^{0.001}_{0.001}$	$0.103^{0.007}_{0.004}$	(3)	3728^{94}_{178}	$0.026^{0.004}_{0.002}$	$0.175^{0.011}_{0.008}$	(10)	1091^{29}_{45}	$0.226^{0.006}_{0.006}$	66^{1}_{3}	-1116

4.4 Results of the Kilonova Models

We fit three different models to the data: a spherical two-component model, a spherical three-component model, and an asymmetric three-component model. The results are shown in Figures 4.1–4.5 and summarized in Table 4.2.

For the spherical two-component model we allow the opacity of the red component to vary freely. This model has a total of 8 free parameters: two ejecta masses, velocities and temperatures, one free opacity, and one scatter term. We find best-fit values of $M_{\rm ej}^{\rm blue} = 0.023^{+0.005}_{-0.001}$ M$_\odot$, $v_{\rm ej}^{\rm blue} = 0.256^{+0.005}_{-0.002}c$, $M_{\rm ej}^{\rm red} = 0.050^{+0.001}_{-0.001}$ M$_\odot$, $v_{\rm ej}^{\rm red} = 0.149^{+0.001}_{-0.002}c$, and $\kappa^{\rm red} = 3.65^{+0.09}_{-0.28}$ cm^2 g^{-1}. Although the model provides an adequate fit, it predicts a double-peaked structure in the NIR light curves at $\approx 2-5$ days that is not seen in the data (Figure 4.5).

Our best fitting model, the spherical three-component model, has a total of 10 free parameters: three ejecta masses, velocities and temperatures, and one scatter term. The best-fit values are $M_{\rm ej}^{\rm blue} = 0.020^{+0.001}_{-0.001}$ M$_\odot$, $v_{\rm ej}^{\rm blue} = 0.266^{+0.008}_{-0.008}c$, $M_{\rm ej}^{\rm purple} = 0.047^{+0.001}_{-0.002}$ M$_\odot$, $v_{\rm ej}^{\rm purple} = 0.152^{+0.005}_{-0.005}c$, $M_{\rm ej}^{\rm red} = 0.011^{+0.002}_{-0.001}$ M$_\odot$, and $v_{\rm ej}^{\rm red} = 0.137^{+0.025}_{-0.021}c$. The parameters in this model are overall comparable to the two-component model in terms of the ejecta masses and velocities of the bluer and redder components, but here the ejecta in the redder component is distributed amongst the purple and red components. This model underpredicts some of the optical data at $\lesssim 1$ day and overpredicts the late time ($\gtrsim 15$ days) $K, K_{\rm s}$-band data; however, these deviations are less significant than for the two-component model. We additionally explored a version of this model in which the three opacities were allowed to vary freely, but found that these values fell close to our fixed values and did not significantly improve the fit.

Finally, the three-component model with an asymmetric ejecta distribution has a total of 11 free parameters: three ejecta masses, velocities and temperatures, one scatter term, and the opening angle. We find best-fit values of $M_{\rm ej}^{\rm blue} = 0.009^{+0.001}_{-0.001}$ M$_\odot$, $v_{\rm ej}^{\rm blue} = 0.256^{+0.009}_{-0.004}c$, $M_{\rm ej}^{\rm purple} = 0.007^{+0.001}_{-0.001}$ M$_\odot$, $v_{\rm ej}^{\rm purple} = 0.103^{+0.007}_{-0.004}c$, $M_{\rm ej}^{\rm red} = 0.026^{+0.004}_{-0.002}$ M$_\odot$, $v_{\rm ej}^{\rm red} = 0.175^{+0.011}_{-0.008}c$, and $\theta = 66^{+1}_{-3}$ degrees. This model overpredicts the intermediate time ($\approx$ 5 days) optical photometry and underpredicts the early NIR photometry. Although this model has additional freedom due to the opening angle, the ejecta masses become linked through this additional parameter. Due to the simplicity of the asymmetric model, we do not take the derived parameters and uncertainties at face value, and instead use them as a guide for the effects of asymmetry. We find that an asymmetric ejecta distribution leads to masses that are $\approx 50\%$ lower than in the spherical case.

We note that the inferred value of θ is consistent with the blue component being visible at an orbital inclination angle of $\approx 20 - 50^\circ$, as inferred from a comparison of the GW waveform to the source distance, and from an analysis of the radio and X-ray data in the context of an off-axis jet (Abbott et al. 2017; Alexander et al. 2017a; Guidorzi et al. 2017; Hallinan et al. 2017a; Margutti et al. 2017a; Murguia-Berthier et al. 2017). The relatively large angle is also consistent with the low polarization found by Covino et al. (2017).

Our spherical three-component model realization of highest likelihood (the "best fit") is shown with the complete dataset in Figure 4.1, and its corresponding corner plot is shown in Figure 4.2. Overall the model provides a good fit to the complete dataset. We find that most parameters are constrained to within $\lesssim 10\%$. The true errors in our models are likely larger, suggesting that the uncertainty is likely dominated by

systematic effects (e.g., uncertainty in thermalization efficiency, heating rate, etc.).

We show the individual filters with each of the three components (and their sum) in Figure 4.4. We find that the blue component dominates across all bands at $\lesssim 2-3$ days, while the purple component dominates at later times. Because of its low ejecta mass, the reddest component is sub-dominant at all times but contributes necessary flux to the redder bands at late times.

We explore the color evolution of our model compared to that of the kilonova in Figure 4.3, and again find that the model largely recovers the rapid color evolution, although it slightly deviates from the observed NIR colors at $\gtrsim 12$ days. Finally, we show specific representative filters (r, H, $K_{\rm s}$) with a comparison of all three models in Figure 4.5. Although the differences are subtle, the three-component model provides a statistically better fit to the overall light curves. We stress that the overall success of all three models is remarkable given the extensive scope of the data in time and wavelengths, and the simplifying assumptions in our analytic approach.

4.5 Discussion and Implications

Our best fit three-component model, dominated by an intermediate purple component, is consistent with previous findings (e.g., Cowperthwaite et al. 2017; Nicholl et al. 2017b; Chornock et al. 2017). Compared to our previous modeling presented in Cowperthwaite et al. (2017), both the blue and purple ejecta masses and the purple velocity increased by $\approx 40\%$. The other parameters remained within $\approx 1\sigma$ of the previously reported values. The uncertainties on the fitted parameters have decreased by $\approx 10-50\%$ due to

the dramatic increase in the number of data points. Our inferred total ejecta mass of ≈ 0.078 $M_\odot$, somewhat higher than the values inferred by several groups based on their individual subsets of the dataset we modeled here ($\approx 0.02 - 0.06$ $M_\odot$; Kasliwal et al. 2017; Kilpatrick et al. 2017a; Tanaka et al. 2017b). Additionally, modeling of the optical and NIR spectra indicates that the early blue emission is best described by material with a gradient of lanthanide fraction, with the fraction increasing with time (Nicholl et al. 2017b; Chornock et al. 2017). This is consistent with our findings that the purple component begins to dominate the UVOIR light curves at $\approx 2 - 3$ days post-merger.

The inferred high velocity of the blue ejecta is most naturally explained by relatively proton-rich (high electron fraction, Y_e) polar dynamical ejecta created by the shock from the collision between the merging neutron stars (e.g., Oechslin & Janka 2006; Bauswein et al. 2013; Sekiguchi et al. 2016; Radice et al. 2016). In this scenario, the inferred high ejecta mass (≈ 0.02 $M_\odot$) is indicative of a small neutron star radius of $\lesssim 12$ km when compared to the results of numerical simulations (Hotokezaka et al. 2013; Bauswein et al. 2013; see also Nicholl et al. 2017b). Alternatively, the blue ejecta could arise from a neutrino-heated outflow from a hyper-massive neutron star (e.g., Rosswog & Ramirez-Ruiz 2002; Dessart et al. 2009), although the high mass and velocity of the blue ejecta greatly exceed the expectations from a standard neutrino wind and would likely require additional acceleration of the wind by strong magnetic fields (e.g., Metzger et al. 2008).

The red ejecta component could in principle originate from the dynamically-ejected tidal tails in the equatorial plane of the binary (e.g., Rosswog et al. 1999; Hotokezaka et al. 2013), in which case the high ejecta mass would require a highly asymmetric merger with a binary mass ratio of $q \lesssim 0.8$ (Hotokezaka et al. 2013). However, the velocity

of this component ($\approx 0.1c$) is much lower than those typically found in simulations of NS mergers with extreme mass ratios ($\approx 0.2 - 0.3c$; Kilpatrick et al. 2017b) potentially disfavoring this explanation. Additionally, our large mass estimate is on the upper end of the dynamical ejecta mass estimated by The LIGO Scientific Collaboration et al. (2017), suggesting that not all of this mass is dynamically ejected.

A more promising source for the red and purple ejecta components is a delayed outflow from the accretion disk formed in the merger (Metzger et al. 2009; Fernández & Metzger 2013; Perego et al. 2014; Just et al. 2015; Siegel & Metzger 2017), for which the outflow velocity is expected to be $\approx 0.03 - 0.1c$. The relatively high neutron abundance of this matter ($Y_e \lesssim 0.25 - 0.3$ as needed to synthesize lanthanide nuclei) would be consistent with the moderate amount of neutrino irradiation of the outflow from a black hole accretion disk (Just et al. 2015) but would disfavor a particularly long-lived ($\gtrsim 100$ ms) hyper-massive or supra-massive neutron star remnant (Metzger & Fernández 2014; Murguia-Berthier et al. 2014; Kasen et al. 2015; Lippuner et al. 2017; see also Margalit & Metzger 2017). In this context, the properties of the red/purple ejecta provide evidence for a relatively prompt formation of a black hole remnant.

The asymmetric model indicates a half-opening angle for the blue component of $\theta \approx 66^\circ$. This is consistent with the blue component being visible given the inclination angle of the system inferred both from a comparison of the GW waveform and the distance of the event, and from off-axis jet models of the radio and X-ray light curves ($\approx 20 - 50^\circ$; Abbott et al. 2017; Alexander et al. 2017a; Margutti et al. 2017a). Our simple asymmetric model suggests that the total ejecta mass may be $\approx 50\%$ smaller than inferred in the spherical model. The effects of other simplifying assumptions, such as the blackbody SED and constant opacities as a function of time and wavelength, should be

explored in future work.

Finally, we compare our inferred total ejecta mass to the amount necessary to reproduce the Milk Way r-process production rate using the updated BNS merger rate inferred from Advanced LIGO of $R_0 = 1500^{+3200}_{-1220}$ Gpc^{-3} yr^{-1} (Abbott et al. 2017) following a similar methodology as Cowperthwaite et al. (2017) and Kasen et al. (2017). For light r-process nuclei, the primary source of ejecta in our three component model, the inferred Milky Way production rate is $\dot{M}_{\rm rp,A\lesssim 140} \approx 7 \times 10^{-7}$ M$_\odot$ yr^{-1} (Qian 2000). Combining this with the BNS rate and density of Milky Way-like galaxies (≈ 0.01 Mpc^{-3}), we estimate the Milky Way rate of BNS mergers as $R_{\rm MW} \approx 150$ Myr^{-1}. Thus, the average ejecta mass necessary for a blue/purple kilonova is $\dot{M}_{\rm rp,A\lesssim 140}/R_{\rm MW} \approx 5 \times 10^{-3}$ M$_\odot$, with an uncertainty of about a factor of ≈ 5 due to the large range of R_0. For heavy r-process elements (our red component), the Milky Way inferred production rate is $\dot{M}_{\rm rp;A\gtrsim 140} \approx 10^{-7}$ M$_\odot$ yr^{-1} (Bauswein et al. 2014). The average ejecta mass necessary for a red kilonova is therefore $\dot{M}_{\rm rp,A\lesssim 140}/R_{\rm MW} \approx 7 \times 10^{-4}$ M$_\odot$, again with an uncertainty of about a factor of 5. In both cases, this order of magnitude estimate is about a factor 10 times smaller than our estimated ejecta masses for this event, although the rate errors (and potentially lower ejecta masses in the asymmetric case) are large enough to account for the discrepancy[4]. However, we note that the ratio of red to blue/purple ejecta masses in our model, ≈ 0.16, is in good agreement with the relative production rates of $A \gtrsim 140$ and $A \lesssim 140$ nuclei in the Milky Way.

If the BNS merger rate from future events is shown to be at the high end of the current estimates, the results inferred here would indicate that a large fraction of

[4]Our results are consist with those found in The LIGO Scientific Collaboration et al. 2017.

synthesized r-process material may remain in the gas phase within the ISM or escape the galaxy entirely via galactic winds (Shen et al. 2015). It may also suggest that the kilonova in GW170817 is an outlier in terms of total r-process material produced. Future events will clarify the population parameters of kilonovae.

4.6 Conclusions

We presented the first effort to aggregate, homogenize, and uniformly model the complete UV, optical and NIR dataset for the electromagnetic counterpart of the binary neutron star merger GW170817, allowing us to better determine the likely combinations of parameters responsible for the observed kilonova. We are able to remove systematic offsets from several datasets and to identify outlying data points, providing the community with cleaned and uniform photometry for future analyses. Our key findings are as follows:

- We present 647 photometric measurements from the kilonova accompanying the binary neutron star merger GW170817, spanning from 0.45 to 29.4 days post-merger and providing nearly complete color coverage at all times. We make the homogenized dataset available to the public in Table 4.3, in the OKC, and through `https://kilonova.org/`
- The kilonova UVOIR light curves are well fit by a spherically symmetric, three-component model with an overall ejecta mass of ≈ 0.078 $M_\odot$, dominated by light r-process material ($A < 140$) with moderate velocities of $\approx 0.15c$.
- We find evidence for a lanthanide-free component with mass and velocity of

≈ 0.020 $M_\odot$ and $\approx 0.27c$, respectively. This component is indicative of polar dynamical ejecta, and hence a BNS origin (instead of NS-BH). The large ejecta mass implies a small neutron star radius of $\lesssim 12$ km.

- The mass and velocities of the purple/red components are consistent with a delayed outflow from an accretion disk formed in the merger. This disfavors a long-lived ($\gtrsim 100$ ms) hyper-massive neutron star remnant and provides evidence for relatively prompt formation of a black hole remnant.

- The asymmetric model extension implies that the total ejecta mass may be up to a factor of 2 times lower than for the symmetric model.

- Given the large uncertainties in BNS merger rates, we find that the r-process production rates are comfortably above the Galactic production rate, consistent with the idea that BNS mergers are the dominant source of r-process nucleosynthesis in the universe.

The sheer size of the dataset for this event, which was the subject of unprecedented follow-up efforts by the observational astronomy community, represents a departure from typical transient events, allowing for more detailed modeling than typically feasible. Although future observing runs of Advanced LIGO/Virgo will lead to many more kilonova detections, it is likely that this event will remain one of the best-observed objects for years to come due to its vicinity and hence ease of follow-up. Thus, the broad UVOIR dataset collected by multiple teams, and aggregated and homogenized here, will be an invaluable resource to explore questions about kilonova phenomenology that may be otherwise intractable using more sparsely sampled data.

Table 4.3:: Truncated Photometric Data

MJD	Phase	Instrument	Telescope	Filter	AB Mag[a]	Err.	Δ(Mag)[b]	Ref.	Note[c]
57982.981	0.452	E2V 4kx4k ccd	Swope	i	17.48	0.02	0	Coulter et al.	*
57982.990	0.461	FourStar	Magellan	H	18.26	0.15	0	Drout et al.	*
57982.993	0.464	Alta U47+	Prompt5	r	17.46	0.03	0	Valenti et al.	*
57982.999	0.470	VIRCAM	VISTA	Ks	18.62	0.05	0	Tanvir et al.	*
57983.000	0.471	FourStar	Magellan	J	17.83	0.15	0	Drout et al.	*
57983.000	0.471	LDSS	Magellan	V	17.35	0.02	0	Drout et al.	*
57983.000	0.471	LDSS	Magellan	r	17.33	0.02	0	Drout et al.	*
57983.000	0.471	LDSS	Magellan	z	17.67	0.03	0	Drout et al.	*
57983.001	0.472	MASTER	OAFA	W	17.50	0.20	0	Lipunov et al.	*
57983.003	0.474	DECam	Blanco/CTIO	i	17.48	0.03	0	Cowperthwaite et al.	*
57983.004	0.475	DECam	Blanco/CTIO	z	17.59	0.03	0	Cowperthwaite et al.	*
57983.006	0.477	LDSS	Magellan	g	17.41	0.02	0	Drout et al.	*
57983.009	0.480	VIRCAM	VISTA	Y	17.88	0.03	0	Tanvir et al.	*
57983.011	0.482	LDSS	Magellan	g	17.41	0.04	0	Drout et al.	*
57983.011	0.482	Sinistro	LCO 1m	w	17.49	0.04	0	Arcavi et al.	X
57983.014	0.485	LDSS	Magellan	g	17.39	0.02	0	Drout et al.	*

Table 4.3 – continued from previous page

MJD	Phase	Instrument	Telescope	Filter	AB Mag[a]	Err.	Δ(Mag)[b]	Ref.	Note[c]
57983.015	0.486	MASTER	OAFA	W	17.10	0.20	0	Lipunov et al.	*
57983.019	0.490	VIRCAM	VISTA	Y	17.46	0.01	0	Tanvir et al.	*
57983.028	0.499	Alta U47+	Prompt5	r	17.56	0.04	0	Valenti et al.	*
57983.029	0.500	VIRCAM	VISTA	Ks	18.64	0.06	0	Tanvir et al.	*
57983.030	0.501	FourStar	Magellan	Ks	18.41	0.15	0	Drout et al.	*
57983.039	0.510	VIRCAM	VISTA	Y	17.82	0.03	0	Tanvir et al.	*
57983.050	0.521	ROS2	REM	g	17.32	0.07	0	Pian et al.	*
57983.050	0.521	ROS2	REM	i	16.98	0.05	0	Pian et al.	*
57983.050	0.521	ROS2	REM	r	17.14	0.08	0	Pian et al.	*
57983.050	0.521	ROS2	REM	z	16.85	0.10	0	Pian et al.	*,O
57983.059	0.530	FLAMINGOS-2	Gemini-S	Ks	18.42	0.04	0	Kasliwal et al.	*
57983.156	0.627	UVOT	Swift	M2	21.12	0.22	0	Evans et al.	*
57983.162	0.633	UVOT	Swift	W1	19.46	0.11	0	Evans et al.	*
57983.167	0.638	UVOT	Swift	U	18.19	0.09	0	Evans et al.	*
57983.172	0.643	UVOT	Swift	W2	21.13	0.23	0	Evans et al.	*
57983.229	0.700	HSC	Subaru	z	17.40	0.01	0	Utsumi et al.	*

Table 4.3 – continued from previous page

MJD	Phase	Instrument	Telescope	Filter	AB Mag[a]	Err.	Δ(Mag)[b]	Ref.	Note[c]
57983.231	0.702	GFC	Pan-STARRS	i	17.24	0.06	0	Smartt et al.	*
57983.231	0.702	GFC	Pan-STARRS	y	17.38	0.10	0	Smartt et al.	*
57983.231	0.702	GFC	Pan-STARRS	z	17.26	0.06	0	Smartt et al.	*
57983.382	0.853	Sinistro	LCO 1m	w	17.31	0.04	0	Arcavi et al.	X
57983.387	0.858	Skymapper	Skymapper	i	17.42	0.05	0	Andreoni et al.	*
57983.401	0.872	Sinistro	LCO 1m	g	17.28	0.12	-0.04	Arcavi et al.	*
57983.405	0.876	Sinistro	LCO 1m	r	17.20	0.02	-0.02	Arcavi et al.	*
57983.419	0.890	Skymapper	Skymapper	r	17.32	0.07	0.0	Andreoni et al.	*
57983.421	0.892	Skymapper	Skymapper	g	17.46	0.08	0.0	Andreoni et al.	*
57983.550	1.021	10k10k ccd	AST3-2	i	17.14	0.13	-0.09	Hu et al.	*
57983.569	1.040	UVOT	Swift	W1	20.21	0.21	0	Evans et al.	*
57983.572	1.042	UVOT	Swift	U	19.00	0.16	0	Evans et al.	*
57983.575	1.046	UVOT	Swift	W2	>21.45	-	0	Evans et al.	*
57983.594	1.065	10k10k ccd	AST3-2	i	17.48	0.07	-0.13	Hu et al.	*
57983.594	1.065	UVOT	Swift	M2	22.52	0.50	0	Evans et al.	*
57983.625	1.096	10k10k ccd	AST3-2	i	17.58	0.09	-0.14	Hu et al.	*

Table 4.3 – continued from previous page

MJD	Phase	Instrument	Telescope	Filter	AB Mag[a]	Err.	Δ(Mag)[b]	Ref.	Note[c]
57983.699	1.170	SIRIUS	IRSF	H	17.64	0.04	0	Utsumi et al.	*
57983.699	1.170	SIRIUS	IRSF	J	17.51	0.03	0	Utsumi et al.	*
57983.699	1.170	SIRIUS	IRSF	Ks	17.91	0.05	0	Utsumi et al.	*
57983.717	1.188	MASTER	SAAO	W	17.30	0.20	0	Lipunov et al.	*
57983.719	1.190	-	KMTNet-SAAO	B	18.47	0.11	0	Troja et al.	*
57983.719	1.190	-	KMTNet-SAAO	I	17.58	0.10	0	Troja et al.	*
57983.719	1.190	-	KMTNet-SAAO	R	17.65	0.05	0	Troja et al.	*
57983.719	1.190	-	KMTNet-SAAO	V	17.81	0.04	0	Troja et al.	*
57983.726	1.197	MASTER	SAAO	R	17.00	0.20	0	Lipunov et al.	*,O
57983.733	1.204	Sinistro	LCO 1m	w	17.95	0.04	0	Arcavi et al.	X
57983.736	1.207	MASTER	SAAO	B	18.10	0.10	0	Lipunov et al.	*
57983.741	1.212	Sinistro	LCO 1m	r	17.75	0.02	-0.03	Arcavi et al.	*
57983.745	1.216	Sinistro	LCO 1m	g	18.05	0.12	-0.07	Arcavi et al.	*
57983.758	1.229	-	1.5B	r	17.89	0.03	0	Smartt et al.	*
57983.964	1.435	EFOSC2	NTT	V	18.22	0.08	0	Drout et al.	*
57983.968	1.439	T80Cam	T80S	g	18.43	0.06	0	Evans et al.	*

Table 4.3 – continued from previous page

MJD	Phase	Instrument	Telescope	Filter	AB Mag[a]	Err.	Δ(Mag)[b]	Ref.	Note[c]
57983.968	1.439	Sinistro	LCO 1m	w	18.23	0.04	0	Arcavi et al.	X
57983.969	1.440	EFOSC2	NTT	V	18.16	0.05	0	Drout et al.	*
57983.969	1.440	GROND	LaSilla	H	17.64	0.08	0	Smartt et al.	*
57983.969	1.440	GROND	LaSilla	J	17.58	0.07	0	Smartt et al.	*
57983.969	1.440	GROND	LaSilla	K	17.85	0.15	-0.29	Smartt et al.	*
57983.969	1.440	GROND	LaSilla	g	18.49	0.04	0	Smartt et al.	*
57983.969	1.440	GROND	LaSilla	i	17.85	0.05	0	Smartt et al.	*
57983.969	1.440	GROND	LaSilla	r	17.99	0.01	0	Smartt et al.	*
57983.969	1.440	GROND	LaSilla	z	17.72	0.03	0	Smartt et al.	*
57983.969	1.440	FORS	VLT	r	17.69	0.02	0	Tanvir et al.	*
57983.970	1.441	EFOSC2	NTT	V	18.13	0.08	0	Drout et al.	*
57983.972	1.443	Sinistro	LCO 1m	i	17.88	0.10	-0.25	Arcavi et al.	*
57983.974	1.445	T80Cam	T80S	g	18.51	0.04	0	Díaz et al.	*
57983.975	1.446	T80Cam	T80S	g	18.48	0.04	0	Díaz et al.	*
57983.976	1.447	T80Cam	T80S	g	18.61	0.04	0	Díaz et al.	*
57983.976	1.447	Sinistro	LCO 1m	r	17.98	0.08	-0.04	Arcavi et al.	*

Table 4.3 – continued from previous page

MJD	Phase	Instrument	Telescope	Filter	AB Mag[a]	Err.	Δ(Mag)[b]	Ref.	Note[c]
57983.976	1.447	DECam	Blanco/CTIO	Y	17.32	0.03	0	Cowperthwaite et al.	*
57983.977	1.448	LDSS	Magellan	z	17.62	0.06	0	Drout et al.	*
57983.977	1.448	DECam	Blanco/CTIO	z	17.59	0.02	0	Cowperthwaite et al.	*
57983.977	1.448	T80Cam	T80S	r	17.93	0.02	0	Díaz et al.	*
57983.978	1.449	DECam	Blanco/CTIO	i	17.78	0.02	0	Cowperthwaite et al.	*
57983.978	1.449	T80Cam	T80S	r	17.97	0.02	0	Díaz et al.	*
57983.978	1.449	DECam	Blanco/CTIO	r	18.04	0.02	0	Cowperthwaite et al.	*
57983.978	1.449	LDSS	Magellan	z	17.61	0.06	0	Drout et al.	*
57983.979	1.450	LDSS	Magellan	z	17.61	0.06	0	Drout et al.	*
57983.979	1.450	DECam	Blanco/CTIO	g	18.66	0.03	0	Cowperthwaite et al.	*
57983.979	1.450	T80Cam	T80S	r	17.94	0.02	0	Díaz et al.	*
57983.980	1.451	DECam	Blanco/CTIO	u	19.94	0.05	0	Cowperthwaite et al.	*
57983.980	1.451	LDSS	Magellan	i	17.77	0.03	0	Drout et al.	*
57983.980	1.451	ROS2	REM	I	17.66	0.06	0	Pian et al.	*
57983.980	1.451	Sinistro	LCO 1m	g	18.61	0.14	-0.13	Arcavi et al.	*
57983.980	1.451	ROS2	REM	r	17.68	0.13	0	Pian et al.	*

Table 4.3 – continued from previous page

MJD	Phase	Instrument	Telescope	Filter	AB Mag[a]	Err.	Δ(Mag)[b]	Ref.	Note[c]
57983.980	1.451	ROS2	REM	z	17.61	0.10	0	Pian et al.	*
57983.980	1.451	T80Cam	T80S	i	17.74	0.03	0	Díaz et al.	*
57983.981	1.452	LDSS	Magellan	r	17.91	0.03	0	Drout et al.	*
57983.981	1.452	FourStar	Magellan	Ks	17.61	0.04	0	Drout et al.	*
57983.981	1.452	FourStar	Magellan	J	17.47	0.01	0	Drout et al.	*
57983.981	1.452	LDSS	Magellan	g	18.61	0.03	0	Drout et al.	*
57983.982	1.452	T80Cam	T80S	i	17.80	0.03	0	Díaz et al.	*
57983.983	1.454	T80Cam	T80S	i	17.81	0.03	0	Díaz et al.	*
57983.983	1.454	LDSS	Magellan	B	19.04	0.06	0	Drout et al.	*
57983.984	1.455	T80Cam	T80S	g	18.58	0.03	0	Díaz et al.	*
57983.984	1.455	LDSS	Magellan	B	19.04	0.07	0	Drout et al.	*
57983.985	1.456	T80Cam	T80S	g	18.55	0.03	0	Díaz et al.	*
57983.986	1.457	T80Cam	T80S	g	18.61	0.04	0	Díaz et al.	*
57983.987	1.458	T80Cam	T80S	r	17.95	0.02	0	Díaz et al.	*
57983.988	1.459	LDSS	Magellan	g	18.66	0.03	0	Drout et al.	*
57983.988	1.459	T80Cam	T80S	r	17.98	0.02	0	Díaz et al.	*

Table 4.3 – continued from previous page

MJD	Phase	Instrument	Telescope	Filter	AB Mag[a]	Err.	Δ(Mag)[b]	Ref.	Note[c]
57983.989	1.460	-	KMTNet/CTIO	B	19.09	0.11	0	Troja et al.	*
57983.989	1.460	-	KMTNet/CTIO	I	17.77	0.09	0	Troja et al.	*
57983.989	1.460	-	KMTNet/CTIO	R	17.94	0.05	0	Troja et al.	*
57983.989	1.460	-	KMTNet/CTIO	V	18.28	0.04	0	Troja et al.	*
57983.989	1.460	VIRCAM	VISTA	Ks	17.77	0.02	0	Tanvir et al.	*
57983.989	1.460	VIRCAM	VISTA	Y	17.45	0.01	0	Tanvir et al.	*
57983.990	1.461	T80Cam	T80S	r	17.99	0.03	0	Díaz et al.	*
57983.990	1.461	FourStar	Magellan	H	17.52	0.01	0	Drout et al.	*
57983.991	1.462	T80Cam	T80S	i	17.78	0.02	0	Díaz et al.	*
57983.991	1.462	Alta U47+	Prompt5	r	18.00	0.06	0	Valenti et al.	*
57983.992	1.463	T80Cam	T80S	i	17.79	0.02	0	Díaz et al.	*
57983.993	1.464	T80Cam	T80S	i	17.80	0.03	0	Díaz et al.	*
57983.994	1.465	T80Cam	T80S	g	18.65	0.03	0	Díaz et al.	*
57983.995	1.466	E2V 4kx4k ccd	Swope	V	18.22	0.04	0	Coulter et al.	*
57983.995	1.466	T80Cam	T80S	g	18.60	0.04	0	Díaz et al.	*
57983.996	1.467	T80Cam	T80S	g	18.63	0.04	0	Díaz et al.	*

Table 4.3 – continued from previous page

MJD	Phase	Instrument	Telescope	Filter	AB Mag[a]	Err.	Δ(Mag)[b]	Ref.	Note[c]
57983.997	1.468	T80Cam	T80S	r	18.02	0.03	0	Díaz et al.	*
57983.999	1.470	T80Cam	T80S	r	18.02	0.02	0	Díaz et al.	*
57983.999	1.470	VIRCAM	VISTA	Y	17.23	0.01	0	Tanvir et al.	*
57984.000	1.471	T80Cam	T80S	r	18.04	0.02	0	Díaz et al.	*
57984.000	1.471	XS	VLT	r	17.95	0.02	0	Pian et al.	*
57984.000	1.471	XS	VLT	z	17.65	0.07	0	Pian et al.	*
57984.000	1.471	FLAMINGOS-2	Gemini-S	H	17.63	0.10	0	Cowperthwaite et al.	*
57984.001	1.472	T80Cam	T80S	i	17.74	0.02	0	Díaz et al.	*
57984.002	1.473	T80Cam	T80S	i	17.86	0.03	0	Díaz et al.	*
57984.002	1.473	FourStar	Magellan	J1	17.32	0.01	0	Drout et al.	*
57984.003	1.474	T80Cam	T80S	i	17.85	0.03	0	Díaz et al.	*
57984.004	1.475	T80Cam	T80S	g	18.69	0.04	0	Díaz et al.	*
57984.005	1.476	T80Cam	T80S	g	18.67	0.03	0	Díaz et al.	*
57984.007	1.478	T80Cam	T80S	g	18.62	0.04	0	Díaz et al.	*
57984.008	1.479	T80Cam	T80S	r	18.01	0.02	0	Díaz et al.	*
57984.009	1.480	T80Cam	T80S	r	18.01	0.02	0	Díaz et al.	*

Table 4.3 – continued from previous page

MJD	Phase	Instrument	Telescope	Filter	AB Mag[a]	Err.	Δ(Mag)[b]	Ref.	Note[c]
57984.010	1.481	T80Cam	T80S	r	18.07	0.03	0	Díaz et al.	*
57984.010	1.481	T80Cam	Prompt5	r	18.29	0.06	0	Valenti et al.	*
57984.010	1.481	EFOSC2	NTT	V	18.14	0.04	0	Drout et al.	*
57984.011	1.482	T80Cam	T80S	i	17.82	0.03	0	Díaz et al.	*
57984.012	1.483	EFOSC2	NTT	V	18.16	0.06	0	Drout et al.	*
57984.012	1.483	T80Cam	T80S	i	17.77	0.03	0	Díaz et al.	*
57984.013	1.484	EFOSC2	NTT	V	18.18	0.04	0	Drout et al.	*
57984.013	1.484	T80Cam	T80S	i	17.87	0.03	0	Díaz et al.	*
57984.014	1.485	T80Cam	T80S	g	18.68	0.04	0	Díaz et al.	*
57984.016	1.487	T80Cam	T80S	g	18.67	0.04	0	Díaz et al.	*
57984.017	1.488	T80Cam	T80S	g	18.57	0.03	0	Díaz et al.	*
57984.018	1.489	T80Cam	T80S	r	18.03	0.02	0	Díaz et al.	*
57984.019	1.490	T80Cam	T80S	r	18.05	0.03	0	Díaz et al.	*
57984.020	1.491	T80Cam	T80S	r	18.04	0.02	0	Díaz et al.	*
57984.021	1.492	T80Cam	T80S	i	17.83	0.03	0	Díaz et al.	*
57984.022	1.493	T80Cam	T80S	i	17.90	0.03	0	Díaz et al.	*

Table 4.3 – continued from previous page

MJD	Phase	Instrument	Telescope	Filter	AB Mag[a]	Err.	Δ(Mag)[b]	Ref.	Note[c]
57984.023	1.494	T80Cam	T80S	i	17.88	0.03	0	Díaz et al.	*
57984.034	1.505	E2V 4kx4k ccd	Swope	B	19.07	0.04	0	Coulter et al.	*
57984.036	1.507	UVOT	Swift	U	20.79	0.50	0	Evans et al.	*
57984.036	1.507	UVOT	Swift	W2	>21.66	-	0	Evans et al.	*
57984.044	1.515	E2V 4kx4k ccd	Swope	i	17.80	0.02	0	Coulter et al.	*
57984.046	1.517	EFOSC2	NTT	V	18.25	0.06	0	Drout et al.	*
57984.047	1.518	EFOSC2	NTT	V	18.18	0.10	0	Drout et al.	*
57984.047	1.518	E2V 4kx4k ccd	Swope	r	17.98	0.02	0	Coulter et al.	*
57984.048	1.519	EFOSC2	NTT	U	20.11	0.23	0	Drout et al.	R
57984.048	1.519	EFOSC2	NTT	U	20.25	0.29	0	Smartt et al.	R
57984.052	1.523	EFOSC2	NTT	U	20.21	0.28	0	Drout et al.	R
57984.052	1.523	EFOSC2	NTT	U	20.18	0.23	0	this Chapter	*,A
57984.052	1.523	UVOT	Swift	M2	>22.07	-	0	Evans et al.	*
57984.055	1.526	E2V 4kx4k ccd	Swope	g	18.49	0.12	0	Coulter et al.	*
57984.056	1.527	EFOSC2	NTT	U	20.10	0.28	0	Drout et al.	*
57984.058	1.529	UVOT	Swift	W1	>21.20	-	0	Evans et al.	*

Table 4.3 – continued from previous page

MJD	Phase	Instrument	Telescope	Filter	AB Mag[a]	Err.	Δ(Mag)[b]	Ref.	Note[c]
57984.229	1.700	HSC	Subaru	z	17.74	0.01	0	Utsumi et al.	*
57984.231	1.702	GFC	Pan-STARRS	i	17.87	0.06	0	Smartt et al.	*
57984.231	1.702	GFC	Pan-STARRS	y	17.58	0.11	0	Smartt et al.	*
57984.231	1.702	GFC	Pan-STARRS	z	17.78	0.07	0	Smartt et al.	*
57984.309	1.780	Tripol5	B&C	g	18.80	0.07	0	Utsumi et al.	*
57984.309	1.780	Tripol5	B&C	i	18.19	0.06	0	Utsumi et al.	*
57984.309	1.780	Tripol5	B&C	r	18.26	0.04	0	Utsumi et al.	*
57984.357	1.828	Sinistro	LCO 1m	w	18.69	0.05	0	Arcavi et al.	X
57984.359	1.830	-	KMTNet-SSO	B	20.10	0.12	0	Troja et al.	*
57984.359	1.830	-	KMTNet-SSO	V	18.79	0.05	0	Troja et al.	*
57984.361	1.832	Sinistro	LCO 1m	i	18.07	0.13	-0.30	Arcavi et al.	*
57984.365	1.836	Sinistro	LCO 1m	r	18.34	0.11	-0.06	Arcavi et al.	*
57984.369	1.840	-	KMTNet-SSO	I	17.98	0.09	0	Troja et al.	*
57984.369	1.840	-	KMTNet-SSO	R	18.34	0.05	0	Troja et al.	*
57984.369	1.840	Sinistro	LCO 1m	g	19.28	0.17	-0.25	Arcavi et al.	*
57984.379	1.850	Skymapper	Skymapper	i	17.96	0.07	0	Andreoni et al.	*

Table 4.3 – continued from previous page

MJD	Phase	Instrument	Telescope	Filter	AB Mag[a]	Err.	Δ(Mag)[b]	Ref.	Note[c]
57984.392	1.863	Skymapper	Skymapper	i	18.18	0.08	0	Andreoni et al.	*
57984.456	1.927	Skymapper	Skymapper	r	18.46	0.17	0	Andreoni et al.	*
57984.601	2.072	UVOT	Swift	M2	>21.97	-	0	Evans et al.	*
57984.606	2.077	UVOT	Swift	W1	>21.79	-	0	Evans et al.	*
57984.628	2.099	UVOT	Swift	W2	>21.98	-	0	Evans et al.	*
57984.699	2.170	SIRIUS	IRSF	H	17.52	0.04	0	Utsumi et al.	*
57984.699	2.170	SIRIUS	IRSF	J	17.69	0.04	0	Utsumi et al.	*
57984.699	2.170	SIRIUS	IRSF	Ks	17.61	0.04	0	Utsumi et al.	*
57984.717	2.188	MASTER	SAAO	W	18.40	0.20	0	Lipunov et al.	*
57984.719	2.190	-	KMTNet-SAAO	B	20.45	0.09	0	Troja et al.	*
57984.719	2.190	-	KMTNet-SAAO	I	18.26	0.12	0	Troja et al.	*
57984.719	2.190	-	KMTNet-SAAO	R	18.59	0.05	0	Troja et al.	*
57984.719	2.190	-	KMTNet-SAAO	V	19.25	0.05	0	Troja et al.	*
57984.738	2.209	Sinistro	LCO 1m	r	18.93	0.10	-0.10	Arcavi et al.	*
57984.741	2.212	Sinistro	LCO 1m	r	18.90	0.11	-0.10	Arcavi et al.	*
57984.745	2.216	Sinistro	LCO 1m	i	18.33	0.12	-0.41	Arcavi et al.	*

Table 4.3 – continued from previous page

MJD	Phase	Instrument	Telescope	Filter	AB Mag[a]	Err.	Δ(Mag)[b]	Ref.	Note[c]
57984.748	2.219	Sinistro	LCO 1m	i	18.26	0.15	-0.38	Arcavi et al.	*
57984.749	2.220	MASTER	SAAO	R	18.00	0.30	0	Lipunov et al.	*,O
57984.751	2.222	Sinistro	LCO 1m	V	19.06	0.07	0	Arcavi et al.	*
57984.751	2.222	Sinistro	LCO 1m	z	18.25	0.30	-0.58	Arcavi et al.	*
57984.757	2.228	MASTER	SAAO	B	>19.50	-	0	Lipunov et al.	*
57984.758	2.229	Sinistro	LCO 1m	g	19.93	0.21	-0.51	Arcavi et al.	*
57984.758	2.229	Sinistro	LCO 1m	w	19.11	0.06	0	Arcavi et al.	X
57984.761	2.232	Sinistro	LCO 1m	g	19.80	0.20	-1.44	Arcavi et al.	*
57984.761	2.232	Sinistro	LCO 1m	w	19.11	0.06	0	Arcavi et al.	X
57984.761	2.232	GFC	Pan-STARRS	r	18.80	0.07	0	Smartt et al.	*
57984.883	2.354	UVOT	Swift	U	>20.41	-	0	Evans et al.	*
57984.885	2.356	UVOT	Swift	B	>19.31	-	0	Evans et al.	*
57984.890	2.361	UVOT	Swift	W2	>22.16	-	0	Evans et al.	*
57984.895	2.366	UVOT	Swift	V	>18.72	-	0	Evans et al.	*
57984.960	2.431	ROS2	REM	I	18.35	0.10	0	Pian et al.	*
57984.960	2.431	ROS2	REM	g	20.31	0.28	0	Pian et al.	*

Table 4.3 – continued from previous page

MJD	Phase	Instrument	Telescope	Filter	AB Mag[a]	Err.	Δ(Mag)[b]	Ref.	Note[c]
57984.960	2.431	ROS2	REM	r	19.18	0.10	0	Pian et al.	*
57984.962	2.433	FourStar	Magellan	Ks	17.55	0.06	0	Drout et al.	*
57984.963	2.433	FourStar	Magellan	J	17.55	0.01	0	Drout et al.	*
57984.968	2.439	FLAMINGOS-2	Gemini-S	H	17.71	0.09	0	Cowperthwaite et al.	*
57984.968	2.439	Sinistro	LCO 1m	r	19.10	0.11	-0.11	Arcavi et al.	*
57984.969	2.440	GROND	LaSilla	H	17.64	0.08	0	Smartt et al.	*
57984.969	2.440	GROND	LaSilla	J	17.73	0.09	0	Smartt et al.	*
57984.969	2.440	GROND	LaSilla	K	17.66	0.10	-0.24	Smartt et al.	*
57984.969	2.440	GROND	LaSilla	g	20.19	0.11	0	Smartt et al.	*
57984.969	2.440	GROND	LaSilla	i	18.58	0.04	0	Smartt et al.	*
57984.969	2.440	GROND	LaSilla	r	19.13	0.17	0	Smartt et al.	*
57984.969	2.440	GROND	LaSilla	z	18.33	0.06	0	Smartt et al.	*
57984.969	2.440	FORS	VLT	r	18.77	0.04	0	Tanvir et al.	*
57984.971	2.442	FourStar	Magellan	H	17.57	0.01	0	Drout et al.	*
57984.971	2.442	EFOSC2	NTT	V	19.40	0.11	0	Drout et al.	*
57984.975	2.446	DECam	Blanco/CTIO	Y	17.77	0.03	0	Cowperthwaite et al.	*

Table 4.3 – continued from previous page

MJD	Phase	Instrument	Telescope	Filter	AB Mag[a]	Err.	Δ(Mag)[b]	Ref.	Note[c]
57984.975	2.446	Sinistro	LCO 1m	i	18.61	0.15	-0.56	Arcavi et al.	*
57984.976	2.447	DECam	Blanco/CTIO	z	18.18	0.03	0	Cowperthwaite et al.	*
57984.976	2.447	Alta U47+	Prompt5	r	19.34	0.08	0	Valenti et al.	*
57984.976	2.447	DECam	Blanco/CTIO	i	18.38	0.03	0	Cowperthwaite et al.	*
57984.977	2.448	DECam	Blanco/CTIO	r	19.03	0.03	0	Cowperthwaite et al.	*
57984.978	2.449	DECam	Blanco/CTIO	g	20.21	0.05	0	Cowperthwaite et al.	*
57984.978	2.449	Sinistro	LCO 1m	i	18.46	0.10	-0.47	Arcavi et al.	*
57984.978	2.449	Alta U47+	Prompt5	r	19.29	0.12	0	Valenti et al.	*
57984.979	2.450	-	KMTNet/CTIO	B	20.82	0.10	0	Troja et al.	*
57984.979	2.450	-	KMTNet/CTIO	R	18.81	0.05	0	Troja et al.	*
57984.979	2.450	-	KMTNet/CTIO	V	19.51	0.05	0	Troja et al.	*
57984.979	2.450	VIRCAM	VISTA	Ks	17.67	0.03	0	Tanvir et al.	*
57984.980	2.451	-	RC-1000	r	19.12	0.06	0	Pozanenko et al.	*
57984.980	2.451	DECam	Blanco/CTIO	u	22.26	0.16	0	Cowperthwaite et al.	*
57984.980	2.451	FourStar	Magellan	J1	17.52	0.01	0	Drout et al.	*
57984.980	2.451	MASTER	OAFA	W	18.80	0.20	0	Lipunov et al.	*

Table 4.3 – continued from previous page

MJD	Phase	Instrument	Telescope	Filter	AB Mag[a]	Err.	Δ(Mag)[b]	Ref.	Note[c]
57984.982	2.453	Sinistro	LCO 1m	z	18.19	0.20	-0.54	Arcavi et al.	*
57984.985	2.456	T80Cam	T80S	r	18.78	0.03	0	Díaz et al.	*
57984.985	2.456	T80Cam	T80S	r	19.15	0.06	0	Díaz et al.	*
57984.988	2.459	DK1.5	VLT	i	18.37	0.03	0	Tanvir et al.	*
57984.988	2.459	Sinistro	LCO 1m	w	19.56	0.07	0	Arcavi et al.	X
57984.989	2.460	-	KMTNet/CTIO	I	18.40	0.13	0	Troja et al.	*
57984.989	2.460	VIRCAM	VISTA	Y	17.66	0.02	0	Tanvir et al.	*
57984.990	2.461	DK1.5	DK1.5	z	18.01	0.13	0	Tanvir et al.	*
57984.992	2.463	Sinistro	LCO 1m	w	19.48	0.07	0	Arcavi et al.	X
57984.999	2.470	VIRCAM	VISTA	Y	17.51	0.02	0	Tanvir et al.	*
57985.000	2.471	IMACS	Magellan	V	19.51	0.08	0	Drout et al.	*
57985.000	2.471	IMACS	Magellan	i	18.36	0.02	0	Drout et al.	*
57985.002	2.473	Sinistro	LCO 1m	i	18.46	0.10	-0.46	Arcavi et al.	*
57985.006	2.477	Sinistro	LCO 1m	i	18.45	0.11	-0.46	Arcavi et al.	*
57985.008	2.479	1k2k CCD	VIRT	C	18.90	0.28	0.0	Andreoni et al.	X
57985.009	2.480	IMACS	Magellan	r	18.93	0.02	0	Drout et al.	*

Table 4.3 – continued from previous page

MJD	Phase	Instrument	Telescope	Filter	AB Mag[a]	Err.	Δ(Mag)[b]	Ref.	Note[c]
57985.010	2.481	Sinistro	LCO 1m	V	19.33	0.18	0	Arcavi et al.	*
57985.016	2.487	Sinistro	LCO 1m	w	19.46	0.06	0	Arcavi et al.	X
57985.016	2.487	EFOSC2	NTT	V	19.53	0.12	0	Drout et al.	*
57985.017	2.488	Sinistro	LCO 1m	g	20.15	0.33	-0.66	Arcavi et al.	*
57985.019	2.490	FLAMINGOS-2	Gemini-S	J	17.76	0.02	0	Kasliwal et al.	*
57985.019	2.490	FLAMINGOS-2	Gemini-S	Ks	17.60	0.04	0	Kasliwal et al.	*
57985.019	2.490	Sinistro	LCO 1m	w	19.36	0.05	0	Arcavi et al.	X
57985.054	2.525	EFOSC2	NTT	V	19.59	0.20	0	Drout et al.	*
57985.054	2.525	EFOSC2	NTT	U	>20.19	-	0	Drout et al.	R
57985.055	2.526	EFOSC2	NTT	U	>19.60	-	0	Smartt et al.	R
57985.055	2.526	EFOSC2	NTT	U	>19.90	-	0	this Chapter	A,*
57985.184	2.655	UVOT	Swift	B	19.93	0.10	0	Evans et al.	*,O
57985.189	2.660	UVOT	Swift	W2	>22.21	-	0	Evans et al.	*
57985.194	2.665	UVOT	Swift	V	>18.67	-	0	Evans et al.	*
57985.231	2.702	GFC	Pan-STARRS	i	18.44	0.09	0	Smartt et al.	*
57985.231	2.702	GFC	Pan-STARRS	y	18.08	0.11	0	Smartt et al.	*

Table 4.3 – continued from previous page

MJD	Phase	Instrument	Telescope	Filter	AB Mag[a]	Err.	Δ(Mag)[b]	Ref.	Note[c]
57985.231	2.702	GFC	Pan-STARRS	z	18.31	0.07	0	Smartt et al.	*
57985.357	2.828	Sinistro	LCO 1m	r	19.36	0.09	-0.15	Arcavi et al.	*
57985.359	2.830	-	KMTNet-SSO	I	18.62	0.10	0	Troja et al.	*
57985.359	2.830	-	KMTNet-SSO	R	19.10	0.05	0	Troja et al.	*
57985.364	2.835	Sinistro	LCO 1m	i	18.53	0.13	-0.50	Arcavi et al.	*
57985.367	2.838	Sinistro	LCO 1m	i	18.62	0.14	-0.57	Arcavi et al.	*
57985.377	2.848	Sinistro	LCO 1m	w	19.68	0.05	0	Arcavi et al.	X
57985.381	2.852	Sinistro	LCO 1m	w	19.61	0.05	0	Arcavi et al.	X
57985.384	2.855	Skymapper	Skymapper	r	19.34	0.08	0	Andreoni et al.	*
57984.385	2.856	Skymapper	Skymapper	g	20.43	0.11	0	Andreoni et al.	*
57985.385	2.856	Sinistro	LCO 1m	V	19.77	0.20	0	Arcavi et al.	*
57985.391	2.862	Sinistro	LCO 1m	i	18.70	0.18	-0.63	Arcavi et al.	*
57985.395	2.866	Sinistro	LCO 1m	i	18.63	0.15	-0.57	Arcavi et al.	*
57985.397	2.868	Skymapper	Skymapper	r	19.37	0.09	0	Andreoni et al.	*
57985.398	2.869	Skymapper	Skymapper	g	20.21	0.12	0	Andreoni et al.	*
57985.405	2.876	Sinistro	LCO 1m	w	19.53	0.07	0	Arcavi et al.	X

Table 4.3 – continued from previous page

MJD	Phase	Instrument	Telescope	Filter	AB Mag[a]	Err.	Δ(Mag)[b]	Ref.	Note[c]
57985.408	2.879	Sinistro	LCO 1m	w	19.56	0.08	0	Arcavi et al.	X
57985.479	2.950	zadko	zadko	r	19.18	0.12	0	Andreoni et al.	*
57985.531	3.002	UVOT	Swift	V	>18.72	-	0	Evans et al.	*
57985.550	3.021	UVOT	Swift	W1	>22.05	-	0	Evans et al.	*
57985.554	3.025	UVOT	Swift	B	>19.71	-	0	Evans et al.	*
57985.558	3.029	UVOT	Swift	W2	>22.42	-	0	Evans et al.	*
57985.672	3.143	10k10k ccd	AST3-2	i	>18.67	-	0	Hu et al.	*
57985.699	3.170	SIRIUS	IRSF	H	17.57	0.04	0	Utsumi et al.	*
57985.699	3.170	SIRIUS	IRSF	J	17.78	0.05	0	Utsumi et al.	*
57985.699	3.170	SIRIUS	IRSF	Ks	17.55	0.05	0	Utsumi et al.	*
57985.715	3.186	MASTER	SAAO	W	>19.10	-	0	Lipunov et al.	*
57985.719	3.190	-	KMTNet-SAAO	I	18.73	0.11	0	Troja et al.	*
57985.719	3.190	-	KMTNet-SAAO	R	19.30	0.05	0	Troja et al.	*
57985.726	3.197	Sinistro	LCO 1m	r	19.75	0.12	-0.22	Arcavi et al.	*
57985.730	3.201	MASTER	SAAO	R	>18.60	-	0	Lipunov et al.	*
57985.733	3.204	Sinistro	LCO 1m	i	18.84	0.20	-0.57	Arcavi et al.	*

Table 4.3 – continued from previous page

MJD	Phase	Instrument	Telescope	Filter	AB Mag[a]	Err.	Δ(Mag)[b]	Ref.	Note[c]
57985.736	3.207	Sinistro	LCO 1m	i	18.76	0.15	-0.68	Arcavi et al.	*
57985.738	3.209	MASTER	SAAO	B	>19.30	-	0	Lipunov et al.	*
57985.740	3.211	Sinistro	LCO 1m	z	18.42	0.34	-0.72	Arcavi et al.	*
57985.743	3.214	Sinistro	LCO 1m	V	19.89	0.19	0	Arcavi et al.	*
57985.746	3.217	Sinistro	LCO 1m	w	20.13	0.13	0	Arcavi et al.	X
57985.750	3.221	Sinistro	LCO 1m	w	19.99	0.06	0	Arcavi et al.	X
57985.776	3.247	-	1.5B	r	19.52	0.13	0	Smartt et al.	*
57985.969	3.440	EFOSC2	NTT	V	20.54	0.20	0	Drout et al.	*
57985.973	3.444	FourStar	Magellan	J	17.85	0.01	0	Drout et al.	*
57985.973	3.444	-	RC-1000	r	20.04	0.08	0	Pozanenko et al.	*
57985.974	3.445	GROND	LaSilla	H	17.72	0.07	0	Smartt et al.	*
57985.974	3.445	GROND	LaSilla	J	17.95	0.07	0	Smartt et al.	*
57985.974	3.445	GROND	LaSilla	K	17.63	0.10	0	Smartt et al.	*
57985.974	3.445	GROND	LaSilla	g	21.13	0.16	0	Smartt et al.	*
57985.974	3.445	GROND	LaSilla	i	19.03	0.01	0	Smartt et al.	*
57985.974	3.445	GROND	LaSilla	r	19.81	0.02	0	Smartt et al.	*

Table 4.3 – continued from previous page

MJD	Phase	Instrument	Telescope	Filter	AB Mag[a]	Err.	Δ(Mag)[b]	Ref.	Note[c]
57985.974	3.445	GROND	LaSilla	z	18.74	0.02	0	Smartt et al.	*
57985.979	3.450	-	KMTNet/CTIO	I	18.87	0.11	0	Troja et al.	*
57985.979	3.450	-	KMTNet/CTIO	R	19.54	0.06	0	Troja et al.	*
57985.979	3.450	VIRCAM	VISTA	Ks	17.54	0.02	0	Tanvir et al.	*
57985.979	3.450	FORS	VLT	r	19.28	0.01	0	Tanvir et al.	*
57985.983	3.454	DECam	Blanco/CTIO	Y	18.05	0.03	0	Cowperthwaite et al.	*
57985.984	3.455	DECam	Blanco/CTIO	z	18.56	0.03	0	Cowperthwaite et al.	*
57985.984	3.455	DECam	Blanco/CTIO	u	23.06	0.32	0	Cowperthwaite et al.	*
57985.984	3.455	DECam	Blanco/CTIO	i	18.73	0.03	0	Cowperthwaite et al.	*
57985.985	3.456	DECam	Blanco/CTIO	r	19.29	0.04	0	Cowperthwaite et al.	*
57985.986	3.457	DECam	Blanco/CTIO	g	20.93	0.08	0	Cowperthwaite et al.	*
57985.989	3.460	VIRCAM	VISTA	Y	17.76	0.01	0	Tanvir et al.	*
57985.989	3.460	VIRCAM	VISTA	Y	17.86	0.02	0	Tanvir et al.	*
57985.989	3.460	E2V 4kx4k ccd	Swope	V	20.52	0.12	0	Coulter et al.	*
57985.995	3.466	E2V 4kx4k ccd	Swope	B	21.72	0.13	0	Coulter et al.	*
57986.000	3.471	LDSS	Magellan	z	18.38	0.05	0	Drout et al.	*

Table 4.3 – continued from previous page

MJD	Phase	Instrument	Telescope	Filter	AB Mag[a]	Err.	Δ(Mag)[b]	Ref.	Note[c]
57986.001	3.472	E2V 4kx4k ccd	Swope	g	20.77	0.05	0	Coulter et al.	*
57986.003	3.474	Alta U47+	Prompt5	r	20.18	0.10	0	Valenti et al.	*
57986.005	3.476	E2V 4kx4k ccd	Swope	i	18.92	0.05	0	Coulter et al.	*
57986.008	3.479	E2V 4kx4k ccd	Swope	r	19.82	0.09	0	Coulter et al.	*
57986.016	3.487	EFOSC2	NTT	V	20.55	0.15	0	Drout et al.	*
57986.020	3.491	XS	VLT	g	20.94	0.06	0	Pian et al.	*
57986.020	3.491	XS	VLT	r	19.74	0.02	0	Pian et al.	*
57986.020	3.491	XS	VLT	z	18.30	0.02	0	Pian et al.	*
57986.029	3.500	FLAMINGOS-2	Gemini-S	H	17.72	0.04	0	Kasliwal et al.	R
57986.029	3.500	FLAMINGOS-2	Gemini-S	H	17.69	0.02	0	Troja et al.	R
57986.029	3.500	FLAMINGOS-2	Gemini-S	H	17.70	0.02	0	this Chapter	*,A
57986.029	3.500	FLAMINGOS-2	Gemini-S	J	17.93	0.06	0	Kasliwal et al.	R
57986.029	3.500	FLAMINGOS-2	Gemini-S	J	17.94	0.02	0	Troja et al.	R
57986.029	3.500	FLAMINGOS-2	Gemini-S	J	17.94	0.02	0	this Chapter	*,A
57986.029	3.500	FLAMINGOS-2	Gemini-S	Ks	17.61	0.06	0	Kasliwal et al.	R
57986.029	3.500	FLAMINGOS-2	Gemini-S	Ks	17.62	0.02	0	Troja et al.	R

Table 4.3 – continued from previous page

MJD	Phase	Instrument	Telescope	Filter	AB Mag[a]	Err.	Δ(Mag)[b]	Ref.	Note[c]
57986.029	3.500	FLAMINGOS-2	Gemini-S	Ks	17.61	0.02	0	this Chapter	*,A
57986.031	3.502	MASTER	OAFA	W	>19.80	-	0	Lipunov et al.	*
57986.039	3.510	GMOS	Gemini-S	g	20.90	0.01	0	Troja et al.	*
57986.039	3.510	GMOS	Gemini-S	i	18.93	0.01	0	Troja et al.	*
57986.039	3.510	GMOS	Gemini-S	r	19.66	0.01	0	Troja et al.	*
57986.049	3.520	GMOS	Gemini-S	z	18.46	0.01	0	Troja et al.	*
57986.053	3.524	EFOSC2	NTT	V	20.68	0.31	0	Drout et al.	*
57986.180	3.651	UVOT	Swift	B	>19.37	-	0	Evans et al.	*
57986.191	3.662	UVOT	Swift	V	>18.95	-	0	Evans et al.	*
57986.236	3.707	GFC	Pan-STARRS	i	>17.80	-	0	Smartt et al.	*
57986.236	3.707	GFC	Pan-STARRS	y	>17.70	-	0	Smartt et al.	*
57986.236	3.707	GFC	Pan-STARRS	z	18.10	0.30	0	Smartt et al.	*,O
57986.359	3.830	-	KMTNet-SSO	I	19.00	0.10	0	Troja et al.	*
57986.359	3.830	-	KMTNet-SSO	R	19.64	0.09	0	Troja et al.	*
57986.494	3.965	zadko	zadko	r	19.86	0.21	0.0	Andreoni et al.	*
57986.651	4.122	10k10k ccd	AST3-2	i	>18.38	-	0	Hu et al.	*

Table 4.3 – continued from previous page

MJD	Phase	Instrument	Telescope	Filter	AB Mag[a]	Err.	Δ(Mag)[b]	Ref.	Note[c]
57986.709	4.180	SIRIUS	IRSF	H	17.77	0.04	0	Utsumi et al.	*
57986.709	4.180	SIRIUS	IRSF	J	18.13	0.12	0	Utsumi et al.	*
57986.709	4.180	SIRIUS	IRSF	Ks	17.57	0.07	0	Utsumi et al.	*
57986.715	4.186	Sinistro	LCO 1m	r	20.30	0.31	-0.39	Arcavi et al.	*
57986.718	4.189	MASTER	SAAO	W	>20.00	-	0	Lipunov et al.	*
57986.719	4.190	-	KMTNet-SAAO	I	19.23	0.10	0	Troja et al.	*
57986.719	4.190	-	KMTNet-SAAO	R	19.94	0.06	0	Troja et al.	*
57986.758	4.229	MASTER	SAAO	R	>19.50	-	0	Lipunov et al.	*
57986.810	4.281	MASTER	SAAO	B	>19.00	-	0	Lipunov et al.	*
57986.969	4.440	-	KMTNet/CTIO	I	19.22	0.10	0	Troja et al.	*
57986.969	4.440	-	KMTNet/CTIO	R	20.12	0.08	0	Troja et al.	*
57986.969	4.440	Sinistro	LCO 1m	r	20.25	0.28	-0.37	Arcavi et al.	*
57986.970	4.441	FORS2	VLT	R	20.24	0.06	0	Pian et al.	*
57986.973	4.444	FLAMINGOS-2	Gemini-S	H	17.92	0.10	0	Cowperthwaite et al.	*
57986.974	4.445	GROND	LaSilla	H	18.02	0.10	0	Smartt et al.	*
57986.974	4.445	GROND	LaSilla	J	18.17	0.07	0	Smartt et al.	*

Table 4.3 – continued from previous page

MJD	Phase	Instrument	Telescope	Filter	AB Mag[a]	Err.	Δ(Mag)[b]	Ref.	Note[c]
57986.974	4.445	GROND	LaSilla	K	17.53	0.11	-0.21	Smartt et al.	*
57986.974	4.445	GROND	LaSilla	g	21.58	0.22	0	Smartt et al.	*
57986.974	4.445	GROND	LaSilla	i	19.51	0.04	0	Smartt et al.	*
57986.974	4.445	GROND	LaSilla	r	20.53	0.05	0	Smartt et al.	*
57986.974	4.445	GROND	LaSilla	z	19.07	0.06	0	Smartt et al.	*
57986.975	4.446	DECam	Blanco/CTIO	Y	18.35	0.03	0	Cowperthwaite et al.	*
57986.978	4.449	DECam	Blanco/CTIO	z	18.81	0.03	0	Cowperthwaite et al.	*
57986.979	4.450	VIRCAM	VISTA	Ks	17.60	0.02	0	Tanvir et al.	*
57986.980	4.451	VIMOS	VLT	z	18.73	0.01	0	Tanvir et al.	*
57986.980	4.451	DECam	Blanco/CTIO	i	19.22	0.03	0	Cowperthwaite et al.	*
57986.981	4.452	-	RC-1000	R	20.14	0.12	0	Pozanenko et al.	*
57986.984	4.455	DECam	Blanco/CTIO	r	20.25	0.05	0	Cowperthwaite et al.	*
57986.988	4.459	E2V 4kx4k ccd	Swope	i	19.39	0.04	0	Coulter et al.	*
57986.989	4.460	VIRCAM	VISTA	Y	18.07	0.02	0	Tanvir et al.	*
57986.989	4.460	VIRCAM	VISTA	Y	18.08	0.03	0	Tanvir et al.	*
57986.989	4.460	VIMOS	VLT	r	19.86	0.01	0	Tanvir et al.	*,O

Table 4.3 – continued from previous page

MJD	Phase	Instrument	Telescope	Filter	AB Mag[a]	Err.	Δ(Mag)[b]	Ref.	Note[c]
57986.991	4.462	DECam	Blanco/CTIO	g	21.73	0.11	0	Cowperthwaite et al.	*
57986.992	4.463	Sinistro	LCO 1m	w	20.64	0.09	0	Arcavi et al.	X
57986.997	4.467	E2V 4kx4k ccd	Swope	r	20.58	0.12	0	Coulter et al.	*
57987.000	4.471	LDSS	Magellan	V	21.85	0.22	0	Drout et al.	*,O
57987.000	4.471	FORS2	VLT	z	18.93	0.03	0	Pian et al.	*
57987.004	4.475	Alta U47+	Prompt5	r	20.92	0.12	0	Valenti et al.	*,O
57987.004	4.475	E2V 4kx4k ccd	Swope	g	21.75	0.10	0	Coulter et al.	*
57987.010	4.481	FORS2	VLT	I	19.28	0.06	0	Pian et al.	*
57987.019	4.490	LDSS	Magellan	g	21.78	0.06	0	Drout et al.	*
57987.020	4.491	FORS2	VLT	B	22.73	0.13	0	Pian et al.	*
57987.020	4.491	FORS2	VLT	V	21.08	0.05	0	Pian et al.	*
57987.022	4.493	LDSS	Magellan	B	22.52	0.14	0	Drout et al.	*
57987.039	4.510	FLAMINGOS-2	Gemini-S	Ks	17.72	0.09	0	Kasliwal et al.	*
57987.049	4.520	FLAMINGOS-2	Gemini-S	H	18.02	0.07	0	Kasliwal et al.	*
57987.049	4.520	FLAMINGOS-2	Gemini-S	J	18.15	0.06	0	Kasliwal et al.	*
57987.236	4.707	GFC	Pan-STARRS	z	>18.80	-	0	Smartt et al.	*

Table 4.3 – continued from previous page

MJD	Phase	Instrument	Telescope	Filter	AB Mag[a]	Err.	Δ(Mag)[b]	Ref.	Note[c]
57987.319	4.790	WFC3/IR	HST	F110W	18.26	0.01	0	Tanvir et al.	R
57987.319	4.790	WFC3/IR	HST	F110W	18.43	0.03	0	Troja et al.	R,*
57987.358	4.829	Sinistro	LCO 1m	r	20.69	0.33	-0.62	Arcavi et al.	*
57987.359	4.830	-	KMTNet-SSO	I	19.52	0.13	0	Troja et al.	*
57987.359	4.830	-	KMTNet-SSO	R	20.33	0.05	0	Troja et al.	*
57987.382	4.853	Skymapper	Skymapper	r	>20.51	-	0	Andreoni et al.	*
57987.383	4.854	Skymapper	Skymapper	g	>20.60	-	0	Andreoni et al.	*
57987.394	4.865	Skymapper	Skymapper	r	>20.47	-	0	Andreoni et al.	*
57987.395	4.866	Skymapper	Skymapper	g	>20.66	-	0	Andreoni et al.	*
57987.452	4.923	WFC3/IR	HST	F160W	18.06	0.03	0	Tanvir et al.	R
57987.452	4.923	WFC3/IR	HST	F160W	18.12	0.03	0	Troja et al.	R
57987.452	4.923	WFC3/IR	HST	F160W	18.09	0.03	0	this Chapter	*,A
57987.475	4.946	UVOT	Swift	U	>20.85	-	0	Evans et al.	*
57987.482	4.953	UVOT	Swift	M2	>22.47	-	0	Evans et al.	*
57987.490	4.961	zadko	zadko	r	20.23	0.23	0.0	Andreoni et al.	*,O
57987.709	5.180	SIRIUS	IRSF	H	17.94	0.05	0	Utsumi et al.	*

Table 4.3 – continued from previous page

MJD	Phase	Instrument	Telescope	Filter	AB Mag[a]	Err.	Δ(Mag)[b]	Ref.	Note[c]
57987.709	5.180	SIRIUS	IRSF	J	18.31	0.06	0	Utsumi et al.	*
57987.709	5.180	SIRIUS	IRSF	Ks	17.68	0.04	0	Utsumi et al.	*
57987.719	5.190	-	KMTNet-SAAO	I	19.68	0.10	0	Troja et al.	*
57987.719	5.190	-	KMTNet-SAAO	R	20.64	0.07	0	Troja et al.	*
57987.849	5.320	WFC3/UVIS	HST	F336W	24.97	0.11	0	Kasliwal et al.	*
57987.849	5.320	WFC3/UVIS	HST	F336W	25.05	0.11	0	Kasliwal et al.	*
57987.879	5.350	WFC3/UVIS	HST	F336W	25.18	0.11	0	Kasliwal et al.	*
57987.969	5.440	FORS	VLT	r	20.39	0.03	0	Tanvir et al.	*
57987.971	5.442	LDSS	Magellan	z	19.08	0.12	0	Drout et al.	*
57987.975	5.446	DECam	Blanco/CTIO	Y	18.83	0.18	0	Cowperthwaite et al.	*
57987.977	5.448	DECam	Blanco/CTIO	z	19.17	0.11	0	Cowperthwaite et al.	*
57987.979	5.450	DECam	Blanco/CTIO	i	19.55	0.18	0	Cowperthwaite et al.	*
57987.983	5.454	DECam	Blanco/CTIO	r	20.79	0.24	0	Cowperthwaite et al.	*
57987.990	5.461	OmegaCam	VST	g	22.51	0.12	0	Pian et al.	*
57987.990	5.461	DECam	Blanco/CTIO	g	22.03	0.42	0	Cowperthwaite et al.	*
57988.002	5.473	E2V 4kx4k ccd	Swope	i	20.27	0.12	0	Coulter et al.	*,O

Table 4.3 – continued from previous page

MJD	Phase	Instrument	Telescope	Filter	AB Mag[a]	Err.	Δ(Mag)[b]	Ref.	Note[c]
57988.020	5.491	XS	VLT	r	20.74	0.03	0	Pian et al.	*
57988.020	5.491	XS	VLT	z	19.16	0.03	0	Pian et al.	*
57988.234	5.705	GFC	Pan-STARRS	y	18.95	0.44	0	Smartt et al.	*
57988.359	5.830	-	KMTNet-SSO	R	20.95	0.07	0	Troja et al.	*
57988.369	5.840	-	KMTNet-SSO	I	19.99	0.14	0	Troja et al.	*
57988.438	5.909	UVOT	Swift	B	>19.50	-	0	Evans et al.	*
57988.445	5.916	UVOT	Swift	V	>18.54	-	0	Evans et al.	*
57988.481	5.952	zadko	zadko	r	>20.60	-	0.0	Andreoni et al.	*
57988.729	6.200	-	KMTNet-SAAO	I	20.31	0.11	0	Troja et al.	*
57988.729	6.200	SIRIUS	IRSF	H	18.12	0.04	0	Utsumi et al.	*
57988.729	6.200	SIRIUS	IRSF	H	18.60	0.18	0	Kasliwal et al.	*
57988.729	6.200	SIRIUS	IRSF	J	18.36	0.05	0	Utsumi et al.	*
57988.729	6.200	SIRIUS	IRSF	J	18.65	0.19	0	Kasliwal et al.	*
57988.729	6.200	SIRIUS	IRSF	Ks	17.69	0.03	0	Utsumi et al.	*
57988.729	6.200	SIRIUS	IRSF	Ks	18.01	0.10	0	Kasliwal et al.	*
57988.970	6.441	OmegaCam	VST	i	20.33	0.09	0	Pian et al.	*

Table 4.3 – continued from previous page

MJD	Phase	Instrument	Telescope	Filter	AB Mag[a]	Err.	Δ(Mag)[b]	Ref.	Note[c]
57988.974	6.445	DECam	Blanco/CTIO	Y	19.06	0.31	0	Cowperthwaite et al.	*
57988.979	6.450	VISIR	VLT	J8.9	>8.26	-	0	Kasliwal et al.	*
57988.980	6.451	FORS2	VLT	I	20.14	0.07	0	Pian et al.	*
57988.980	6.451	OmegaCam	VST	r	21.31	0.07	0	Pian et al.	*
57988.980	6.451	FORS2	VLT	z	19.63	0.04	0	Pian et al.	*
57988.985	6.456	DECam	Blanco/CTIO	r	20.95	0.35	0	Cowperthwaite et al.	*
57988.989	6.460	VIRCAM	VISTA	Ks	17.84	0.03	0	Tanvir et al.	*
57988.996	6.467	DECam	Blanco/CTIO	g	22.08	0.52	0	Cowperthwaite et al.	*
57988.999	6.470	VIRCAM	VISTA	Y	18.71	0.04	0	Tanvir et al.	*
57988.999	6.470	VIRCAM	VISTA	Y	18.74	0.04	0	Tanvir et al.	*
57989.000	6.471	FORS2	VLT	R	21.27	0.11	0	Pian et al.	*
57989.020	6.491	FORS2	VLT	B	23.81	0.25	0	Pian et al.	*
57989.020	6.491	FORS2	VLT	V	22.36	0.16	0	Pian et al.	*
57989.230	6.701	GFC	Pan-STARRS	y	19.31	0.43	0	Smartt et al.	*
57989.234	6.705	LRIS	Keck-I	I	20.83	0.09	0	Drout et al.	*
57989.235	6.706	LRIS	Keck-I	g	>22.20	-	0	Drout et al.	*

Table 4.3 – continued from previous page

MJD	Phase	Instrument	Telescope	Filter	AB Mag[a]	Err.	Δ(Mag)[b]	Ref.	Note[c]
57989.369	6.840	-	KMTNet-SSO	I	20.39	0.12	0	Troja et al.	*
57989.699	7.170	SIRIUS	IRSF	H	18.51	0.05	0	Utsumi et al.	*
57989.699	7.170	SIRIUS	IRSF	H	18.53	0.17	0	Kasliwal et al.	*
57989.699	7.170	SIRIUS	IRSF	J	18.95	0.32	0	Kasliwal et al.	*
57989.699	7.170	SIRIUS	IRSF	J	18.98	0.08	0	Utsumi et al.	*
57989.699	7.170	SIRIUS	IRSF	Ks	17.95	0.04	0	Utsumi et al.	*
57989.699	7.170	SIRIUS	IRSF	Ks	18.02	0.12	0	Kasliwal et al.	*
57989.729	7.200	-	KMTNet-SAAO	I	20.89	0.13	0	Troja et al.	*
57989.769	7.240	WFC3/IR	HST	F110W	19.06	0.01	0	Tanvir et al.	R
57989.769	7.240	WFC3/IR	HST	F110W	19.37	0.04	0	Troja et al.	R,*
57989.966	7.437	FLAMINGOS-2	Gemini-S	H	18.79	0.14	0	Cowperthwaite et al.	*
57989.969	7.440	ANDICAM	1.3m/CTIO	K	18.06	0.17	0	Kasliwal et al.	*
57989.970	7.441	LDSS	Magellan	z	19.87	0.07	0	Drout et al.	*
57989.973	7.444	DECam	Blanco/CTIO	Y	19.44	0.05	0	Cowperthwaite et al.	*
57989.979	7.450	VIRCAM	VISTA	Ks	17.95	0.04	0	Tanvir et al.	*
57989.979	7.450	DECam	Blanco/CTIO	z	19.89	0.05	0	Cowperthwaite et al.	*

Table 4.3 – continued from previous page

MJD	Phase	Instrument	Telescope	Filter	AB Mag[a]	Err.	Δ(Mag)[b]	Ref.	Note[c]
57989.982	7.453	DECam	Blanco/CTIO	i	20.54	0.05	0	Cowperthwaite et al.	*
57989.983	7.454	GROND	LaSilla	H	18.74	0.06	0	Smartt et al.	*
57989.983	7.454	GROND	LaSilla	J	19.26	0.28	0	Smartt et al.	*
57989.983	7.454	GROND	LaSilla	K	18.04	0.12	-0.36	Smartt et al.	*
57989.983	7.454	GROND	LaSilla	g	>20.50	-	0	Smartt et al.	*
57989.983	7.454	GROND	LaSilla	i	>20.50	-	0	Smartt et al.	*
57989.983	7.454	GROND	LaSilla	r	>20.60	-	0	Smartt et al.	*
57989.983	7.454	GROND	LaSilla	z	>19.70	-	0	Smartt et al.	*
57989.987	7.458	DECam	Blanco/CTIO	r	21.23	0.11	0	Cowperthwaite et al.	*
57989.989	7.460	VIRCAM	VISTA	Y	19.07	0.08	0	Tanvir et al.	*
57989.990	7.461	E2V 4kx4k ccd	Swope	i	21.42	0.18	0	Coulter et al.	*,O
57989.996	7.467	-	RC-1000	r	>21.00	-	0	Pozanenko et al.	*
57989.997	7.468	DECam	Blanco/CTIO	g	23.28	0.34	0	Cowperthwaite et al.	*
57989.999	7.470	VIRCAM	VISTA	Y	19.24	0.07	0	Tanvir et al.	*
57990.004	7.475	Alta U47+	Prompt5	r	>20.89	-	0	Valenti et al.	*
57990.030	7.501	LDSS	Magellan	B	23.85	0.31	0	Drout et al.	*

Table 4.3 – continued from previous page

MJD	Phase	Instrument	Telescope	Filter	AB Mag[a]	Err.	Δ(Mag)[b]	Ref.	Note[c]
57990.039	7.510	GMOS	Gemini-S	i	20.91	0.03	0	Troja et al.	*
57990.039	7.510	GMOS	Gemini-S	r	21.74	0.04	0	Troja et al.	*
57990.229	7.700	HSC	Subaru	z	20.21	0.04	0	Utsumi et al.	*
57990.230	7.701	GFC	Pan-STARRS	y	>18.90	-	0	Smartt et al.	*
57990.585	8.056	WFC3/UVIS	HST	F606W	22.49	0.17	0	Troja et al.	*
57990.645	8.116	WFC3/UVIS	HST	F475W	23.14	0.02	0	Tanvir et al.	R
57990.645	8.116	WFC3/UVIS	HST	F475W	23.66	0.42	0	Troja et al.	R
57990.645	8.116	WFC3/UVIS	HST	F475W	23.14	0.02	0	this Chapter	*,A
57990.968	8.439	GROND	LaSilla	H	19.26	0.26	0	Smartt et al.	*
57990.968	8.439	GROND	LaSilla	J	19.64	0.11	0	Smartt et al.	*
57990.968	8.439	GROND	LaSilla	K	18.35	0.16	-0.51	Smartt et al.	*
57990.968	8.439	GROND	LaSilla	g	>22.20	-	0	Smartt et al.	*
57990.968	8.439	GROND	LaSilla	i	>21.10	-	0	Smartt et al.	*
57990.968	8.439	GROND	LaSilla	r	>21.70	-	0	Smartt et al.	*
57990.968	8.439	GROND	LaSilla	z	>21.50	-	0	Smartt et al.	*
57990.972	8.443	VIMOS	VLT	z	20.28	0.03	0	Tanvir et al.	*

Table 4.3 – continued from previous page

MJD	Phase	Instrument	Telescope	Filter	AB Mag[a]	Err.	Δ(Mag)[b]	Ref.	Note[c]
57990.972	8.443	LDSS	Magellan	z	20.40	0.07	0	Drout et al.	*
57990.973	8.444	DECam	Blanco/CTIO	Y	20.06	0.07	0	Cowperthwaite et al.	*
57990.979	8.450	ANDICAM	1.3m/CTIO	K	18.44	0.18	0	Kasliwal et al.	*
57990.979	8.450	VIRCAM	VISTA	Ks	18.25	0.03	0	Tanvir et al.	*
57990.979	8.450	VIRCAM	VISTA	Y	19.69	0.09	0	Tanvir et al.	*
57990.980	8.451	EFOSC2	NTT	g	>21.00	-	0	Smartt et al.	*
57990.980	8.451	EFOSC2	NTT	i	>21.10	-	0	Smartt et al.	*
57990.980	8.451	EFOSC2	NTT	r	>21.40	-	0	Smartt et al.	*
57990.980	8.451	EFOSC2	NTT	z	>20.40	-	0	Smartt et al.	*
57990.980	8.451	FLAMINGOS-2	Gemini-S	H	19.22	0.18	0	Cowperthwaite et al.	*
57990.983	8.454	DECam	Blanco/CTIO	z	20.40	0.06	0	Cowperthwaite et al.	*
57990.988	8.459	DECam	Blanco/CTIO	i	20.72	0.06	0	Cowperthwaite et al.	*
57990.989	8.460	VIRCAM	VISTA	Y	19.67	0.09	0	Tanvir et al.	*
57990.989	8.460	VIMOS	VLT	r	21.75	0.05	0	Tanvir et al.	*
57990.990	8.461	FORS2	VLT	I	21.13	0.12	0	Pian et al.	*
57990.990	8.461	FORS2	VLT	z	20.61	0.09	0	Pian et al.	*

Table 4.3 – continued from previous page

MJD	Phase	Instrument	Telescope	Filter	AB Mag[a]	Err.	Δ(Mag)[b]	Ref.	Note[c]
57990.997	8.468	DECam	Blanco/CTIO	r	21.95	0.18	0	Cowperthwaite et al.	*
57991.000	8.471	FORS2	VLT	R	22.50	0.24	0	Pian et al.	*
57991.004	8.475	Alta U47+	Prompt5	r	>20.37	-	0	Valenti et al.	*
57991.010	8.481	FORS2	VLT	V	23.15	0.26	0	Pian et al.	*
57991.034	8.505	LDSS	Magellan	g	>22.64	-	0	Drout et al.	*
57991.709	9.180	SIRIUS	IRSF	H	18.83	0.23	0	Kasliwal et al.	*
57991.709	9.180	SIRIUS	IRSF	H	18.90	0.09	0	Utsumi et al.	*
57991.709	9.180	SIRIUS	IRSF	J	>18.87	-	0	Kasliwal et al.	*
57991.709	9.180	SIRIUS	IRSF	J	19.32	0.08	0	Utsumi et al.	o
57991.709	9.180	SIRIUS	IRSF	Ks	18.25	0.21	0	Kasliwal et al.	*
57991.709	9.180	SIRIUS	IRSF	Ks	18.34	0.06	0	Utsumi et al.	*
57991.956	9.427	WFC3/IR	HST	F160W	19.60	0.06	0	Tanvir et al.	R
57991.956	9.427	WFC3/IR	HST	F160W	19.77	0.07	0	Troja et al.	R,*
57991.959	9.430	FLAMINGOS-2	Gemini-S	H	19.62	0.15	0	Cowperthwaite et al.	R
57991.959	9.430	FLAMINGOS-2	Gemini-S	H	19.68	0.08	0	Kasliwal et al.	R
57991.959	9.430	FLAMINGOS-2	Gemini-S	H	19.67	0.08	0	this Chapter	*,A

Table 4.3 – continued from previous page

MJD	Phase	Instrument	Telescope	Filter	AB Mag[a]	Err.	Δ(Mag)[b]	Ref.	Note[c]
57991.959	9.430	FLAMINGOS-2	Gemini-S	J	20.57	0.20	0	Kasliwal et al.	*
57991.959	9.430	FLAMINGOS-2	Gemini-S	Ks	18.50	0.08	0	Kasliwal et al.	*
57991.969	9.440	ANDICAM	1.3m/CTIO	K	18.43	0.17	0	Kasliwal et al.	*
57991.969	9.440	GROND	LaSilla	H	19.66	0.14	0	Smartt et al.	*
57991.969	9.440	GROND	LaSilla	J	20.23	0.10	0	Smartt et al.	*
57991.969	9.440	GROND	LaSilla	K	18.46	0.20	-0.57	Smartt et al.	*
57991.974	9.445	VIMOS	VLT	z	20.85	0.04	0	Tanvir et al.	*
57991.974	9.445	DECam	Blanco/CTIO	Y	20.78	0.11	0	Cowperthwaite et al.	*
57991.979	9.450	VIRCAM	VISTA	Ks	18.49	0.05	0	Tanvir et al.	*
57991.979	9.450	VIRCAM	VISTA	Y	20.06	0.14	0	Tanvir et al.	*
57991.989	9.460	VIRCAM	VISTA	Y	20.09	0.14	0	Tanvir et al.	*
57991.989	9.460	Alta U47+	Prompt5	r	>19.90	-	0	Valenti et al.	*
57991.989	9.460	VIMOS	VLT	r	22.20	0.04	0	Tanvir et al.	*
57991.991	9.462	FORS	VLT	z	20.69	0.11	0	Tanvir et al.	*
57991.994	9.465	DECam	Blanco/CTIO	z	21.19	0.07	0	Cowperthwaite et al.	*
57992.000	9.471	DECam	Blanco/CTIO	i	21.37	0.06	0	Cowperthwaite et al.	*

Table 4.3 – continued from previous page

MJD	Phase	Instrument	Telescope	Filter	AB Mag[a]	Err.	Δ(Mag)[b]	Ref.	Note[c]
57992.099	9.570	NICFPS	APO	Ks	>17.99	-	0	Kasliwal et al.	*
57992.119	9.590	WHIRC	Palomar5m	Ks	>17.64	-	0	Kasliwal et al.	*
57992.282	9.753	WFC3/IR	HST	F110W	20.57	0.04	0	Cowperthwaite et al.	*
57992.296	9.767	WFC3/IR	HST	F160W	19.89	0.04	0	Cowperthwaite et al.	*
57992.348	9.819	WFC3/UVIS1	HST	F336W	26.92	0.27	0	Cowperthwaite et al.	*
57992.433	9.904	ACS/WFC	HST	F475W	23.95	0.06	0	Cowperthwaite et al.	*
57992.498	9.969	ACS/WFC	HST	F625W	22.88	0.07	0	Cowperthwaite et al.	*
57992.561	10.032	ACS/WFC	HST	F775W	22.35	0.08	0	Cowperthwaite et al.	*
57992.573	10.044	ACS/WFC	HST	F850W	21.53	0.05	0	Cowperthwaite et al.	*
57992.959	10.430	FLAMINGOS-2	Gemini-S	Ks	18.77	0.07	0	Kasliwal et al.	*
57992.969	10.440	FLAMINGOS-2	Gemini-S	H	19.63	0.08	0	Kasliwal et al.	*
57992.969	10.440	FLAMINGOS-2	Gemini-S	J	21.33	0.30	0	Kasliwal et al.	*
57992.969	10.440	ANDICAM	1.3m/CTIO	K	18.91	0.19	0	Kasliwal et al.	*
57992.975	10.446	DECam	Blanco/CTIO	Y	21.67	0.21	0	Cowperthwaite et al.	*
57992.975	10.446	EFOSC2	NTT	J	21.02	0.22	0	Smartt et al.	*
57992.978	10.449	FLAMINGOS-2	Gemini-S	Ks	18.43	0.25	0	Cowperthwaite et al.	*

Table 4.3 – continued from previous page

MJD	Phase	Instrument	Telescope	Filter	AB Mag[a]	Err.	Δ(Mag)[b]	Ref.	Note[c]
57992.979	10.450	VIRCAM	VISTA	Ks	18.74	0.06	0	Tanvir et al.	*
57992.980	10.451	FORS2	VLT	z	22.01	0.21	0	Pian et al.	*
57992.981	10.452	FLAMINGOS-2	Gemini-S	H	20.04	0.15	0	Cowperthwaite et al.	*
57992.987	10.458	DECam	Blanco/CTIO	z	22.06	0.13	0	Cowperthwaite et al.	*
57992.989	10.460	VIRCAM	VISTA	Y	20.94	0.35	0	Tanvir et al.	*
57992.989	10.460	VIMOS	VLT	r	22.45	0.07	0	Tanvir et al.	*
57992.990	10.461	FORS2	VLT	I	22.05	0.29	0	Pian et al.	*
57993.000	10.471	DECam	Blanco/CTIO	i	22.38	0.10	0	Cowperthwaite et al.	*
57993.010	10.481	FORS2	VLT	R	23.38	0.28	0	Pian et al.	*
57993.010	10.481	FORS2	VLT	V	23.76	0.28	0	Pian et al.	*
57993.016	10.487	GROND	LaSilla	H	20.17	0.34	0	Smartt et al.	*
57993.016	10.487	GROND	LaSilla	K	18.71	0.22	-0.79	Smartt et al.	*
57993.079	10.550	WFC3/IR	HST	F110W	20.82	0.02	0	Tanvir et al.	R
57993.079	10.550	WFC3/IR	HST	F110W	21.37	0.12	0	Troja et al.	*,R
57993.148	10.619	WFC3/IR	HST	F160W	20.28	0.09	0	Tanvir et al.	R
57993.148	10.619	WFC3/IR	HST	F160W	20.45	0.10	0	Troja et al.	R

Table 4.3 – continued from previous page

MJD	Phase	Instrument	Telescope	Filter	AB Mag[a]	Err.	Δ(Mag)[b]	Ref.	Note[c]
57993.148	10.619	WFC3/IR	HST	F160W	20.36	0.09	0	-	*,A
57993.387	10.858	Skymapper	Skymapper	r	>19.36	-	0.0	Andreoni et al.	*
57993.388	10.859	Skymapper	Skymapper	g	>19.53	-	0.0	Andreoni et al.	*
57993.400	10.871	Skymapper	Skymapper	r	>19.39	-	0.0	Andreoni et al.	*
57993.401	10.872	Skymapper	Skymapper	g	>19.50	-	0.0	Andreoni et al.	*
57993.699	11.170	SIRIUS	IRSF	H	>18.43	-	0	Kasliwal et al.	*
57993.699	11.170	SIRIUS	IRSF	H	19.53	0.21	0	Utsumi et al.	*
57993.699	11.170	SIRIUS	IRSF	J	>18.37	-	0	Kasliwal et al.	*
57993.699	11.170	SIRIUS	IRSF	Ks	>18.48	-	0	Kasliwal et al.	*
57993.699	11.170	SIRIUS	IRSF	Ks	18.64	0.12	0	Utsumi et al.	*
57993.814	11.285	WFC3/UVIS	HST	F606W	23.77	0.38	0	Troja et al.	*
57993.829	11.300	WFC3/UVIS	HST	F475W	24.08	0.05	0	Tanvir et al.	R
57993.829	11.300	WFC3/UVIS	HST	F475W	24.75	0.69	0	Troja et al.	R
57993.829	11.300	WFC3/UVIS	HST	F475W	24.08	0.05	0	this Chapter	A,*
57993.940	11.411	WFC3/UVIS	HST	F475W	23.96	0.05	0	Tanvir et al.	R
57993.940	11.411	WFC3/UVIS	HST	F475W	24.55	0.64	0	Troja et al.	R

Table 4.3 – continued from previous page

MJD	Phase	Instrument	Telescope	Filter	AB Mag[a]	Err.	Δ(Mag)[b]	Ref.	Note[c]
57993.940	11.411	WFC3/UVIS	HST	F475W	23.96	0.05	0	this Chapter	*,A
57993.957	11.428	WFC3/UVIS	HST	F814W	22.32	0.02	0	Tanvir et al.	R
57993.957	11.428	WFC3/UVIS	HST	F814W	22.58	0.34	0	Troja et al.	R
57993.957	11.428	WFC3/UVIS	HST	F814W	22.32	0.02	0	this Chapter	*,A
57993.960	11.431	EFOSC2	NTT	H	20.05	0.20	0	Smartt et al.	*
57993.968	11.439	WFC3/UVIS	HST	F606W	23.66	0.36	0	Troja et al.	R
57993.968	11.439	WFC3/UVIS	HST	F606W	23.09	0.03	0	Tanvir et al.	R
57993.968	11.439	WFC3/UVIS	HST	F606W	23.09	0.03	0	this Chapter	*,A
57993.969	11.440	ANDICAM	1.3m/CTIO	K	>19.11	-	0	Kasliwal et al.	*
57993.979	11.450	FLAMINGOS-2	Gemini-S	Ks	19.03	0.17	0	Cowperthwaite et al.	R
57993.979	11.450	FLAMINGOS-2	Gemini-S	Ks	19.41	0.09	0	Kasliwal et al.	R,O
57993.979	11.450	FLAMINGOS-2	Gemini-S	Ks	18.99	0.05	0	Troja et al.	R
57993.979	11.450	FLAMINGOS-2	Gemini-S	Ks	18.99	0.05	0	this Chapter	*,A
57993.980	11.451	FORS2	VLT	z	22.82	0.47	0	Pian et al.	*
57993.989	11.460	FLAMINGOS-2	Gemini-S	H	>20.63	-	0	Kasliwal et al.	R
57993.989	11.460	FLAMINGOS-2	Gemini-S	H	20.24	0.18	0	Troja et al.	*,R

Table 4.3 – continued from previous page

MJD	Phase	Instrument	Telescope	Filter	AB Mag[a]	Err.	Δ(Mag)[b]	Ref.	Note[c]
57993.989	11.460	FLAMINGOS-2	Gemini-S	J	>21.07	-	0	Kasliwal et al.	r, O
57993.989	11.460	FLAMINGOS-2	Gemini-S	J	20.35	0.12	0	Troja et al.	*,R
57993.989	11.460	VIRCAM	VISTA	Y	21.16	0.40	0	Tanvir et al.	*
57993.997	11.468	SOFI	NTT	H	19.64	0.14	0	Drout et al.	*
57994.000	11.471	FORS2	VLT	I	23.00	0.31	0	Pian et al.	*
57994.029	11.500	WFC3/UVIS	HST	F225W	>26.04	-	0	Kasliwal et al.	*
57994.029	11.500	WFC3/UVIS	HST	F275W	>26.13	-	0	Kasliwal et al.	*
57994.029	11.500	WFC3/UVIS	HST	F336W	>26.37	-	0	Kasliwal et al.	*
57994.962	12.433	FourStar	Magellan	Ks	19.36	0.09	0	Drout et al.	*
57994.969	12.440	FLAMINGOS-2	Gemini-S	Ks	19.42	0.16	0	Cowperthwaite et al.	R
57994.969	12.440	FLAMINGOS-2	Gemini-S	Ks	19.44	0.08	0	Kasliwal et al.	R
57994.969	12.440	FLAMINGOS-2	Gemini-S	Ks	19.46	0.04	0	Troja et al.	R
57994.969	12.440	FLAMINGOS-2	Gemini-S	Ks	19.45	0.04	0	this Chapter	*,A
57994.969	12.440	VIMOS	VLT	r	23.12	0.31	0	Tanvir et al.	*
57994.979	12.450	FLAMINGOS-2	Gemini-S	H	20.99	0.21	0	Troja et al.	R
57994.979	12.450	FLAMINGOS-2	Gemini-S	H	20.57	0.19	0	Kasliwal et al.	R

Table 4.3 – continued from previous page

MJD	Phase	Instrument	Telescope	Filter	AB Mag[a]	Err.	Δ(Mag)[b]	Ref.	Note[c]
57994.979	12.450	FLAMINGOS-2	Gemini-S	H	20.76	0.19	0	this Chapter	*,A
57994.985	12.456	SOFI	NTT	Ks	19.32	0.09	0	Drout et al.	*
57994.989	12.460	FLAMINGOS-2	Gemini-S	J	>21.55	-	0	Kasliwal et al.	*
57994.989	12.460	VIRCAM	VISTA	Ks	19.34	0.08	0	Tanvir et al.	*
57995.388	12.859	Skymapper	Skymapper	g	>19.36	-	0	Andreoni et al.	*
57995.389	12.860	Skymapper	Skymapper	r	>19.32	-	0	Andreoni et al.	*
57995.401	12.872	Skymapper	Skymapper	g	>19.24	-	0	Andreoni et al.	*
57995.959	13.430	FLAMINGOS-2	Gemini-S	Ks	19.63	0.23	0	Cowperthwaite et al.	R
57995.959	13.430	FLAMINGOS-2	Gemini-S	Ks	19.84	0.09	0	Kasliwal et al.	R
57995.959	13.430	FLAMINGOS-2	Gemini-S	Ks	19.81	0.09	0	this Chapter	*,A
57995.961	13.432	EFOSC2	NTT	K	19.67	0.14	0	Smartt et al.	*
57995.962	13.433	FourStar	Magellan	H	>20.50	-	0	Drout et al.	*
57995.969	13.440	VIMOS	VLT	z	22.30	0.28	0	Tanvir et al.	*
57995.978	13.449	FourStar	Magellan	Ks	19.52	0.09	0	Drout et al.	*
57995.979	13.450	FLAMINGOS-2	Gemini-S	H	21.48	0.30	0	Kasliwal et al.	R
57995.979	13.450	FLAMINGOS-2	Gemini-S	H	21.01	0.14	0	Troja et al.	R

Table 4.3 – continued from previous page

MJD	Phase	Instrument	Telescope	Filter	AB Mag[a]	Err.	Δ(Mag)[b]	Ref.	Note[c]
57995.979	13.450	FLAMINGOS-2	Gemini-S	H	21.09	0.14	0	this Chapter	*,A
57995.989	13.460	FLAMINGOS-2	Gemini-S	J	>21.94	-	0	Kasliwal et al.	*
57995.990	13.461	SOFI	NTT	Ks	19.43	0.09	0	Drout et al.	*
57996.799	14.270	MOIRCS	Subaru	Ks	19.35	0.04	0	Utsumi et al.	O
57996.974	14.445	FLAMINGOS-2	Gemini-S	Ks	19.90	0.21	0	Cowperthwaite et al.	R
57996.974	14.445	FLAMINGOS-2	Gemini-S	Ks	20.06	0.10	0	Kasliwal et al.	R
57996.974	14.445	FLAMINGOS-2	Gemini-S	Ks	19.93	0.03	0	Troja et al.	R
57996.974	14.445	FLAMINGOS-2	Gemini-S	Ks	19.94	0.03	0	this Chapter	*,A
57996.969	14.440	VISIR	VLT	J8.9	>7.74	-	0	Kasliwal et al.	*
57996.980	14.451	FORS2	VLT	z	23.34	0.37	0	Pian et al.	*
57996.989	14.460	VIRCAM	VISTA	Ks	20.02	0.13	0	Tanvir et al.	*
57996.999	14.470	FLAMINGOS-2	Gemini-S	H	21.63	0.36	0	Kasliwal et al.	*
57997.009	14.480	GMOS	Gemini-S	i	>23.20	-	0	Kasliwal et al.	*
57997.799	15.270	MOIRCS	Subaru	Ks	19.97	0.05	0	Utsumi et al.	*
57997.969	15.440	VISIR	VLT	J8.9	>7.57	-	0	Kasliwal et al.	*
57997.970	15.441	FourStar	Magellan	Ks	20.23	0.10	0	Drout et al.	*

Table 4.3 – continued from previous page

MJD	Phase	Instrument	Telescope	Filter	AB Mag[a]	Err.	Δ(Mag)[b]	Ref.	Note[c]
57997.976	15.447	FLAMINGOS-2	Gemini-S	Ks	20.13	0.25	0	Cowperthwaite et al.	R
57997.976	15.447	FLAMINGOS-2	Gemini-S	Ks	20.43	0.13	0	Kasliwal et al.	R,O
57997.976	15.447	FLAMINGOS-2	Gemini-S	Ks	20.06	0.05	0	Troja et al.	R
57997.976	15.447	FLAMINGOS-2	Gemini-S	Ks	20.06	0.05	0	this Chapter	*,A
57998.029	15.500	GMOS	Gemini-S	i	>23.40	-	0	Kasliwal et al.	*
57998.979	16.450	FLAMINGOS-2	Gemini-S	Ks	20.43	0.30	0	Cowperthwaite et al.	R
57998.979	16.450	FLAMINGOS-2	Gemini-S	Ks	20.31	0.08	0	Troja et al.	R
57998.979	16.450	FLAMINGOS-2	Gemini-S	Ks	20.95	0.18	0	Kasliwal et al.	R,O
57998.979	16.450	FLAMINGOS-2	Gemini-S	Ks	20.32	0.08	0	this Chapter	*,A
57998.999	16.470	GMOS	Gemini-S	r	>21.18	-	0	Kasliwal et al.	*
57999.979	17.450	HAWKI	VLT	Ks	20.77	0.13	0	Tanvir et al.	*
57999.989	17.460	FLAMINGOS-2	Gemini-S	Ks	>19.92	-	0	Kasliwal et al.	R
57999.989	17.460	FLAMINGOS-2	Gemini-S	Ks	20.61	0.09	0	Troja et al.	*,R
58000.009	17.480	GMOS	Gemini-S	r	>21.98	-	0	Kasliwal et al.	*
58000.960	18.431	FourStar	Magellan	Ks	20.81	0.13	0	Drout et al.	*
58000.966	18.437	EFOSC2	NTT	K	20.76	0.35	0	Smartt et al.	*

Table 4.3 – continued from previous page

MJD	Phase	Instrument	Telescope	Filter	AB Mag[a]	Err.	Δ(Mag)[b]	Ref.	Note[c]
58000.978	18.449	FLAMINGOS-2	Gemini-S	Ks	20.84	0.26	0	Cowperthwaite et al.	R
58000.978	18.449	FLAMINGOS-2	Gemini-S	Ks	21.04	0.09	0	Kasliwal et al.	R
58000.978	18.449	FLAMINGOS-2	Gemini-S	Ks	21.02	0.09	0	this Chapter	*,A
58000.990	18.461	FourStar	Magellan	Ks	20.93	0.17	0	Drout et al.	*
58000.999	18.470	GMOS	Gemini-S	i	>21.90	-	0	Kasliwal et al.	*
58001.989	19.460	FLAMINGOS-2	Gemini-S	Ks	21.23	0.37	0	Kasliwal et al.	R
58001.989	19.460	FLAMINGOS-2	Gemini-S	Ks	20.85	0.13	0	Troja et al.	R
58001.989	19.460	FLAMINGOS-2	Gemini-S	Ks	20.89	0.13	0	this Chapter	*,A
58001.992	19.463	VIMOS	VLT	z	23.37	0.48	0	Tanvir et al.	*
58002.979	20.450	FLAMINGOS-2	Gemini-S	H	>21.22	-	0	Kasliwal et al.	*
58002.979	20.450	VISIR	VLT	J8.9	>7.42	-	0	Kasliwal et al.	*
58003.969	21.440	HAWKI	VLT	Ks	21.46	0.08	0	Tanvir et al.	*
58003.989	21.460	FLAMINGOS-2	Gemini-S	Ks	>21.48	-	0	Kasliwal et al.	*
58007.969	25.440	HAWKI	VLT	Ks	22.06	0.22	0	Tanvir et al.	*
58007.989	25.460	FLAMINGOS-2	Gemini-S	J	>20.21	-	0	Kasliwal et al.	*
58010.969	28.440	FLAMINGOS-2	Gemini-S	Ks	>19.96	-	0	Kasliwal et al.	*

Table 4.3 – continued from previous page

MJD	Phase	Instrument	Telescope	Filter	AB Mag[a]	Err.	Δ(Mag)[b]	Ref.	Note[c]
58011.969	29.440	FLAMINGOS-2	Gemini-S	Ks	>20.60	-	0	Kasliwal et al.	*

Note: A complete table is available online in the original publication.

a: New magnitude value used in modeling.

b: Difference between new value and originally reported value.

c: Photometry listed with an "X" is not included in our model fit, photometry listed with an "O" has been visually flagged as an outlier, photometry reported in multiple sources with unique reduction routines are listed with an "'R", photometry generated by averaging repeated photometry is listed with an "A", and photometry used in modeling is listed with an "*".

Acknowledgments

We thank the anonymous referee and the larger community for valuable feedback on this work. The Berger Time-Domain Group at Harvard is supported in part by the NSF through grant AST-1714498, and by NASA through grants NNX15AE50G and NNX16AC22G. VAV acknowledges support by the National Science Foundation through a Graduate Research Fellowship. This research has made use of NASA's Astrophysics Data System.

Chapter 5

Spitzer Space Telescope Infrared Observations of the Binary Neutron Star Merger GW170817

This thesis chapter originally appeared in the literature as

V. A. Villar, P. Cowperthwaite, E. Berger et al., *The Astrophysical Journal* 862, L11

Abstract

We present *Spitzer Space Telescope* 3.6 and 4.5 μm observations of the binary neutron star merger GW170817 at 43, 74, and 264 days post-merger. Using the final observation as a template, we uncover a source at the position of GW170817 at 4.5 μm with a brightness of 22.9 ± 0.3 AB mag at 43 days and 23.8 ± 0.3 AB mag at 74 days (the

uncertainty is dominated by systematics from the image subtraction); no obvious source is detected at 3.6 μm to a 3σ limit of > 23.3 AB mag in both epochs. The measured brightness is dimmer by a factor of about $2-3$ times compared to our previously published kilonova model, which is based on UV, optical, and near-IR data at $\lesssim 30$ days. However, the observed fading rate and color ($m_{3.6} - m_{4.5} \gtrsim 0$ AB mag) are consistent with our model. We suggest that the discrepancy is likely due to a transition to the nebular phase, or a reduced thermalization efficiency at such late time. Using the *Spitzer* data as a guide, we briefly discuss the prospects of observing future binary neutron star mergers with *Spitzer*(in LIGO/Virgo Observing Run 3) and the *James Webb Space Telescope* (in LIGO/Virgo Observing Run 4 and beyond).

5.1 Introduction

The gravitational wave discovery of the binary neutron star (BNS) merger GW170817 (Abbott et al. 2017), and the subsequent identification of its electromagnetic counterpart (Abbott et al. 2017) provided the first multi-messenger view of a compact object merger and its aftermath. In the ultraviolet, optical, and near-infrared (hereafter, UVOIR) the emission was observed in the first month post-merger, before the source became sun-constrained (Andreoni et al. 2017; Arcavi et al. 2017; Coulter et al. 2017b; Cowperthwaite et al. 2017; Díaz et al. 2017; Drout et al. 2017; Evans et al. 2017; Hu et al. 2017; Kasliwal et al. 2017; Lipunov et al. 2017; Pian et al. 2017; Pozanenko et al. 2018; Smartt et al. 2017; Soares-Santos et al. 2017; Tanvir et al. 2017; Troja et al. 2017; Utsumi et al. 2017; Valenti et al. 2017; Villar et al. 2017a). This emission was produced by the radioactive decay of r-process nuclei synthesized in the merger ejecta, a so-called

kilonova (e.g., Li & Paczyński 1998; Rosswog et al. 1999; Metzger et al. 2010; Roberts et al. 2011; Metzger & Berger 2012; Barnes & Kasen 2013; Tanaka & Hotokezaka 2013).

From these observations, most authors concluded that GW170817 produced at least two distinct non-relativistic ejecta components: a rapidly-evolving "blue" component dominated by light r-process nuclei (atomic mass number $A < 140$) with a mass of ≈ 0.02 $M_\odot$ and a velocity of $\approx 0.3c$; and a more slowly-evolving "red" component dominated by heavy r-process elements ($A > 140$, including lanthanides) with a mass of ≈ 0.05 $M_\odot$ and a velocity of $\approx 0.15c$ (e.g., Villar et al. 2017a; although see Smartt et al. 2017; Waxman et al. 2017). The multi-component nature of the ejecta is also evident in optical and NIR spectroscopic observations (Chornock et al. 2017; Nicholl et al. 2017b; Pian et al. 2017; Shappee et al. 2017; Smartt et al. 2017). Subsequently, X-ray, radio, and optical observations of the non-thermal afterglow provided insight into the production of relativistic ejecta (Alexander et al. 2017b; Gottlieb et al. 2017; Haggard et al. 2017; Hallinan et al. 2017b; Lazzati et al. 2017; Margutti et al. 2017a; Troja et al. 2017; Alexander et al. 2018; D'Avanzo et al. 2018; Dobie et al. 2018; Lyman et al. 2018; Margutti et al. 2018a; Mooley et al. 2018; Nynka et al. 2018; Ruan et al. 2018; Troja et al. 2018).

At $\gtrsim 10$ days the kilonova spectral energy distribution (SED) peaked in the NIR, with a blackbody temperature of $\lesssim 1300$ K, and hence an expected substantial contribution into the mid-IR (Chornock et al. 2017; Nicholl et al. 2017b; Kasliwal et al. 2017). Here, we present the full set of *Spitzer Space Telescope* IR observations of GW170817, obtained at 43, 74, and 264 days post-merger, which extend the kilonova observations to 3.6 and 4.5 μm (see Lau et al. 2017); we uncover clear detections at 4.5 μm. In 5.2 we present the observations and our data analysis, image subtraction,

and photometry procedures. We compare the results to our kilonova models from Villar et al. (2017a) in 5.3. Motivated by the results, in 5.4 we discuss the prospects for IR observations of future events with *Spitzer*and the *James Webb Space Telescope* (JWST).

All magnitudes presented in this Chapter are given in the AB system and corrected for Galactic reddening with $E(B-V) = 0.105$ mag (Schlafly & Finkbeiner 2011). All uncertainties are reported at the 1σ level. We assume negligible reddening contribution from the host galaxy (Blanchard et al. 2017), and a luminosity distance to NGC 4993 of 40.7 Mpc (Cantiello et al. 2018).

5.2 Observations and Data Analysis

We downloaded public *Spitzer*(Werner et al. 2004) observations of GW170817 taken on 2017 September 29, 2017 October 30, and 2018 May 8 with the InfraRed Array Camera (IRAC; Fazio et al. 2004) in the 3.6 and 4.5 μm bands during the "warm" *Spitzer*mission (Director's Discretionary Time Program 13202; PI: Kasliwal); see Table 5.1. Each visit consisted of 466 frames with exposure times of 30 sec per frame, for a total on-source time of ≈ 3.9 hours in each band. We processed the images using standard procedures in `Mopex` (Makovoz & Marleau 2005) to generate mosaic images. `Mopex` cleans the images of cosmic rays and applies appropriate distortion corrections before drizzling the images. We used a drizzling factor of 0.8 and an output pixel scale of $0.4''$. We compare the native astrometry to seven 2MASS point sources in the field, and find that the astrometric solution is good to about 1 pixel.

We performed image subtraction with the `HOTPANTS` package (Alard 2000; Becker

2015), using the 2018 May 8 observations as a template in each band. We note that at 264 days post-merger, the emission from the relativistic ejecta (which dominates in the radio and X-ray bands) has $m_{3.6} = 25.9$ and $m_{4.5} = 25.7$ mag (Alexander et al. 2018; Margutti et al. 2018a; Xie et al. 2018), more than an order of magnitude below the expected brightness of the kilonova emission, and well below the detection level of the *Spitzer*data. A composite 3.6 and 4.5 μm image, and the subtracted 4.5 μm image at 43 days are shown in Figure 5.1. A point source is apparent in the difference image.

Although `HOTPANTS` computes and utilizes a spatially-variable convolution kernel, and is therefore able to match dissimilar point spread functions (PSFs), we find that the location of GW170817 is heavily contaminated by residual artifacts from the bright host galaxy. To remove the remaining contamination, we first mask the source location in the difference image with a region the size of the expected PSF (≈ 5 pixels). We then smooth the masked image with a Gaussian kernel, interpolating across the masked region. We use a kernel standard deviation of one pixel (but find that the kernel width has little effect on our results). We then subtract the smoothed image from the original difference image to isolate the point source. The resulting final 4.5 μm images from 43 and 74 days are shown in Figure 5.1 and clearly reveal the presence of a point source at the location of GW170817.

We measure the brightness of the source using both fixed aperture photometry and PSF-fitting assuming a Gaussian PSF. We injected fake point sources around the host galaxy at a similar offset to that of GW170817 to quantify the systematic uncertainties of the subtraction methods and photometry. For the observations with a detected source at the location of GW170817 (4.5 μm), we specifically injected fake sources of the same measured magnitude. For each injected source, we executed the same method of

smoothing and subtraction from a masked image. We used the spread in the recovered magnitudes as our overall uncertainty. For the observations without a significantly detected source (3.6 μm), we injected sources with a range of fluxes to determine 3σ upper limits. The results are summarized in Table 5.1. We additionally confirmed that the 4.5 μm detection is not an artifact of the subtraction process or the IRAC PSF by searching for sources at the same relative location as the GW170817 counterpart around a nearby saturated star within the field of view, following the same procedure. We did not find any significant sources around the star.

The detected source at 4.5 μm has 22.9 ± 0.3 mag at 43 days and 23.8 ± 0.3 mag at 74 days post-merger. The source is detected with a signal-to-noise ratio (SNR) of ≈ 10 at 43 days and ≈ 5 at 74 days. However, the final uncertainties are dominated by systematic effects, as determined from the spread in magnitudes for the injected fake point sources. We do not detect a source at 3.6 μm in either epoch to a 3σ limit of $\gtrsim 23.3$ mag. The exact significance of our (non)detections may be better constrained through other methods (e.g., Zackay et al. 2016).

5.3 Comparison to a Kilonova Model

We compare the observations to our three-component kilonova model, which was previously used to fit all available UVOIR photometry (Villar et al. 2017a); see Figure 5.2. Each component is characterized by a unique gray opacity roughly corresponding to its lanthanide fraction (Tanaka et al. 2018), and is independently described by a blackbody SED. The blackbody SEDs cool as a function of time until they reach a minimal "temperature floor", at which point we assume that the photosphere

recedes into the ejecta, at a constant temperature. At late times ($\gtrsim$ 10 days), our three-component model predicts that the light curve is dominated by the intermediate r-process component and that this component has reached its temperature floor of $\approx$ 1300 K, somewhat cooler than the lowest lanthanide ionization temperature (e.g., Kasen et al. 2013).

We find that our model over-predicts the *Spitzer*measurements at 43 and 74 days by about a factor of ≈ 3 (1.2 mag) and ≈ 2.5 (1 mag), respectively (Figure 5.2). However, the decline rate between the two measurements is in good agreement with the model prediction. Similarly, the temperature implied by the flat or red color in the 3.6 and 4.5 μm bands ($\lesssim$ 1200 K) is consistent with the temperature floor in our model. We observe a similar late-time deviation from our model in the K_s-band (2.2 μm) at $\gtrsim$ 20 days.

Assuming a blackbody SED with $T = 1200$ K we find that the bolometric luminosity implied by the 4.5 μm detections is $\approx 6 \times 10^{38}$ erg s^{-1} and $\approx 2 \times 10^{38}$ erg s^{-1}at 43 and 74 days, respectively. This is consistent with the drop off in bolometric luminosity starting at $\approx$ 10 days, when the estimated bolometric luminosity is $\approx 2 \times 10^{40}$ erg s^{-1} (Cowperthwaite et al. 2017; Arcavi 2018; Waxman et al. 2017)

Relaxing some of the assumptions in our model may eliminate the brightness discrepancy. For example, at the time of the *Spitzer*observations the kilonova is likely transitioning into the nebular phase, and the blackbody SED approximation may break down. Using the parameters of the dominant intermediate-opacity component of our model (Villar et al. 2017a), we find that at 43 days the optical depth is $\tau \approx 1$, suggesting that the ejecta are becoming optically thin. Additionally, the shape of the late-time light curve is also dictated by the time-dependent thermalization efficiency of the merger

ejecta (Barnes et al. 2016). A steeper decline of the thermalization efficiency at $\gtrsim 20$ days will better capture the lower observed fluxes in the K_s and *Spitzer*bands. The thermalization is highly dependent on the nuclear mass models assumed (see e.g., Barnes et al. 2016; Rosswog et al. 2017), and is uncertain by almost an order of magnitude at $\gtrsim 1$ month. Our observations would imply an efficiency of $f_{\rm tot} \lesssim 0.1$ at $t > 40$ days.

We also consider the possibility that the observed IR emission is due to reprocessing of bluer kilonova emission by newly formed dust. The warm temperature implied by our observations requires carbon-based dust, due to its high condensation temperature ($T_c \approx 1800$ K; Takami et al. 2014). We fit a modified blackbody to the *Spitzer*photometry at day 43, assuming $m_{3.5} \approx m_{4.5}$ (following Equations 1 and 2 of Gall et al. 2017). We find that the carbon dust mass required to reproduce the observed luminosity is $\approx 5 \times 10^{-7}$ M$_\odot$. However, Gall et al. (2017) explored a range of theoretical kilonova wind models and found that at most $\sim 10^{-9}$ M$_\odot$ of carbon dust can be produced. We therefore conclude that the observed IR emission is not due to dust reprocessing.

5.4 Implications for IR Observations of Future BNS Mergers

The *Spitzer*detections of GW170817 at 43 and 74 days post-merger indicate that future BNS mergers should be observed at IR wavelengths. Indeed, taking our models at face value, at least in the well-characterized regime at $\lesssim 20$ days, it appears that the peak of the kilonova emission shifts into the NIR/MIR bands at $\gtrsim 10$ days. This suggests that significant effort should be focused on robust characterization of the IR

emission of kilonovae. This will provide numerous benefits, including more accurate determination of the bolometric luminosity and therefore total r-process ejecta mass, improved measurements of the r-process opacity at long wavelengths, observational constraints on the late-time thermalization efficiency, and continued insight into BNS mergers as sites of cosmic r-process production.

Advanced LIGO/Virgo (ALV) Observing Run 3 (O3) is expected to begin in early 2019 and span a full year, with an expected BNS merger detection distance of ≈ 120 Mpc. The timing of O3 overlaps favorably with *Spitzer*Cycle 14 (the final *Spitzer*cycle), and the sensitivity should be sufficient to detect events with a similar IR luminosity to GW170817 in the first ≈ 40 days to ≈ 120 Mpc. For example, observations of about 9 hours on-source can achieve 5σ limiting magnitudes of $m_{3.6} \approx 25.5$ mag and $m_{4.6} \approx 25$ mag, assuming no significant contamination from host galaxy subtraction. In reality, host galaxy contamination may prove to be problematic for dim events to the $\approx 10\%$ photometry level. A full exploration of these systematics is not possible with only one observed event.

Beyond O3 (2021 and later), the ALV network is expected to achieve design sensitivity, with typical BNS merger detections to ≈ 200 Mpc and a maximal detection distance of ≈ 450 Mpc (for favorably oriented and positioned BNS mergers). The timing is ideal for overlap with JWST, which will be able to provide NIR and MIR spectra. In the NIR, NIRSpec can produce low-resolution ($R \approx 100$) spectra at $0.6 - 5.3$ μm; this resolution is sufficient for kilonovae given the typical velocities of $\sim 0.1 - 0.3c$. In particular, spectra with SNR $\gtrsim 50$ can be obtained near peak for a GW170817-like kilonova to 450 Mpc in just 1 hour of on-source time. At later times, BNS mergers could be tracked to ≈ 40 days at ≈ 200 Mpc with SNR ≈ 10 in about 6 hours of on-source

time.

In the MIR, the Mid-Infrared Instrument (MIRI) can produce low-resolution ($R \approx 40$–160) spectra covering $5 - 14$ μm. In particular, SNR $\approx 10 - 20$ at $5 - 9$ μm (and lower SNR at longer wavelengths) can be achieved for a GW170817-like kilonova near peak to ≈ 450 Mpc with ≈ 5 hours of on-source time. At late times (≈ 40 days), MIRI can produce SNR ≈ 5 spectra at $5 - 7$ μm to ≈ 100 Mpc.

We do not yet know the full range of brightnesses and SEDs of kilonovae, as well as the potential contribution of dust reprocessing, but the discussion above illustrates that NIR/MIR characterization of kilonovae can be achieved with *Spitzer*in ALV O3 and with JWST when ALV reaches design sensitivity. This can be achieved with a modest time investment, but will require target-of-opportunity response to BNS mergers.

5.5 Conclusions

We present *Spitzer*IR observations of the kilonova associated with GW170817 spanning to 264 days post-merger. We detect the kilonova at 4.5 μm at 43 and 74 days post-merger with a brightness of ≈ 22.9 and ≈ 23.8 mag, respectively. We do not identify a confident detection at 3.6 μm, to a 3σ upper limit of $\gtrsim 23.3$ mag. The inferred color of the kilonova indicates that the ejecta has cooled to $\lesssim 1200$ K at these late times. These magnitudes are fainter than an extrapolation of our model to the UVOIR data at $\lesssim 30$ days, highlighting the need for improved models at late times (for example, the details of the ejecta thermalization). Finally, we show that future BNS mergers with kilonovae similar to GW170817 will be detectable with *Spitzer*to 120 Mpc at 40 days post-merger,

and will be accessible to NIR and MIR spectroscopy with JWST to ≈ 450 Mpc at peak and to $\approx 100-200$ Mpc at 40 days post-merger (and to later times with JWST imaging).

Acknowledgments

We thank B. Metzger for useful discussions and an anonymous referee for constructive feedback. The Berger Time-Domain Group at Harvard is supported in part by the NSF through grant AST-1714498, and by NASA through grants NNX15AE50G and NNX16AC22G. This work is based in part on observations made with the *Spitzer Space Telescope*, which is operated by the Jet Propulsion Laboratory, California Institute of Technology under a contract with NASA.

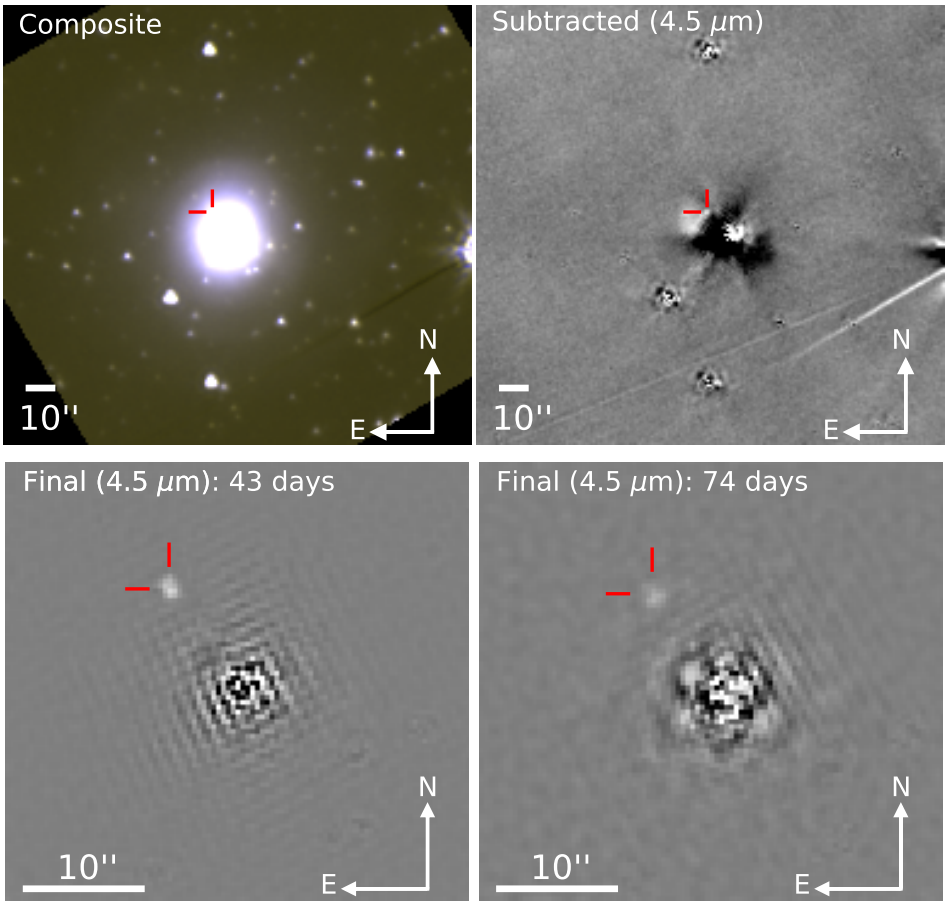

Figure 5.1: *Upper Left: Spitzer*3.6 and 4.5 μm color composite image from the observations on 2017 September 29 (43 days post-merger). The location of GW170817 is marked by the red cross hairs. *Upper Right:* Residual from `HOTPANTS` image subtraction of the 4.5 μm images at 43 and 264 days. While a point source is visible at the position of GW170817, its location is contaminated by subtraction residuals from the host galaxy. *Bottom:* Residual images (Left: 43 days; Right: 74 days) after subtracting a masked and smoothed version of the image from itself (see Section 5.2). An isolated point source is clearly visible at the location of GW170817.

Table 5.1:: *Spitzer*/IRAC Observations and Photometry of GW170817

UT Date	Epoch (days)	λ (μm)	Magnitude
2017 Sep 29	43	3.6	> 23.3
2017 Sep 29	43	4.5	22.9 ± 0.3
2017 Oct 30	74	3.6	> 23.3
2017 Oct 30	74	4.5	23.8 ± 0.3
2018 May 8	264	3.6	Template
2018 May 8	264	4.5	Template

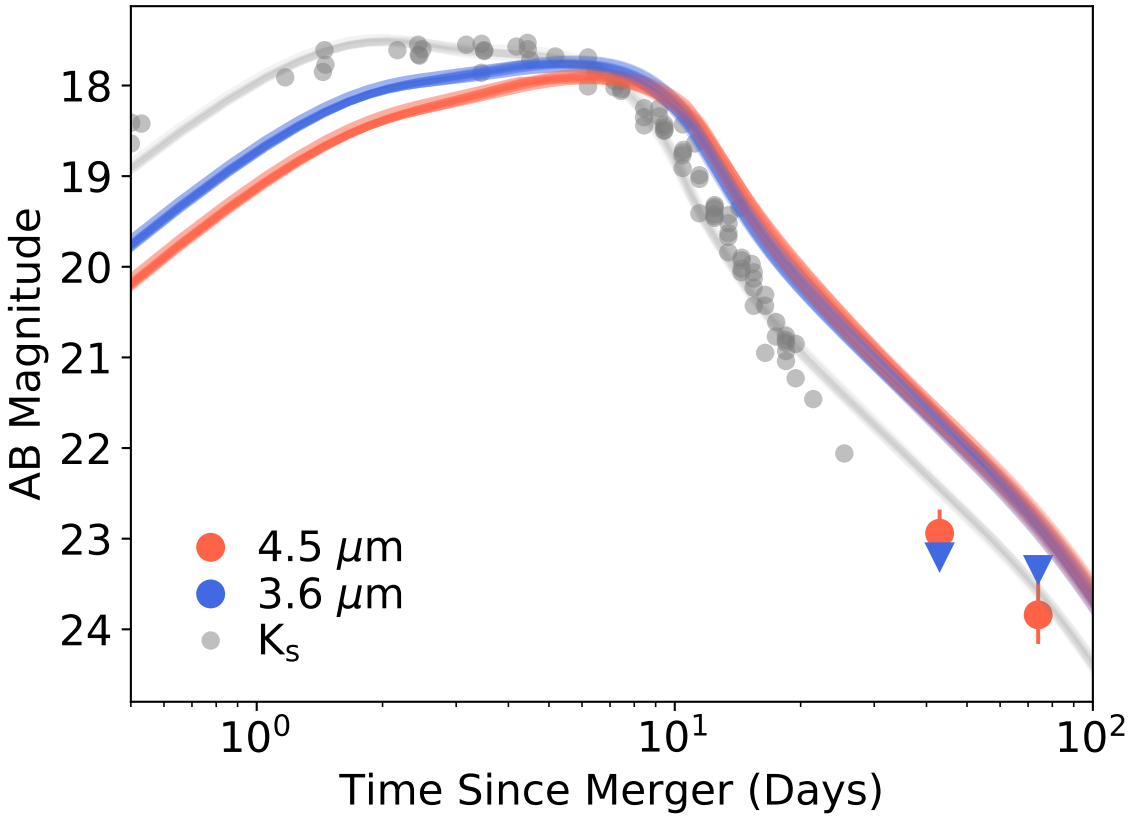

Figure 5.2: *Spitzer*data at 3.6 μm (blue) and 4.5 μm (red); upper limits are marked as triangles. Also shown are light curves from our model fit to the complete UVOIR data set at $\lesssim$ 30 days (Villar et al. 2017a). For comparison we also show the K_s-band (2.2 μm) data and model (gray; Cowperthwaite et al. 2017; Drout et al. 2017; Kasliwal et al. 2017; Smartt et al. 2017; Tanvir et al. 2017; Troja et al. 2017; Utsumi et al. 2017; Villar et al. 2017a).

Chapter 6

Superluminous Supernovae in LSST: Rates, Detection Metrics, and Light Curve Modeling

This thesis chapter originally appeared in the literature as

V. A. Villar, M. Nicholl, E. Berger, *The Astrophysical Journal* 869, 166

Abstract

We explore and demonstrate the capabilities of the upcoming Large Synoptic Survey Telescope (LSST) to study Type I superluminous supernovae (SLSNe). We first fit the light curves of 58 known SLSNe at $z \approx 0.1 - 1.6$, using an analytical magnetar spin-down model implemented in `MOSFiT`. We then use the posterior distributions of the magnetar and ejecta parameters to generate thousands of synthetic SLSN light curves, and we

inject those into the LSST Operations Simulator (OpSim) to generate realistic *ugrizy* light curves. We define simple, measurable metrics to quantify the detectability and utility of the light curve, and to measure the efficiency of LSST in returning SLSN light curves satisfying these metrics. We combine the metric efficiencies with the volumetric rate of SLSNe to estimate the overall discovery rate of LSST, and we find that $\approx 10^4$ SLSNe per year with > 10 data points will be discovered in the Wide-Fast-Deep (WFD) survey at $z \lesssim 3.0$, while only ≈ 15 SLSNe per year will be discovered in each Deep Drilling Field at $z \lesssim 4.0$. To evaluate the information content in the LSST data, we refit representative output light curves with the same model that was used to generate them. We correlate our ability to recover magnetar and ejecta parameters with the simple light curve metrics to evaluate the most important metrics. We find that we can recover physical parameters to within 30% of their true values from $\approx 18\%$ of WFD light curves. Light curves with measurements of both the rise and decline in *gri*-bands, and those with at least fifty observations in all bands combined, are most information rich, with $\approx 30\%$ of these light curves having recoverable physical parameters to $\approx 30\%$ accuracy. WFD survey strategies which increase cadence in these bands and minimize seasonal gaps will maximize the number of scientifically useful SLSN light curves. Finally, although the Deep Drilling Fields will provide more densely sampled light curves, we expect only ≈ 50 SLSNe with recoverable parameters in each field in the decade-long survey.

6.1 Introduction

Type I Superluminous supernovae (SLSNe) are an observationally-classified class of transients that typically reach a peak absolute magnitude of $\lesssim -20$ mag and display

unique early-time spectra with OII absorption superposed on a hydrogen-free blue continuum (Chomiuk et al. 2011; Quimby et al. 2011; Gal-Yam 2012). These events also typically exhibit long durations, with a time to rise and decline by one magnitude of $t_{\rm dur} \gtrsim 50$ days, allowing them to radiate $\approx 10^{51}$ erg in the optical/UV, comparable to the kinetic energies of normal core-collapse SNe. Despite their high luminosities and long durations, SLSNe are a relatively recent discovery due to the advent of untargeted wide-field time-domain surveys. These surveys are essential due to the low volumetric rate and low-luminosity host galaxies of SLSNe (Neill et al. 2010; Lunnan et al. 2014; Chen et al. 2017a; Leloudas et al. 2015; Angus et al. 2016; Perley et al. 2016; Schulze et al. 2018).

There is ongoing debate about the energy source of SLSNe. Unlike hydrogen-rich Type II SLSNe which appear to be powered by interaction with a dense circumstellar medium (Chevalier & Irwin 2011), such interaction is disfavored as the dominant heating source for Type I SLSNe, due to the exceptionally large CSM mass required to reproduce the bright observed light curves (Moriya et al. 2018), coupled with low-density environments suggested by X-ray (Margutti et al. 2017) and radio (Nicholl et al. 2016a; Coppejans et al. 2018) observations. Instead, a central engine model is preferred, and it appears to explain the light curve shapes and diversity (Nicholl et al. 2017), early-time spectra (e.g., Dessart et al. 2012; Howell et al. 2013; Mazzali et al. 2016), and the velocity and density structures inferred from nebular spectra (Nicholl et al. 2016b; Jerkstrand et al. 2017; Nicholl et al. 2018).

Currently, the best central engine candidate to power SLSNe is a rapidly spinning *magnetar*, or a pulsar with a strong magnetic field ($B \gtrsim 10^{13}$ G; Kasen & Bildsten 2010; Woosley 2010; Inserra et al. 2013; Chatzopoulos et al. 2013; Metzger et al. 2015; Nicholl

et al. 2017). The magnetar model can explain the diversity of SLSN light curves (Nicholl et al. 2017; Villar et al. 2017b), and the inferred velocities and temperatures (Moriya et al. 2018). Recently, Nicholl et al. 2017 fit a sample of 38 well-observed SLSNe with a semi-analytical magnetar model and found that this model is able to reproduce the observed light curves using a fraction of parameter space (see also, Nicholl et al. 2015b; Prajs et al. 2016; Yu et al. 2017; Liu et al. 2017).

Statistical population studies like these are essential for mapping the properties of SLSNe. Currently, about 10 SLSNe are discovered per year (Guillochon et al. 2017)[1], and this low rate allows for detailed spectroscopic follow-up of each event. However, future surveys will lead to a substantial increase in the discovery rate. For example, Tanaka et al. (2012) and Tanaka et al. (2013) explored several future optical and near-infrared (NIR) surveys, concluding that missions like WFIRST and LSST will find $\sim 10^2 - 10^4$ SLSNe per year. Due to limited spectroscopic resources, it is essential to explore what information can be obtained about these large samples from light curves alone; namely, their diverse observational properties (Nicholl et al. 2015b), progenitor populations (Lunnan et al. 2014), host galaxies (Berger et al. 2012; Schulze et al. 2018), and potentially cosmological parameters (Inserra & Smartt 2014; Scovacricchi et al. 2015).

Here, we explore and study the characteristics of SLSNe observed by the upcoming Large Synoptic Survey Telescope (LSST), an 8.4-m diameter telescope with a 9.6 deg^2 field-of-view that will conduct several 10-year wide-field surveys across the Southern hemisphere in the *ugrizy* filters. The current LSST observing strategy spends the

[1]See `sne.space`.

majority ($\gtrsim 90\%$) of the time executing the Wide-Fast-Deep (WFD) survey, covering 18,000 deg^2 with a cadence of roughly four days in any filter and ten days in a specific filter, and with a per-visit limiting magnitude of $m_{\rm lim,gr} \approx 24.5$ mag. About 5% of the observing time will focus on several Deep Drilling fields (DDFs), each comprised of a single pointing (9.6 deg^2) with five times more cumulative imaging than a typical field in the WFD survey and with a nightly stack limiting magnitude of $m_{\rm lim,gr} \approx 26.5$ mag. The remaining time will be split between the Galactic Plane and South Celestial Pole surveys. We focus on the WFD survey and DDFs in this study (see LSST Science Collaboration et al. 2017 for technical details).

The large survey area, cadence and depth make LSST a potential powerhouse for time-domain astronomy, particularly in the case of volumetrically-rare events like SLSNe. However, there are two key questions that must be addressed to maximize the potential of LSST. First, it is essential to quantify the number of SLSNe that LSST will discover, their redshift distribution, and their observational properties. Second, it is vital to predict the information content from LSST light curves alone to account for cases which will lack spectroscopic follow up. In this work we perform the first detailed study of SLSNe discovered with LSST using an observationally-motivated suite of SLSN models and a realistic observational simulator provided by the LSST collaboration.

The Chapter is structured as follows. In §6.2, we outline the simulations used to produce realistic SLSN light curves as they would appear in the LSST WFD survey and DDFs. In §6.3, we describe the characteristics of the SLSNe discovered by LSST based on our simulation results. In §6.4, we discuss the ability to recover physical parameters from the LSST light curves, and quantify the information content of the simulated light curves. We conclude in §6.5. All magnitudes are reported in the AB system, and

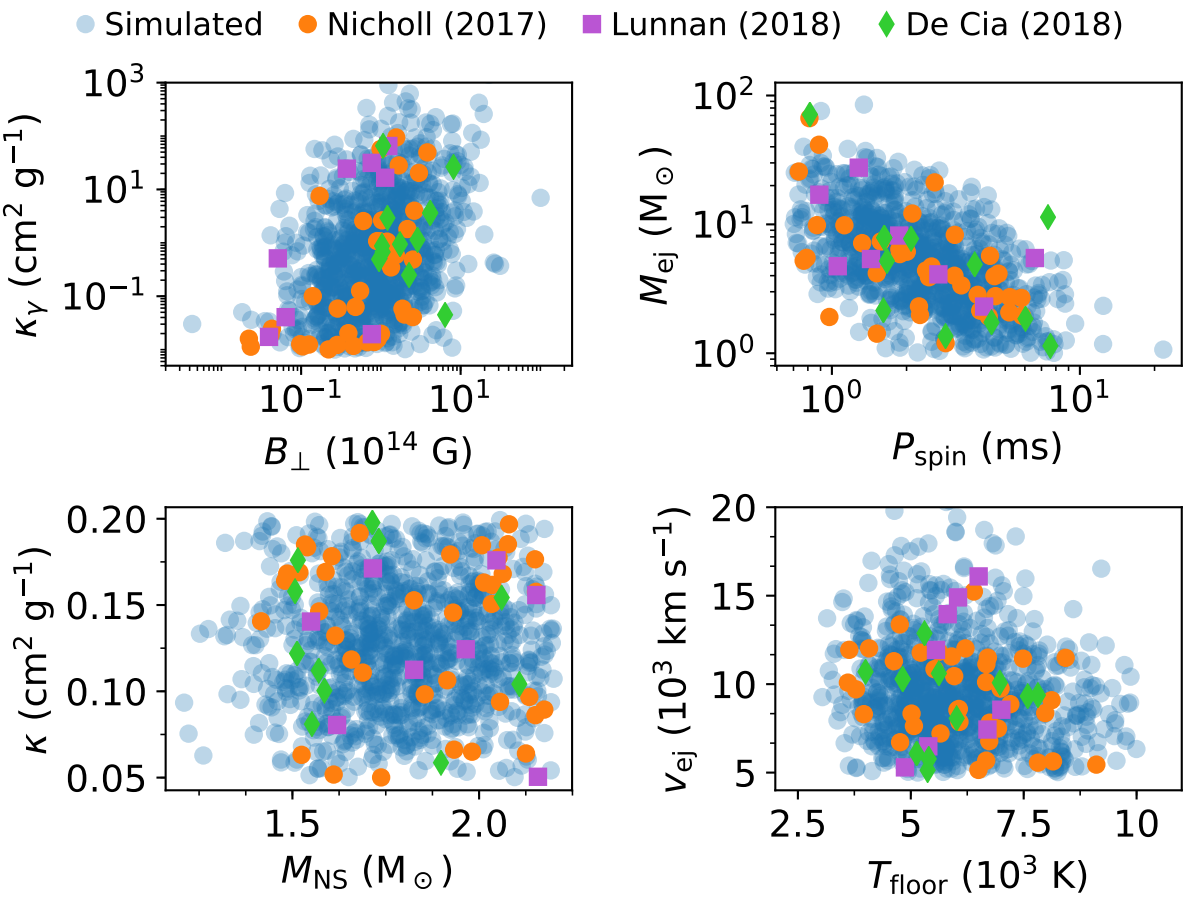

Figure 6.1: A subset of the model parameters for the SLSN magnetar model, showing the results for the observed sample (orange circles: Nicholl et al. 2017; purple squares: Lunnan et al. 2018; green diamonds; De Cia et al. 2017), and our simulated population (blue circles). The simulated sample captures intrinsic correlations between parameters (including nuisance parameters) that are seen within the observed population.

we assume a standard cosmology, with $H_0 = 67.7$ km s^{-1} Mpc^{-1}, $\Omega_M = 0.307$, and $\Omega_\Lambda = 0.691$ (Planck Collaboration et al. 2016).

6.2 Simulation Set-Up

To simulate the observable SLSN population in the LSST surveys we construct a sample of light curve models and inject these into the LSST Operations Simulator (`OpSim`). We describe these steps in the following subsections.

6.2.1 Constructing Simulated SLSN Light Curves

We construct a sample of simulated light curves based on known events from the literature. Several studies have previously aggregated SLSN light curves (e.g. Nicholl et al. 2015b; Prajs et al. 2017; Liu et al. 2017; De Cia et al. 2017; Lunnan et al. 2018). Recently, Nicholl et al. (2017) uniformly modeled a sample of 38 SLSNe requiring the events to be spectroscopically classified and to have some photometric data near peak. As such, the sample spans a range of peak luminosities and light curve timescales. Here we combine the sample of Nicholl et al. (2017) with 12 events discovered by the Palomar Transient Factory (PTF; De Cia et al. 2017) and 8 events discovered in the Pan-STARRS1 Medium Deep Survey (PS1-MDS; Lunnan et al. 2018), leading to 58 spectroscopically classified SLSNe spanning a wide range of observational properties (see Table 6.1).

We model the 21 PTF and PS1-MDS SLSNe with the same model described in Nicholl et al. (2017). In short, we use the open-source code `MOSFiT` (Guillochon et al. 2018) to fit a magnetar spin-down model to the multi-band light curves. We assume a modified blackbody spectral energy distribution (SED) in which flux is linearly suppressed below a "cutoff" frequency of 3000Å. This SED shape is consistent with

observed SEDs (Chomiuk et al. 2011; Nicholl et al. 2016, but see also Yan et al. 2018 who argue that more UV variation is seen in SLSN SEDs). We remove data in which a pre-peak "bump" is observed (see Nicholl & Smartt 2016). Our model additionally assumes a one-zone treatment of the ejecta and a grey opacity dominated by electron scattering, both assumptions being typical during the photospheric phase. Several choices, such as the precise definition of spin-down time, lead to additional uncertainties that can affect best-fit values to the tens of percent level (see Nicholl et al. 2017 for detailed discussion). In this work, we explore only our ability to recover known model parameters. Our best-fit parameters and their 1σ error bars are provided in Table 6.3.

We use the sample of 58 fitted events to generate our simulated SLSN light curves. Because drawing walkers directly from the model posteriors would lead to undersampling of the parameter space, we sample from a model of the underlying population distribution as follows. We draw one walker from the posterior of each event to create a distribution of the model parameters of the underlying population. We fit this distribution to a truncated multivariate log-Gaussian which allows us to capture the correlations between parameters observed in the sample events. We place physically-motivated limits on the parameters, as listed in Table 6.2. We then draw samples from the population distribution to generate 1,000 events per redshift bin of $\Delta z = 0.1$ from $z = 0.1$ to $z = 6.0$. Finally, from this sample we eliminate events with $M_{\rm r} > -20$ mag; although these magnetar-powered events may exist in nature, they are not necessarily distinguishable from the broader population of Type I SNe. The parameters for the modeled SLSNe and for our simulated events are shown in Figure 6.1.

Table 6.1:: Type I SLSNe Used in this Analysis

Name	Redshift	Reference	Name	Redshift	Reference
PTF11hrq	0.057	De Cia et al. (2017)	PTF09cwl*	0.350	Quimby et al. (2011)
PTF10hgi*	0.099	Inserra et al. (2013)			De Cia et al. (2017)
		De Cia et al. (2017)	SN2006oz*	0.376	Leloudas et al. (2012)
Gaia16apd*	0.102	Yan et al. (2017a)	PTF13cjq	0.396	De Cia et al. (2017)
		Nicholl et al. (2017)	PTF13bdl	0.403	De Cia et al. (2017)
		Kangas et al. (2017)	iPTF13dcc*	0.431	Vreeswijk et al. (2017)
PTF12hni	0.106	De Cia et al. (2017)			De Cia et al. (2017)
PTF12dam*	0.107	Nicholl et al. (2013)	PTF10vqv	0.452	De Cia et al. (2017)
		Chen et al. (2015)	PTF09atu*	0.502	Quimby et al. (2011)
		De Cia et al. (2017)			De Cia et al. (2017)
		Vreeswijk et al. (2017)	PS1-14bj*	0.522	Lunnan et al. (2016)
SN2015bn*	0.114	Nicholl et al. (2016a)			Lunnan et al. (2018)
		Nicholl et al. (2016b)	PS1-12bqf	0.522	Lunnan et al. (2018)
PTF10nmn	0.124	De Cia et al. (2017)	PS1-11ap*	0.524	McCrum et al. (2013)
SN2007bi*	0.128	Gal-Yam et al. (2009)			Lunnan et al. (2018)

Table 6.1 – continued from previous page

Name	Redshift	Reference	Name	Redshift	Reference
SN2011ke*	0.143	Inserra et al. (2013)	DES14X3taz*	0.608	Smith et al. (2016a)
		De Cia et al. (2017)	PS1-10bzj*	0.650	Lunnan et al. (2013)
SSS120810*	0.156	Nicholl et al. (2014)			Lunnan et al. (2018)
PTF10bfz	0.170	De Cia et al. (2017)	DES13S2cmm*	0.663	Papadopoulos et al. (2015)
SN2012il*	0.175	Inserra et al. (2013)	PS1-11bdn	0.738	Lunnan et al. (2018)
PTF12gty	0.177	De Cia et al. (2017)	iPTF13ajg*	0.740	Vreeswijk et al. (2014)
PTF11rks*	0.192	Inserra et al. (2013)			De Cia et al. (2017)
		De Cia et al. (2017)	PS1-13gt	0.884	Lunnan et al. (2018)
PTF10aagc	0.207	De Cia et al. (2017)	PS1-10awh*	0.908	Chomiuk et al. (2011)
iPTF15esb*	0.224	Yan et al. (2017b)			Lunnan et al. (2018)
SN2010gx*	0.230	Pastorello et al. (2010)	PS1-10ky*	0.956	Chomiuk et al. (2011)
		Quimby et al. (2011)			Lunnan et al. (2018)
		De Cia et al. (2017)	PS1-11aib	0.997	Lunnan et al. (2018)
SN2011kf*	0.245	Inserra et al. (2013)	PS1-10ahf*	1.1	McCrum et al. (2015)
iPTF16bad*	0.247	Yan et al. (2017b)			Lunnan et al. (2018)

Table 6.1 – continued from previous page

Name	Redshift	Reference	Name	Redshift	Reference
LSQ14mo*	0.253	Chen et al. (2017b)	SCP-06F6*	1.190	Barbary et al. (2008)
LSQ12dlf*	0.255	Nicholl et al. (2014)	PS1-10pm*	1.206	McCrum et al. (2015)
		De Cia et al. (2017)			Lunnan et al. (2018)
PTF09cnd*	0.258	Quimby et al. (2011)	PS1-11tt	1.283	Lunnan et al. (2018)
SN2013dg*	0.265	Nicholl et al. (2014)	PS1-11afv	1.407	Lunnan et al. (2018)
PTF13bjz	0.271	De Cia et al. (2017)	SNLS-07D2bv*	1.50	Howell et al. (2013)
SN2005ap*	0.283	Quimby et al. (2007)	PS1-13or	1.52	Lunnan et al. (2018)
PTF10uhf	0.288	De Cia et al. (2017)	PS1-11bam*	1.565	Berger et al. (2012)
PTF12mxx	0.327	De Cia et al. (2017)	PS1-12bmy	1.572	Lunnan et al. (2018)
iPTF13ehe*	0.343	Yan et al. (2015)			Lunnan et al. (2018)
		De Cia et al. (2017)	SNLS-06D4eu*	1.588	Howell et al. (2013)
LSQ14bdq*	0.345	Nicholl et al. (2015a)			

*Best fit magnetar parameters presented in Nicholl et al. 2017.

The resulting r-band peak-luminosity function of our simulated events and the observed sample are shown in Figure 6.2. Our simulated luminosity function is consistent with that derived by Nicholl et al. 2017. We do not attempt to correct for any potential observational biases within the various surveys, as we expect these effects to be small relative to the overall uncertainty in the volumetric rate (approximately a factor $\approx 3-5$; see Quimby et al. 2013; McCrum et al. 2015; Prajs et al. 2016 and §6.4). Similarly, we show the duration distribution of the known SLSNe and of our simulated events in Figure 6.3, finding a good agreement between the two.

Table 6.2:: Model Parameters and Imposed Limits Parameters described in detail in Nicholl et al. 2017.

*Indicates limits well within the tail of the Gaussian distribution.

Parameter	Mini	Max
$P_{\rm spin}$/ms	0.7	100*
$B_{\perp}/10^{14}$ G	10^{-2}*	10
$M_{\rm ej}/{\rm M}_{\odot}$	1	100*
$v_{\rm ej}/10^{4}$ km s^{-1}	0.5	100*
κ/ g cm^{-2}	0.05	0.2
κ_{γ}/ g cm^{-2}	10^{-2}	10^{3}
$M_{\rm NS}/{\rm M}_{\odot}$	1.4	2.2
$T_{\rm floor}/10^{3}$ K	0.1*	50*

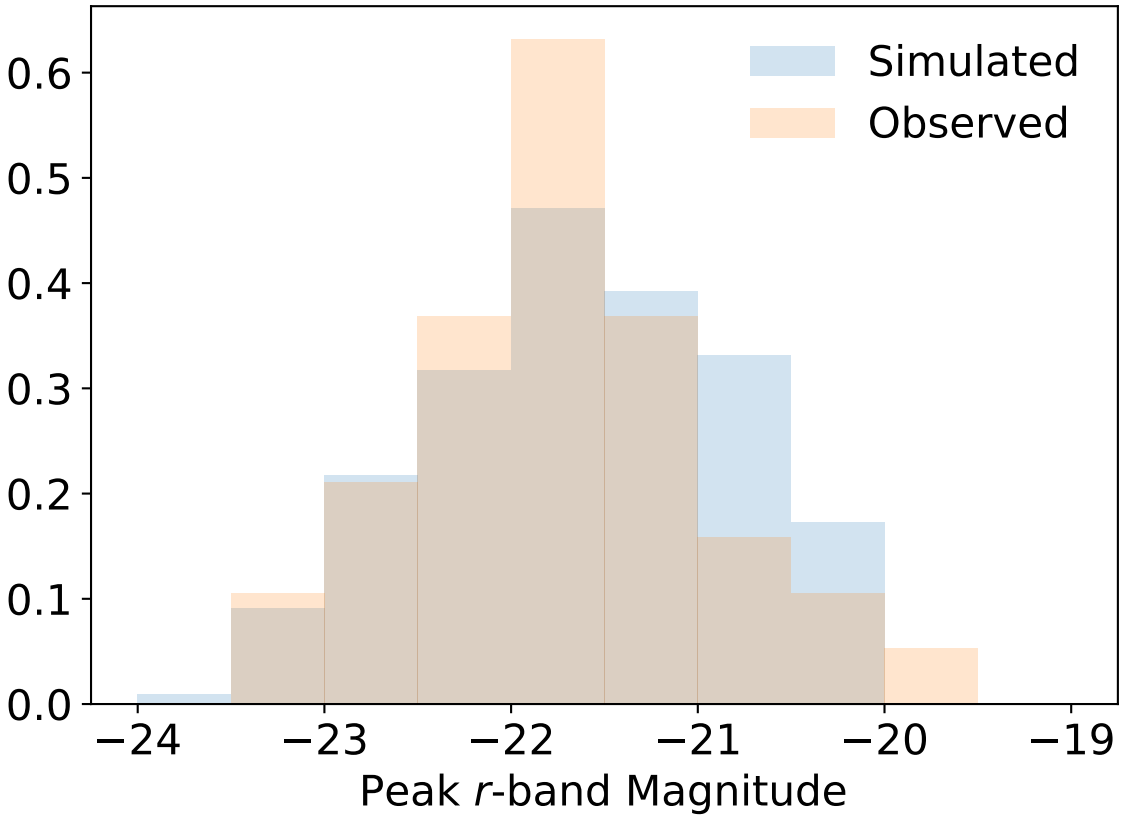

Figure 6.2: Observed (orange) and simulated (blue) r-band peak luminosity function for SLSNe. The luminosity functions are in good agreement, with only $\approx 5\%$ of our models extending to brighter r-band peak luminosities ($M_r \lesssim -23$) than currently observed.

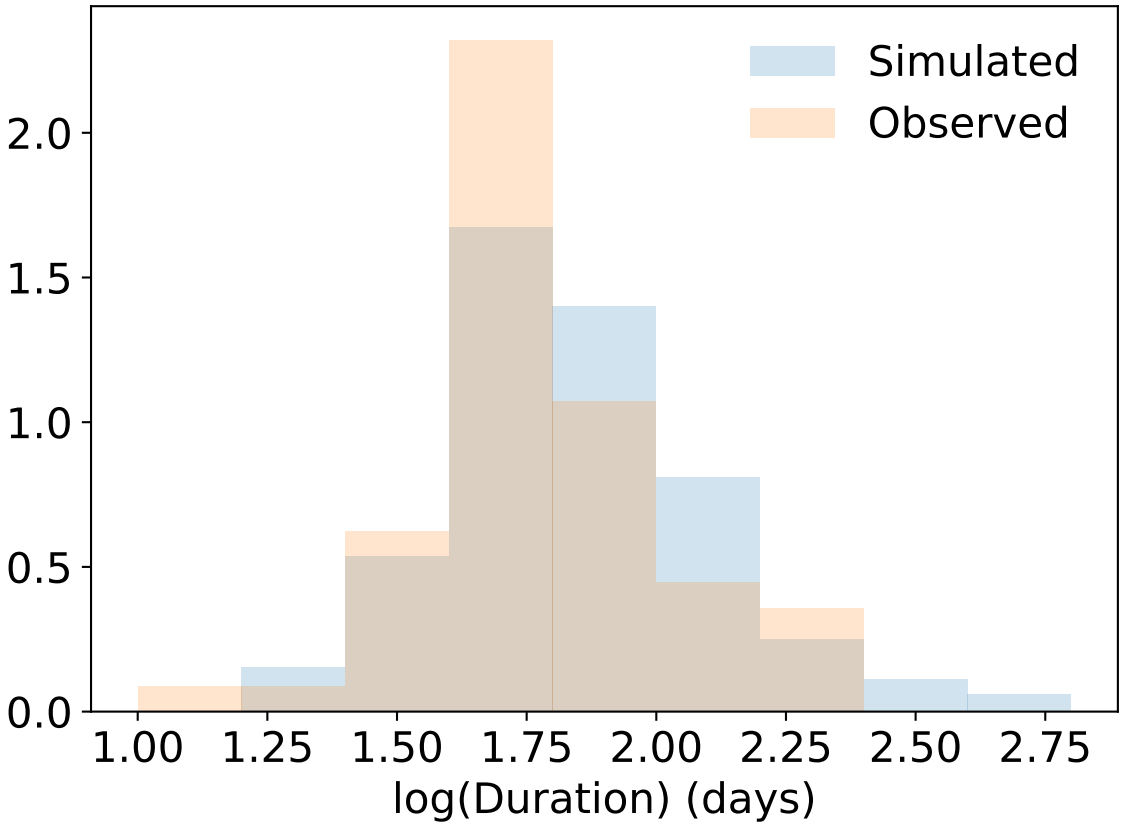

Figure 6.3: Same as Figure 6.2 but for the r-band duration ($t_{\rm dur}$) of the observed (orange) and simulated (blue) SLSNe. The duration distributions are in good agreement, with only $\approx 2\%$ of our models extending to durations longer than those in our observed sample.

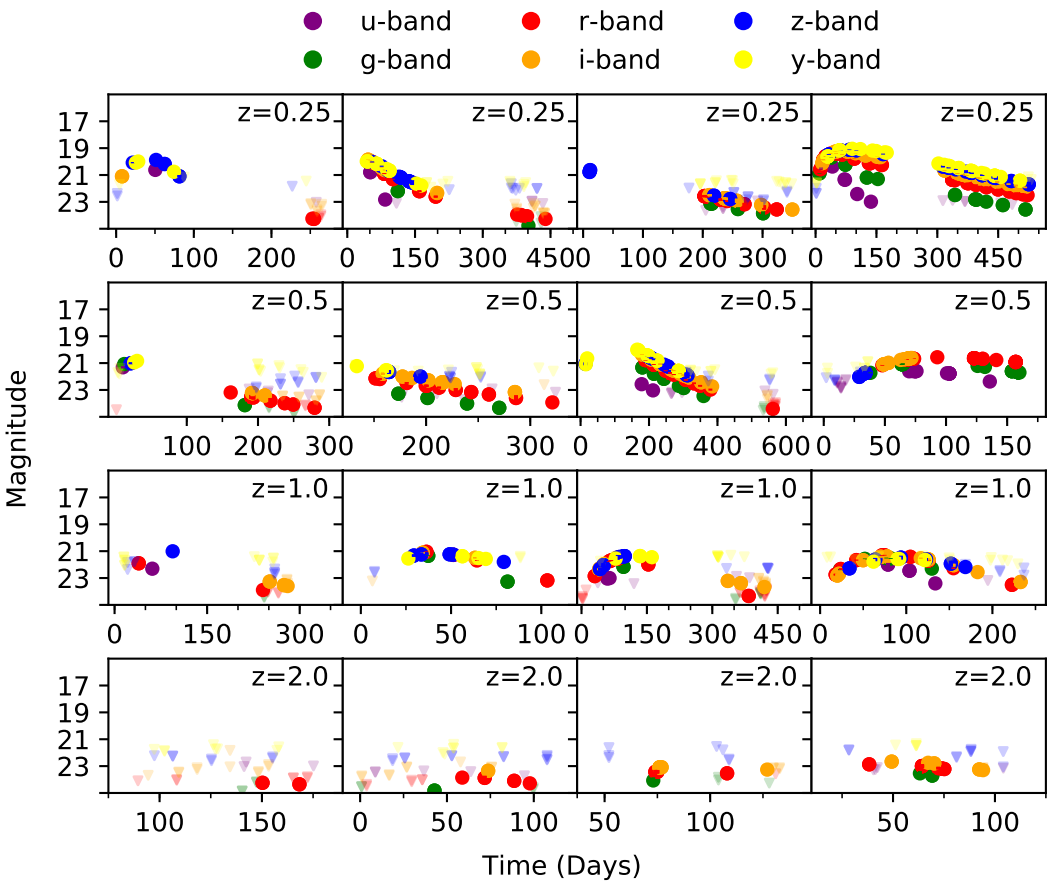

Figure 6.4: Sample *ugrizy* LSST light curves from `OpSim` at four representative redshifts. For each redshift, the light curves are ordered by the number of observations, with the left-most representing the bottom 10th percentile, the two middle panels representing the 50th percentile, and the right-most panel representing the 90th percentile.

Table 6.3:: SLSNe Parameters for Events Modeled in this Chapter

Object	z	P	B	$M_{\rm ej}$	$v_{\rm ph}$	$E_{\rm min}$	κ	κ_γ	$M_{\rm NS}$	$T_{\rm f}$	$A_{\rm V}$	σ	WAIC*
		(ms)	10^{14} G	$M_\odot$	10^3 km s^{-1}	10^{51} erg	cm^{2}g^{-1}	cm^{2}g^{-1}	$M_\odot$	10^3 K	mag	mag	
PS1-11afv	1.41	$1.63^{+0.57}_{-0.68}$	$0.20^{+0.29}_{-0.15}$	$4.36^{+4.75}_{-1.85}$	$11.21^{+2.23}_{-1.97}$	$8.25^{+7.52}_{-3.87}$	$0.14^{+0.04}_{-0.05}$	$0.97^{+10.94}_{-0.92}$	$1.87^{+0.23}_{-0.33}$	$6.15^{+1.10}_{-1.13}$	$0.26^{+0.15}_{-0.21}$	$0.01^{+0.03}_{-0.01}$	34
PS1-11aib	1.00	$1.24^{+0.28}_{-0.22}$	$0.60^{+0.14}_{-0.16}$	$28.78^{+10.89}_{-5.68}$	$5.44^{+0.37}_{-0.26}$	$12.47^{+5.91}_{-2.16}$	$0.11^{+0.04}_{-0.04}$	$1.48^{+36.52}_{-1.43}$	$1.83^{+0.28}_{-0.27}$	$6.71^{+1.02}_{-1.27}$	$0.44^{+0.04}_{-0.07}$	$0.09^{+0.02}_{-0.01}$	137
PS1-11bdn	0.52	$3.47^{+0.56}_{-0.57}$	$0.90^{+0.30}_{-0.23}$	$1.09^{+0.85}_{-0.49}$	$8.07^{+1.17}_{-1.27}$	$1.10^{+1.42}_{-0.64}$	$0.10^{+0.06}_{-0.04}$	$21.65^{+36.82}_{-14.03}$	$1.82^{+0.27}_{-0.28}$	$6.77^{+0.82}_{-0.95}$	$0.13^{+0.16}_{-0.07}$	$0.07^{+0.05}_{-0.03}$	15
PS1-11tt	1.28	$1.11^{+0.34}_{-0.25}$	$0.06^{+0.05}_{-0.03}$	$9.24^{+4.30}_{-3.27}$	$13.77^{+1.87}_{-1.14}$	$28.70^{+11.37}_{-10.82}$	$0.16^{+0.03}_{-0.04}$	$0.03^{+0.02}_{-0.02}$	$1.85^{+0.23}_{-0.30}$	$6.07^{+0.87}_{-1.14}$	$0.20^{+0.18}_{-0.14}$	$0.01^{+0.04}_{-0.01}$	80
PS1-12bmy	1.57	$2.31^{+0.29}_{-0.37}$	$0.52^{+0.16}_{-0.17}$	$2.93^{+1.17}_{-0.70}$	$13.10^{+1.40}_{-1.67}$	$7.79^{+2.33}_{-1.71}$	$0.14^{+0.05}_{-0.05}$	$1.05^{+14.40}_{-0.95}$	$1.90^{+0.22}_{-0.29}$	$5.87^{+1.05}_{-1.10}$	$0.36^{+0.09}_{-0.19}$	$0.01^{+0.04}_{-0.00}$	47
PS1-12bqf	0.52	$5.15^{+0.61}_{-0.51}$	$0.83^{+0.24}_{-0.16}$	$2.82^{+1.42}_{-1.19}$	$5.98^{+0.46}_{-0.44}$	$1.51^{+0.61}_{-0.67}$	$0.09^{+0.06}_{-0.03}$	$4.21^{+19.42}_{-3.95}$	$1.81^{+0.29}_{-0.28}$	$6.06^{+0.80}_{-1.05}$	$0.19^{+0.16}_{-0.14}$	$0.01^{+0.02}_{-0.01}$	108
PS1-13gt	0.88	$1.03^{+0.45}_{-0.20}$	$0.04^{+0.03}_{-0.01}$	$7.04^{+2.51}_{-2.30}$	$17.90^{+3.58}_{-3.39}$	$35.96^{+26.63}_{-19.34}$	$0.16^{+0.03}_{-0.04}$	$0.02^{+0.03}_{-0.01}$	$1.75^{+0.36}_{-0.19}$	$6.79^{+0.76}_{-0.67}$	$0.27^{+0.16}_{-0.14}$	$0.01^{+0.03}_{-0.01}$	76
PS1-13or	1.52	$1.82^{+0.33}_{-0.44}$	$0.56^{+0.31}_{-0.25}$	$8.43^{+4.60}_{-3.87}$	$8.84^{+1.16}_{-0.69}$	$9.37^{+11.94}_{-4.93}$	$0.14^{+0.04}_{-0.05}$	$0.48^{+17.72}_{-0.42}$	$1.78^{+0.30}_{-0.27}$	$5.99^{+0.81}_{-0.97}$	$0.02^{+0.04}_{-0.01}$	$0.10^{+0.02}_{-0.02}$	69
PTF10aagc	0.21	$4.48^{+1.01}_{-1.32}$	$7.81^{+1.35}_{-1.74}$	$1.62^{+0.37}_{-0.70}$	$8.16^{+0.49}_{-0.44}$	$1.63^{+0.35}_{-0.70}$	$0.07^{+0.05}_{-0.01}$	$7.34^{+38.67}_{-6.71}$	$1.84^{+0.20}_{-0.27}$	$5.98^{+0.64}_{-0.53}$	$0.14^{+0.16}_{-0.11}$	$0.19^{+0.04}_{-0.03}$	50
PTF10bfz	0.17	$1.21^{+0.51}_{-0.33}$	$4.48^{+0.95}_{-1.02}$	$10.23^{+7.23}_{-2.98}$	$9.84^{+1.03}_{-0.73}$	$17.29^{+10.35}_{-7.13}$	$0.13^{+0.05}_{-0.05}$	$0.88^{+13.69}_{-0.85}$	$1.88^{+0.25}_{-0.28}$	$5.23^{+0.38}_{-0.38}$	$0.20^{+0.16}_{-0.14}$	$0.09^{+0.02}_{-0.02}$	82
PTF10nmn	0.12	$2.21^{+1.46}_{-0.92}$	$1.03^{+0.33}_{-0.27}$	$5.12^{+3.64}_{-2.54}$	$10.38^{+3.40}_{-3.37}$	$7.06^{+9.53}_{-3.72}$	$0.13^{+0.05}_{-0.05}$	$0.43^{+0.47}_{-0.27}$	$1.87^{+0.23}_{-0.31}$	$7.22^{+0.47}_{-0.36}$	$0.19^{+0.17}_{-0.11}$	$0.13^{+0.05}_{-0.06}$	35
PTF10uhf	0.29	$4.35^{+1.52}_{-2.47}$	$3.19^{+1.72}_{-1.12}$	$2.39^{+3.14}_{-0.79}$	$10.54^{+1.10}_{-1.49}$	$3.69^{+6.20}_{-1.51}$	$0.15^{+0.04}_{-0.04}$	$1.56^{+9.36}_{-1.49}$	$1.84^{+0.25}_{-0.30}$	$5.94^{+1.17}_{-1.03}$	$0.35^{+0.10}_{-0.21}$	$0.14^{+0.04}_{-0.03}$	27
PTF10vqv	0.45	$3.12^{+0.42}_{-0.68}$	$1.43^{+0.29}_{-0.34}$	$2.71^{+2.51}_{-1.03}$	$9.30^{+1.61}_{-1.80}$	$3.59^{+1.75}_{-1.31}$	$0.11^{+0.06}_{-0.04}$	$3.44^{+34.25}_{-2.92}$	$1.87^{+0.23}_{-0.26}$	$8.72^{+0.63}_{-0.73}$	$0.05^{+0.07}_{-0.03}$	$0.01^{+0.02}_{-0.01}$	35
PTF11hrq	0.06	$7.68^{+1.37}_{-0.90}$	$1.15^{+0.29}_{-0.28}$	$1.73^{+0.34}_{-0.44}$	$11.36^{+1.50}_{-2.08}$	$3.30^{+0.99}_{-1.03}$	$0.16^{+0.03}_{-0.04}$	$0.38^{+0.14}_{-0.14}$	$1.89^{+0.22}_{-0.30}$	$5.31^{+1.40}_{-0.33}$	$0.19^{+0.17}_{-0.12}$	$0.06^{+0.01}_{-0.01}$	170
PTF12gty	0.18	$6.38^{+0.61}_{-0.97}$	$1.56^{+0.34}_{-0.32}$	$7.92^{+1.53}_{-1.43}$	$5.67^{+0.44}_{-0.21}$	$3.95^{+0.94}_{-0.83}$	$0.17^{+0.02}_{-0.04}$	$1.85^{+30.95}_{-1.69}$	$1.84^{+0.25}_{-0.28}$	$5.71^{+0.34}_{-0.33}$	$0.27^{+0.16}_{-0.17}$	$0.13^{+0.03}_{-0.02}$	97
PTF12hni	0.11	$6.85^{+2.00}_{-1.82}$	$3.21^{+0.67}_{-0.67}$	$3.77^{+1.93}_{-1.73}$	$6.67^{+1.12}_{-1.09}$	$2.56^{+0.90}_{-0.89}$	$0.13^{+0.04}_{-0.05}$	$3.23^{+25.48}_{-2.72}$	$1.84^{+0.23}_{-0.26}$	$5.22^{+0.34}_{-0.25}$	$0.15^{+0.20}_{-0.10}$	$0.33^{+0.03}_{-0.03}$	39
PTF12mxx	0.33	$2.24^{+0.44}_{-0.48}$	$0.95^{+0.35}_{-0.27}$	$6.71^{+2.36}_{-1.76}$	$8.16^{+0.51}_{-0.35}$	$6.78^{+2.83}_{-2.12}$	$0.16^{+0.03}_{-0.05}$	$0.03^{+4.70}_{-0.02}$	$1.85^{+0.22}_{-0.32}$	$6.04^{+0.89}_{-0.88}$	$0.26^{+0.11}_{-0.13}$	$0.05^{+0.01}_{-0.01}$	197
PTF13bdl	0.40	$1.09^{+0.34}_{-0.28}$	$1.40^{+0.46}_{-0.33}$	$68.80^{+19.94}_{-21.18}$	$5.76^{+0.78}_{-0.48}$	$35.18^{+17.68}_{-12.45}$	$0.18^{+0.02}_{-0.03}$	$0.90^{+25.42}_{-0.86}$	$1.84^{+0.26}_{-0.31}$	$5.97^{+0.80}_{-1.11}$	$0.36^{+0.08}_{-0.17}$	$0.01^{+0.02}_{-0.01}$	59
PTF13bjz	0.27	$2.98^{+2.19}_{-1.67}$	$5.51^{+2.87}_{-2.91}$	$2.07^{+2.26}_{-0.68}$	$11.09^{+2.05}_{-2.22}$	$3.90^{+5.66}_{-2.20}$	$0.13^{+0.05}_{-0.05}$	$0.66^{+14.75}_{-0.62}$	$1.75^{+0.31}_{-0.22}$	$5.88^{+1.01}_{-0.81}$	$0.21^{+0.19}_{-0.14}$	$0.18^{+0.04}_{-0.03}$	19
PTF13cjq	0.40	$1.75^{+0.85}_{-0.54}$	$1.49^{+0.31}_{-0.38}$	$7.75^{+4.52}_{-2.93}$	$8.33^{+1.26}_{-1.13}$	$6.96^{+4.55}_{-1.76}$	$0.12^{+0.04}_{-0.04}$	$10.02^{+44.17}_{-8.14}$	$1.86^{+0.23}_{-0.33}$	$6.83^{+0.66}_{-0.52}$	$0.10^{+0.11}_{-0.07}$	$0.22^{+0.03}_{-0.02}$	63

*The Watanabe-Akaike information criteria (or "widely applicable Bayesian criteria"; Watanabe 2010; Gelman et al. 2014

6.2.2 Description of the LSST Simulation

After generating the sample of SLSN models, we inject the simulated events into `OpSim`, a publicly available application that simulates LSST's scheduler and image acquisition process over its 10-year survey. `OpSim` realistically accounts for the science program requirements, mechanics of the telescope design and potential environmental conditions to produce a database of observations. We use `OpSim` to calculate the estimated signal-to-noise ratios and limiting magnitudes of each observation, using the formulae outlined in the Appendix. `OpSim` offers a number of unique schedulers, each designed to optimize distinct scientific goals; we use the most recent simulation, dubbed `minion_1016` (Delgado et al. 2014).

For both the WFD survey and DDFs, we inject our simulated models uniformly at $z = 0 - 6$ in bins of $\Delta z = 0.1$. In each bin, a sample of 1,000 models are randomly injected uniformly across the sky and in time to calculate the "discovery efficiency" (see §6.3.1) of the LSST observing strategy as a function of redshift. We resample the simulated models to the observed times and add white noise corresponding to the estimated signal-to-noise ratio reported by `OpSim`. Additionally, we add Milky Way extinction based on the injected sky positions. We disregard host galaxy extinction since most known SLSN host galaxies appear to have negligible extinction (e.g., Chen et al. 2015; Leloudas et al. 2015; Nicholl et al. 2017; Lunnan et al. 2014). Example light curves at representative redshifts are shown in Figure 6.4; featured light curves are selected to highlight a combination of best, typical and worst cases in the WFD survey.

6.3 Characteristics of SLSNe discovered by LSST

The thousands of injected simulated light curves reflect the wide range of observed SLSN properties expected from LSST. Here we summarize these properties, define our criteria for detection, and determine the rate of detected SLSNe as a function of redshift for both the WFD survey and DDFs.

We calculate the expected number of SLSNe within each redshift bin by multiplying the sample recovered from `OpSim` by the estimated volumetric rate from Quimby et al. (2013) normalized to the cosmic star formation history (Madau & Dickinson 2014):

$$R = R_0 \frac{(1+z)^{2.7}}{1+[(1+z)/2.9]^{5.6}}\,\mathrm{Gpc}^{-3}\mathrm{yr}^{-1}, \tag{6.1}$$

where $R_0 \approx 21\,\mathrm{Gpc}^{-3}\mathrm{yr}^{-1}$ is the normalized SLSNe rate at $z = 0$ with an uncertainty range of $R_0 \approx 4 - 72$ Gpc^{-3} (Quimby et al. 2013; Prajs et al. 2016). Using this prescription, the volumetric SLSN rate peaks at $z \approx 1.5 - 2$.

We first focus on the r-band light curves to provide an overview of the broad observational properties. In Figure 6.5, we show the observed duration-luminosity phase space for our injected light curves (weighted by their volumetric rate) using a kernel density estimate. For the WFD survey, peak observed magnitudes span $\approx 19 - 23$ mag, with the distribution peaking at ≈ 21.2 mag. We also find that the observed durations of the SLSNe span $t_{\mathrm{dur}} \approx 60 - 300$ days. This timescale is comparable to the expected LSST season length ($\approx 4 - 6$ months), implying that for a substantial fraction of events the rise or decline will be missed in seasonal gaps. We find that a typical SLSN is tracked for $\approx 100 - 400$ days (1σ uncertainty range). For the DDFs, we find that average peak magnitudes are slightly dimmer, with the distribution peaking at ≈ 21.8 mag. The

observed durations are similar to those in the WFD survey.

The total number of observed light curve data points (combined in all filters) rapidly decreases with redshift; see Figure 6.6. For the WFD survey, SLSNe at $z \lesssim 1$ will have $\approx 50 - 100$ data points, while the majority of SLSNe have light curves with $\lesssim 50$ data points. The number of observed data points roughly doubles for the SLSNe in the DDFs due to both their higher cadence and deeper limits, enabling a longer temporal baseline.

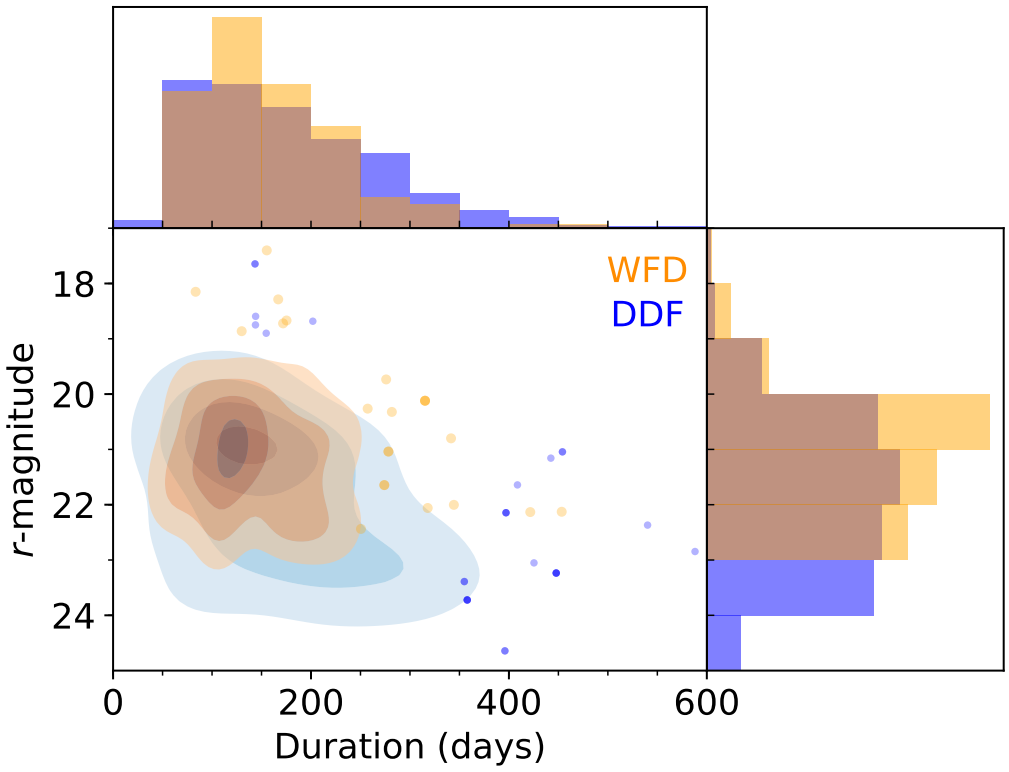

Figure 6.5: Duration-luminosity phase space for a representative sample of our simulated SLSNe as observed with LSST in the WFD survey (orange) and DDFs (blue). Contours are a kernel density estimate of the two populations, while points represent outliers. The majority of objects have a peak magnitude of $r \approx 21 - 22$ mag and durations of ≈ 100 days. The events in the DDFs extend to lower peak magnitudes and longer durations.

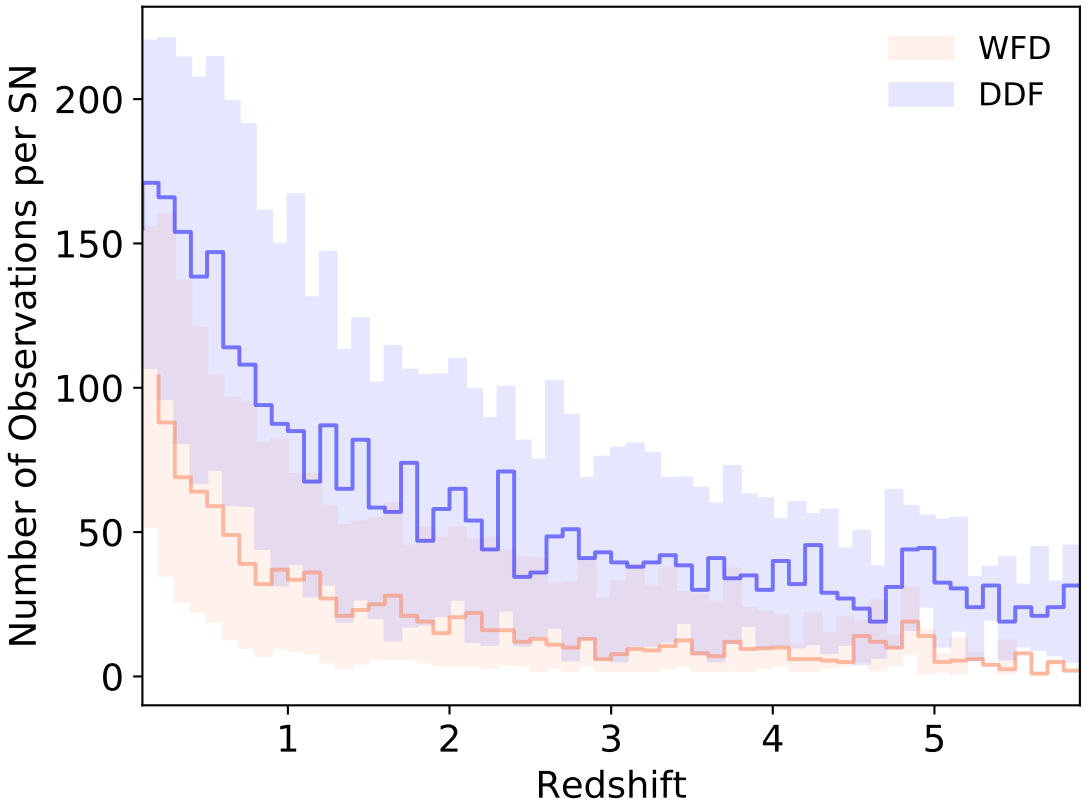

Figure 6.6: Number of observed data points per event as a function of redshift. Bold lines show the mean in each redshift bin, with the shaded regions representing 1σ ranges due to event-to-event variations. The number of observed points drops to < 10 (our minimum criterion for a detection) at $z \approx 3$ in the WFD survey, while it typically remains at > 20 in the DDFs even to $z \approx 6$.

Table 6.4:: Observational Metrics

	WFD				DDF			
Metric	Limiting z[1]	Discovered[2] (yr^{-1})	Useful (lenient)[3]	Useful (strict)[4]	Limiting z[1]	Discovered[2] (yr^{-1})	Useful (lenient)[3]	Useful (strict)[4]
>10 detections	2.9	9600	4810 (0.50)	1680 (0.18)	3.9	13	5 (0.40)	1 (0.13)
>50 detections	2.3	3320	2170 (0.65)	900 (0.27)	3.5	9	4 (0.50)	1 (0.17)
>100 detections	2.0	590	416 (0.71)	216 (0.37)	2.7	3	2 (0.62)	0 (0.24)
>10 detections in u	2.5	50	30 (0.65)	20 (0.37)	2.4	4	2 (0.61)	0 (0.22)
>10 detections in g	2.3	1090	720 (0.66)	320 (0.29)	3.1	6	3 (0.55)	1 (0.20)
>10 detections in r	2.8	6600	3190 (0.48)	1170 (0.18)	3.7	10	4 (0.40)	1 (0.13)
>10 detections in i	2.7	6120	3170 (0.52)	1170 (0.19)	3.8	10	4 (0.41)	1 (0.13)
>10 detections in z	2.3	2770	1730 (0.63)	730 (0.27)	3.8	10	4 (0.45)	1 (0.15)
>10 detections in y	2.0	1300	890 (0.69)	420 (0.33)	3.2	6	3 (0.53)	1 (0.19)
>10 observations in rise	3.6	2240	577 (0.26)	131 (0.06)	4.0	8	2 (0.35)	0 (0.10)
>20 during peak[5]	2.2	2690	1740 (0.65)	780 (0.29)	3.4	9	4 (0.49)	1 (0.17)
Detected <5 days after explosion	2.9	100	36 (0.36)	13 (0.14)	3.7	2	0 (0.31)	0 (0.10)
Detected <10 days after explosion	3.2	350	119 (0.34)	42 (0.12)	3.9	5	1 (0.28)	0 (0.09)
Measurable duration in u	1.2	50	39 (0.77)	23 (0.46)	1.8	0	0 (0.71)	0 (0.34)
Measurable duration in g	2.1	280	185 (0.66)	78 (0.28)	2.2	1	0 (0.65)	0 (0.27)
Measurable duration in r	2.2	960	618 (0.65)	261 (0.27)	2.7	2	1 (0.59)	0 (0.22)

Table 6.4 – continued from previous page

	WFD				DDF			
Metric	Limiting z[1]	Discovered[2]	Useful	Useful	Limiting z[1]	Discovered[2]	Useful	Useful
Measurable duration in i	2.0	770	514 (0.67)	221 (0.29)	3.1	2	1 (0.60)	0 (0.22)
Measurable duration in z	2.1	310	215 (0.70)	108 (0.35)	3.2	2	1 (0.57)	0 (0.22)
Measurable duration in y	2.0	90	64 (0.69)	41 (0.44)	2.0	0	0 (0.63)	0 (0.26)

[1]Cumulative redshift at which 90% of SLSNe are discovered.

[2]Total number of discovered SLSNe satisfying given metric.

[3]Total Number of discovered SLSNe satisfying given metric with recoverable parameters to within a factor of two.

[4]Total Number of discovered SLSNe satisfying given metric with recoverable parameters to within 30%.

[5]Here we define "peak" as within one magnitude of peak brightness.

6.3.1 Efficiency and Metrics for Detectability

We now focus on more quantitative measures of "detectability" for the simulated light curves. There can be many definitions of a detection of a transient. We are most interested in the ability to: (1) accurately estimate the physical parameters from the light curve, and (2) discover events sufficiently early to enable follow up with other instruments. To address these points, we quantify the information content of the observed light curves by defining several properties that can be easily measured directly from the light curve. We focus on 19 representative properties, summarized in Table 6.4.

Using each property as an independent criterion of detection, we calculate the total detection efficiency for SLSNe in LSST. The efficiency can be divided into two multiplicative parts. The first is the survey efficiency, ϵ_s, arising from the survey footprint and cadence. We calculate this by injecting events uniformly across the complete survey duration and the sky. We then calculate the fraction of events that are in the LSST footprint during at least one observation. This efficiency is effectively the area covered by the survey, given the long duration of SLSNe compared to the cadence of LSST. The second efficiency, ϵ_m, is the fraction of simulated events that satisfy the metrics listed in Table 6.4.

The total efficiency, $\epsilon \equiv \epsilon_s \times \epsilon_m$, as a function of redshift is shown in Figure 6.7 for light curves with > 10 observations (one of our 19 metrics). For both the WFD survey and DDFs, the efficiencies decline monotonically as a function of redshift; however, the decline is shallower in the case of the deeper DDFs. Within the WFD survey footprint, the efficiency peaks at $\approx 70\%$ at low redshift; in the DDF fields, the efficiency peaks at $\approx 100\%$. The WFD survey peaks at a lower efficiency due to the fact that SLSNe

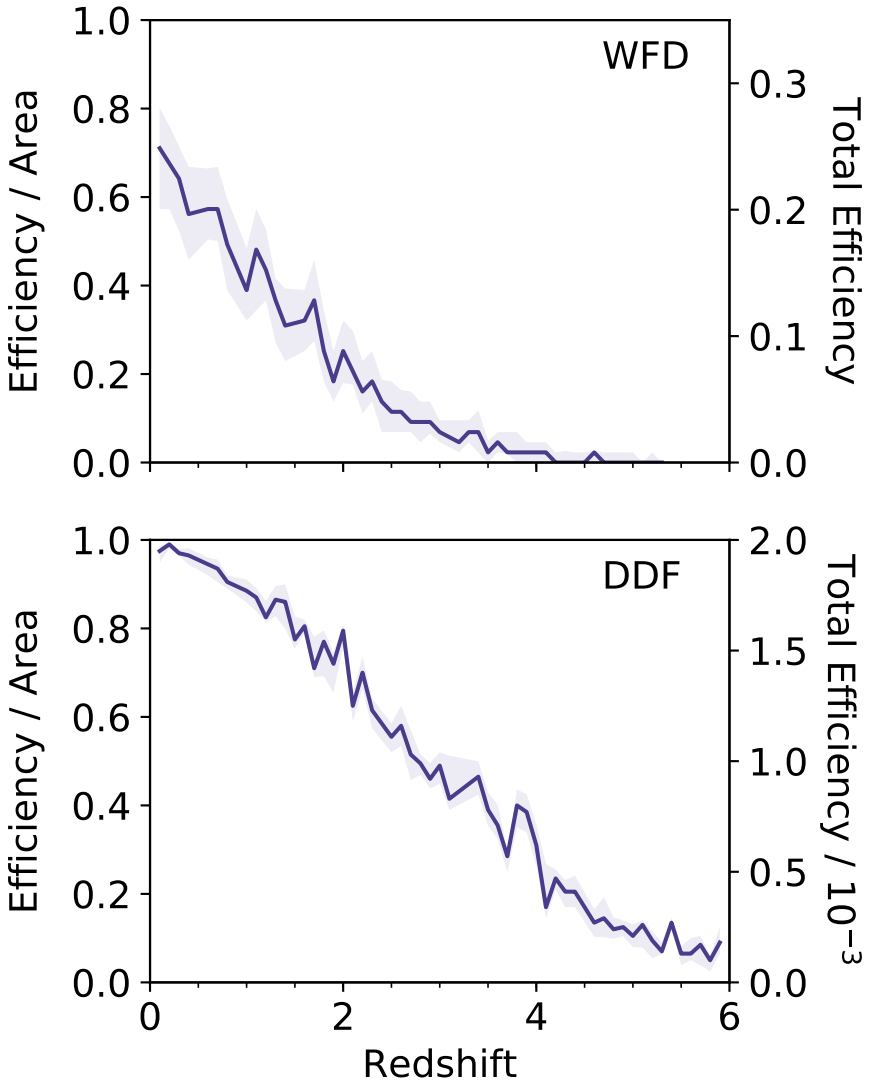

Figure 6.7: WFD survey and DDFs efficiencies as a function of redshift. The left-hand y-axis shows the efficiency of SLSN detection, assuming the SLSNe are within the survey footprint (i.e., a SLSN may be in the footprint but too dim to detect). The right-hand y-axis shows the total efficiency, ϵ, including the effect of survey area. The shaded region represents the 1σ error bars from bootstrap analysis.

(particularly if they explode outside of the observing season for their part of the sky) can be discovered well beyond peak, at which point they may already be below the LSST detection limit. The WFD survey efficiency reaches 50% at $z \approx 1$ and declines to 10% at $z \approx 3$. For the DDFs, the efficiency reaches 50% at $z \approx 3$ and declines to 10% at $z \approx 5$.

We combine the efficiency and the estimated volumetric rate to calculate the total expected number of SLSNe, the integral of the observed rate over the comoving volume, corrected for time dilation:

$$N = \epsilon \int_{z_{\min}}^{z_{\max}} \frac{4\pi R}{1+z} \frac{dV}{dz} dz. \tag{6.2}$$

We estimate the statistical uncertainty in the number of detections due to the uncertainty in ϵ using a bootstrap analysis; namely, we resample the properties of the observed light curves repeatedly, recalculating the efficiencies each time. There is an overall scaling uncertainty due to the systematic uncertainty in the volumetric rate, but we expect this to be improved with new rate measurements from DES (The Dark Energy Survey Collaboration 2005) and ZTF (Kulkarni 2018). Therefore, in Figures 6.7–6.9 we show only the statistical uncertainties.

The number of SLSNe discovered per year as a function of redshift is shown in Figures 6.8 and 6.9. For our most lenient definition of a detection (at least 10 light curve points), we find that LSST will discover $\approx 9,600$ SLSNe per year. This is in agreement with the rate reported in the Scientific Handbook (LSST Science Collaboration et al. 2017) and previous studies (Tanaka et al. 2013; Scovacricchi et al. 2015). The distribution roughly traces the cosmic star formation history to $z \approx 1$, at which point the observed distribution drops more rapidly due to the declining detection efficiency. The distribution extends to $z \approx 3$ in the WFD survey and to $z \approx 5$ in the DDFs.

Measuring both the peak brightness and duration can lead to robust measurements of the SLSN properties. About 2,700 SLSNe per year will have more than 20 observations within one magnitude of their peak brightness. We find that the duration is most readily measurable in r-band, and that for about 950 SLSNe per year $t_{\rm dur}$ (as defined above) will be measured; we note that this represents only 10% of the overall SLSN sample.

Capturing the light curve rise can be especially important for constraining the underlying power source in SLSNe and to search for early bumps in the light curve. We find that ≈ 800 SLSNe per year will be discovered within ten days (in the rest frame) of their explosion time, comparable to the typical time frame of the early pre-peak bumps seen to date (Nicholl & Smartt 2016; Leloudas et al. 2012; Nicholl et al. 2015a; Smith et al. 2016a). About 100 SLSNe per year will be discovered within five days of explosion, most being located at $z \lesssim 1$. About $4,200$ SLSNe will be detected with at least ten observations during the rising phase; however, fewer than 10 SLSNe with this property will be found annually in each DDF, due to their small areal footprint.

6.4 Recovering the SLSN Parameters

In the previous section we explored the overall detection rates and the redshift distributions for a range of observational light curve metrics. Here we fit the simulated LSST light curves with the same model used to generate them to determine how well we can recover the injected model parameters. Our goals are to understand how well we can determine the model parameters from LSST data, and to correlate our simple light curve metrics to the information content of the light curves. The latter goal is important because the final survey strategies of LSST will be determined by providing a simple,

measurable metric that can be optimized for a specific science goal.

6.4.1 Injection and Recovery of Representative SLSNe

We fit the output light curves using `MOSFiT` in the same manner that was used to generate them (§6.2). We focus on three SLSNe representative of the larger population: SN2013dg ($t_{\rm dur} \approx 45$ days), LSQ12dlf ($t_{\rm dur} \approx 60$ days), and SN2015bn ($t_{\rm dur} \approx 130$ days). All three have roughly the same peak luminosity, $\approx 3 \times 10^{44}$ erg s^{-1}. We inject and recover about 100 iterations of these SLSNe at $z = 0.5, 1.0, 1.5, 2.0, 3.0$.

We fix the redshift to its input value when fitting, finding that without doing so it is nearly impossible to constrain the explosion parameters. In reality, it is unclear how well we will know the redshift a priori through photometry or (in some cases) spectroscopic measurements of their host galaxies. SLSNe are typically found in low-luminosity ($M_{\rm B} \approx -17$ mag) host galaxies (Lunnan et al. 2014). For $z \lesssim 0.5$, most of these hosts will fall in the so-called LSST "gold" galaxy sample (defined as galaxies with $m_{\rm i} < 25.3$ mag), which will have a root-mean-square scatter in the photometric redshifts of $\sigma_{\rm z}/(1+z) \lesssim 0.05$ (see LSST Science Collaboration et al. 2017). We additionally fix the host reddening to be negligible.

We are interested in our ability to recover four key parameters: the ejecta mass, the ejecta velocity, the initial magnetar spin period, and the magnetic field. In our model, the spin period and magnetic field have strong degeneracies with several nuisance parameters, making them difficult to directly measure. We therefore recover the following variables, which directly correlate with the rotational energy and spindown timescales of

the magnetar (Nicholl et al. 2017; Villar et al. 2017b):

$$B^* \equiv B^{-2}(\sin\theta)^{-2} M_{\rm NS}^{3/2}$$

$$P^* \equiv P_{\rm spin}^{-2} M_{\rm NS}^{3/2}$$

, where θ is the angle between the rotational axis and magnetic dipole, and $M_{\rm NS}$ is the neutron star mass.

How well we need to recover the SLSN parameters depends on the scientific goal. For cosmological studies, determining the average distance modulus (assuming SLSNe are standardizable; see Inserra & Smartt 2014) to ≈ 0.25 mag is sufficient to constrain, for example, Ω_m to within 2% (Scovacricchi et al. 2015). In Nicholl et al. (2017), constraining parameters to an average of $\approx 30-50\%$ was sufficient to probe the underlying population with a sample of ≈ 50 events. We track our ability to recover the four key parameters to (1) $\lesssim 30\%$ of their input values and with error bars of $< 50\%$ ("strict"), and (2) within a factor of two of their input values with error bars of $< 50\%$ ("lenient").

Example light curves and their best-fit models are shown in Figure 6.10. At low redshifts, many of the light curves are well-sampled both near and post peak, leading to better recovery of the input parameters. At higher redshifts, the majority of light curves are caught near peak and quickly drop below the detection limit, leading to typically poorer recovery. Additionally, due to the much deeper limits available in *gri*-bands, the light curves of higher redshift events are typically limited to these filters. Thus our ability to recover the input parameters significantly drops with redshift. At $z \lesssim 0.5$, our strict recovery rate is $\approx 60\%$ and our lenient recovery rate is $\approx 100\%$ for light curves with > 10 data points. By $z = 2$, the strict recovery rate drops to zero, while the lenient

recovery rate is $\approx 50\%$. By $z = 3$, the lenient recovery rate also drops to zero.

The parameter recovery rate is a function of both redshift and luminosity. The above calculations used a peak luminosity of $L_0 \approx 3 \times 10^{44}$ erg s^{-1}. We now consider the full luminosity function of our simulated SLSNe (Figure 6.2) to capture the overall recovery rate. For any luminosity, the recovery curve as a function of redshift, $\epsilon_{\rm recov}(z)$, is set to 1 at $z = 0$ and to zero at $z = z_{\rm lim}$, where $z = z_{\rm lim}$ is the limiting redshift for a given luminosity. For SLSNe with peak luminosity L_0, the limiting redshift is $z_{\rm lim,0} \approx 3.0$. We assume that for all other peak luminosities, the recovery rate can be described as $\epsilon_{\rm recov} = (z * z_{\rm lim,0}/z_{\rm lim})$. This allows brighter events to be captured at higher redshifts, and all events will be capped to their limiting redshifts. After reweighting the recovery rate through this process with our simulated luminosity function, we find that the overall efficiencies decline more rapidly with redshift. For example, the lenient recovery rate drops to $\approx 40\%$ at $z = 2$, rather than to $\approx 50\%$ when we used just a single peak luminosity.

Multiplying our corrected recovery rates by the overall discovery efficiency from §6.3, we find that $\approx 18\%$ (about 1,700 out of 9,600 discovered annually) of SLSNe discovered in the WFD survey will have light curves that satisfy our strict criterion, and $\approx 50\%$ will satisfy the lenient criterion. Even at the high redshift end ($z \approx 3$), ≈ 50 SLSNe per year will satisfy the lenient criterion.

For the DDFs, we find that the fraction of useful light curves is slightly smaller than that of the WFD survey. This is likely due to the fact that the overall efficiency reaches to higher redshifts, although fewer of the high-redshift light curves are useful due to their lower luminosities.

Finally, we test the robustness of our results given an uncertain redshift. For each model at a representative $z = 1$, we rerun our fits with a uniform prior on redshift with three levels of uncertainty: 5%, 10% and 20%. These levels range from the expected "gold standard" (5%) and a worst-case scenario (20%). Using a bootstrap analysis, we find no statistically significant ($p > 0.05$) bias or error inflation in any of the four key parameters given the different redshift priors. This is likely due to the fact that the errors are dominated by the other eleven parameters being fit. At higher redshift, it is possible that similar uncertainties will have a larger effect on the models, but we expect these to still remain at the $\approx 10\%$-level.

6.4.2 Correlating SLSN Properties to Parameter Recovery

Finally, we turn to the question of what properties of a SLSN light curve allow us to best recover key physical parameters. Unsurprisingly, the number of observations strongly correlates with our ability to recover parameters. This is demonstrated in Figure 6.11, in which we show the average parameter residual for each of the four important physical parameters (e.g., $|M_{\rm ej,fit} - M_{\rm ej,true}|/M_{\rm ej,true}$) as a function of the number of observations for a sample of light curves spanning from $z = 0.5$ to $z = 2$. We consider both the total number of observations (taken at any point during the event) and observations taken within the first $2t_{\rm dur}$ days in the rest-frame (i.e., near-peak). In both cases, light curves with $\gtrsim 50$ points are significantly more likely to have recoverable physical parameters compared to the average light curve with ≈ 20 observations ($\approx 65\%$ compared to $\approx 50\%$ recovery rate). Light curves with $\gtrsim 100$ observations are only somewhat more useful than those with $\gtrsim 50$ observations when using the lenient definition ($\approx 70\%$ vs $\approx 65\%$);

however, they are more useful when using the strict criterion, with $\approx 40\%$ compared to $\approx 30\%$.

Additionally, having a measurable duration in any filter is a good indicator of an information-rich light curve, with $\approx 65\%$ compared to $\approx 50\%$ recovery rate for the typical light curve. This is likely due to the fact that the light curve peak and width greatly constrain the model parameter space. For example, a bright and broad light curve cannot be produced by a small ejecta mass or weak magnetic field. The most "useful" filter for measuring duration appears to be u-band, although this is likely due to the fact that light curves which are well-sampled in u-band tend to be at low redshifts (i.e., the limiting redshift for this metric is only $z = 1.2$). In contrast, light curves with a measurable r-band duration can occur at higher redshift ($z \approx 2$). Again, this suggests that well-sampled light curves near peak are more scientifically useful.

These findings indicate that a survey strategy which optimizes a higher cadence in the most sensitive bands, gri, will provide the greatest return on scientifically useful light curves even at high redshift. Given the average SLSN duration of ≈ 100 days (Figure 6.5), a cadence of roughly two to four days (similar to the nominal cadence) in any filter would be sufficient to recover magnetar parameters directly from most SLSN light curves at $z < 3.0$. Perhaps more importantly, the current WFD observing strategy has large seasonal gaps every $4 - 6$ months which interrupt many SLSN light curves. This is due to the fact that the WFD survey observes fields with airmass ≤ 1.4 (LSST Science Collaboration et al. 2017). Reducing these gaps with even a few observations at higher airmass would be beneficial to provide more comprehensive temporal coverage and greater opportunity to recover SLSN properties. In a similar vein, stacking late-time observations can significantly extend our light curve coverage accross seasons.

6.5 Summary and Conclusions

We presented detailed simulations of Type-I SLSNe in the upcoming LSST survey. We constructed a realistic distribution of magnetar and explosion parameters from an existing sample of 58 SLSNe spanning $z = 0.1 - 1.6$ and used this to simulate thousands of SLSNe at $z = 0 - 6$ in the LSST Operations Simulator.

We define a number of measurable light curve metrics which we use to define a "detection". For our loosest definition of a detection (observing > 10 data points in all filters combined), we find that the detection efficiency of the WFD survey quickly declines from $\approx 50\%$ at $z = 1$ to $\approx 10\%$ at $z = 3$, while for the DDFs, the efficiency declines from $\approx 100\%$ at $z = 0.5$ to $\approx 50\%$ at $z = 3$ and 10% at $z = 5$. We combine this detection efficiency with an estimate for the cosmic SLSN rate to find that LSST will discover $\approx 10^4$ SLSNe per year within the WFD survey and ≈ 15 per year in each DDF. Most (90%) of the discovered SLSNe are found at $z \lesssim 3$, although ≈ 1 SLSN per year should be discovered at $z \approx 5$.

We refit the light curves of representative SLSNe injected into the LSST WFD survey and DDFs, and test how well we can recover four key physical parameters (initial magnetar spin period, magnetic field strength, ejecta velocity and ejecta mass). We find that we can successfully recover the four parameters in $\approx 18\%$ of all SLSNe to within 30% with error bars of $< 50\%$ of the parameter values. We can recover the parameters to within a factor of two for $\approx 50\%$ of all SLSNe. The majority of SLSNe with recoverable parameters will be found at low redshift ($z \lesssim 1.5$). Parameter recovery relies on having accurate redshifts; while LSST will provide photometric redshifts for many host galaxies this may become a challenge at the high redshift end.

We correlate our ability to recover physical parameters with the defined light curve metrics. In both the WFD survey and DDFs, light curves with $\gtrsim 50$ observations, especially concentrated near-peak, are typically those with recoverable parameters. LSST survey strategies which maintain a rapid cadence ($\approx 2-4$ day) in the most sensitive *gri* bands will provide the most scientifically useful SLSN light curves. Similarly, strategies which minimize seasonal gaps with some high airmass observations will increase our chance of covering the light curves peak and duration, and therefore provide more scientifically useful light curves. Finally, stacking observations at late times may allow us to probe more SLSNe across multiple seasons and better anchor our models.

Compared to the WFD survey, we find that the DDFs (in their current form) will not provide higher quality SLSNe, or SLSNe at significantly higher redshifts in large quantities due to the small area covered by these fields. It is therefore imperative to maximize the scientific return from events in the WFD survey, rather than relying on a small number of events from the DDFs.

Overall, our simulations indicate that LSST will be a powerhouse for discovering SLSNe. About 1,700 SLSNe per year will have sufficient photometry to extract key physical parameters directly from the light curves (given an accurate redshift estimate) to within 30%, significantly increasing our current sample by at least two orders of magnitude.

6.6 Appendix

Using information provided by OpSim, we can calculate the signal-to-noise ratio (SNR) of our injected observations [2]:

$$SNR = \frac{C}{\sqrt{C/g + (B/g + \sigma^2_{\rm instr}) * n_{\rm eff}}}, \tag{6.3}$$

where C is the source counts in ADU, B is the background count per pixel in ADU, $\sigma_{\rm instr} = 12.7$ e$^-$ is the instrumental noise in ADU, $g = 2.3$ e$^-$/ADU is the gain, and $n_{\rm eff}$ is the effective number of source pixels. Both B and $\sigma_{\rm instr}$ are provided by `OpSim`. The source counts are calculated using:

$$C = \frac{A_{\rm eff}\Delta t}{gh} \int F_\nu(\lambda) \frac{S(\lambda)}{\lambda} d\lambda, \tag{6.4}$$

where F_ν is source spectrum, and $S(\lambda)$ is the filter throughput, $\Delta t = 30$s is the integration time, $A_{\rm eff} = 3.24 \times 10^{10}$cm^2 is the effective collecting area and h is Plank's constant. The effective number of pixels can be calculated as:

$$n_{\rm eff} = 2.266({\rm FWHM_{eff}/px})^2, \tag{6.5}$$

where FWHM$_{\rm eff}$ is the effective full-width-at-half-max of the source PSF as reported by `OpSim` and px $= 0.2$"/pixel is the pixel scale.

For the DDFs, the exposure time is increased according to the number of exposures taken in a single night in each filter, allowing us to probe deeper limiting magnitudes.

[2] See `https://smtn-002.lsst.io`

Acknowledgments

We thank J. Guillochon and P. Cowperthwaite for useful discussions and an anonymous referee for valuable feedback. The computations presented in this work were performed on Harvard University's Odyssey computer cluster, which is maintained by the Research Computing Group within the Faculty of Arts and Sciences. The Berger Time Domain group is supported in part by NSF grant AST-1714498 and NASA ADA grant NNX15AE50G.

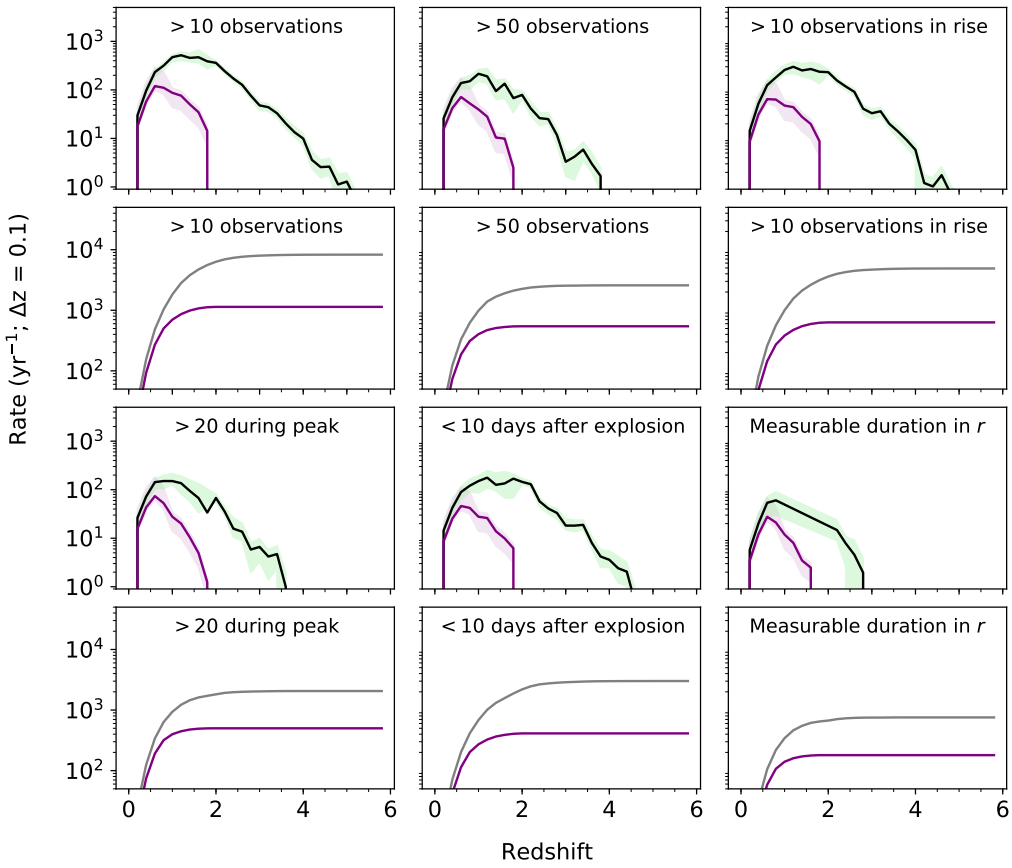

Figure 6.8: *First and third rows*: The WFD survey annual detection rate of SLSNe as a function of redshift (black lines) for various metrics. The green shaded regions represent 1σ errors from our bootstrap analysis. Also shown are the rates for SLSNe with (strict) recoverable parameters (purple line and shaded area); note that the purple line is calculated assuming the same information efficiency for each metric. *Second and fourth rows*: Cumulative distributions of SLSNe that satisfy each metric (black) and those that have lenient recoverable parameters (purple).

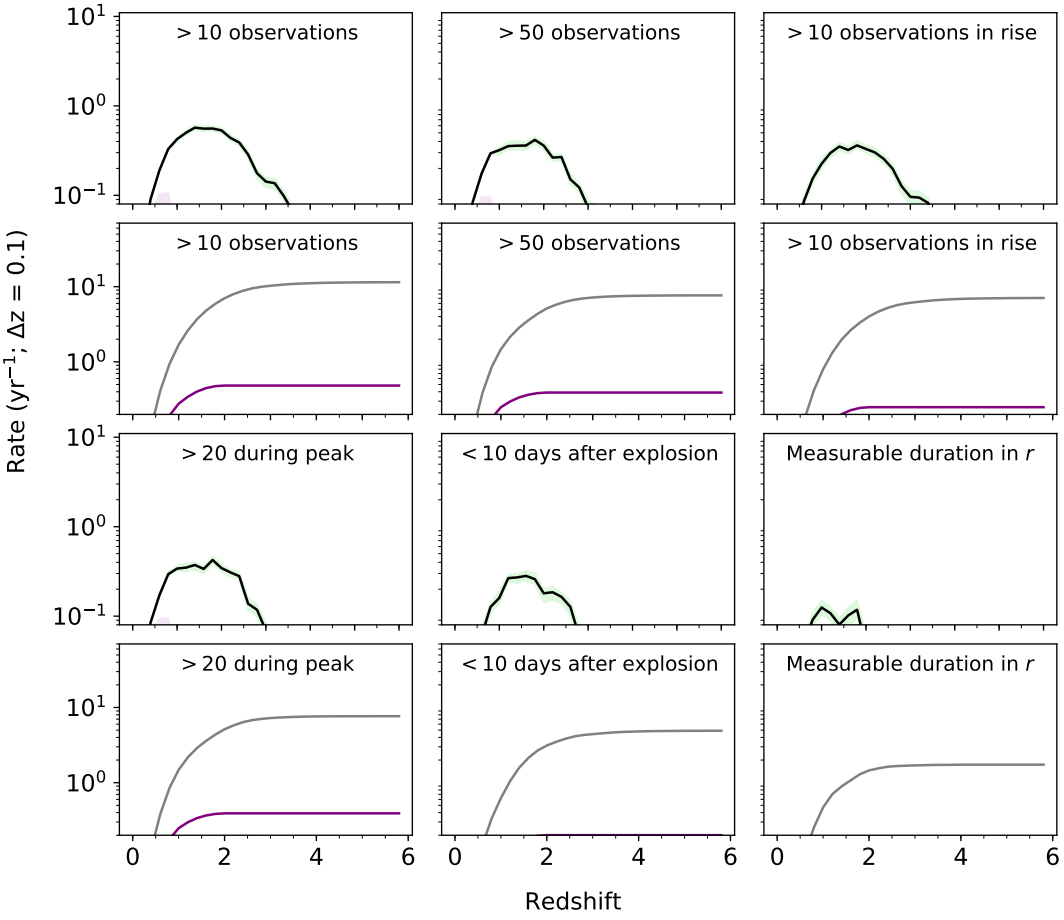

Figure 6.9: Same as Figure 6.8 but for each DDF.

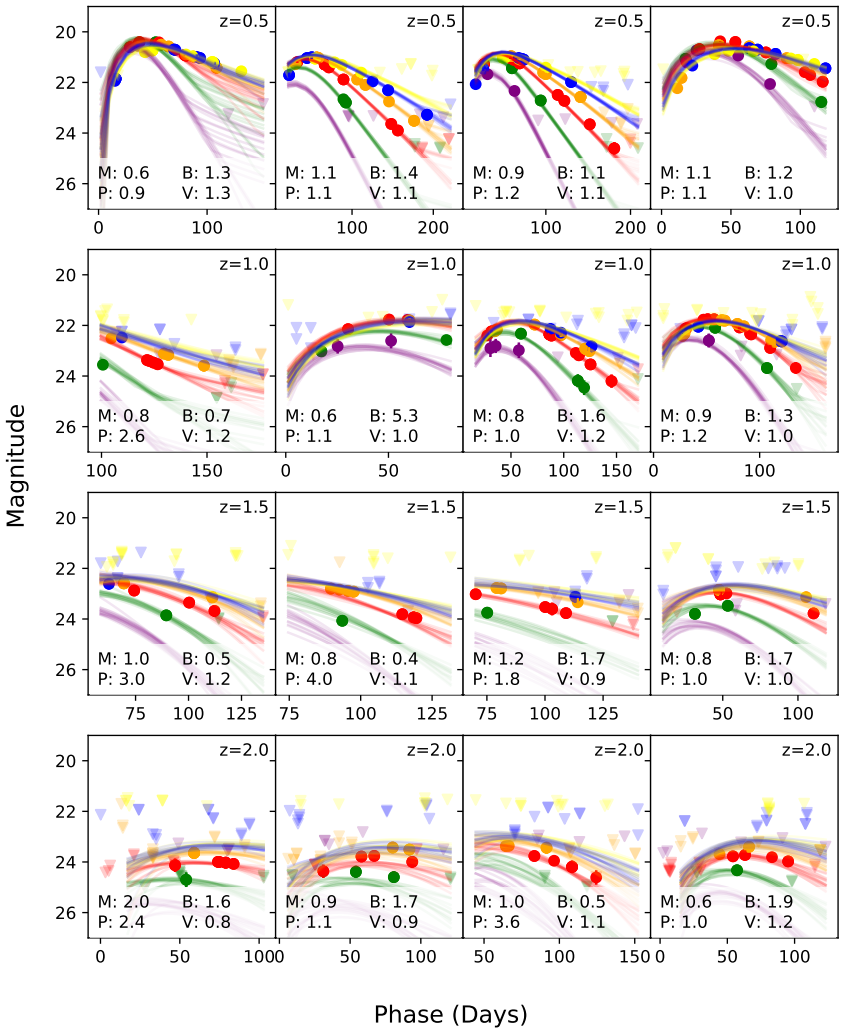

Figure 6.10: Light curves fits from `MOSFiT` to a sample of simulated LSST light curves at representative redshifts. For each event we list the ratio of the injected to fitted values for the four key model parameters. The light curves are ordered by the quality of parameter recovery from left (worst) to right (best).

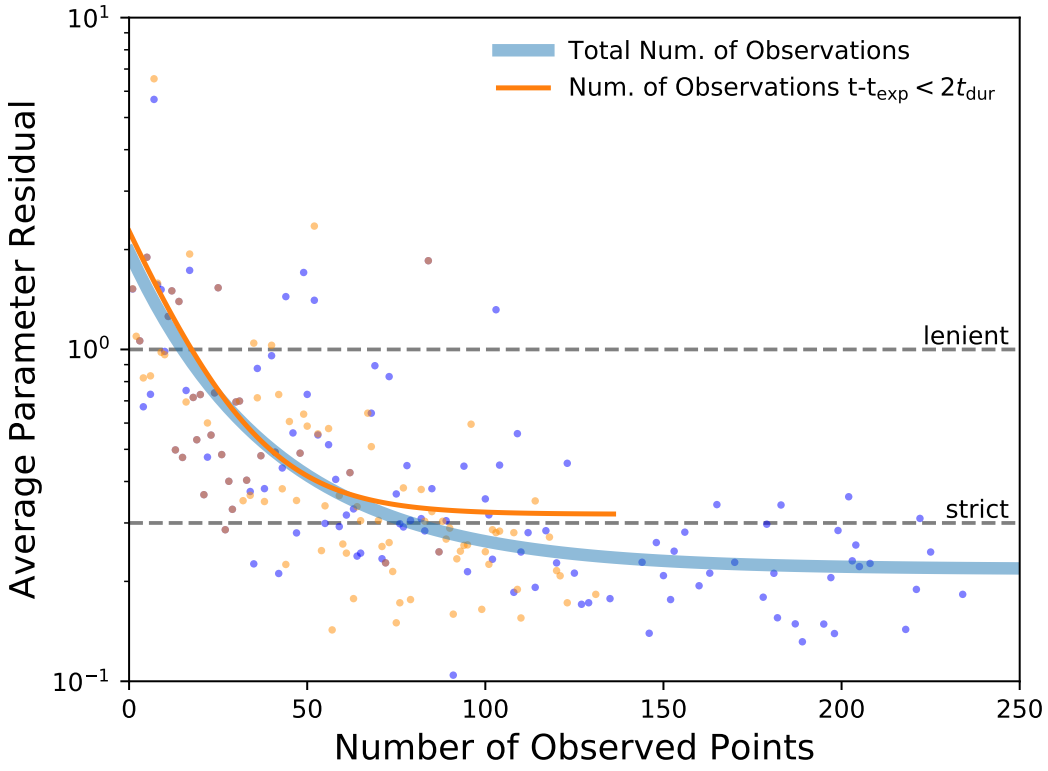

Figure 6.11: Average parameter residuals (for $M_{\rm ej}, v_{\rm ej}, B^*, P^*$) as a function of number of observations per light curve. The blue points show *total* number of observations per light curve, while the oranges points show the number of observations within $2t_{\rm dur}$ days of explosion (in the event's rest frame). The solid lines are fits to exponential functions to guide the eye. Dotted lines show both the lenient and strict information criteria. There is little gain beyond ≈ 50 observations per light curve, and almost no light curves have more than 50 observations within $2t_{\rm dur}$ days post-explosion.

Chapter 7

Supernova Photometric Classification Pipelines Trained on Spectroscopically Classified Supernovae from the Pan-STARRS1 Medium-deep Survey

This thesis chapter originally appeared in the literature as

V. A. Villar, E. Berger, G. Miller et al., *The Astrophysical Journal* 884, 83

Abstract

Photometric classification of supernovae (SNe) is imperative as recent and upcoming optical time-domain surveys, such as the Large Synoptic Survey Telescope (LSST), overwhelm the available resources for spectrosopic follow-up. Here we develop a range of light curve classification pipelines, trained on 513 spectroscopically-classified SNe from the Pan-STARRS1 Medium-Deep Survey (PS1-MDS): 357 Type Ia, 93 Type II, 25 Type IIn, 21 Type Ibc, and 17 Type I SLSNe. We present a new parametric analytical model that can accommodate a broad range of SN light curve morphologies, including those with a plateau, and fit this model to data in four PS1 filters ($g_{\rm P1}r_{\rm P1}i_{\rm P1}z_{\rm P1}$). We test a number of feature extraction methods, data augmentation strategies, and machine learning algorithms to predict the class of each SN. Our best pipelines result in $\approx 90\%$ average accuracy, $\approx 70\%$ average purity, and $\approx 80\%$ average completeness for all SN classes, with the highest success rates for Type Ia SNe and SLSNe and the lowest for Type Ibc SNe. Despite the greater complexity of our classification scheme, the purity of our Type Ia SN classification, $\approx 95\%$, is on par with methods developed specifically for Type Ia versus non-Type Ia binary classification. As the first of its kind, this study serves as a guide to developing and training classification algorithms for a wide range of SN types with a purely empirical training set, particularly one that is similar in its characteristics to the expected LSST main survey strategy. Future work will implement this classification pipeline on ≈ 3000 PS1/MDS light curves that lack spectroscopic classification.

7.1 Introduction

Optical time-domain astronomy has entered a new era of large photometric datasets thanks to current and upcoming deep and wide-field surveys, such as the Panoramic Survey Telescope and Rapid Response System (Pan-STARRS; Kaiser et al. 2010), the Asteroid Terrestrial-impact Last Alert System (ATLAS; Jedicke et al. 2012), the Zwicky Transient Facility (ZTF; Kulkarni 2018), the Large Synoptic Survey Telescope (LSST; Ivezic et al. 2011), and the Wide Field Infrared Survey Telescope (WFIRST; Spergel et al. 2015). The current surveys are already discovering $\sim 10^4$ SNe per year, a hundred-fold increase over the rate of discovery only a decade ago. LSST will increase this discovery rate to $\sim 10^6$ SNe per year.

Supernovae have traditionally been classified based on their spectra (Filippenko 1997). In the early days this was accomplished through visual inspection, then with template-matching techniques (e.g., SNID; Blondin & Tonry 2007), and most recently with deep learning techniques (e.g., Muthukrishna et al. 2019b). However, given the current discovery rate, and the anticipated LSST discovery rate, spectroscopic follow up is severely limited. The consequence of this fact is twofold. First, we need a way to effectively identify "needles" in the haystack – the events that will yield the greatest scientific return with detailed follow up observations (e.g., spectroscopy, radio, X-ray). Second, we need to devise methods to extract as much information and physical insight as possible from the "haystack" of SNe for which no spectroscopy or other data will be available. Here, we specifically focus on the latter issue and explore the question: Given complete optical light curves, can we classify SNe into their main spectroscopic classes (Ia, Ibc, IIP, etc.)?

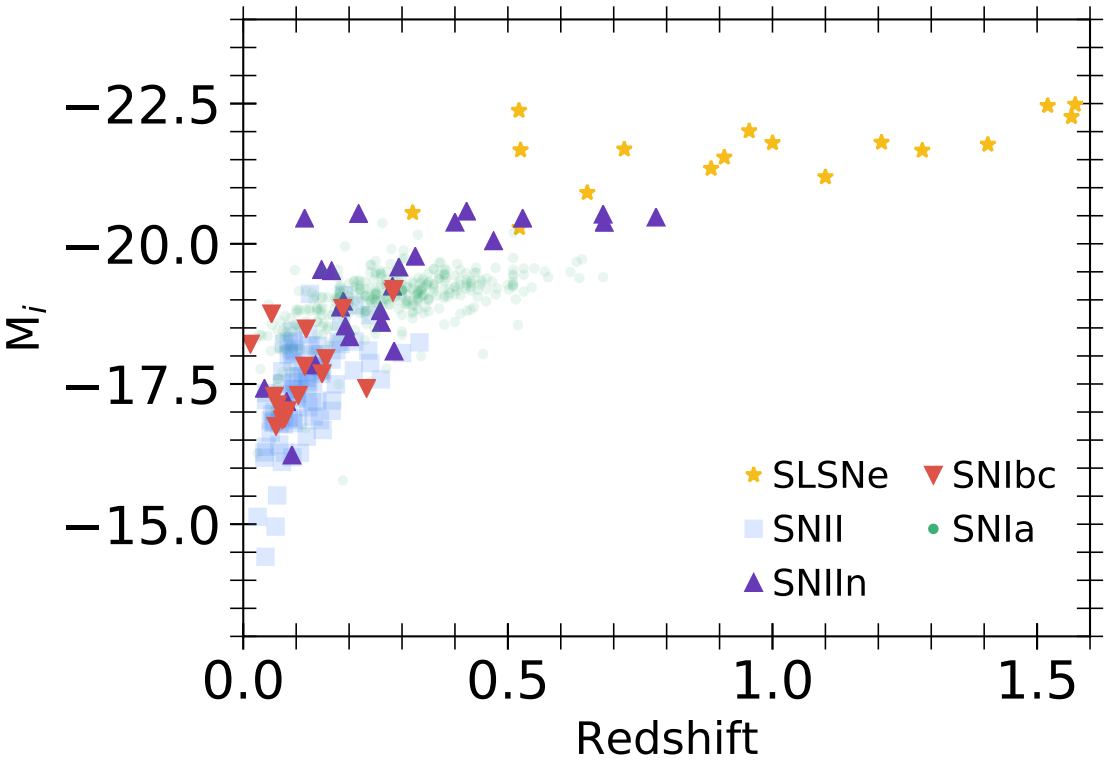

Figure 7.1: Peak $i_{\rm P1}$-band absolute magnitude versus redshift for the sample of PS1-MDS spectroscopically-classified SNe used in this study. We apply a cosmological k-correction to the peak magnitudes, but do not correct for the intrinsic spectral energy distribution of the various SNe. The sample includes five SN classes: Ia (green circle), Ibc (red downward triangle), II (blue sqaure), IIn (purple upward triangle), and SLSNe (yellow star).

Previous studies in this area have largely focused on the simpler task of separating thermonuclear Type Ia SNe from non-Type Ia SNe, motivated by the use of Type Ia SNe as standardizable cosmological candles, and taking advantage of their uniformity (e.g., Möller et al. 2016; Kimura et al. 2017). Separating the classes of core-collapse SNe

(CCSNe) is a broader and more challenging problem. First, unlike Type Ia SNe, CCSNe exhibit broad diversity between and within each class in terms of basic properties such as luminosity, timescale, and color (e.g., Drout et al. 2011; Taddia et al. 2013; Sanders et al. 2015; Nicholl et al. 2017; Villar et al. 2017b). This is due to their wide variety of progenitor systems, energy sources, and circumstellar environments. Second, the overall diversity of CCSNe is less thoroughly explored, due to small sample sizes and few published uniform studies. As a consequence, most previous works on photometric classification of CCSNe have relied on simulated datasets to train and test classification algorithms (e.g., Richards et al. 2011; Charnock & Moss 2017b; Kimura et al. 2017; Ishida et al. 2018). Simulated datasets are based on strong assumptions about the underlying populations of each SN class and often do not reflect the true event diversity, or the effects of actual survey conditions.

Here, we approach the question of SN photometric classification using a large and uniform dataset of 513 spectroscopically-classified SNe from the PS1-MDS. Importantly, the characteristics of this dataset in terms of filters, depth, and cadence are the closest available analogue to the LSST main survey design. We fit the observed light curves with a flexible analytical model that can accommodate all existing light curve shapes, using a Markov chain Monte Carlo (MCMC) approach. We then train and evaluate 24 classification pipelines that span different feature extraction, data augmentation, and classifications methods. We further use the posteriors of our MCMC fits to determine overall uncertainties on our classifications.

The Chapter is organized as follows. In §7.2 we introduce the PS1-MDS dataset utilized here. In §7.3 we describe our analytical light curve model and iterative MCMC fitting approach. In §7.4 we describe the key components of our various classification

pipelines, including feature extraction, data augmentation, and classification approaches. We present the results of our classifications in §7.5, compare to previous classifications efforts in §7.6, and discuss limitations and future directions in §7.7.

Throughout this Chapter, we assume a flat ΛCDM cosmology with $\Omega_M = 0.286$, $\Omega_\Lambda = 0.712$ and $H_0 = 69.3$ km s^{-1} Mpc^{-1} (Hinshaw et al. 2013).

7.2 PS1-MDS Supernova Light Curves and Spectroscopic Classifications

Pan-STARRS1 (PS1) is a wide-field survey telescope with a 1.8 m diameter primary mirror located on Haleakala, Hawaii (Kaiser et al. 2010). The PS1 1.4 gigapixel camera (GPC1) is an array of 60 4800 × 4800 pixel detectors with a pixel scale of 0.″258 and an overall field of view of 7.1 deg^2. The PS1 survey used five broadband filters, $g_{\rm P1}r_{\rm P1}i_{\rm P1}z_{\rm P1}y_{\rm P1}$. The details of the filters and the photometry system are given in Stubbs et al. (2010) and Tonry et al. (2012).

The PS1-MDS, conducted in 2010 − 2014, consisted of ten single-pointing fields for a total area of about 70 deg^2 (Chambers et al. 2016). About 25% of the overall survey observing time was dedicated to the MDS fields, which were observed with a cadence of about 3 days per filter in $g_{\rm P1}r_{\rm P1}i_{\rm P1}z_{\rm P1}$ to a 5σ depth of ≈ 23.3 mag per visit. The typical sequence consisted of $g_{\rm P1}$ and $r_{\rm P1}$ on the same night, followed by $i_{\rm P1}$ and then $z_{\rm P1}$ on subsequent nights. Observations in $y_{\rm P1}$-band were concentrated near full moon with a shallower 5σ depth of ≈ 21.7 mag; we do not use the $y_{\rm P1}$-band data in this study due to its significantly shallower depth and poorer cadence.

The reduction, astrometry, and stacking of the nightly images were carried out by the Pan-STARRS1 Image Processing Pipeline (IPP; Magnier et al. 2016b,a; Waters et al. 2016). The nightly stacks were then transferred to the Harvard FAS Research Computing Odyssey cluster for a transient search using the `photpipe` pipeline, previously used in the SuperMACHO and ESSENCE surveys (Rest et al. 2005; Miknaitis et al. 2007) and described in detail in our previous analyses of PS1-MDS data (Rest et al. 2014; Scolnic et al. 2017; Jones et al. 2018).

In the full PS1-MDS dataset we have identified 5235 likely SNe (Jones et al. 2017, 2018). During the course of the survey, spectroscopic observations were obtained for over 500 events using the MMT 6.5-m telescope, the Magellan 6.5-m telescopes, and the Gemini 8-m telescopes. We further obtained spectroscopic host galaxy redshifts for 3147 SN-like transients. The transients spectroscopically and photometrically classified as Type Ia SNe were published in Jones et al. (2017); the light curves and photometric classification of the remaining objects will be presented in future work. Similarly, the bulk of the Type IIP SNe (76 events) were published in Sanders et al. (2015), and the Type I SLSNe (17 events) were published in Lunnan et al. (2018). Here we focus on 513 spectroscopically classified events, which were classified using the SNID software package (Blondin & Tonry 2007). The sample contains 357 Type Ia SNe, 93 IIP/L SNe, 25 Type IIn SNe, 21 Type Ibc SNe, and 17 Type I SLSNe[1].

Our sample is limited events with high-confidence spectroscopic classifications with a statistically useful number of members in each class. As part of the PS1-MDS we

[1]Three of the 17 SLSNe (PS1-12cil, PS1-10ahf, and PS1-13or) do not have spectroscopic host redshift measurements. Lunnan et al. (2018) estimated their redshifts (0.32, 1.10 and 1.52, respectively) from strong rest-frame UV features for the $z > 1$ objects and SN Ic-like post-peak features for PS1-12cil.

discovered several other rare transients, including tidal disruption events (Gezari et al. 2012; Chornock et al. 2014b) and fast-evolving luminous transients (Drout et al. 2014), but the sample sizes for those are too small for inclusion in this study. It is possible that SNID misclassification exist in our dataset; e.g., low SNR events are more likely to match to Type Ia SNe (Blondin & Tonry 2007). To partially counteract this, we check each member of our Type Ibc and SLSNe classes (our smallest classes) by eye to ensure high purities. Finally, we note that the magnitude limit for our spectroscopic follow up was generally shallower by about 1.5 mag relative to the PS1-MDS nominal per-visit depth. This does not affect our ability to test classifiers on the spectroscopic sample itself, but will be considered when extending our method to the full photometric dataset in future work (see §7.6).

The light curves range from a minimum of 3 to ≈ 150 total data points in any filter with a signal-to-noise ratio of S/N > 3, with a median of about 30 data points in each light curve. We have only eliminated events with light curves that contain fewer than two 3σ detections in three or more filters, eliminating 7 SNe from our sample[2] (6 Type Ia SNe and 1 Type II SN) leaving 506 remaining SNe for our training set.

In Figure 7.1 we plot the peak absolute $i_{\rm P1}$ magnitude versus redshift for our spectroscopic sample. The sample spans $M_i \approx -14.5$ to -22.5 and extends in redshift to $z \approx 1.6$, with only the brightest classes (SLSNe and Type IIn) being observed at $z \gtrsim 0.6$. Specifically, we find a range of $M_i \approx -14.5$ to -18.5 mag for the Type II SNe, ≈ -16.5 to -19.5 mag for the Type Ibc SNe, -16 to -20.5 for the Type IIn SNe, and ≈ -20.5

[2]For completeness, we ran our final classifier on these light curves as well and found that 5 of the 6 Type Ia SNe, as well as the one Type II SN were actually correctly classified, albeit with a low classification confidence.

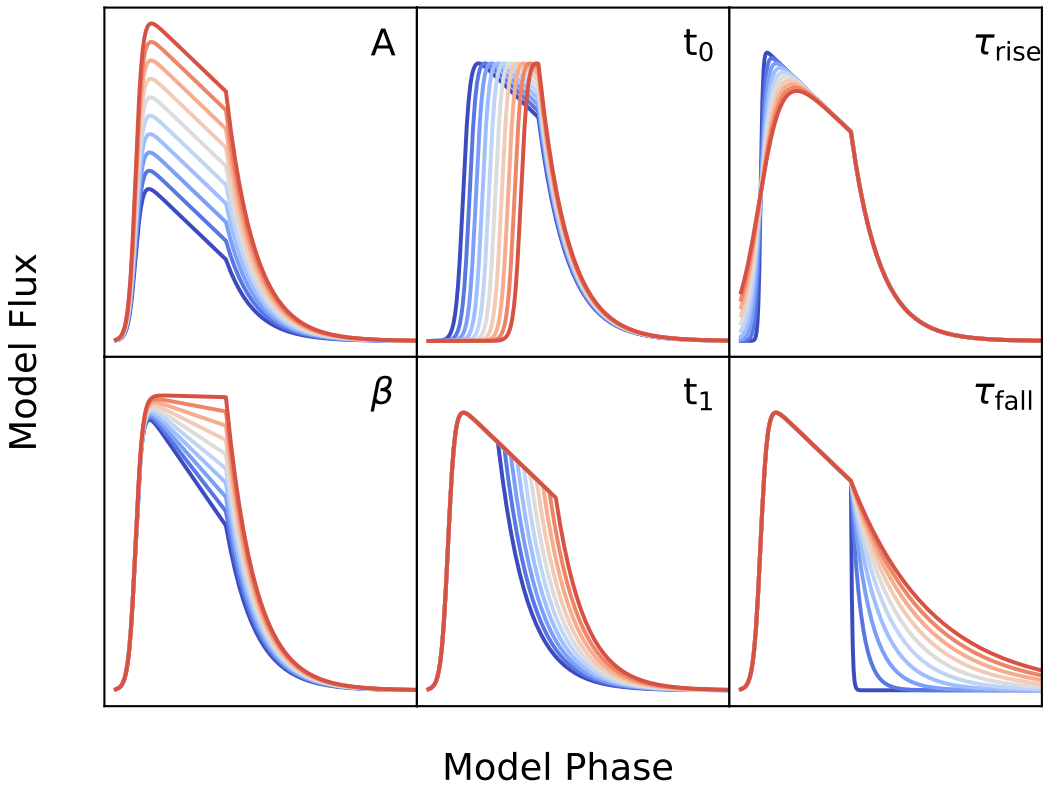

Figure 7.2: Example model light curves based on Equation 7.1 highlighting how each of the free parameters affects the light curves. The parameters are individually varied from low (blue) to high (red) values.

to −22.5 for the SLSNe.

7.3 Analytical Light Curve Model and Fitting

Rather than interpolating data points, a common method to standardize data is to fit a simple parametric model to the light curves (e.g., Bazin et al. 2009; Newling et al.

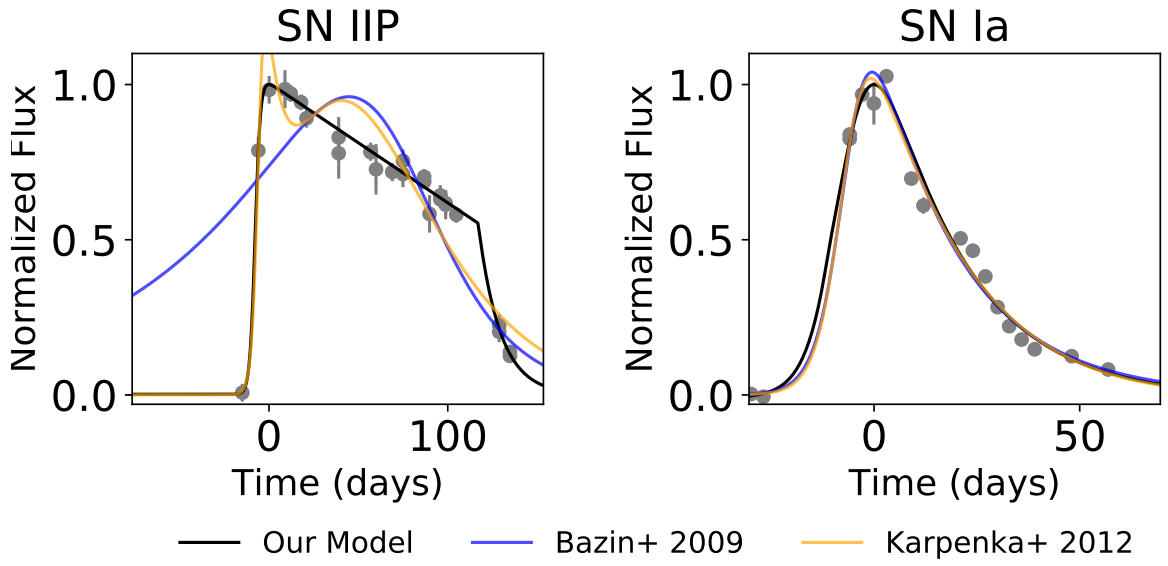

Figure 7.3: A comparison of our analytical light curve model (Equation 7.1; black line) to that of Bazin et al. (2009) (blue line) and Karpenka et al. (2013) (yellow line) for i-band lightcurves of both a Type IIP SN (*Left*) and a Type Ia SN (*Right*). Our model performs similarly for a Type Ia SN, but is superior at fitting SNe with a light curve plateau.

2011; Karpenka et al. 2013). However, the majority of existing analytical light curve models are best-suited for Type Ia SNe and have limited flexibility for the full observed range of SN light curve shapes. Here we present and fit our data with a new parametric piecewise model that is designed to be flexible enough for a broad range of light curve morphologies:

$$F = \begin{cases} \frac{A+\beta(t-t_0)}{1+e^{-(t-t_0)/\tau_{\rm rise}}} & t < t_1 \\ \frac{(A+\beta(t_1-t_0))e^{-(t-t_1)/\tau_{\rm fall}}}{1+e^{-(t-t_0)/\tau_{\rm rise}}} & t \geq t_1 \end{cases} \tag{7.1}$$

The model contains seven free parameters, whose effects on the resulting light curves

are shown in Figure 7.2. Although each parameter has a unique and interpretable effect, some degeneracies between the parameters exist. For example, the parameter A affects the amplitude of the light curve, although its value does not exactly correspond to the peak flux. Similarly, t_0 acts as a temporal shift in the light curve, but does not directly correspond to the time of explosion or the time of peak. The parameters, $t_{\rm rise}$, t_1, and $t_{\rm fall}$ control the rise, plateau onset, and fall time of the light curve, respectively. For the purposes of fitting, we reparameterize t_1 into a new parameter $\gamma \equiv t_1 - t_0$, which better represents the plateau duration of the light curve and results in fewer degeneracies when fitting. Finally, the parameter β controls the slope of the plateau phase.

This functional form is similar to those presented in Bazin et al. (2009) (with five free parameters) and Karpenka et al. (2013) (with six free parameters), but incorporates a plateau component. In Figure 7.3 we show examples of fits to a Type IIP SN and a Type Ia SN with our model, the Bazin model and the Karpenka model. Our model provides a better fit to both the fast rise time and plateau phase of the Type IIP SN light curve, and is flexible enough to also fit the smoother light curve of a Type Ia SN. We note that Sanders et al. (2015) presented a similar piecewise model with 11 free parameters to fit a sample of 76 PS1-MDS Type II SNe; however, Lochner et al. (2016b) found that this model was not robust when fitting data without the use of informative priors, due to the large number of free parameters. Additionally, the sharp transitions between rise and decline in the Sanders model make it difficult to fit CCSNe with smooth peaks.

One common Type Ia SN light curve feature missing from our model is the second peak in the red light curves at about 1 month post-explosion (e.g., Kasen 2006; Mandel et al. 2011; Dhawan et al. 2015). We find that this feature manifests itself as a "plateau"

in our analytical model in the i- and z-bands. However, as we show in §7.5, our classification pipelines can reliably classify Type Ia SNe without explicitly including a second peak in our model.

We fit the light curves using PyMC (V2; Patil et al. 2010), a Python module that implements a Metropolis-Hastings MCMC sampling algorithm. We assume uniform priors on all parameters with the exception of γ. We found that light curves typically fall in one of two solutions: light curves with a long plateau (in the case of Type IIP SNe) and light curves that lack a plateau (all other types). To best reflect this fact, we set the prior of γ to a double Gaussian peaked at 5 and 60 days. This prior helps to remove a degeneracy in which a steep exponential decline can resemble a linear decline. The priors are listed in Table 7.1. We use a standard likelihood function, incorporating both the observational error and a scalar white noise scatter term added in quadrature.

We find that several of our model parameters are correlated (degenerate) with one another. In particular, the amplitude (A) is negatively correlated with both the rise time ($t_{\rm rise}$) and plateau duration (γ) but negatively correlated with the start time (t_0). Additionally, duration is negatively correlated to both the rise time and start time, while the rise time is positively correlated with the start time.

We fit the light curve in each of the 4 filters independently, in the observer frame, but use an iterative fitting routine to incorporate combined information from all filters. We first run the MCMC to convergence on each filter independently with the same set of priors. We then combine the marginalized posteriors (i.e., we ignore parameter covariances) from each filter and use the combined posterior as a new prior for a second iteration of fitting. We can apply this process repeatedly, but we find that a single

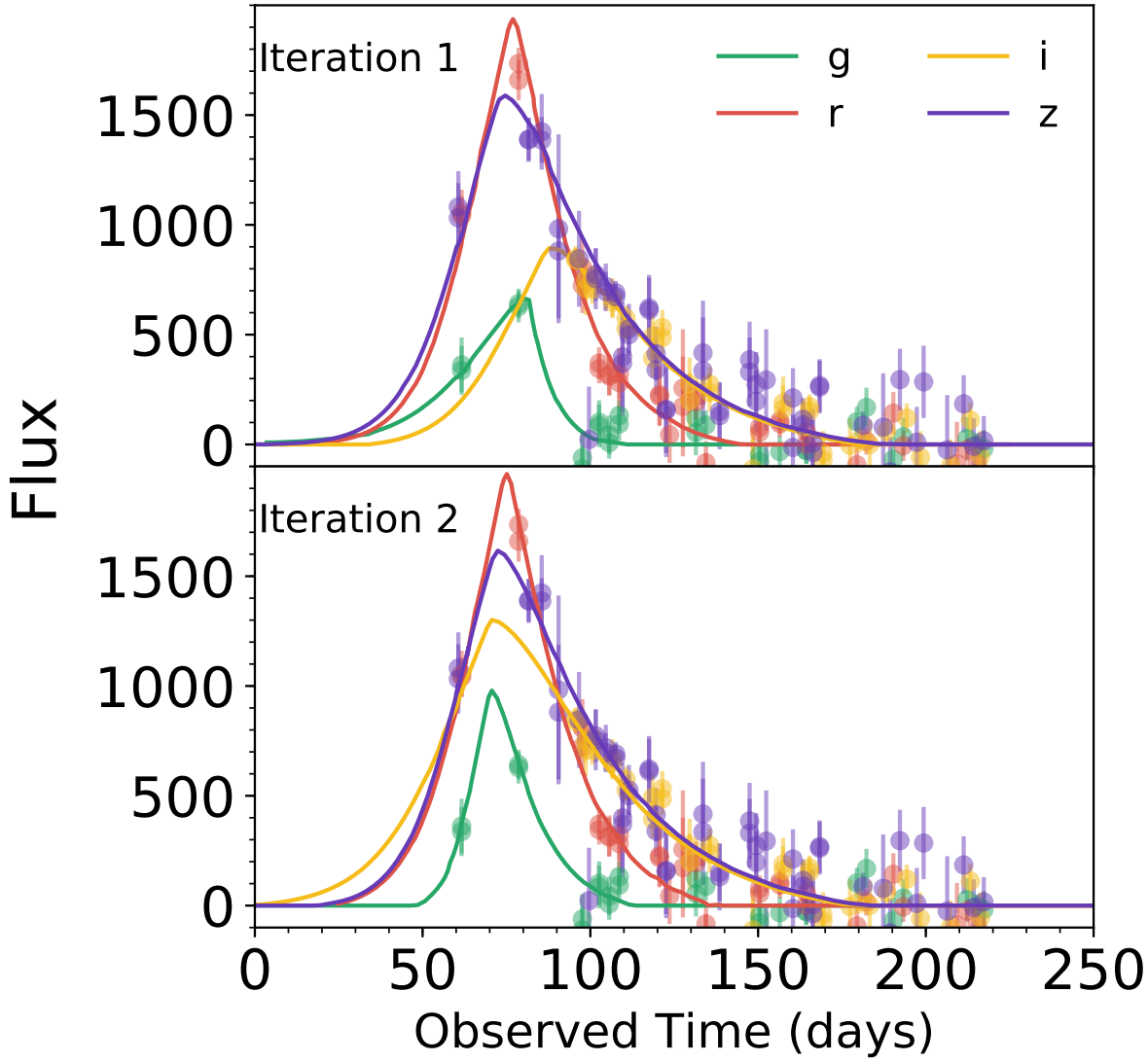

Figure 7.4: Example best-fit light curves in the 4 PS1 filters after the first (top) and second (bottom) MCMC iterations. Following the first iteration, the peak time varies significantly between the filters due to differences in the data quality and time sampling. The best-fit solution of the second iteration, using the combined posteriors from the first iteration, provides much better agreement in the light curve properties.

iteration is sufficient for the vast majority of events. Our iterative procedure is essential for fitting light curves in which some filters have significantly fewer data points, a situation that is common in photometric surveys due to differences in relative sensitivity, the intrinsic colors and color evolution of SNe, and varying observing conditions. An example of the best-fit solutions given by the first and second iterations is shown in Figure 7.4. In this example, the peak times in g- and i are in disagreement with r- and z due to poorly-sampled data in the former two filters. Following the second iteration, this disagreement is removed, leading to more realistic fits.

Representative light curves and their best fits are shown in Figure 7.5. The solutions are constrained for well-sampled light curves (e.g., the Type Ia SN shown) but more poorly constrained for sparse light curves (e.g., the SLSN shown). Crucially, because we have access to the full posterior of light curve solutions, we can feed many samples of the posterior through our classification algorithm to quantify the classification uncertainty for each event.

Unless otherwise specified, we use the observer-frame light curve fits to extract features. We then include the redshift to transform to absolute magnitudes, including a cosmological k-correction: $M = m - 5\log(d_L/10\text{pc}) + 2.5\log(1+z)$, where d_L is the luminosity distance. We do not apply k-corrections to account for the intrinsic spectral energy distribution of the various SN types.

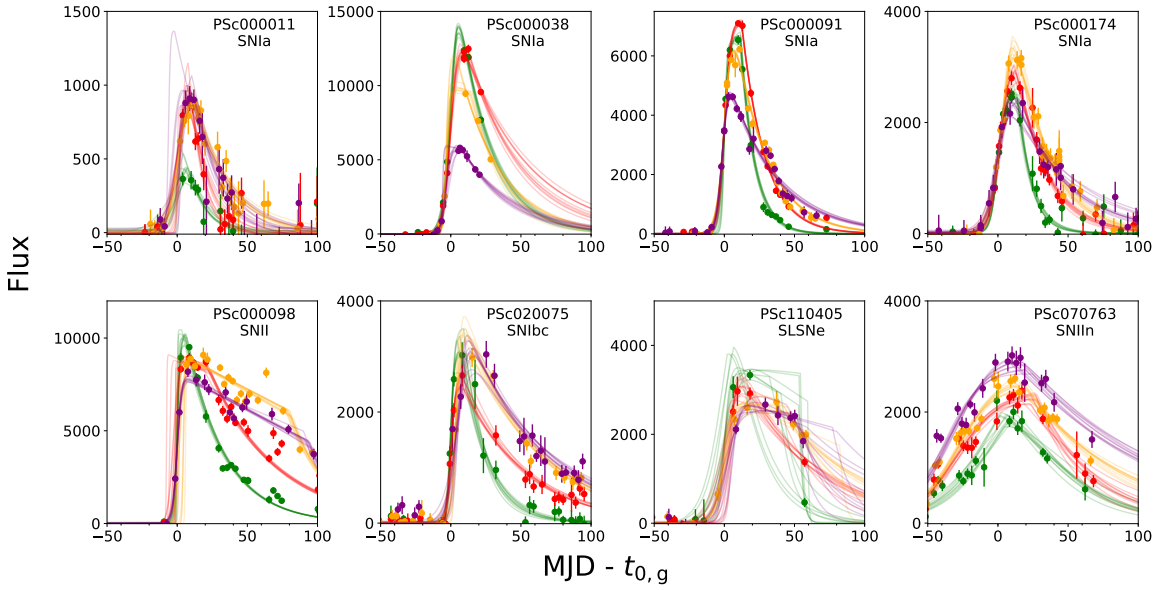

Figure 7.5: Example light curves and sample posterior draws of associated model fits in the 4 filters for various SN types. The model is described by Equation 7.1 and the fitting procedure is described in §7.3.

7.4 Classification Pipelines

For each SN, our MCMC fitting generates posterior distributions for the model light curve parameters. To train a classifier, we need to extract features from the light curves generated by the fitted parameters. We test several methods of feature extraction, data augmentation and classification. We describe each method in the following subsections, and we compare the algorithms in terms of classification purity, completeness, and accuracy in §7.5. *Purity* (also called *precision*) is defined as the fraction of events in a predicted class that are correctly identified; for example, if our classifier predicts a total of 100 Type Ia SNe, but only 70 of those are spectroscopically-classified as Type Ia

SNe, the purity would be 0.7. *Completeness* (also called *recall*) is defined as the fraction of events in an observed class that are correctly identified; for example, if our sample contains 100 spectrosopically-classified Type Ia SNe, but our classifier has only identified 70 of those events as Type Ia SNe, then our completeness would be 0.7. *Accuracy* is defined as the total fraction of events that are classified correctly as being a member or not a member of a given class; for example, if a sample of 100 SNe contains 70 spectrosopically-classified Type Ia SNe, and our classifier correctly identifies the 70 Type Ia SNe but incorrectly classifies 20 more CCSNe as Type Ia SNe, the overall accuracy is 0.8. The three terms are mathematically defined as follows:

$$\text{Purity} = \frac{\text{TP}}{\text{TP} + \text{FP}} \tag{7.2}$$

$$\text{Completeness} = \frac{\text{TP}}{\text{TP} + \text{FN}} \tag{7.3}$$

$$\text{Accuracy} = \frac{\text{TP} + \text{TN}}{\text{TS}}, \tag{7.4}$$

where TP (FP) is the number of true (false) positives, TN (FN) is the number true (false) negatives, and TS is the total sample size.

7.4.1 Feature Selection

Although our analytical model produces interpretable features for each light curve (albeit ones that are somewhat degenerate) we would like to explore various methods of feature extraction, based on the analytical fits. In particular, we explore the following four types of features:

- **Model Parameters (M):** We use the analytical model parameters as features, as well as the peak absolute magnitude in each filter, including a cosmological

k-correction but no correction for intrinsic SN colors and color evolution.

- **Hand-Selected Features (HS):** We use hand-selected interpretable features: the peak absolute magnitude in each filter, including a cosmological k-correction but no correction for intrinsic SN colors and color evolution; and the rest-frame rise and fall times by 1, 2 and 3 mag relative to peak (where we do *not* correct the rise and fall times for cosmological time-dilation).

- **Principal Component Analysis (PCA):** We fit a PCA decomposition model to the full set of analytical model fits (without any redshift corrections) independently for each filter. We use the first 6 PCA components from each filter, corresponding to an explained variance within the light curves of $\sim 99.9\%$. We also use the peak absolute magnitude, including a cosmological k-correction, in each filter in addition to the PCA components.

- **Light Curves (LC):** We use the model light curves as the features. We renormalize the flux of each light curve, correcting for luminosity distance; however, we find that neglecting time dilation corrections improves classification accuracy, and therefore we do not make these corrections. We down-sample each filter model to 10 observations logarithmic-spacing between t_0 and $t_0 + 300$ to decrease the number of features.

To provide some intuition, we highlight a sub-space of the hand-selected features ($M_{\rm peak}$ versus duration time to rise and fall by 2 mag) in Figure 7.6. We find that some SN classes, such as SLSNe versus Type II, or Type Ia versus Type IIn, easily separate in the duration-luminosity feature space. However, other classes, such as Type Ibc versus Type Ia and IIP, have substantial overlap in this space, regardless of filter. This

highlights that while simple heuristics can be used as first-order classifiers for some SN classes, other classes are intrinsically difficult to disentangle from light curve information alone.

7.4.2 Data Augmentation

Data augmentation is ubiquitous in machine learning applications, as a larger dataset can significantly improve the accuracy and generalizability of most classification algorithms. Data augmentation methods have already been utilized in the astrophysical context (e.g., Hoyle et al. 2015).

Here, we augment our training set with simulated events for two key reasons. First, our training set is unbalanced in terms of SN classes due to the differing observed rates of transients, with Type Ia SNe representing $\approx 70\%$ of our sample (and more generally, of any magnitude-limited optical survey). Classification algorithms trained on unbalanced training sets tend to over-classify all objects as the dominant class. This is because the algorithms can minimize the decision-making complexity by ignoring minority classes in favor of correctly classifying the majority class. In our case, a classification algorithm may preferentially label all objects as Type Ia SNe to achieve an overall high accuracy. Second, our training set is small in the context of machine learning, with the smallest class (SLSNe) containing just 17 events.

One approach to overcome this in the context of our method is to augment our training set with many draws from the MCMC posteriors. However, this would lead to clustering of solutions in feature-space that may bias the training algorithms. Instead, we address the issue of a small and imbalanced training set by synthesizing more event

samples using two techniques. First, we use the Synthetic Minority Over-sampling Technique (SMOTE; Chawla et al. 2002) to over-sample all the non-Type Ia SN classes to be equally represented as the Type Ia SNe. SMOTE creates synthetic samples in feature space by randomly sampling along line segments joining the k nearest neighbors of a sample, where k is a free parameter of the algorithm. Here we find that $k = 5$ performs well for sampling the minority classes. An example of the SMOTE resampling algorithm is shown in Figure 7.7. A key feature of SMOTE resampling is that it produces realistic samples within each class, but it cannot produce samples outside the extent of the original sample. While this prevents the generation of unphysical models, it may overly constrain the properties of classes with only a few samples (e.g., SLSNe).

Second, we augment the non-Type Ia SN classes by fitting the feature space of each class to a multivariate-Gaussian (MVG) and resampling from the fitted MVG. This is similar to the SMOTE algorithm in that it allows for the generation of new events that encompass a larger potential feature space. However, one key difference is that this method allows for synthesized events beyond the feature boundaries seen in the data. While this may lead to some unphysical models, it better reflects the potential spread in light curve parameters in poorly-sampled classes. An example of the MVG resampling is shown in Figure 7.7.

Both augmentation methods aim to increase our training set in a way which is representative of the set and therefore makes no attempt to correct for potential biases. This can potentially lead to increased misclassifications if our labelled training set is unrepresentative of a future test set; however, we expect no such effects within the training set of 513 objects.

7.4.3 Classification

Following the work of Lochner et al. (2016b), we test three classification algorithms: a support vector machine (SVM), a random forest (RF), and a multilayer perceptron (MLP). We optimize the hyperparameters of each algorithm independently using a grid search. Each algorithm and its tunable hyperparameters are described below. We use the `scikit-learn` python package throughout the classification portion of our pipeline.

Support Vector Machine (SVM)

A SVM classifies the training set by finding the optimal hyperplane in feature space to minimize the number of misclassified samples. In particular, the SVM will select a hyperplane that maximizes the distance between class samples nearest the hyperplane (also known as the support vectors). In the majority of cases, the classes are not linearly separable within the feature space alone (i.e., there may be significant overlap between classes). Instead, the features are expanded into an infinite basis function using the so-called Kernel trick (Aizerman 1964), allowing one to find a feature space in which the separating hyperplane is linear. We optimize the kernel and a regularization term using a coarse grid search, allowing the kernel size to logarithmically range from $\sigma = 1$ to $\sigma = 100$ and the normalization to logarithmically range from 1 to 1000. We find that a radial basis function kernel with width $\sigma = 10$ typically results in optimal classification, with normalization values ranging depending on the pipeline.

Random Forest (RF)

RF classifiers (Breiman 2001) are built on the idea of a decision tree, which is a model that generates a set of rules to map input features to classes. This mapping is based on a series of branching decisions based on feature values (e.g., "is the peak g-band magnitude brighter than -19?"). While single trees are theoretically sufficient for classification problems, they often lead to over-fitting due to specialized branching required for each class. Random forests overcome this problem by combining decision trees that are trained on different subsets of the training data and features. The ensemble of decision trees is then used as the classifier. There are a number of free parameters within a RF, including the number of decision trees, the number of nodes for each tree and the splitting rules for each node. Through a grid search of hyperparameters, we find that 100 decision trees utilizing the Gini impurity (the probability that a randomly chosen SN from a labelled class is misclassified) as a splitting criterion and allowing nodes to be split until all leaves are pure results in the highest accuracy.

Multilayer Perceptron (MLP)

A fully-connected MLP is the simplest artificial neural network (e.g., Schmidhuber 2015). It is composed of a series of layers of neurons, where each neuron is the dot product of the previous layer and a set of optimizable weights, passed through a nonlinear activation function. A "fully-connected" MLP means that each neuron is connected to all neurons in the preceding layer. The nonlinear activation function is what allows a MLP to model nonlinear mappings between the feature set and classes. MLPs have many tunable parameters, including the number of layers, the number of neurons within each layer,

the learning rate and a regularization term. We optimize the hyperparameters using a grid search, finding that two layers with ten neurons each typically performs best, and use the `Adam` optimization algorithm (Kingma & Ba 2014) to train the MLP.

An example of a complete pipeline, excluding the MCMC fitting step, is available on GitHub[3].

7.5 Classification Results

We combine each of the four feature extraction methods (M, HS, PCA, and LC), two data augmentation methods (SMOTE and MVG), and three classification algorithms (SVM, RF, and MLP) to test a total of 24 classification pipelines. For each pipeline, we use the full dataset to find the hyperparameters which optimize overall accuracy for the classification method. We optimize the hyperparameters over a coarse grid, due to the computational costs of performing a large grid search. We then perform leave-one-out cross-validation by iteratively removing one object from the sample, performing data augmentation on the remaining dataset, and training a classifier on the new set. We then test the trained classifier on the median posterior values of the removed object and record the predicted label. Due to computational costs, we only utilize the full posteriors for classification error estimation using our optimal pipeline.

[3] `https://github.com/villrv/ps1ml`

7.5.1 General Trends

In Figures 7.8 and 7.9 we plot the purity, completeness and accuracy for each of the 24 pipelines and each of the 5 SN classes. Figure 7.8 provides a matrix representation with the percentage score noted for each combination of pipeline and SN class, while Figure 7.9 shows the same results in histogram format to aid in visualizing the range of completeness, purity, and accuracy values across the 24 pipelines for each SN class.

We find that SLSNe and Type Ia SNe are consistently the classes with the highest purity and completeness, reaching $\gtrsim 90\%$ for the best classification pipelines. This is due to the fact that SLSNe are easily separable from the other classes due to their high luminosity and longer durations (Figures 7.1 and 7.6), while Type Ia SNe are tightly clustered in feature space due to their intrinstic uniformity.

In contrast, we find that Type Ibc SNe typically have the lowest purity and completeness, with $\approx 15-35\%$ and $\approx 25-65\%$, respectively, and a much wider spread in performance for the various pipelines. The lower classification success rate is due to broader diversity within Type Ibc SNe, as well as their significant overlap with Type Ia SNe (e.g., Figure 7.6).

For Type II SNe we find high values of purity and completeness of $\approx 65-85\%$ and $\approx 60-80\%$, respectively. This overall high success rate is mainly due to the presence of a plateau phase that helps to distinguish most Type II SNe from the other classes. However, the failed classifications are most likely due to the faster evolving Type II SNe (often called Type IIL), which tend to be misclassified as Type Ibc or Type Ia SNe due to overlap in light curve shapes (e.g., Figure 7.6).

Finally, for Type IIn SNe we find purity and completeness of $\approx 30-80\%$ and $\approx 45-70\%$, respectively, reflecting the broad diversity of light curve morphologies and luminosities, with some events overlapping similar areas in feature space with Type Ia and Ibc SNe (e.g., Figure 7.6). As for the Type Ibc SNe, we find quite a broad dispersion in performance between the various pipelines.

For the overall accuracy across the 5 SN classes, we find generally high values of $\approx 100\%$ for SLSNe, $\approx 95\%$ for Type IIn SNe, $\approx 90\%$ for Type II SNe, $\approx 85-95\%$ for Type Ibc SNe, and $\approx 85-90\%$ for Type Ia SNe. These values are essentially independent of the classification pipeline used.

To further explore the relative performance of the various pipelines, in Figure 7.10 we plot the distribution of completeness across the full dataset, grouping the classification pipelines by feature extraction method, classification method, and data augmentation method. We find that the classification method has the largest impact on completeness, with the RF classifiers performing noticeably better, and more uniformly, than the SVM and NN classifiers. In terms of feature extraction we find that use of the model parameters (M) and PCA are somewhat advantageous compared to hand-selected (HS) features and the LC approach, although the PCA extraction leads to a broader range of outcomes. Finally, the MVG augmentation method performs slightly better than SMOTE.

The top three pipelines in terms of purity, completeness and accuracy share RF classification and PCA feature extraction, with both MVG and SMOTE augmentation. Between these pipelines, the overall accuracy differs by $\lesssim 5\%$ across the 5 SN classes. In addition to performing well, the RF classifier also has the advantage of allowing us

to measure the relative important of each feature. For example, we test the relative importance of our hand-selected and model features in the RF classification pipeline using the "gini importance", a measure of the average gini impurity decrease across descending nodes (Leo et al. 1984). We find that the peak magnitudes are the most important interpretable features, with durations and other parameters being roughly equally important.

For simplicity, below we focus on the results of our pipeline with the highest purity (72%) and completeness (78%) scores with an average accuracy of 93% across the 5 SN classes. This pipeline consists of PCA feature extraction, MVG data augmentation, and RF classifier; however, we emphasize that this pipeline does not significantly outperform the others. In Figure 7.11 we present the final confusion matrix for this pipeline across the full training set. The confusion matrix is a quick-look visualization of how each class is correctly or incorrectly classified. We generate the confusion matrix using the full posteriors for each SN, so the probability densities have been effectively smoothed out across the matrix. To specifically assess the role of poor quality classifications, we show the confusion matrix for the full sample, as well as separately for classifications with a confidence of $p > 0.8$ only (representing $\sim 85\%$ of the original sample). In practice, one can optimize pipeline parameters to maximize sample purity, completeness or some other metric.

7.5.2 Assessing Misclassifications

Although the overall completeness for each SN class is high, we note several common misclassifications. First, Type II and Ia are the most likely classes to be misclassified as

Type Ibc SNe. The Type II SNe that are misclassified as Type Ibc SNe are typically either poorly sampled or are rapidly evolving (the so-called IIL events). Second, Type Ibc, IIn, and II SNe are the most likely classes to be misclassified as Type Ia SNe. This is again due to specific events in those diverse classes that occupy the region in feature space that overlaps with the uniform Type Ia SNe. Finally, Type IIn and Ibc SNe are the most likely classes to be misclassified as Type II SNe, again due to overlaps in feature space. Comparing the full sample to the subset of events with high classification confidence ($p > 0.8$) we find that the fraction of misclassified events indeed declines (most notably for Type Ibc and Ia SNe), indicating that some misclassifications are simply due to poorly sampled light curves. However, the overall trends for which classes are most likely to be misclassified as others remains the same, indicating that there is an inherent limitation to the classification success rate that is due to real overlaps in feature space.

We highlight several SNe that are misclassified, but with high confidence in Figure 7.12. In these examples, a spectroscopic Type II SN with a rapid linear decline is misclassified as a Type Ibc SN; a slightly dim Type Ia SN is misclassified as a Type Ibc SN; and a fairly luminous Type Ibc SN is misclassified as a Type Ia SN. In each of these cases, the posterior of the fitted light curves is narrow, leading to little variability (i.e., a high confidence) in the final classification. These events indicate that even with good photometric data quality there is inherent overlap of SNe in feature space that leads to misclassification.

The misclassifications of SNe are further highlighted in Figure 7.13. Each panel in the top part of Figure 7.13 represents a spectroscopically classified class, while in the bottom part each panel represents a photometrically assigned class. The misclassified events in both cases are labeled to provide insight into the most common

misclassification. In all panels the ordinate represents the overall classification certainty, based on many draws from the posteriors of each event. In all cases, the majority of misclassifications occur at the low confidence end ($p < 0.8$), but there are also high confidence misclassifications.

We explore the role of data quantity in Figure 7.14, where we plot the classification accuracy as a function of total light curve data points for all 5 SN classes. We again find that misclassifications are more likely in the regime of low number of data points, specifically $\lesssim 20$ data points. However, as noted above, there are also high confidence misclassifications for events with a large number of data points.

7.6 Comparison to Previous Photometric Classification Approaches

The photometric classification of optical transients has been previously explored in the existing literature. Previous studies on machine learning methods have focused almost exclusively on the binary problem of Type Ia versus non-Type Ia SN classifications (e.g., Campbell et al. 2013; Ishida & de Souza 2013; Jones et al. 2017), or have been trained and tested on simulated datasets (e.g., Kessler et al. 2010; Tonry et al. 2012; Möller et al. 2016; Charnock & Moss 2017b; Möller & de Boissière 2019; Muthukrishna et al. 2019b). We highlight the strengths and weaknesses of both approaches (which we note are disjoint) compared to our methodology. We emphasize that classification pipelines should ideally be compared using the same dataset and set of labels. No machine learning method, including the one presented in this Chapter, can be applied to a new

test set without retraining or careful consideration of training-vs-test set biases. This is especially crucial when comparing our method to those created for simulated datasets, which have known biases, uncertainties and simulated physics.

Identification of Type Ia SNe from photometric light curves is essential for precision cosmology in the era of large photometric surveys (Scolnic et al. 2014; Jones et al. 2017), which is why many studies have specifically focused on Type Ia SN classification. However, the binary problem of Type Ia vs non-Typa Ia SN classification is much narrower (and simpler) than full classification of CCSN classes. As standardizable candles, Type Ia SNe are fairly homogeneous with observational variations (excluding reddening) that are well described by two observable features: stretch and peak luminosity. As a result, it is easier to separate the small area of feature-space corresponding to Type Ia SNe from other transients. Studies that focus on this approach achieve a classification accuracy of $\gtrsim 0.95$ (e.g., Ishida & de Souza 2013; Charnock & Moss 2017b; Jones et al. 2017; Narayan et al. 2018; Pasquet et al. 2019). Although our pipeline is trained and tested on an empirical dataset for 5 distinct SN classes, we find that our achieved purity ($\approx 95\%$), completeness ($\approx 90\%$) and accuracy ($\approx 95\%$) for Type Ia SN classification are actually comparable to methods that specifically train on the binary classification. However, we note that studies such as Möller et al. (2016) achieve this high purity rate without redshift information, which our method currently requires.

The vast majority of previous photometric classification studies used simulated datasets to train classifiers. This is largely due to the fact that few homogeneous photometric datasets with large numbers of spectroscopically-classified SNe exist. Most studies that train on simulated datasets use the Supernova Photometric Classification Challenge (SNPCC) training set (Kessler et al. 2010). The SNPCC dataset consists

of 20,000 simulated SNe with *griz* light curves, generated from templates of Type Ia, Ibc, IIP and IIn SNe (they do not include SLSNe). This dataset was presented as a community-wide classification challenge in preparation for the Dark Energy Survey, and was widely successful, with the top algorithms reaching an average Type Ia SN classification purity of $\approx 80\%$ and completeness of $\approx 95\%$. Works such as Möller & de Boissière (2019) and Moss (2018) have reported average classification accuracies of $\approx 90\%$ for CCSNe classes (similar to our reported accuracies here). Similarly, Lochner et al. 2016b report an average Type Ia classification accuracy of $\sim 84\%$ using SALT2 light curve features. They further break down the CCSNe subclass into Type Ibc and Type II, where they report accuracies of $\sim 63\%$ and $\sim 93\%$, respectively. We caution that the SNPCC dataset is not representative of the real diversity we encounter in on-going and future surveys, and should not be used as a benchmark for CCSN classification. In particular, to generate synthetic light curves, Kessler et al. (2010) fit well-sampled real light curves from each CCSN class with a Bazin function. Then they stretch Nugent CCSN templates[4] to match the Bazin light curves. Variations within each class are included from both the sample of templates available and from random color variations derived from the Hubble scatter of Type Ia SNe and the peak luminosity derived from Richardson et al. (2002). While the collection of simulated Type Ia SNe likely samples the full phase-space of light curves, the non-Type Ia templates used to build the model light curve were severely limited. For example, only 2 Type IIn SN templates were used to generate 800 template light curves, and only 16 Type Ibc SN templates were used to generate 3,200 light curves. Because of this, we can expect methods that rely on this dataset to overestimate the accuracy of classifications for CCSN classes.

[4] `https://c3.lbl.gov/nugent/nugent_templates.html`

A new classification challenge, PLAsTiCC (Allam Jr et al. 2018; Kessler et al. 2019), is a more realistic simulated dataset that can be used as a benchmark for CCSN classification, although it too largely relies on theoretical models. Recent work by Muthukrishna et al. (2019) find an average completeness of $\approx 65\%$ over the five SN classes that we have classified here (although we note that the PLAsTiCC challenge combines Type IIP/L and Type IIn SNe into one class). Our average completeness is significantly higher, at $\approx 77\%$.

7.7 Limitations and Future Directions

The challenge of photometric classification for optical transients is broad and cannot be solved with one classification method alone. Like all methods, our classification pipeline aims to solve a simplified version of this problem: Given a complete light curve, a redshift, and a list of SN classes, what is the type of a given transient? Here we highlight several improvements that can be made to our pipeline, and more broadly outline outstanding problems in the field of transient classification.

Our pipeline requires a redshift, which simplifies the problem of classification by anchoring the absolute magnitudes of every light curve. In our training set these redshifts were obtained from spectra of the transients and their host galaxies. However, in the on-going and future surveys we expect that spectroscopic redshifts (from the SNe or host galaxies) will be rare. On the other hand, LSST will provide photometric redshifts (photo-z) for all galaxies with $m < 27.5$ mag, with an expected root-mean-square scatter of $\sigma_z/(1+z) \lesssim 0.05$ for galaxies with $m < 25.3$ (LSST Science Collaboration et al. 2009), and a fraction of outliers of $< 10\%$ (Graham et al. 2017). A classification algorithm that

can associate a transient to its host galaxy will therefore be able to utilize the photo-z value. We anticipate that the additional uncertainty in the model fits due to the photo-z uncertainty will not be a dominant factor. We additionally note that by including redshift information as a feature (even when doing so indirectly) we have limited the use of our pipeline to surveys of similar depth.

Additionally, our classification pipelines best utilizes full light curves, and are thus most naturally applicable for after-the-fact classification. The most natural use is on the yearly samples of $\sim 10^6$ transients from LSST to enable large-scale population studies, as well as targeted studies of specific subsets (e.g., host galaxies of SLSNe). While our method can work on partial light curves for real-time classification, its performance in this context is yet to be evaluated. Several studies that have explored the specific issue of real-time classification have found that recurrent neural networks perform well for this purpose (e.g., Charnock & Moss 2017b; Möller & de Boissière 2019; Muthukrishna et al. 2019a).

Our algorithm currently relies exclusively on information derived from the transient light curves (other than the redshift). However, useful contextual information about a SN can be extracted from the host galaxy. For example, SLSNe prefer low metallicity, dwarf galaxies (Lunnan et al. 2014), other CCSN classes span a wide range of star forming galaxies, and Type Ia SNe are found in both star forming and elliptical galaxies. Simple galaxy features, such as Hubble type, color, and SN offset can be easily incorporated into the classification pipeline (e.g.,Foley & Mandel 2013). This will be explored in follow-up work.

Furthermore, our algorithm is limited to classification within known SN classes

(in this case 5 classes). To add additional classes under our current framework, we would need to incorporate new data into the training set and retrain the classification algorithms. Our pipeline is amenable to rapid training, so it is feasible to incorporate more classes in this way. For a more complex classification pipeline (e.g., one involving a large neural network), one could incorporate new classes cheaply using "one-shot" learning (Lv et al. 2006), in which a classifier learns the characteristics of a new class using very limited examples. However, the addition of new classes will not solve the issue of how to identify unforeseen classes of transients and entirely new phenomena. Such a classifier is challenging to train, since outlier events are (by definition) rare.

Because our original training set is imbalanced and small, we needed to augment our dataset with simulated events drawn from the observed populations. For completeness, we test our best classification pipeline (PCA feature extraction and RF classifier) on the original training set without data augmentation. As expected, we find that we can classify classes with the most samples (Type Ia and II SNe) or those that are well-separated in feature space (SLSNe), as well as or better than our classification pipeline with data augmentation. However, the completeness of the minority classes, like Type Ibc and IIn SNe, falls by $20 - 40\%$. This is a good indication that data augmentation in the extracted feature space is a potential solution to the imbalanced classes.

Our method neglects the possibility of a biased spectroscopic sample. For example, if the spectroscopic samples contains only the brighter end of the luminosity function for rare transients. In our presumed classification case in which we have access to the full light curves, one can use the full dataset to detect and minimize the effects of selection bias without knowing the true underlying distribution. For example, one can

re-weight the importance of each SN in the spectroscopic training sample to better reflect the distribution of features from the full dataset (using, e.g., Huang et al. 2007 and Cortes et al. 2008). A detailed study of the effect of observational biases on transient classification is essential, but beyond the scope of this work.

Finally, we note that classification is only the first step in understanding the uncovered transients. Even for the currently rare SLSN class, LSST will discover $\sim 10^4$ events per year (Villar et al. 2018). Additional data cuts that remove light curves with a minimal *information content* (or those from which we cannot extract physical parameters) may be necessary in order to realistically fit a representative set of light curves.

7.8 Conclusions

Given increasingly large datasets and limited spectroscopic resources, photometric classification of SNe is a pressing problem within the wide scope of time-domain astrophysics. Here we used the PS1-MDS spectroscopiccaly classified SNe dataset (513 events) to test a number of classification pipelines, varying the features extracted from each light curve, the augmentation method to bolster the training set, and the classification algorithms. We used a flexible analytical model with an iterative MCMC process to model the $g_{P1}r_{P1}i_{P1}z_{P1}$ light curves of each event, and to generate posterior distributions. We find that several pipelines (e.g., PCA feature extraction, MVG resampling, and RF classifier) perform well across the 5 relevant SN classes, achieving an average accuracy of about 90% and a Type Ia SN purity of about 95%.

Our study is the first to use an empirical dataset to classify multiple classes of SNe, rather than just Type Ia versus non-Type Ia SN classification. Our overall results rival similar pipelines trained on simulated SN datasets, as well as those that utilize only a binary classification. This indicates that we can utilize this approach to generate robust samples of both common and rare SN type (e.g., Type IIn, SLSNe) from LSST.

Finally, we highlight several areas for future exploration and improvement of our classification approach, including the use of contextual information and the possible application to real-time classification. We plan to extend this work and other classification approaches to the full set of PS1-MDS SN photometric light curves in future work.

Acknowledgments

The Berger Time-Domain Group is supported in part by NSF grant AST-1714498 and NASA grant NNX15AE50G. V.A.V. acknowledges support by the National Science Foundation through a Graduate Research Fellowship. The UCSC team is supported in part by NASA grant NNG17PX03C; NSF grants AST–1518052 and AST–1815935; the Gordon & Betty Moore Foundation; the Heising-Simons Foundation; and by a fellowship from the David and Lucile Packard Foundation to R.J.F. R.L. is supported by a Marie Skłodowska-Curie Individual Fellowship within the Horizon 2020 European Union (EU) Framework Programme for Research and Innovation (H2020-MSCA-IF-2017-794467). Some of the computations in this Chapter were run on the Odyssey cluster supported by the FAS Division of Science, Research Computing Group at Harvard University. The Pan-STARRS1 Surveys (PS1) and the PS1 public science archive have been made

possible through contributions by the Institute for Astronomy, the University of Hawaii, the Pan-STARRS Project Office, the Max-Planck Society and its participating institutes, the Max Planck Institute for Astronomy, Heidelberg and the Max Planck Institute for Extraterrestrial Physics, Garching, The Johns Hopkins University, Durham University, the University of Edinburgh, the Queen's University Belfast, the Harvard-Smithsonian Center for Astrophysics, the Las Cumbres Observatory Global Telescope Network Incorporated, the National Central University of Taiwan, the Space Telescope Science Institute, the National Aeronautics and Space Administration under Grant No. NNX08AR22G issued through the Planetary Science Division of the NASA Science Mission Directorate, the National Science Foundation Grant No. AST-1238877, the University of Maryland, Eotvos Lorand University (ELTE), the Los Alamos National Laboratory, and the Gordon and Betty Moore Foundation.

Table 7.1:: Parameter Descriptions and Priors

Parameter	Description	Prior
$\tau_{\rm rise}$ (days)	Rise Time	U(0.01,50)
$\tau_{\rm fall}$ (days)	Decline Time	U(1,300)
t_0 (MJD)	"Start" Time	U($t_{\rm min} - 50$, $t_{\rm max} + 300$
A	Amplitude	U(3σ,100 $F_{\rm max}$)
β (flux/day)	Plateau slope	U($-F_{\rm max}/150$,0)
c (flux)	Baseline Flux	U(-3σ,3σ)
γ (days)	Plateau duration	$(2/3)N(5,5) + (1/3)N(60,30)$

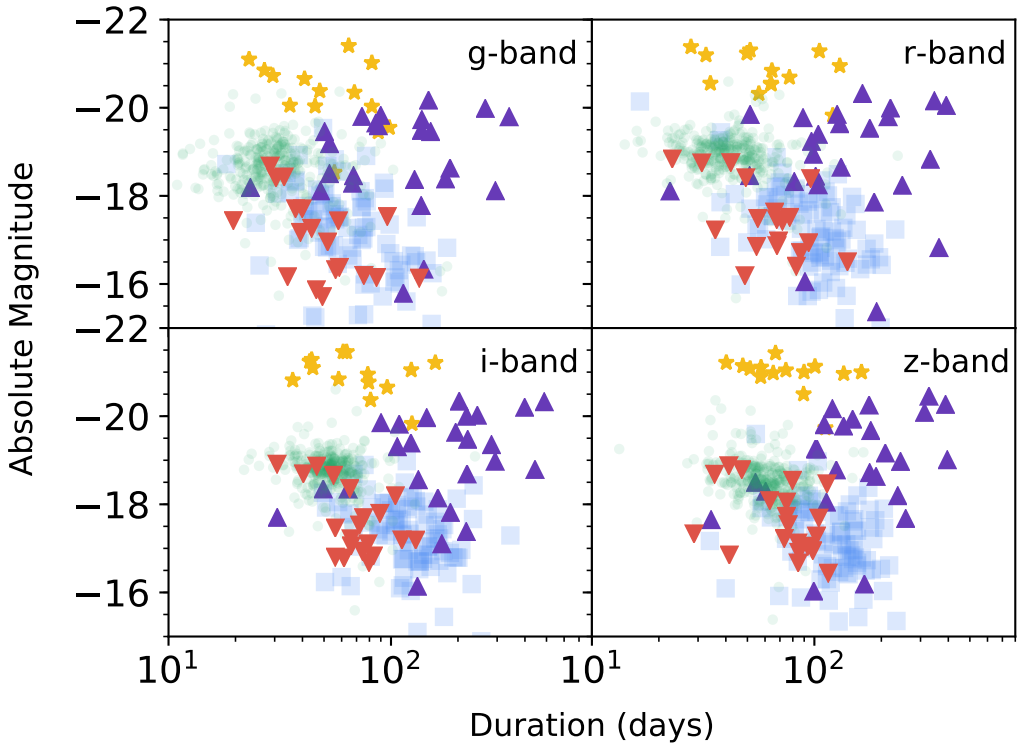

Figure 7.6: Duration-luminosity feature space of the dataset in the 4 PS1 filters. Duration is defined as the total time for the light curves to rise and decline by 2 mag relative to the peak. The plotted values are from the median model fits to the light curves using Equation 7.1. The sample includes the five SN classes: Ia (green circle), Ibc (red downward triangle), II (blue square), IIn (purple upward triangle), and SLSNe (yellow star).

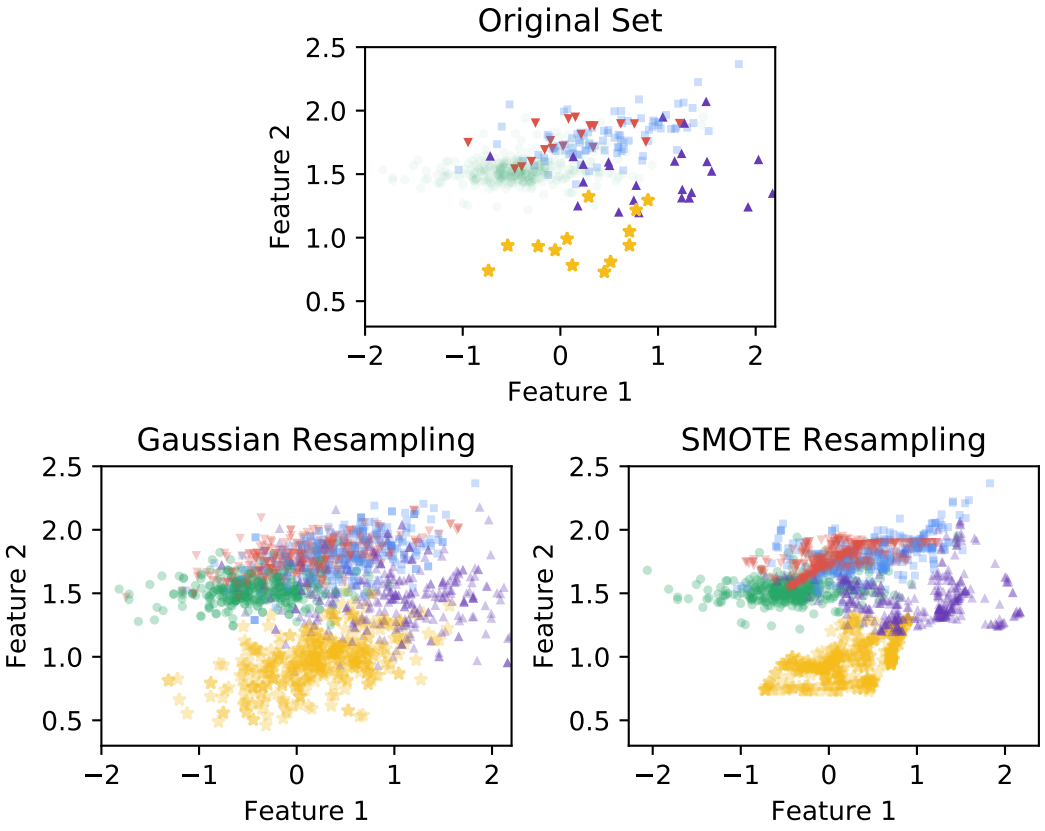

Figure 7.7: *Top:* The original dataset plotted in terms of feature 1 versus feature 2, indicating both the span of the various SN classes and the imbalance in number of events per class. *Bottom:* The augmented dataset using MVG resampling (*Left*) and SMOTE resampling (*Right*).

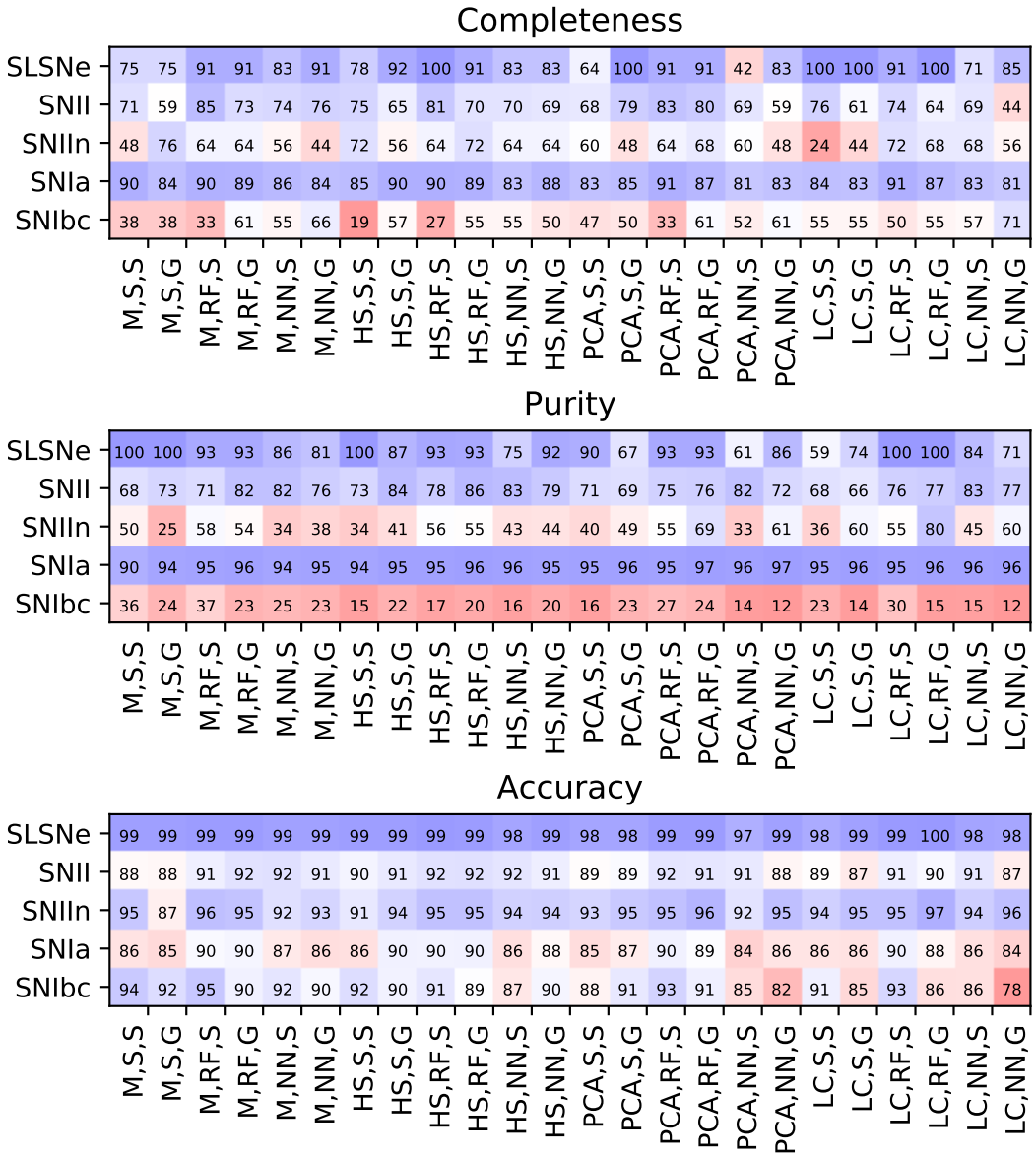

Figure 7.8: Completeness (*Top*), Purity (*Middle*) and Accuracy (*Bottom*) for each of the five spectrosopic SN classes across the 24 classification pipelines. Each pipeline is encoded by its feature extraction method (M, HS, PCA, LC), data augmentation method (S, G) and classification method (SVM, RF, NN).

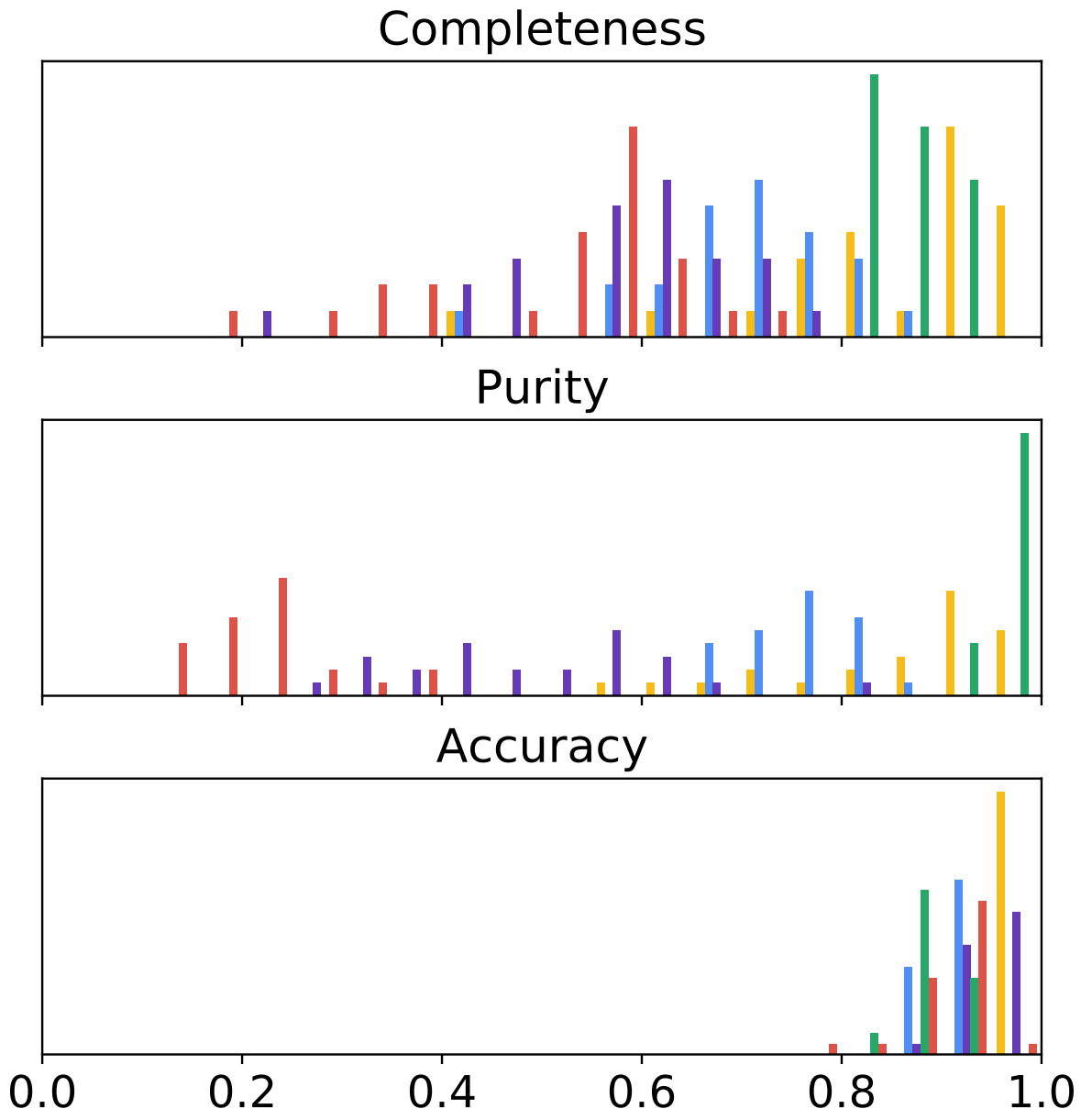

Figure 7.9: Histograms of Completeness (*Top*), Purity (*Middle*) and Accuracy (*Bottom*) for each of the five spectroscopic SN classes across the 24 classification pipelines.

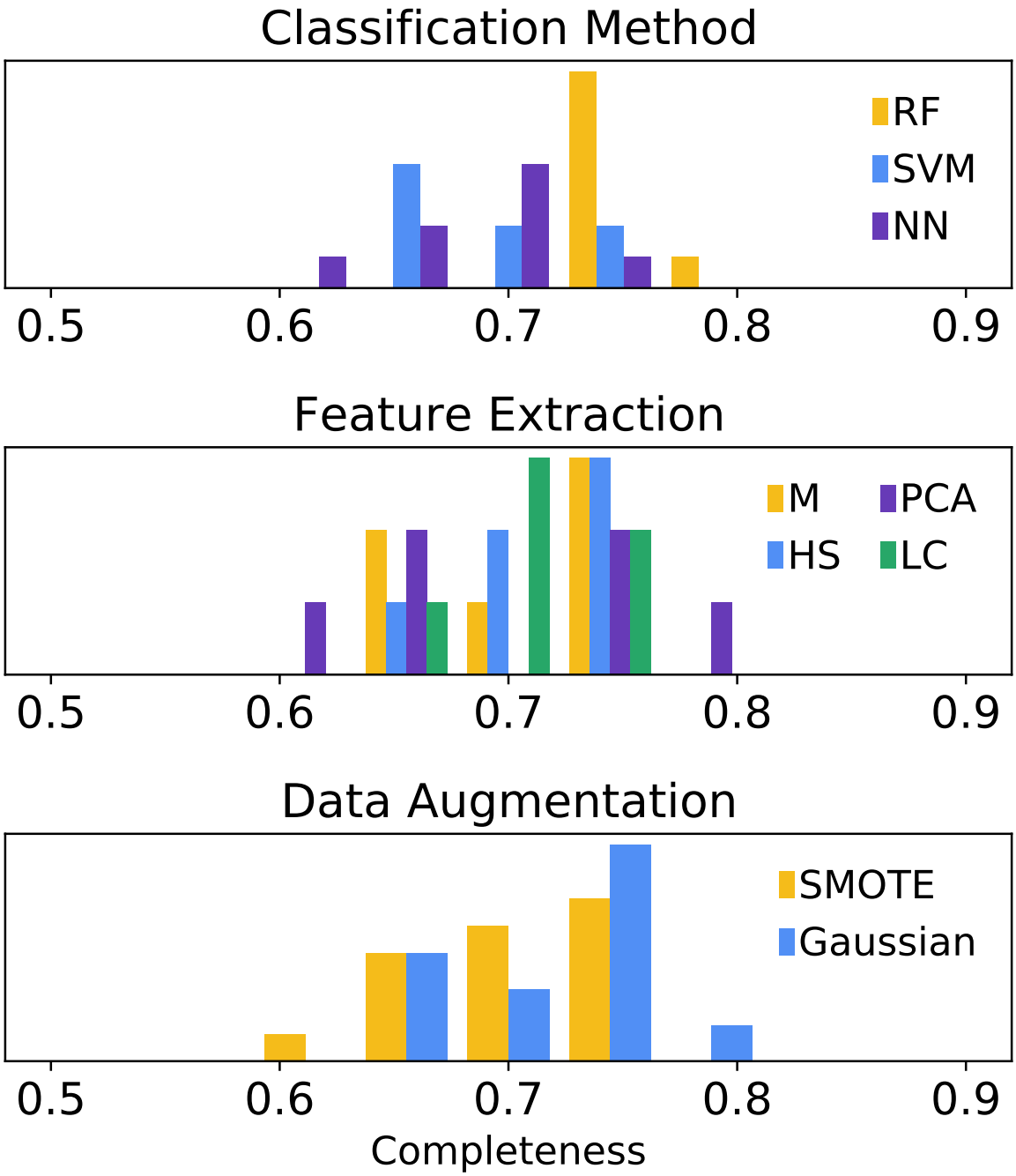

Figure 7.10: Histograms of completeness across all 5 SN classes, grouped by classification method (*Top*), feature extraction method (*Middle*) and data augmentation method (*Bottom*).

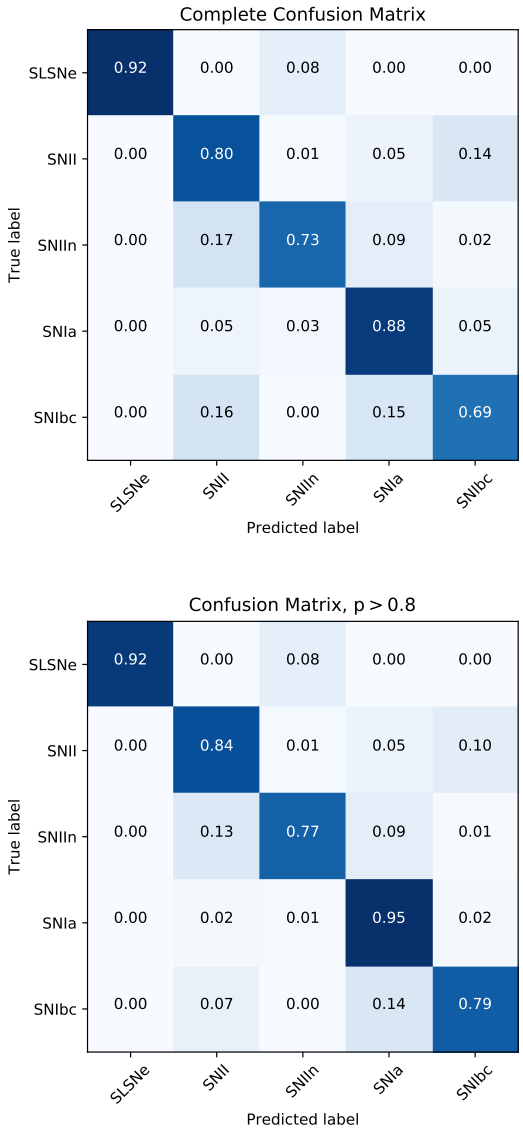

Figure 7.11: Confusion matrix for one of our best performing classification pipelines (PCA feature extraction, MVG data augmentation, and RF classifier) calculated using the full posterior distributions for each SN. We show the confusion matrix for both the full SN sample of 513 objects (*Top*) and only for the 429 events with a high classification confidence probability of $p > 0.8$ (*Bottom*).

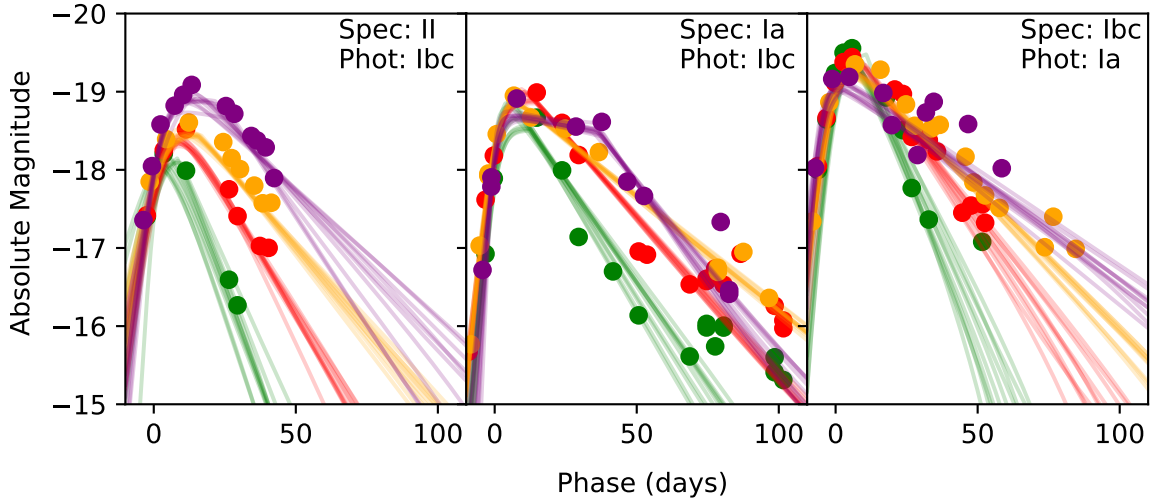

Figure 7.12: Light curves of three SNe classified incorrectly, but with high confidence ($p > 0.9$). We note the spectroscopic and photometric classification of each event. Given the high data quality, these misclassifications are due to inherent overlap between SNe in feature space.

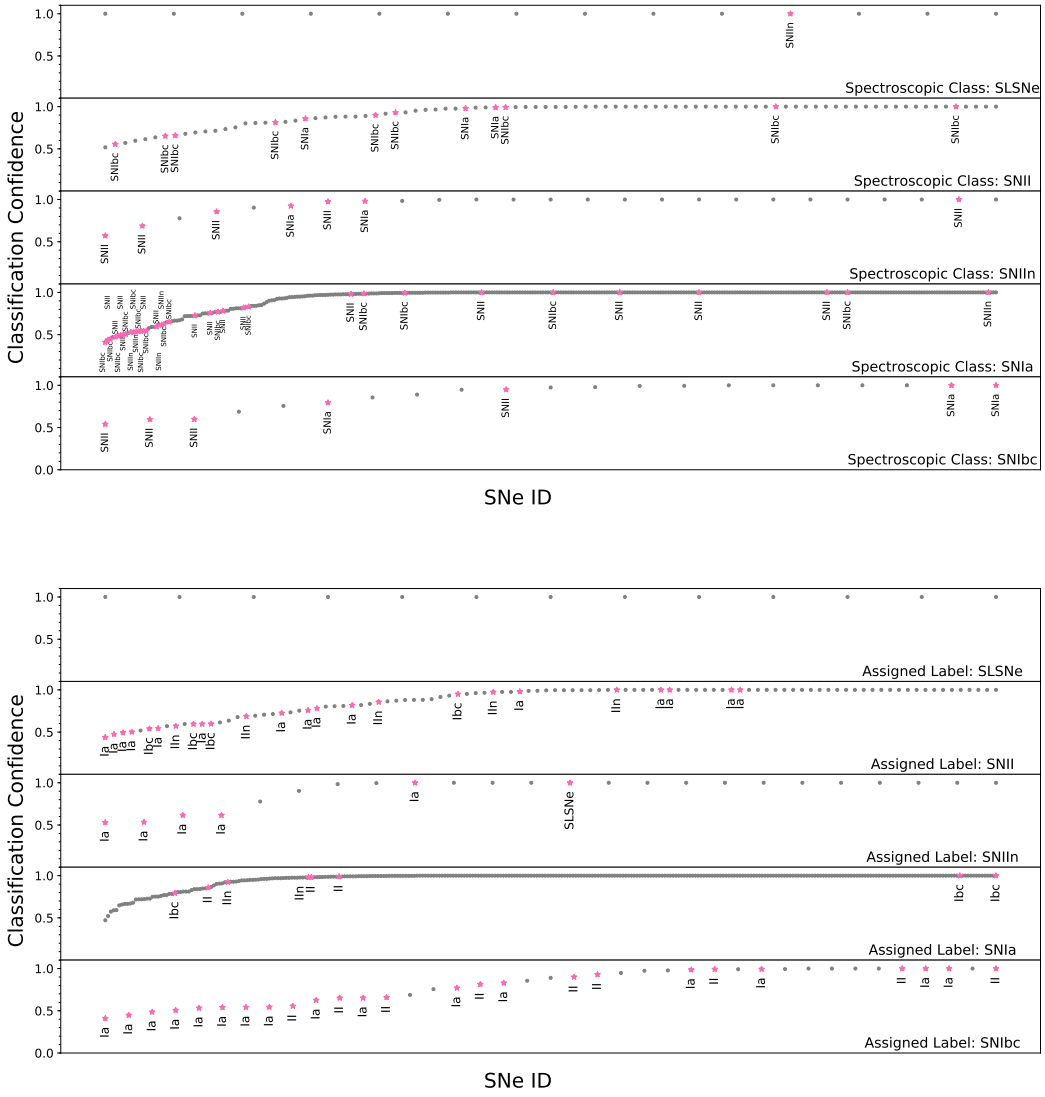

Figure 7.13: *Top:* For each *true* spectroscopic class, we show the correct classifications (grey) and misclassifications (pink), with the classification confidence plotted on the ordinate. The misclassified label is given next to each misclassified event. We find that the bulk of the misclassifications are concentrated at low classification confidence. *Bottom:* For each *assigned label, we again show the correct classifications (grey) and misclassifications (pink). The correct class label of each misclassified event is given.*

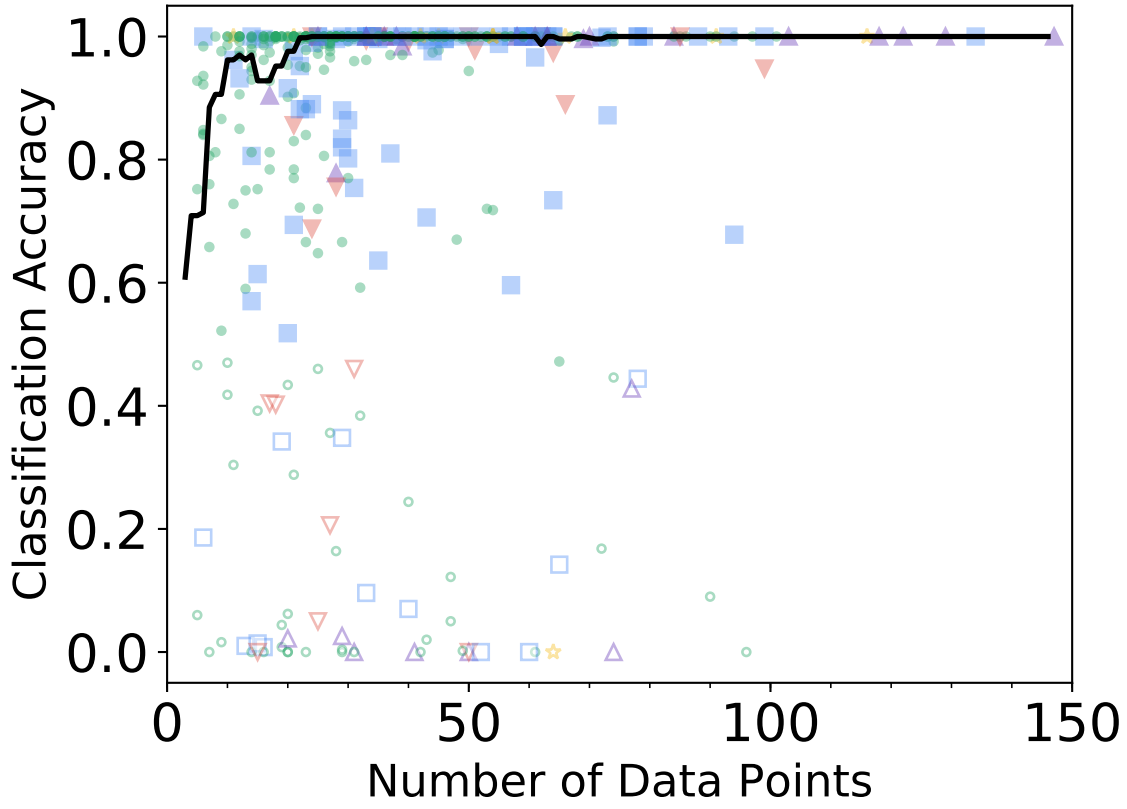

Figure 7.14: Classification accuracy as a function of number of light curve data points. The colors and shapes reflect the SN classes, and the black line represents a smoothed median to guide the eye. Filled symbols are SNe classified correctly, while open symbols are misclassified events. We find that misclassifications are more prevalent for light curves with fewer points, but also that some events are misclassified even with tens of data points, as also highlighted in Figure 7.12.

Chapter 8

Let It RAENN: A Semi-supervised Photometric Classification Pipeline for Spectroscopically-classified PanSTARRs Supernovae

V. A. Villar, et al.,

in Preparation

Abstract

Automated classification of supernovae (SNe) based on optical photometric light curve information is essential in the upcoming era of wide-field time domain surveys, such as

the Legacy Survey of Space and Time (LSST). Photometric classification can enable real-time identification of interesting events for extended multi-wavelength follow-up, as well as archival, population studies. Here we present the complete sample of 5,244 SN-like light curves (in $g_{P1}r_{P1}i_{P1}z_{P1}$) from the Pan-STARRS1 Medium-Deep Survey (PS1-MDS). The PS1-MDS is similar to the planned LSST in terms of cadence, filters and depth, making this a useful training set for the community. Using this dataset, we train a novel semi-supervised machine learning algorithm to photometrically classify 2,870 SN-like light curves with host galaxy redshift estimates. Our algorithm consists of a random forest supervised classification step and a novel unsupervised step in which we introduce a recurrent-neuron based autoencoder architecture (RAENN). Our final pipeline results in a class-averaged accuracy of 95% across five SN classes. We find the highest accuracy rates for Type Ia SNe and SLSNe and the lowest for Type Ibc SNe. Our photometrically-classified sample breaks down into: 67% Type Ia (1923 objects), 19% Type II (545 objects), 6% Type IIn (173 objects), 6% Type Ibc (172 objects), and 2% Type I SLSNe (57 objects). Finally, we discuss how this algorithm can be modified for online LSST data streams.

8.1 Introduction

Time-domain astrophysics has entered a new era of large photometric datasets thanks to on-going and upcoming wide-field surveys, including Pan-STARRS (PS; Kaiser et al. 2010, the Asteroid Terrestrial-impact Last Alert System (ATLAS; Jedicke et al. 2012), the All-Sky Automated Survey for SuperNovae (ASASSN; Kochanek et al. 2017), the Zwicky Transient Facility (ZTF; Kulkarni 2018), the Legacy Survey of Space and Time

(LSST; Ivezic et al. 2011), and the Wide Field Infrared Survey Telescope (WFIRST; Spergel et al. 2015). LSST, conducted by the Vera C. Rubin Observatory between 2022 and 2032, is expected to increase the current annual rate of discovered SNe by two orders of magnitude, to over one million discoveries per year.

Historically, SNe and other optical transients have been classified and studied based on their optical spectra. Class labels are largely phenomenological, dependent on the presence of elements in the photospheric-phase spectra (see e.g., Filippenko 1997 for a review). SNe, for example, have historically been classified as Type I or Type II based on the absence or presence of strong Hydrogen Balmer lines, respectively. As the number of events increased, further classes were created to account for the increased diversity. For example, subclasses of Type I SNe, Type Ib and Type Ic, were created to designated the presence and absence of Helium, respectively. Today, semi-automated software such as `SNID` (Blondin & Tonry 2007) and `Superfit` (Howell et al. 2005) match SN spectra to a library of previously classified events to determine the spectroscopic class.

However, spectroscopic follow up remains an expensive endeavor, taking up to several hours on 8-meter class telescopes to classify a single object. Wide-field surveys have enabled the discovery of tens of thousands of extragalactic transients each year. Of these, roughly 10% of events actually receive a spectroscopic classification[1]. Spectroscopic follow up is not expected to significantly increase when the LSST begins, although the discovery rate of SNe will increase to well over one million events annually. This means that only 0.1% of events will be spectroscopically classified.

Given this growing rate of discovery, and limited spectroscopic resources,

[1]Based on data from the public Open Supernova Catalog (Guillochon et al. 2017).

transient events are increasingly being classified by their photometric light curves into spectroscopically-defined classes. Luckily, the phenomenological labels often correspond to unique underlying astrophysics. For example, while Type Ia SNe are spectroscopically classified by their lack of Hydrogen and strong Si II absorption, these features distinctly originate from the thermonuclear detonations of carbon-oxygen white dwarfs. The unique progenitor system leads to other observable features, some of which are captured in broadband optical light curves. Said features allow transients to be classified into their traditional *spectroscopic* subclasses using only their broadband, optical light curves.

There is a growing literature on light curve classifiers that rely on data-driven and machine learning algorithms. Most studies use *supervised* learning, in which the training set consists of SNe with known classes (e.g., Lochner et al. 2016; Charnock & Moss 2017a; Boone 2019; Villar et al. 2019; Möller & de Boissière 2020) However, SN classification can benefit from *semi-supervised* methods, in which the training set contains both labelled and unlabelled SNe. The unlabelled set is used to better understand low-dimensional structure in the SN dataset to improve classification. Richards et al. (2012), for example, created a diffusion map (a nonlinear dimensionality reduction technique) based on Supernova Photometric Classification Challenge (SPCC; Kessler et al. 2010) light curve similarities in shape and color. They use the diffusion map to extract 120 non-linear SN features from each labelled SN, which are then used to train a random forest classifier. More recently, Pasquet-Itam & Pasquet (2018) introduced the `PELICAN` classifier, also trained on synthetic SPCC data. `PELICAN` uses a convolutional neuron-based autoencoder to encode nonlinear SN features and a set of fully connected neural network layers to classify the full set of light curves.

Here we introduce a new semi-supervised classification method for SNe, which

utilizes a recurrent neuron-based autoencoder (RAENN). This method is uniquely trained on real (rather than simulated) data from the Pan-STARRs Medium Deep Survey (PS1-MDS) and is optimized for general SN classification (as opposed to Ia versus non-Ia classification). We then use the RAENN features with a random forest to classify the PS1-MDS sample of 2,870 SN-like transients. We publish the full sample and associated labels for community use.

The Chapter is organized as follows. In §8.2, we review the PS1-MDS and associated sample of "SN-like" objects. In §8.3 we introduce the RAENN architecture and training procedure. We present the classification results and discuss implications in §8.4 and §8.5. We conclude in §8.6. Throughout this Chapter, we assume a flat ΛCDM cosmology with $\Omega_M = 0.286$, $\Omega_\Lambda = 0.712$ and $H_0 = 69.3$ km s^{-1} Mpc^{-1} (Hinshaw et al. 2013).

8.2 The PS1-MDS Supernova Sample

PS1 is a wide-field survey telescope located near the summit of Haleakala, Hawaii with a 1.8 m diameter primary mirror and a 1.4 gigapixel camera (GPC1) (Kaiser et al. 2010). PS1-MDS was conducted between Jul 2009 and Jul 2014. It consisted of 10 single-pointing fields, each of approximately 7.1 deg^2 with a pixel-scale of $0.''25$. The survey was conducted in five broadband filters ($g_{\rm P1}r_{\rm P1}i_{\rm P1}z_{\rm P1}y_{\rm PS1}$ (Stubbs et al. 2010; Tonry et al. 2012) with a nominal cadence of 3 days per filter in four filters ($g_{\rm P1}r_{\rm P1}i_{\rm P1}z_{\rm P1}$), with a 5σ limiting magnitude of ≈ 23.3 per visit. In general, PS1-MDS observed a field in $g_{\rm P1}$ and $r_{\rm P1}$ on the same night, followed by $i_{\rm P1}$ and then $z_{\rm P1}$ on subsequent nights. PS1-MDS included observations in the $y_{\rm P1}$-band, primarily near full moon and with a shallower 5σ limiting magnitude of ≈ 21.7. Due to the poor cadence and shallow depth,

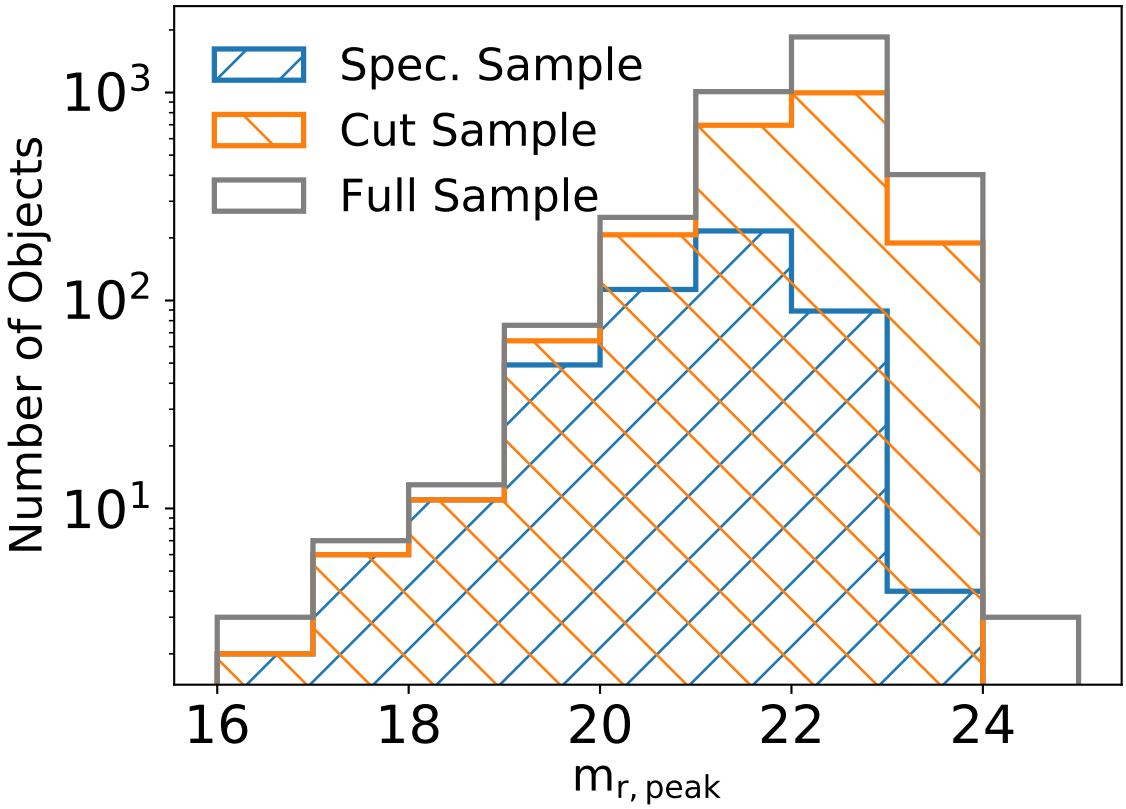

Figure 8.1: Peak apparent r-band magnitude of the full SN-like dataset (grey), objects used in our unsupervised method (orange) and the spectroscopic sample (blue). The spectroscopic dataset is roughly one magnitude brighter than the full dataset.

we do not present or use the $y_{\rm P1}$ here.

During its 5-year survey, PS1-MDS discovered 5,235 SN-like objects (where "SN-like" is defined in Jones et al. 2017). Of these, $\approx 10\%$ of events, generally with $m_r \lesssim 22$ mag, were spectroscopically followed up. In total, 521 SNe were spectroscopically classified. Of the 5,244 SN-like objects, 4,342 host galaxies were targeted through a concerted observational effort. The majority (3,306 objects) were examined in the final year of the survey through a program on the Hectospec multifiber instrument on MMT (Fabricant

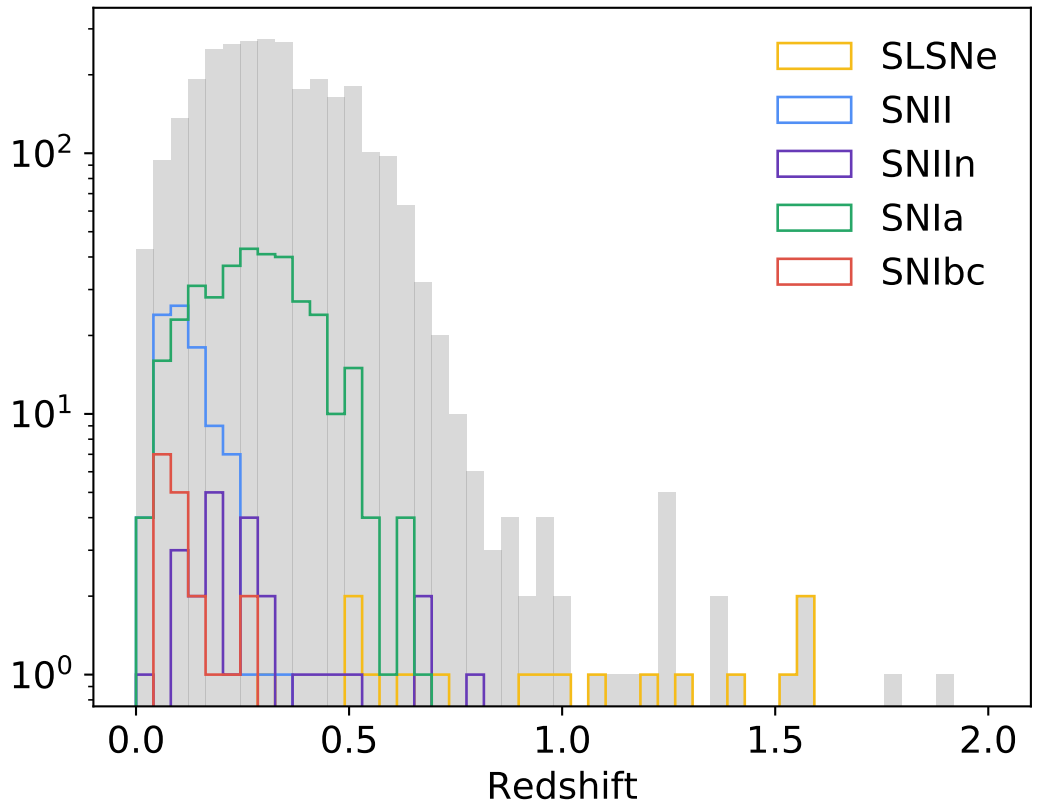

Figure 8.2: Histogram of the redshifts of SN-like transients in PS1-MDS (grey line; 5,244 objects), the subset of host redshift measurements for objects used in our unsupervised learning algorithm (black line; 2,870 objects), and the subset with spectroscopic classification (colored lines). The shaded grey region represents the summed, spectroscopically classified objects. The full sample and spectroscopic distribution peak at $z \approx 0.25$, although the spectroscopic sample has an additional peak near $z \approx 0.1$. At $z \gtrsim 0.75$, our spectroscopic sample is limited to SLSNe.

et al. 2005; Mink et al. 2007). Additional host redshifts were obtained with the Apache Point Observatory 3.5m telescope (APO; 17 objects), the WIYN telescope and the Anglo-Australian Telescope (AAT; 241 objects). Host galaxies selected for follow-up were

largely unbiased in terms of transient properties (i.e., we did not prioritize SNe based on luminosity, color or amount of additional followup). In addition to our programs, approximately 800 host redshifts come from 2dFGRS (Colless et al. 2003), 6dFGS (Jones et al. 2009), DEEP2 (Newman et al. 2013), SDSS (Smee et al. 2013), VIPERS (Scodeggio et al. 2018), VIMOS (Le Fèvre et al. 2005), WiggleZ (Blake et al. 2008) and zCOSMOS (Lilly et al. 2009).

To identify the most likely host galaxy for each SN, we use the galaxy size and orientation-weighted $R_{\rm CC}$-parameter from Sullivan et al. (2006), as outlined in Jones et al. (2017). Jones et al. (2017) finds that only $\approx 1.4\%$ of host galaxies are likely mismatched. Although Jones et al. (2017) restricts the Type Ia SNe sample to z< 0.75 to minimize host mismatch at high redshifts, we keep all SNe in our sample as we are especially interested. In total, 3,147 galaxies have reliable redshifts. Of these, we remove events, which have highly variable light curves or events whose best-match host galaxy is an Active Galactic Nuclei (AGN) or a quasar (QSO). Our final sample includes 2,870 light curves.

A number of transients were spectroscopically followed in real time throughout the survey, without a clear selection function. In this work, we will limit our spectroscopic sample (521 objects) to five potential classes: Type I superluminous SNe (17 objects), which are thought to arise from the birth of highly magnetized neutron stars (Quimby et al. 2007; Nicholl et al. 2017); Type II SNe (93 objects; including Type IIP and Type IIL SNe) which arise from red supergiant progenitors; Type IIn SNe (25 objects) powered by the interaction of a CCSN and pre-existing circumstellar material (see, e.g. Smith et al. 2014); Type Ia SNe (365 objects); and finally Type Ibc SNe (21 objects) with no distinction between the two due to an already small sample).

As expected, our spectroscopic dataset is brighter than our complete photometric dataset. As shown in Figure 8.1, the spectroscopic dataset has a median peak r-band magnitude $\sim$ 1 mag brighter than the full sample. We directly compare the redshift distributions in Figure 8.2. The spectroscopic sample peaks at a slightly lower redshift (z$\sim$ 0.27 vs $z \sim 0.34$), with a slight extended tail to higher redshift ($z \gtrsim 1.0$). The mismatch between the spectroscopic and photometric samples may translate to biases in our classification pipeline, which we will explore in more detail in § 8.5. The complete *grizy* light curves of our sample will be available on `Zenodo`.

We explore the overall data quality of our sample in Figure 8.3, finding that the majority of events have $\sim$ 20 data points with signal-to-noise ratios above three. Given a typical SN duration of a month and our typical cadence of three days, we expect most SNe to have relatively complete light curves.

8.3 A Semi-supervised Classification Pipeline

About 10% of our SN sample is spectroscopically classified. Traditional supervised classification methods are strictly limited to this subset of our data, as they require labelled SN examples. However, information about SN subtypes exists as substructure in the unlabelled dataset as well. For example, SN classes may be clustered in duration and luminosity (e.g., Kasliwal 2012b; Villar et al. 2017b). Because we would like to leverage the information in both the labelled and unlabelled subsets of the training set, we use a recurrent neuron-based autoencoder (RAENN) paired with a random forest classifier for a semi-supervised classification approach. In this Section, we describe the complete algorithm and training process. We summarize the PS1-MDS SN-like objects,

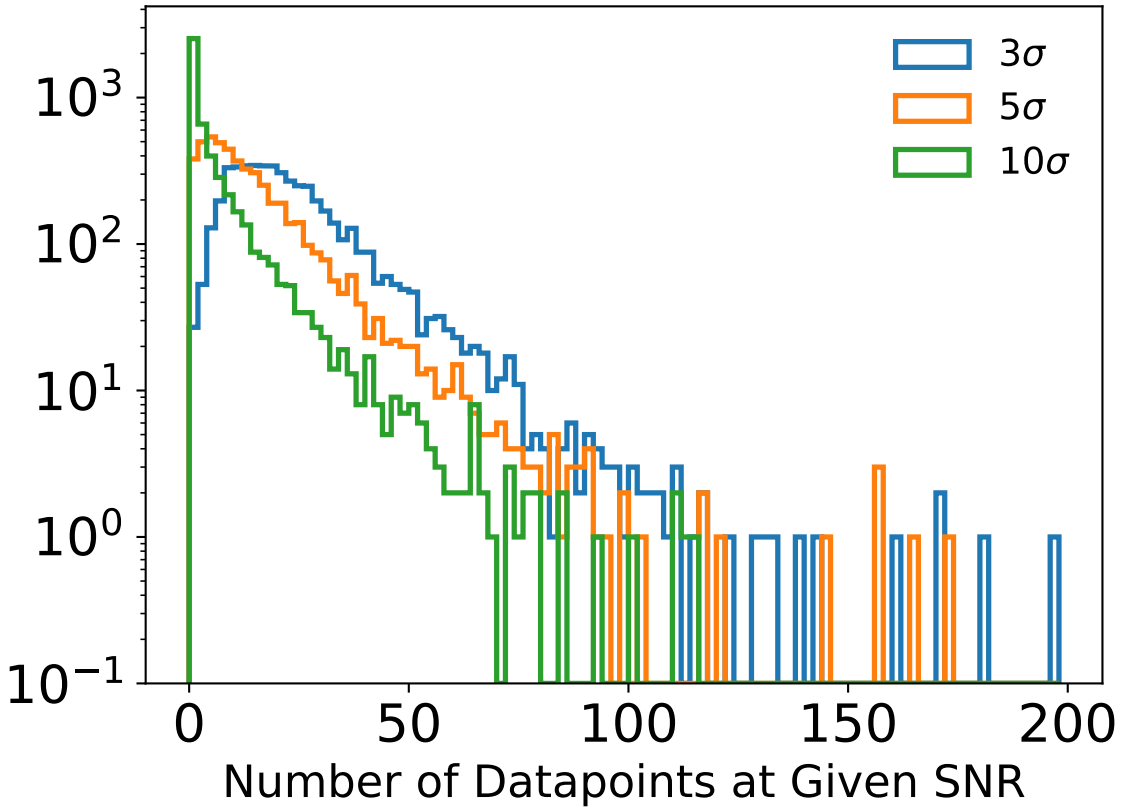

Figure 8.3: Histogram of the number of light curves with N data points with signal-to-noise ratio (SNR) of ≥ 3 (blue), ≥ 5 (orange), and ≥ 10 (green) from the complete sample of SN-like objects (5,244 events). Most events have $\approx 10 - 20$ 3σ data points, with only a handful having > 100 points.

their associated hosts and redshift information in Table 8.1. We also specify which SNe are used in the supervised/unsupervised portions of our classification algorithm.

Our pipeline is composed of three steps: (1) a pre-processing and interpolation step using Gaussian processes; (2) an unsupervised step in which we train a RAENN on the full set of SNe (labelled and unlabelled); and (3) a supervised step in which we train a random forest on the spectroscopically labelled set of SNe.

8.3.1 Pre-processing with Gaussian Processes

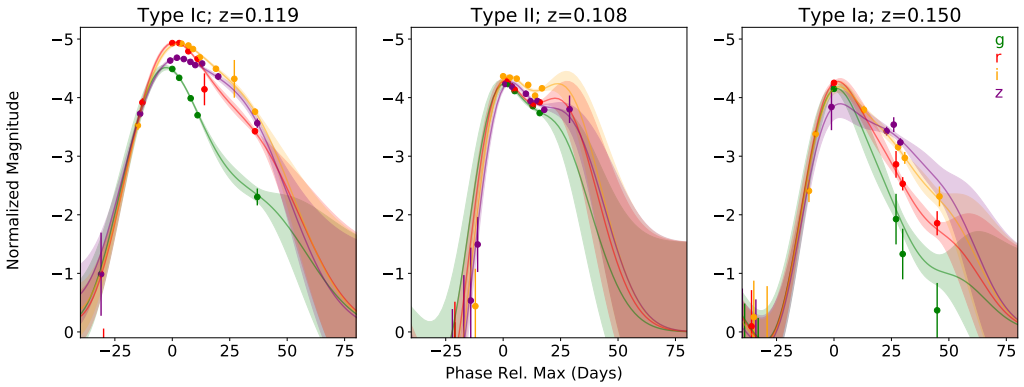

Figure 8.4: Examples of three spectroscopically classified SNe and their associated GP-interpolated light curves in the four PS1 filters. The *griz* light curves (in green, red, orange and purple, respectively) with all detections. Solid lines represent the mean GP prediction, while the shaded regions represent the 1σ estimated uncertainties.

We pre-process the absolute magnitude light curves before extracting features. We estimate and normalize the absolute magnitude using the measured host redshift:

$$M_{\rm norm} = m - 5\log_{10}(d_{\rm L,pc}/10{\rm pc}) \\ +2.5\log_{10}(1+z) - m_{\rm lim} \tag{8.1}$$

, where $m_{\rm lim}$ is the limiting magnitude, which we take to be $m_{\rm lim} = 25$. We do this renormalization so that the base magnitude is equal to zero (see below).

The PS1-MDS light curves are irregularly sampled across the four filters (see §8.2 for the PS1 observing strategy). The architecture of the RAENN will *not* require uniformly sampled light curves. However, it will require that each observation is made in all four filters. For example, if an observation is made in only g-band and r-band on a given night, we will need to fill in interpolated values for i-band and z-band for that night.

To interpolate the $griz$ light curves as described above, we fit a Gaussian process (GP) using the open-source Python package `George` (Foreman-Mackey 2015). GPs are a non-parametric model that has been previously used to interpolate and classify light curves (see e.g., Lochner et al. 2016; Revsbech et al. 2018; Boone 2019). GPs define a prior over a family of functions, which is then conditioned on the light curve observations. A key assumption is that the posterior distribution describing the light curve is Gaussian, described by a mean, $\mu(\vec{t})$, and a covariance matrix, $\Sigma(\vec{t})$, described by $\Sigma_{i,j} = \kappa(\vec{x_i}, \vec{x_j})$ with kernel κ. We use a 2D squared exponential kernel to simultaneously fit all four filtered light curves:

$$\kappa(\vec{t_i}\vec{t_j}\vec{f_i}\vec{f_j}; \sigma, l_t l_f) = \sigma^2 \exp\Big(-\frac{(t_i - t_j)^2}{2l_t^2}\Big) \\ \times \exp\Big(-\frac{(f_i - f_j)^2}{2l_f^2}\Big) \tag{8.2}$$

where f is an integer between 0 and 3 that represents the $griz$ filters, and the parameters

l_t and l_f are characteristic correlation length scales in time and filter integer, respectively. Note that our GP assumes a mean of zero, which is why we renormalize the light curves such that they are equal to zero at their limiting magnitude.

We independently optimize the kernel parameters for each SN using the `minimize` function implemented in `scipy`, with initial values of $l_t = 100$ days and $l_f = 1$. We find that our choice of initialization values has little effect on the resulting best fit. We find that l_t is typically about one week, and l_f is typically $2 - 3$, implying the filters are highly correlated. Examples of the GP interpolation for Type Ia, Type Ic and Type II SNe are shown in Figure 8.4. The GP is able to produce reasonable interpolated SN light curves even in cases with sparse and noisy data.

We note that a GP similar method was implemented by Boone (2019) to classify a variety of SN types in the `PLAsTiCC` dataset. Instead of an integer, Boone 2019 used the rest frame central wavelength of each filter for each object. We avoid this added layer of complexity because the k-corrections and evolving SN spectral energy distribution (SED) change the weighted central filter wavelength. However, the simple 2D kernel still allows the four bands to share mutual information.

Our light curves contain several years of data, most of which are non-detections. To limit our input data, we keep only detections (of any significance) within 100 days of peak flux (in whichever filter is brightest). Although we can use our estimated errors from the GP, we do not end up utilizing these estimates.

For ease of optimization, the light curves need to contain the same number of data points. The data must be a consistent size during the back-propagation step of optimization for the RAENN (see next Section) for each iteration. Our longest light

curve contains 169 data points, so we pad all light curves to match this length. We do so by appending the estimated absolute limiting flux (assumed to be $m_{\rm lim} = 25$) to 100 days after the last detection in the light curve.

8.3.2 Unsupervised Learning: A Recurrent Neuron-based Autoencoder (RAENN)

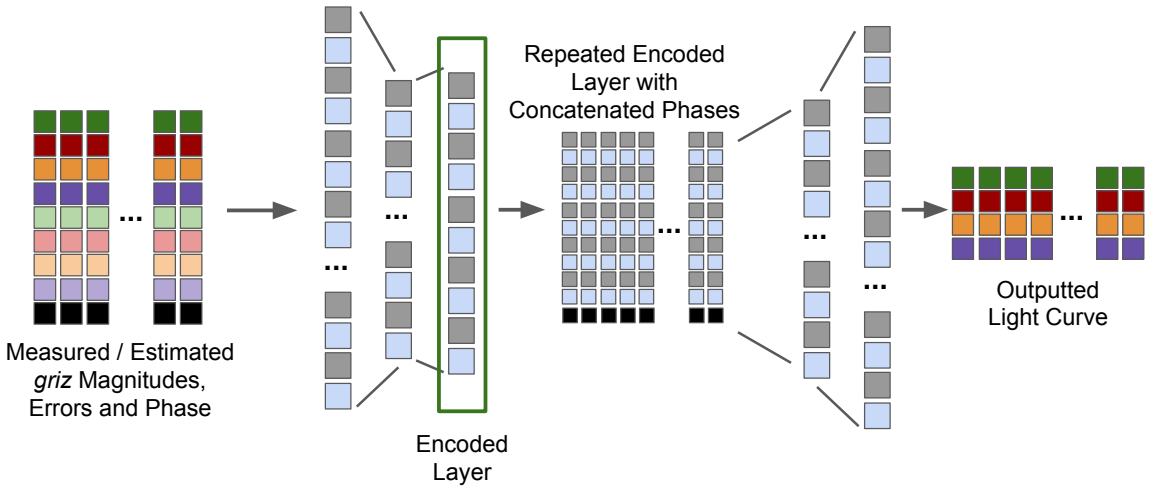

Figure 8.5: Diagram of the RAENN architecture. The pre-processed light curves are fed into the encoder which encodes the light curve into a encoding vector. This vector is then repeated, and new time values are appended to each copy. The final light curve is then predicted at each new time value. The RAENN is trained by comparing the input light curve with the predicted light curve.

To extract unique features from the complete (unlabelled and labelled) PS1-MDS

SN dataset with redshift estimates, we construct a RAENN, inspired by the work of Naul et al. (2018). Autoencoders (AEs, Kramer 1991) are a class of neural network architectures that learn a compressed representation of input data. By training an AE to return the original data given a limited set of variables, it learns an "encoded" version of the data. In astrophysics, AEs have been used for feature-learning in galaxy spectral energy distributions (SEDs, Frontera-Pons et al. 2017), image de-noising (Ma et al. 2018; Lucas et al. 2018), and transient classification (Naul et al. 2018; Pasquet et al. 2019). AEs are increasingly being used in the astrophysics literature for dimensionality reduction (see e.g., Ralph et al. 2019 and Portillo et al. 2020 for recent examples).

Here, our proposed model is designed to address several concerns of SN light curves: (1) the temporal irregularity of data; (2) data across multiple filters; and (3) "live-streaming" data that update nightly. The last point is not a concern for our PS1-MDS archival dataset, but it will become important as LSST comes online and discovers thousands of SNe nightly.

The RAENN uses the GP light curves as input, by codifying the light curves as matrices of size $9 \times T_0$, where $T_0 = 169$, as described in the previous section. The 9 values arise from: one time value, relative to maximum (in whichever filter is brightest), four flux values ($griz$) at that time and four error bars. Recall that the flux values are either measured or estimated from the GP. For the error values, we use the 1σ errors for the measured points. For the GP points, we use a large error of 1 mag. We note that the GP produces estimated errors, but we find that, in practice, using this large error leads to better performance. We emphasize that, while $T_0 = 169$ for training, the RAENN architecture allows a user to input a light curve of any size without needed to pad the light curve.

The RAENN architecture is divided into an encoder and a decoder. Our encoder is a series of fully-connected layers that decrease in size until the final encoded layer with size N_E (i.e., the number of neurons used to fully encode the SN light curve). Note that N_E is a free parameter of our model that needs to be optimized. Similarly, the fully-connected layer has N_N neurons, where $N_N > N_E$ and a tunable parameter. Following the encoded layer, the decoder half of the architecture typically mirrors the encoder with increasing layer sizes. A novel feature of our architecture is the inclusion of a repeat layer immediately after our final encoded layer. In this layer, we repeat the encoded version of the light curve T_N times. In this work, $T_N = T_0$; we repeat the encoded values to match the original light curve length. To each copy, we append the time of each data point, relative to peak brightness in one filter (whichever filter happens to be brightest) via a concatenation layer. Finally, this layer is followed by another fully-connected layer with N_N neurons.

One way to view the purpose of this layer is to imagine the autoencoder as two functions. The first function (the encoder) takes in the original data points, including observation times, and outputs a set of N_E values. A second function (the decoder) takes in a set of N_E values and T_0 times to generate a light curve at the T_0 times. This architecture allows us to generate a light curve at different T_N times; e.g, interpolated or extrapolated light curves, which is further explored in §8.5.

Our autoencoder utilizes gated recurrent neurons (GRUs; Cho et al. 2014; Rumelhart et al. 1988). In addition to the typical hidden weights that are optimized during training, recurrent neurons have additional weights that act as "memory" of previous input. GRUs in particular utilize an *update* value (called a gate) and a *reset* gate. The values of these neurons determine how the current and previous input affect the value of the output.

With each light curve data point, the gates become updated with new information that informs the next prediction. This class of neurons is useful for our light curves with various numbers of observed data points. Our GRU neurons use the tanh activation functions with a hard sigmoid for the gate activation function.

Our RAENN is implemented in `Keras` (Chollet 2015) with a Tensorflow backend (Abadi et al. 2016). A diagram of the architecture is shown in Figure 8.5, and is outlined as follows:

1. **Input Layer**: Input light curve of size $T_0 \times 9$ with each *griz* data point labelled with a time (1 value) in days relative to light curve peak (4 values) and an uncertainty (4 values).
2. **Encoding Layer**: Encoding layer with N_N neurons, where N_N is a free parameter.
3. **Encoded Layer**: Encoded light curve with N_E neurons, where N_E is a free parameter.
4. **Repeat Layer**: Layer to repeat encoded light curve to match with new time-array, with size $T_0 \times N_E$.
5. **Concatenate Layer**: Layer to concatenate new times to encoded light curve, with size $T_0 \times (N_E + 1)$.
6. **Decoding Layer**: Decoding layer with N_N neurons.
7. **Decoded Layer**: $T_0 \times 4$ Decoded *griz* light curve.

To optimize the free parameters (the weights) of the RAENN model, we must define

a *loss function*. Our loss function is simple mean square error function:

$$\mathcal{L} = \sum_{i=0}^{N} \frac{F_{i,\mathrm{True}}(t,f) - F_{i,\mathrm{Predicted}}(t,f)}{N}, \tag{8.3}$$

where F is the SN flux as a function of time t and filter f. Although we feed errors into the network, we find that excluding flux errors in our loss function provided best results. We minimize our loss function using the gradient descent-based optimizer, `Adam` (Kingma & Ba 2014), finding an optimal learning rate of 10^{-4}, which is a typical value.

We randomly split our unlabeled dataset into training (66%) and test (33%) sets. We optimize the number of neurons in both the encoding and decoding layers (fixed to be the same number, N_N) and the number of encoding neurons (N_E) through a grid search, allowing N_N to vary from 20 to 160 in intervals of 20, and N_E to vary between 2 and 24 in intervals of 2. We find that, when optimizing over final classification accuracy, our optimal values are $N_N = 140$ and $N_E = 10$. We note that N_N is slightly below the maximum number of data points in our set of light curves (where the longest light curve has 169 observed data points). The number of encoding neurons N_E is similar to the number of free parameters for the analytical model used in Villar et al. (2019) to capture shape of a single-filter SN light curve.

We contrast our architecture with methods from Naul et al. (2018) and Pasquet et al. (2019), who present similar methodologies. Naul et al. (2018) uses a similar GRU-based RAENN to classify variable stars with unevenly sampled light curves in one filter from the All Sky Automated Survey Catalog of Variable stars (Pojmanski 2002). The flux and time since last observation (Δt) is sequentially read into the recurrent layers. The same time array is fed into the decoder for output. In our case, we feed in a time series across four filters and give a time array relative to peak rather than relative

to the previous data point. This is more natural in our problem, in which the SNe have a clear beginning and end, versus the periodic signals of variable stars. Additionally, our architecture allows us to give the decoder a different time series to allow for interpolation or extrapolation of the data.

Pasquet et al. (2019) uses a semi-supervised method to classify simulated SN light curves from the Supernova Photometric Classification Challenge (SNPCC; Kessler et al. 2010 They use an AE with convolutional layers by transforming the light curves into "light curve images" (see Pasquet-Itam & Pasquet 2018). Rather than interpolate the light curves, Pasquet et al. (2019) applies a mask to filters that are missing data at a certain time. In contrast, we interpolate our light curves but assign interpolated values a large uncertainty of 1 mag, as explained above. We found that the method of transforming light curves into images and masking across 4 filters led to unstable training and poorer performance. This is likely due to the large data gaps in the *real* PS1-MDS light curves, compared to the high-cadence (2-days for each filter) *simulated* light curves of SNPCC (Kessler et al. 2010). Since the LSST data are expected to more closely resemble the PS1-MDS light curves than the SNPCC simulated events, we expect our method to be more robust in a real-life application.

8.3.3 Supervised Learning: Random Forest Classifier

Finally, we use the encoded light curves as features for a supervised classification method. Following Villar et al. (2019), we train a random forest (RF) classifier on the PS1-MDS spectroscopically classified SNe, including the RAENN encodings as features. We use a subset of the 521 SNe that removes outlier light curves that we find decrease the

classification accuracy of our models. In total, we remove 27 SNe either due to data quality (20 Type Ia SNe; 1 Type II SN; 4 Type Ib/c SNe; see Villar et al. 2019) or lack of a host galaxy redshift (2 SLSNe, although SN redshifts are reported in Lunnan et al. 2018). However, in the reported accuracies throughout this Chapter, we utilize the full sample of 521 light curves.

In addition to the encoding (10 features), we use the following 25 features based on the GP-interpolated light curves:

1. **1-4** The *griz* rise times in observer frame, calculated 1-magnitude below peak.
2. **5-8** The *griz* rise times in observer frame, calculated 2-magnitude below peak.
3. **9-12** The *griz* decline times in observer frame, calculated 1-magnitude below peak.
4. **13-16** The *griz* decline times in observer frame, calculated 2-magnitude below peak.
5. **17-20** The *griz* peak absolute magnitudes.
6. **21** The peak absolute magnitude in any filter (a repeated value).
7. **22-25** The median *griz* slope between 10 and 30 days post-peak in observer frame. This area was chosen by eye to specifically help the model differentiate between Type II and Type Ibc SNe.

Note that we measure these values from the GP-interpolated light curves rather than the decoded light curves. The decoded light curves are, at best, approximations of the GP-interpolated light curves. Therefore, using them would only result in noisier

features. The decoded light curves are necessary, however, as a means to train the RAENN to extract the N_E encoding neuron values.

These features were chosen through trial-and-error while optimizing classification accuracy. We find that inclusion of all of these features leads to our optimal classification accuracy. We additionally tried, but ultimately eliminated: the integrated flux values in each filter; the slope values within 10-days of peak; the 3-mag rise/decline times; and the total duration of the transients.

We pass these features through a RF classifier, utilizing 300 trees in the random forest and the Gini-information criterion. To counteract the imbalance across the five spectroscopic classes, we tested several algorithms to generate synthetic data to augment our training set. First following Villar et al. 2019, we use a Synthetic Minority Over-sampling Technique (SMOTE; Chawla et al. 2002) and a multivariate Gaussian (MVG) fit. We find optimal results utilizing a Kernel Density Estimate (KDE) of the training set, using a Gaussian kernel with bandwidth equal to 0.2 (or 20% of the whitened feature standard deviation). Note this is different than the MVG treatment used in Villar et al. (2019) in which each class is assumed to come from a single MVG in feature space. We test our classifier using leave-one-out cross-validation, in which we remove one SN from the sample, over sample the remaining objects using a KDE estimate and then apply the trained RF to the single test For each object, our RF reports probabilities associated to each class, and we take the class with the highest probability as the predicted SN type.

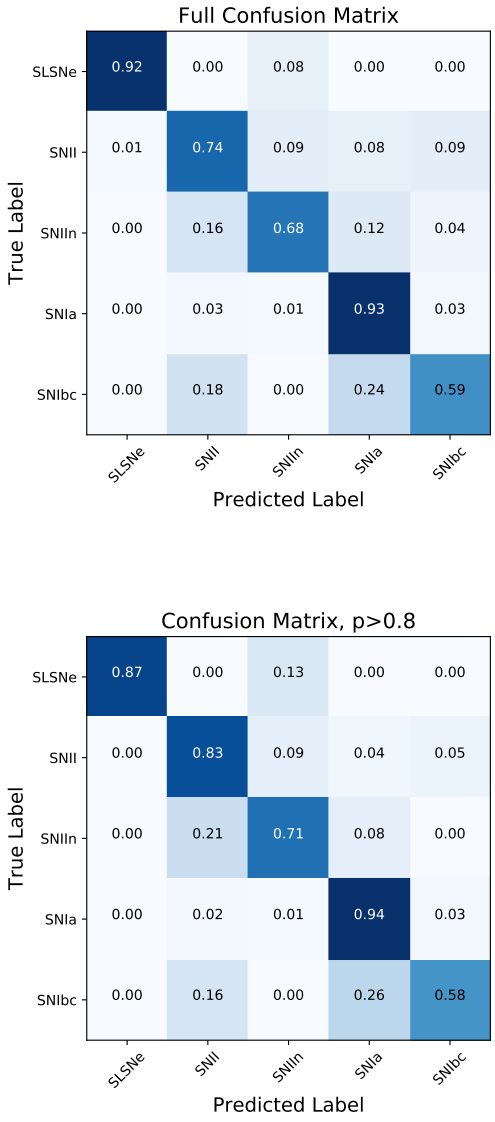

Figure 8.6: Confusion matrix for the full set of 2,870 spectroscopically classified SNe. In the bottom panel, we include only objects where the maximum probability is greater than 80%

8.4 Classification Results

We use leave-one-out cross validation to train the random forest on the 35 features described above. There are several metrics to measure the success of a classifier. We focus on three metrics: the purity, completeness and accuracy. We define the three, calculated for a single class, below:

$$\begin{aligned} \text{Purity} &= \frac{\text{TP}}{\text{TP} + \text{FP}} \\ \text{Completeness} &= \frac{\text{TP}}{\text{TP} + \text{FN}} \\ \text{Accuracy} &= \frac{\text{TP} + \text{TN}}{\text{TS}} \end{aligned} \tag{8.4}$$

where TP (FP) is the number of true (false) positives, TN (FN) is the number true (false) negatives, and TS is the total sample size. We visualize the completeness of the sample of spectroscopically identified SNe using a confusion matrix in Figure 8.6. A confusion matrix compares our RAENN label (x-axis) with the specgroscopic label (y-axis). As with Villar et al. (2019), we find that our classifier performs best for Type Ia SNe and SLSNe and worse for Type Ibc SNe. Our class-averaged classification completeness is 77% across the 5 SNe types. This is slightly worse than the performance of Villar et al. (2019) (with an average completeness of 80%). When limiting the sample to only objects in which the classification probability is $> 80\%$, we find that our performance only somewhat increases. We find a class-averaged accuracy of 95% and class-averaged purity of 71%, consistent with Villar et al. (2019).

The random forest classifier allows us to measure the relative "importance" of the 35 features used to classify the SNe. We define importance as the decrease in the Gini

importance, which accounts for how often a feature is used to split a node and how often a node is reached in the forest (Breiman et al. 1984). We show the importance of each RF feature in Figure 8.7, along with estimated errors. As expected, the peak magnitudes are by far the most important features for classification. However, the RAENN features also have significant influence on the final classifications, with three RAENN features appearing in the top ten important features.

We apply our trained classification algorithm to the PS1-MDS dataset of SN-like transients that pass our quality cuts described in § 8.2. We report the probabilities of each class type for each light curve in Table 8.2. As shown in Figure 8.8, the breakdown of our sample (the 2,870 light curves used to train the RAENN) is largely consistent with the spectroscopic sample, with a slightly lower fraction of SLSNe and Type Ia SNe and otherwise higher fractions of subtypes. However, all fraction agree to within $\sim 2\%$.

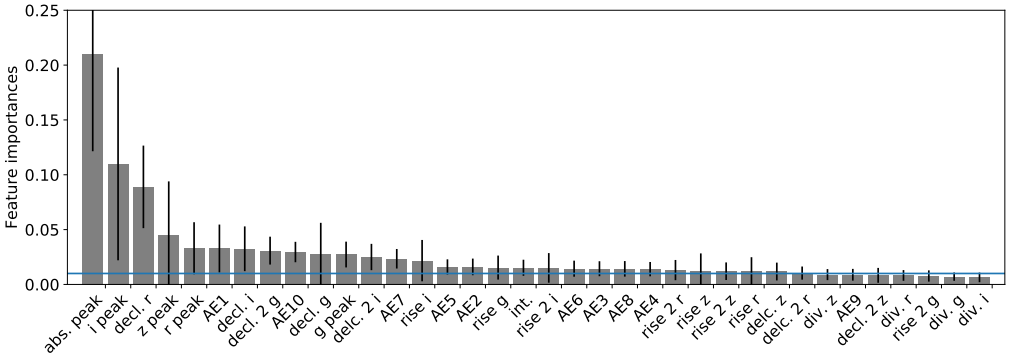

Figure 8.7: Feature importance (grey) with estimated 1σ errors (black lines). The blue horizontal line shows the importance measure for a normally-distributed random variable; features below this line can be considered largely unimportant to the final classification.

8.5 Discussion

As discussed in § 8.2, our spectroscopic sample is somewhat brighter and at a lower redshift than our test set. This difference may introduce biases in our final classifications. De-redshifting the SNe using the measured redshift removes some of this bias, by removing knowledge of the underlying redshift as a feature. The relative fractions of SN subtypes may evolve with redshift as host properties change (see e.g., Graur et al. (2017) for an exploration of the correlations between host properties and SN type). Our training and test set differs most greatly between $0.5 < z < 1.5$ (see Fig. 8.2). In this redshift range, average host metallicity is not expected to drastically shift, implying a small potential bias (Lilly et al. 2003).

As expected, the relative fraction of SN subtypes evolves with redshift as the absolute limiting magnitude increases at higher redshifts. We trace this evolution in Figure 8.9. We show the cumulative fraction (integrating from $z = 0$) of each subclass as a function of redshift. Each subclass peaks in order of luminosity function, with the dimmest subclass, Type II SNe, peaking near $z \sim 0$. The cumulative fractions level out near $z \sim 0.5$, where the cumulative distribution of all SNe reaches approximately 80%.

Using the high redshift sample, we can test if redshift information is playing an unwanted role in our training. The spectroscopic sample at $z \gtrsim 0.75$ is solely made up of SLSNe; however, we do not expect *all* high-z objects to be SLSNe. For $z > 0.75$, we find that our test sample is 45% SLSNe, 17.5% Type SNe and 37.5% Type IIn SNe, implying our classifier has not learned to simply classify all high-z events as SLSNe.

Figure 8.8: Breakdown of SN subclasses in the spectroscopic (left) and full (right) samples. The samples largely agree, suggesting no obvious bias in our spectroscopic vs photometric sample. We note that our breakdown is subject to pipeline and observational biases (e.g., necessity to measure a host redshift) and should therefore not be used for rate calculations.

8.5.1 Comparison to Other Works

For the first time, we can compare multiple photometric classifications of the same real dataset. We directly compare our results to Jones et al. 2017, finding strong overall agreement. Jones et al. (2017) presents a PS1-MDS sample of 1,033 likely Type Ia SNe, as classified by four algorithms: the template-matching algorithm PSNID (Sako et al. 2011), a nearest neighbor approach using the PSNID templates; an algorithm based on fitting light curves to SALT2 templates (Guy et al. 2007); and a method, GALSNID (Foley & Mandel 2013), which only utilizes host galaxy properties. The Jones et al. (2017) sample, similar to our sample, removes objects with unreliable redshifts and potential AGN hosts; however, Jones et al. (2017) additionally removes high redshift $z > 0.75$ objects. Of the 1,033 SNe Jones et al. (2017) identifies as likely Type Ia SNe, we find 979 (95%) agreement. Of the remaining 54 SNe, we identified Type Ia as the second highest choice in 37 cases. Of the remaining 17 cases, 6 have low Type Ia probabilities ($p < 0.8$) or classification probabilities based entirely on host galaxy.

Hosseinzadeh et al. (in prep) extends the work of Villar et al. (2019) to classify the PS1-MDS sample using features extracted from analytical fits to the light curves. Our photometric classifications agree on 71% of the 2,870 events, with 71% of Type Ia agreement, 54% SLSN agreement, 76% Type II agreement, 20% Type IIn agreement and 46% Type Ibc agreement. If we compare the top two labels, the algorithms agree on 93% of objects. Indeed, often the top two classification choices are flipped for either algorithm, occurring most often with Type II/Type Ibc SNe and Type IIn/Type Ia SNe. We find stronger agreement if we exclude objects with low classification confidence. If we exclude objects in which the first choice has a probability < 0.8 in either algorithm, our

classifications agree to 84% (with 1780 objects remaining after the cut). The agreement increases with high probability cuts of > 0.9 (> 0.99), with 90% (96%) agreement with 1,322 (676) objects remaining.

We compare the overall breakdown of SN types to that of the ZTF Bright Transient Survey Fremling et al. (2019) which spectroscopically identified ~ 700 bright SNe with peak $g-$ or $r-$band magnitude of < 18.5. Fremling et al. (2019) find that their magnitude-limited survey breaks down into 72% Type Ia SNe, 16% "normal" Type II SNe (Type IIP/L), 3% Type IIn SNe (including their Type IIn and SLSN-II category), 5% Type Ibc SNe, and 1.6% Type I SLSNe. These are largely in agreement with our spectroscopic and photometric class breakdown, to within reported error bars (ranging from $\sim 1 - 5\%$).

We make special note that our sample is likely biased against discovering SLSNe, due to our requirement of a host galaxy redshift. SLSNe prefer low-mass, low-metallicity hosts (Leloudas et al. 2015), and their relatively small volumetric rate means that they are typically found at higher redshifts. Because of this, we are less likely to have successfully targeted the host galaxies of SLSNe, which may explain the lower fraction of SLSNe in our complete sample. In fact, if we removed the SLSNe in our spectroscopic sample which have redshift estimates from the SN spectra, the fraction of SLSNe would decrease to $\sim 2.7\%$, more in line with our full sample.

8.5.2 RAENN Architecture: Limitations and Benefits

We now turn to the architecture of the RAENN itself and its use in future surveys. The recurrent neurons allow our NN to generate light curve features which can be updated in

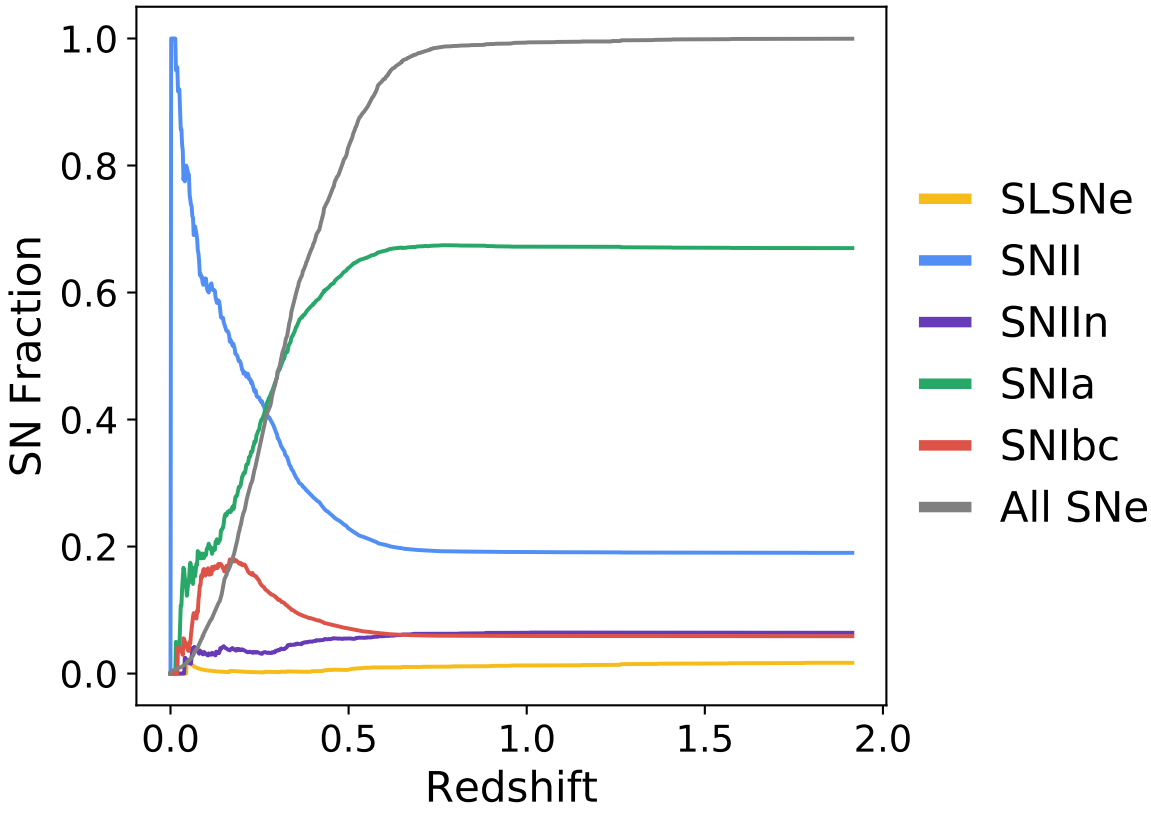

Figure 8.9: SNe subclass cumulative fraction as a function of redshift (colored) and the overall cumulative distribution (grey).

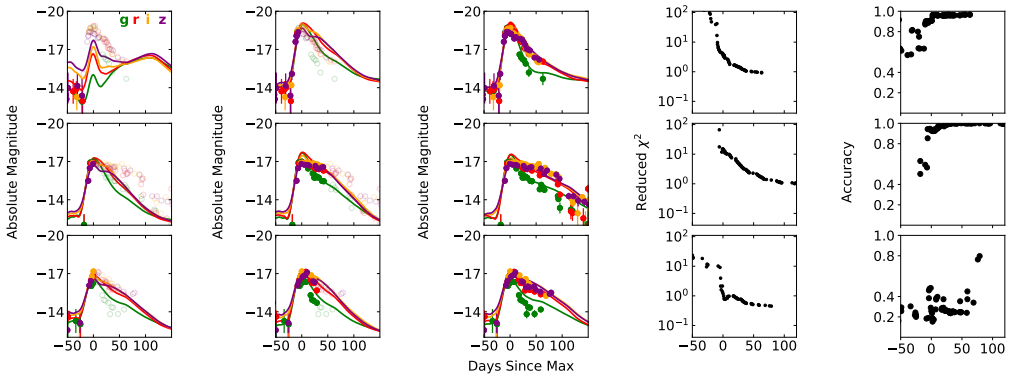

Figure 8.10: Example of a Type Ia SN (*top row*), Type II SN (*middle row*) and Type Ibc SN (*bottom row*). Filled points represent observations used to generate the RAENN model (colored lines), while empty points are the complete set to guide the eye. In the right-most column, we show the root-mean-squared (RMS) error as a function of SN phase. Interestingly, the RMS reaches ~ 1 near peak for all SNe shown. We emphasize that the RAENN model has been optimized to classify complete SN light curves rather than evolving light curves.

real time, in addition to extrapolating and interpolating light curves. We highlight the accuracy of the RAENN light curve model as a function of light curve completeness in Figure 8.10. We track how well the RAENN is able to (1) model the complete light curve with limited data and (2) accurately classify the SNe with limited data by feeding a partial light curve into the RAENN and using the encoded neurons as features. Note that at every step, we hold the other features (e.g., peak luminosity and duration) constant. We find that our classifier's performances generally drastically improves post-peak, but that the can provide accurate classifications and light curves somewhat before peak. To explore this, we track how the RAENN features change as the light curves evolve. In Figure 8.11, track the values several representative encoding values of a Type Ia SN. As expected, the values vary smoothly until ~ 10 days post-peak.

The unique ability of the RAENN to extrapolate light curves without built-in physical assumptions gives it the unique capacity to hunt for anomalous events in real time which require followup during online surveys such as ZTF and LSST. Given the millions of events discovered annually with LSST, it is not unreasonable to search for unexpected physics which appear as observational outliers. One concern is that our algorithm is potentially not robust to noisy live-streaming data; in other words, our algorithm must be able to distinguish between anomalous data and noisy data. We check the stability of our encoded values as a function of scaled white noise by adding white noise to a light curve. We then use our RAENN to encode the noisy light curve and record the scatter of the encoded values. We report the results of this test in Figure 8.12, in which we show the scaled scatter of the encoded values as a function of the magnitude of the injected noise. The scatter grows linearly with noise; however, even with one magnitude of scatter added to the light curve, the overall scatter of the encoded values

only increases to 30% of the overall spread of class's features. This implies that the RAENN is largely robust to noise.

We note that several steps need to be taken to allow our architecture to work on streaming data. First, we use phases relative to maximum light, which will be unavailable during the rise of the SN. A simple shift to an easily measured time, like time of first detection, will allow the RAENN to otherwise perform as designed. Similarly, the features utilized during the supervised portion of our classifier rely on the full light curve being available. All features can be estimated from extrapolated RAENN light curves or a new set of features may be used on streaming data. Finally, although not necessary, our RAENN could output uncertainties on the SN light curves by converting the network into a *variational* AE, which is designed to simultaneously find an encoding space and uncertainties on the encoded data. This more complex architecture would likely require a larger training set to be reliable.

8.6 Conclusions

Deep learning-based classifiers are becoming increasingly important for classification of archival SN light curves. In this Chapter we present a novel, semi-supervised approach to light curve classification which utilizes spectroscopically labelled and unlabelled SN data from the PS1-MDS. Our RAENN model extracts learned, nonlinear features from the sparse light optical light curves. We use these features and other features to classify the complete set of SN-like objects in the PS1-MDS dataset.

We achieve high (95%) class-averaged accuracy for our spectroscopically-labelled

sample. We find best performance for SLSNe and Type Ia SNe due to their distinctive region of feature space. We find worst performance for Type Ibc SNe, likely due to the small sample size (of just 21 events). We perform simple tests for classification bias and method robustness to noise, finding our method robust to both. We apply our classifier to the full, SNe sample of PS1-MDS which pass our quality cuts described in §8.2. We find fractional subclass breakdowns consist with previous studies.

Finally, we note that simple modifications to our presented classifier will allow it to work with live, rather than archival, data streams such as ZTF and LSST. We perform simple tests and find that our classifier performs optimally after peak, although we have not optimized for online data streams. We additionally note that the architecture may also be utilized to search for interesting, anomalous events in real time. We plan to explore this in future work.

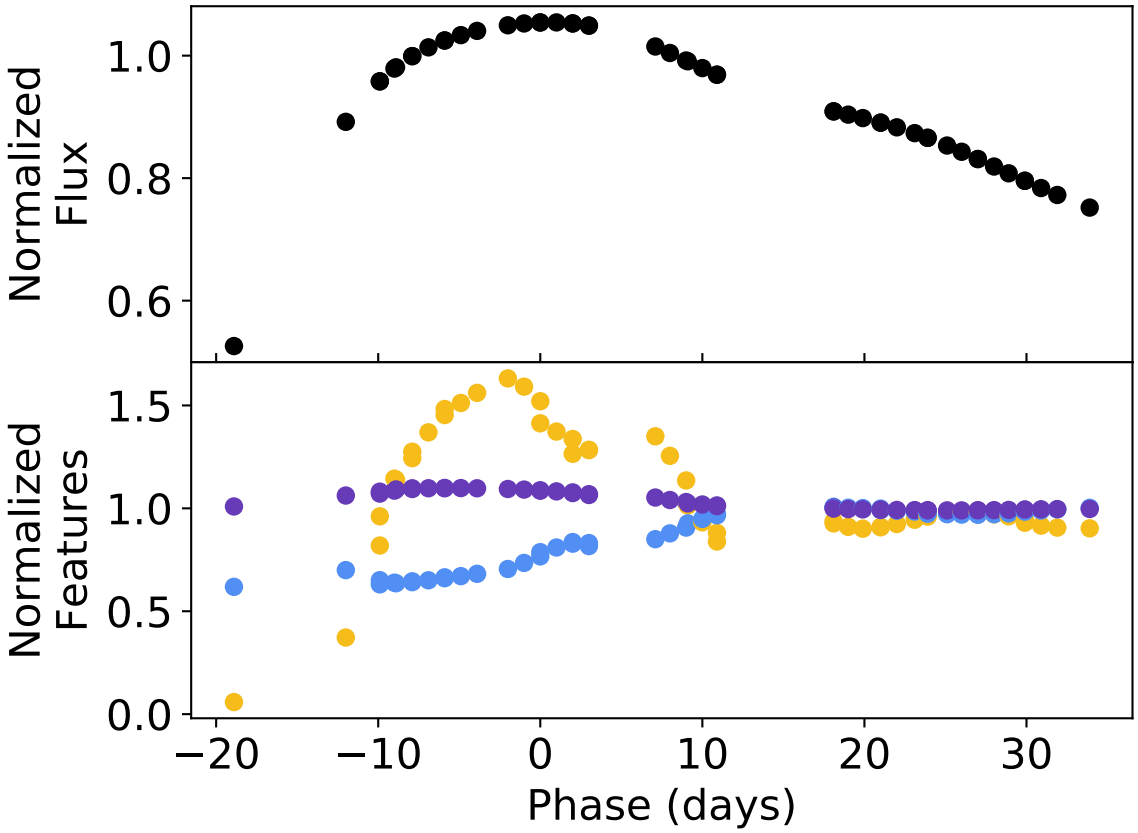

Figure 8.11: *Top:* Normalized light curve of a spectroscopically-classified Type Ia SN. *Bottom:* Normalized AE features as a function of SN phase. To generate these features, we run the light curve data through the RAENN up to a certain phase. We track how these features change as we increase the phase for three representative features. As shown, the values vary smoothly but broadly until roughly a week post-peak.

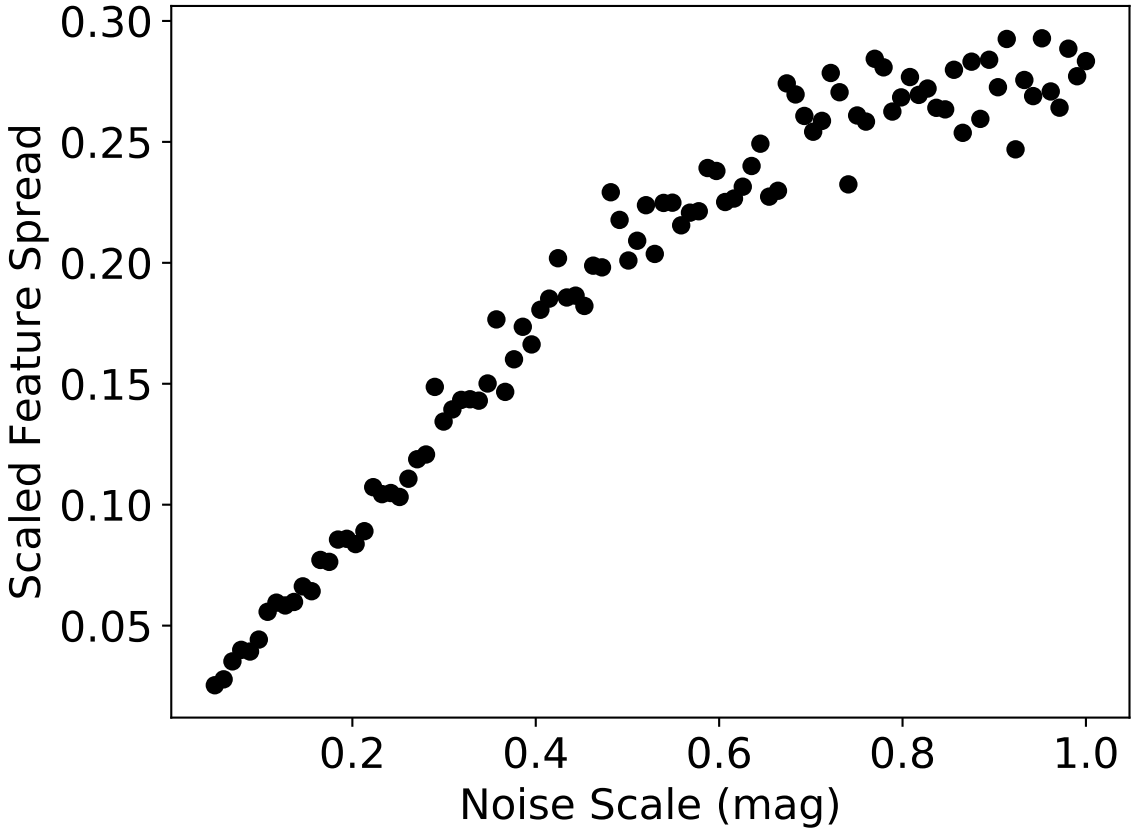

Figure 8.12: Average spread of the RAENN features for a spectroscopic Type Ia SN as a function of light curve noise. For every noise scale, we run 100 simulations, adding random noise to the light curve. We then track the average spread of each parameter. We scale this spread by the total spread in the Type Ia class. Even with an injected error of 0.5 mag, the spread in the RAENN feature space only reaches 20% of the total spread throughout the Type Ia class in feature space, implying the method is robust to noise.

Table 8.1:: SN-like object properties

Object Name	SN RA	SN DEC	SN Type	SN z	Host RA	Host Dec	Host Redshift	Host Template	Condition	R_{CC}	Telescope	Unsup.	Sup.
PSc000001	52.4531	-29.075	SNII	0.1260	52.4536	-29.0744	0.071	-	-	-	2df	Y	N
PSc000006	53.3664	-28.3715	SNIa	0.2308	53.3663	-28.3715	0.23093	-	Q	3.89	Magellan	Y	Y
PSc000010	149.749	3.1575	SNIa	0.2447	149.7495	3.1576	0.24454	-	Q	14.9	Magellan	Y	Y
PSc000011	149.9759	2.4119	SNIa	0.3800	149.976	2.4106	0.25759	-	?	3.61	Gem-S	Y	Y
PSc000014	35.878	-4.6363	SNIa	0.1369	2.3919	-4.6363	0.1369	Late Type	Q	12.19	MMT Hecto	Y	Y
PSc000034	36.0664	-3.1865	SNIa	0.2500	36.0663	-3.1868	0.25418	-	?	3.28	Magellan, MMT-Blue	Y	Y
PSc000038	35.0957	-4.6725	SNIa	0.1500	35.0957	-4.6731	0.15128	-	Q	11.41	Magellan	Y	Y
PSc000076	129.2608	43.738	SNII	0.2600	129.2616	43.7383	0.25963	-	Q	7.03	MMT	Y	Y
PSc000091	129.3289	44.3337	SNIa	0.1520	129.3272	44.3356	0.01911	-	X	3.11	Gem-N	Y	Y
PSc000098	184.9064	46.0322	SNII	0.0570	184.9059	46.0325	0.05714	-	Q	16.31	MMT	Y	Y
PSc000133	160.7182	58.0328	SNII	0.2440	160.7185	58.0328	-	-	Q	5.18	MMT	Y	Y
PSc000137	161.1593	57.8111	SNIa	0.1183	10.7439, 10.7439	57.8111, 57.8111	0.1183, 0.1182	K star	Q,Q	11.70,12.63	SDSS, MMT Hecto	Y	Y
PSc000140	162.418	58.5919	-	0.9680	162.4177	58.5919	0.96698	-	Q	9.75	MMT	N	N
PSc000141	162.5243	58.736	-	0.8270	162.5243	58.7359	0.82787	-	Q	3.72	MMT	N	N
PSc000142	162.3092	58.4672	SNIa	0.4360	162.3102	58.4675	0.6072	-	X	2.39	Gem-N, MMT-Blue, MMT-Blue	Y	Y
PSc000174	162.0294	56.8502	SNIa	0.2440	162.0293	56.8502	0.24431	-	X	2.95	NOT, Gem-N	Y	Y
PSc000187	149.2183	2.5965	-	0.4800	149.2182	2.5965	0.48106	-	Q	10.17	MMT	N	N

A complete, machine-readable version of this table is available in the online version.

Acknowledgments

The Berger Time-Domain Group is supported in part by NSF grant AST-1714498 and NASA grant NNX15AE50G. V.A.V. acknowledges support by the Found Foundation through a Dissertation Fellowship. Some of the computations in this Chapter were run on the Odyssey cluster supported by the FAS Division of Science, Research Computing Group at Harvard University. The Pan-STARRS1 Surveys (PS1) and the PS1 public science archive have been made possible through contributions by the Institute for Astronomy, the University of Hawaii, the Pan-STARRS Project Office, the Max-Planck Society and its participating institutes, the Max Planck Institute for Astronomy, Heidelberg and the Max Planck Institute for Extraterrestrial Physics, Garching, The Johns Hopkins University, Durham University, the University of Edinburgh, the Queen's University Belfast, the Harvard-Smithsonian Center for Astrophysics, the Las Cumbres Observatory Global Telescope Network Incorporated, the National Central University of Taiwan, the Space Telescope Science Institute, the National Aeronautics and Space Administration under Grant No. NNX08AR22G issued through the Planetary Science Division of the NASA Science Mission Directorate, the National Science Foundation Grant No. AST-1238877, the University of Maryland, Eotvos Lorand University (ELTE), the Los Alamos National Laboratory, and the Gordon and Betty Moore Foundation.

Table 8.2:: SNe classification

Object Name	p_{SLSN}	p_{II}	p_{IIn}	p_{Ia}	p_{Ibc}
PSc000001	0.01	0.01	0.13	0.84	0.01
PSc000006	0.0	0.0	0.0	1.0	0.0
PSc000010	0.0	0.0	0.0	1.0	0.0

A complete, machine-readable version

of this table is available in the online version.

Chapter 9

Conclusions and Future Directions

Time-domain astrophysics is concurrently entering two new eras of multi-messenger astrophysics and big data. Wide-field surveys continue to increase the discovery rate of extragalactic transients at an exponential rate, opening the door for statistical studies of even the rarest SN classes. At the same time, the discovery rate of well-localized binary neutron star mergers is growing thanks to improved gravitational wave detectors. This thesis has presented several studies which tackle these new eras, via physical and data-driven methodologies.

Through a theoretical census of extragalactic transients, we quantify the extent of observable features from known astrophysical sources. We build on this work to conduct detailed studies of a massive stellar eruption in a high-mass X-ray binary. We then turn our attention to the collisions of compact objects. We present the first analysis of the complete ultraviolet, optical and near-infrared light curve of the first discovered kilonova, followed by the first late-time infrared observations. Finally, we present several studies addressing the classification of supernova light curves in the upcoming age of large data

streams, thanks to the Vera C. Rubin Observatory (VRO).

The future is an exciting new frontier for time-domain astrophysics. As this thesis has shown, the VRO will increase our discovery rate of transients by two orders of magnitude. Undoubtedly, this exponential growth will lead to new and unexpected discoveries. Machine learning methods, like those developed in this thesis, will be necessary tools to sort the interesting "needles" (or events which require real time, multi-wavelength follow up) from the "hay" of objects. Future algorithms need to utilize all available information (e.g., host galaxy properties or pre-explosion outbursts) and flag anomalous events in real time. The unique nature of transient data will require cutting-edge machine learning techniques founded on astrophysics. In addition, sophisticated statistical methods are necessary to fully analyze the "hay" of extragalactic transients with no follow up. Population studies of millions of probabilistically classified transients will require Bayesian hierarchical studies which simultaneously consider physical progenitors and observational selection effects.

In parallel, Advanced LIGO/Virgo will be joined by the new detectors KAGRA in Japan and LIGO-India. This new generation of gravitational wave detectors will continue to improve sensitivity and localizations of binary mergers. Using VRO in conjunction with this network will lead to dozens of kilonova discoveries annually (Margutti et al. 2018b; Cowperthwaite et al. 2019), opening the doors to studies of kilonova diversity, r-process enrichment over cosmic time and cosmology. As with the area of time-domain astrophysics, machine learning and statistical algorithms for the classification and understanding of kilonovae will become the norm in this new era.

At the same time, future multi-wavelength facilities will enable new means to

study kilonovae. In particular, the James Webb Space Telescope will launch in the early 2020s, opening a new window into the infrared. As this thesis has shown, nebular phase observations of kilonovae are essential to understand the nucleosynthetic products and ejecta thermalization properties of events. In the ultraviolet, missions like the proposed Ultraviolet Transient Astronomy Satellite will provide rapid follow up to better understand the early blue emission of kilonovae.

References

Abadi, M., Barham, P., Chen, J., et al. 2016, in 12th {USENIX} Symposium on Operating Systems Design and Implementation ({OSDI} 16), 265–283

Abbott, B. P., Abbott, R., Adhikari, R., et al. 2009, Reports on Progress in Physics, 72, 076901

Abbott, B. P., Abbott, R., Abbott, T. D., et al. 2017, ApJ, 848, L13

Abbott, B. P., Abbott, R., Abbott, T. D., et al. 2017, Phys. Rev. Lett., 119, 161101

Abbott, B. P., Abbott, R., Abbott, T. D., et al. 2017, ApJ, 848, L12

Adams, S., Kochanek, C., Prieto, J., et al. 2016, Monthly Notices of the Royal Astronomical Society, 460, 1645

Aizerman, M. A. 1964, Automation and remote control, 25, 821

Alard, C. 2000, A&AS, 144, 363

Alexander, K. D., Berger, E., Guillochon, J., Zauderer, B. A., & Williams, P. K. G. 2016, ApJL, 819, L25

Alexander, K. D., Berger, E., Fong, W., et al. 2017a, ApJ, 848, L21

—. 2017b, ApJ, 848, L21

Alexander, K. D., Margutti, R., Blanchard, P. K., et al. 2018, ArXiv e-prints, arXiv:1805.02870

Allam Jr, T., Bahmanyar, A., Biswas, R., et al. 2018, arXiv preprint arXiv:1810.00001

Allington-Smith, J., Breare, M., Ellis, R., et al. 1994, Publications of the Astronomical Society of the Pacific, 106, 983

Andreoni, I., Ackley, K., Cooke, J., et al. 2017, ArXiv e-prints, arXiv:1710.05846

Angus, C., Levan, A., Perley, D., et al. 2016, Monthly Notices of the Royal Astronomical Society, 458, 84

Arcavi, I. 2018, ApJ, 855, L23

Arcavi, I., Gal-Yam, A., Sullivan, M., et al. 2014, The Astrophysical Journal, 793, 38

Arcavi, I., Wolf, W. M., Howell, D. A., et al. 2016, The Astrophysical Journal, 819, 35

Arcavi, I., Hosseinzadeh, G., Howell, D. A., et al. 2017, Nature, 551, 64

Arnaud, K. A. 1996, Astronomical Society of the Pacific Conference Series, Vol. 101, XSPEC: The First Ten Years (APS Books), 17

Arnett, D., & Livne, E. 1994, ApJ, 427, 315

Arnett, W. D. 1979, ApJL, 230, L37

—. 1980, ApJ, 237, 541

—. 1982, ApJ, 253, 785

Baade, W. 1938, ApJ, 88, 285

Baade, W., & Zwicky, F. 1934, Proceedings of the National Academy of Sciences, 20, 254

Bachetti, M., Harrison, F., Walton, D. J., et al. 2014, Nature, 514, 202

Bailey, S., Aragon, C., Romano, R., et al. 2007, The Astrophysical Journal, 665, 1246

Bailyn, C. D., & Grindlay, J. E. 1990, ApJ, 353, 159

Barbary, K., Dawson, K. S., Tokita, K., et al. 2008, The Astrophysical Journal, 690, 1358

Barkat, Z., Rakavy, G., & Sack, N. 1967, PhRvL, 18, 379

Barnes, J., & Kasen, D. 2013, The Astrophysical Journal, 775, 18

Barnes, J., Kasen, D., Wu, M.-R., & Martínez-Pinedo, G. 2016, The Astrophysical Journal, 829, 110

Bauswein, A., Ardevol Pulpillo, R., Janka, H.-T., & Goriely, S. 2014, ApJ, 795, L9

Bauswein, A., Goriely, S., & Janka, H.-T. 2013, ApJ, 773, 78

Bazin, G., Palanque-Delabrouille, N., Rich, J., et al. 2009, Astronomy and Astrophysics, 499, 653

Becker, A. 2015, Astrophysics Source Code Library, ascl:1504.004

Beloborodov, A. M. 2014, MNRAS, 438, 169

Berger, E. 2014, ARA&A, 52, 43

Berger, E., & Chornock, R. 2010, ATel, 2638, 1

Berger, E., Fong, W., & Chornock, R. 2013a, ApJL, 774, L23

Berger, E., Soderberg, A., Chevalier, R., et al. 2009, The Astrophysical Journal, 699, 1850

Berger, E., Chornock, R., Lunnan, R., et al. 2012, The Astrophysical Journal Letters, 755, L29

Berger, E., Leibler, C., Chornock, R., et al. 2013b, The Astrophysical Journal, 779, 18

Bernstein, R., Shectman, S. A., Gunnels, S. M., Mochnacki, S., & Athey, A. E. 2003, SPIE, 4841, 1694

Bersten, M. C., & Hamuy, M. 2009, ApJ, 701, 200

Betoule, M. e. a., Kessler, R., Guy, J., et al. 2014, Astronomy & Astrophysics, 568, A22

Bildsten, L., Shen, K. J., Weinberg, N. N., & Nelemans, G. 2007, ApJL, 662, L95

Binder, B., Williams, B., Kong, A., et al. 2011, The Astrophysical Journal Letters, 739, L51

—. 2016, Monthly Notices of the Royal Astronomical Society, 457, 1636

Blagorodnova, N., Kotak, R., Polshaw, J., et al. 2017, The Astrophysical Journal, 834, 107

Blake, C., Brough, S., Couch, W., et al. 2008, Astronomy & Geophysics, 49, 5

Blanchard, P. K., Berger, E., Fong, W., et al. 2017, ApJ, 848, L22

Blondin, S., & Tonry, J. L. 2007, The Astrophysical Journal, 666, 1024

Bonanos, A., Massa, D., Sewilo, M., et al. 2009, The Astronomical Journal, 138, 1003

Bonanos, A., Lennon, D., Köhlinger, F., et al. 2010, The Astronomical Journal, 140, 416

Bond, H. E. 2010, The Astronomer's Telegram, 2640, 1

Bond, H. E., Bedin, L. R., Bonanos, A. Z., et al. 2009, The Astrophysical Journal Letters, 695, L154

Boone, K. 2019, AJ, 158, 257

Botticella, M. T., Pastorello, A., Smartt, S., et al. 2009, Monthly Notices of the Royal Astronomical Society, 398, 1041

Breeveld, A. A., Landsman, W., Holland, S. T., et al. 2011, in American Institute of Physics Conference Series, Vol. 1358, American Institute of Physics Conference Series, ed. J. E. McEnery, J. L. Racusin, & N. Gehrels, 373–376

Breiman, L. 2001, Machine learning, 45, 5

Breiman, L., Friedman, J., Stone, C. J., & Olshen, R. A. 1984, Classification and regression trees (CRC press)

Brown, P. J. 2010, The Astronomer's Telegram, 2633, 1

Brown, P. J., Breeveld, A. A., H. S., Kuin, P., & Pritchard, T. 2014, Ap&SS, 354, 89

Campbell, H., D'Andrea, C. B., Nichol, R. C., et al. 2013, The Astrophysical Journal, 763, 88

Cantiello, M., Jensen, J., Blakeslee, J., et al. 2018, arXiv preprint arXiv:1801.06080

Cao, Y., Kasliwal, M. M., Neill, J. D., et al. 2012, ApJ, 752, 133

Capaccioli, M., della Valle, M., D'Onofrio, M., & Rosino, L. 1990, ApJ, 360, 63

Carpano, S., Haberl, F., Maitra, C., & Vasilopoulos, G. 2018, Monthly Notices of the Royal Astronomical Society: Letters, 476, L45

Chambers, K. C., Magnier, E. A., Metcalfe, N., et al. 2016, ArXiv e-prints, arXiv:1612.05560

Charnock, T., & Moss, A. 2017a, ApJL, 837, L28

—. 2017b, The Astrophysical Journal Letters, 837, L28

Chaty, S., & Filliatre, P. 2005, in Multiwavelength Approach to Unidentified Gamma-Ray Sources (Springer), 235–244

Chaty, S., & Rahoui, F. 2007, in ESA Special Publication, Vol. 622, The Obscured Universe. Proceedings of the VI INTEGRAL Workshop, 247

Chatzopoulos, E., Wheeler, J. C., & Vinko, J. 2012, The Astrophysical Journal, 746, 121

Chatzopoulos, E., Wheeler, J. C., Vinkó, J., Horvath, Z., & Nagy, A. 2013, The Astrophysical Journal, 773, 76

Chawla, N. V., Bowyer, K. W., Hall, L. O., & Kegelmeyer, W. P. 2002, Journal of artificial intelligence research, 16, 321

Chen, T.-W., Smartt, S. J., Yates, R. M., et al. 2017a, Monthly Notices of the Royal Astronomical Society, 470, 3566

Chen, T.-W., Smartt, S., Jerkstrand, A., et al. 2015, Monthly Notices of the Royal Astronomical Society, 452, 1567

Chen, T.-W., Nicholl, M., Smartt, S., et al. 2017b, Astronomy and Astrophysics, 602, A9

Chevalier, R. A. 1982, ApJ, 258, 790

Chevalier, R. A., & Fransson, C. 1994, ApJ, 420, 268

Chevalier, R. A., & Irwin, C. M. 2011, The Astrophysical Journal Letters, 729, L6

Childress, M. J., Hillier, D. J., Seitenzahl, I., et al. 2015, MNRAS, 454, 3816

Chita, S., Langer, N., van Marle, A., Garcia-Segura, G., & Heger, A. 2008, Astronomy & Astrophysics, 488, L37

Cho, K., Van Merriënboer, B., Gulcehre, C., et al. 2014, arXiv preprint arXiv:1406.1078

Chollet, F. 2015, keras, `https://github.com/fchollet/keras`

Chomiuk, L., & Soderberg, A. 2010, ATel, 2658, 1

Chomiuk, L., Chornock, R., Soderberg, A. M., et al. 2011, The Astrophysical Journal, 743, 114

Chornock, R., & Berger, E. 2010, ATel, 2637, 1

Chornock, R., Berger, E., Gezari, S., et al. 2014a, ApJ, 780, 44

—. 2014b, ApJ, 780, 44

Chornock, R., Berger, E., Kasen, D., et al. 2017, The Astrophysical Journal Letters, 848, L19

Clark, J., Steele, I., Fender, R., & Coe, M. 1999, Astronomy and Astrophysics, 348, 888

Colgate, S. A., & McKee, C. 1969, ApJ, 157, 623

Colless, M., Peterson, B. A., Jackson, C., et al. 2003, arXiv e-prints, astro

Contreras, C., Hamuy, M., Phillips, M. M., et al. 2010, AJ, 139, 519

Coppejans, D., Margutti, R., Guidorzi, C., et al. 2018, The Astrophysical Journal, 856, 56

Corliss, C., & Sugar, J. 1982, JPCRD, 11, 135

Cortes, C., Mohri, M., Riley, M., & Rostamizadeh, A. 2008, in International Conference on Algorithmic Learning Theory, Springer, 38–53

Coulter, D. A., Foley, R. J., Kilpatrick, C. D., et al. 2017a, Sci, 358, 1556

—. 2017b, ArXiv e-prints, arXiv:1710.05452

Covino, S., Wiersema, K., Fan, Y. Z., et al. 2017, ArXiv e-prints, arXiv:1710.05849

Cowperthwaite, P., Villar, V., Scolnic, D., & Berger, E. 2019, The Astrophysical Journal, 874, 88

Cowperthwaite, P. S., Berger, E., Villar, V. A., et al. 2017, ApJ, 848, L17

Dahlen, T., Strolger, L.-G., Riess, A. G., et al. 2004, ApJ, 613, 189

Darbha, S., Metzger, B. D., Quataert, E., et al. 2010a, MNRAS, 409, 846

—. 2010b, MNRAS, 409, 846

D'Avanzo, P., Campana, S., Salafia, O. S., et al. 2018, ArXiv e-prints, arXiv:1801.06164

Davidson, K., & Humphreys, R. M. 1997, Annual Review of Astron and Astrophys, 35, 1

Davies, R. L., Allington-Smith, J. R., Bettess, P., et al. 1997, in Optical telescopes of today and tomorrow, Vol. 2871, International Society for Optics and Photonics, 1099–1106

De Cia, A., Gal-Yam, A., Rubin, A., et al. 2017, ArXiv e-prints, arXiv:1708.01623

Delgado, F., Saha, A., Chandrasekharan, S., et al. 2014, in Modeling, Systems Engineering, and Project Management for Astronomy VI, Vol. 9150, International Society for Optics and Photonics, 915015

Della Valle, M., & Livio, M. 1995, ApJ, 452, 704

Demircan, O., & Kahraman, G. 1991, Ap&SS, 181, 313

Dessart, L., Audit, E., & Hillier, D. J. 2015, MNRAS, 449, 4304

Dessart, L., Burrows, A., Ott, C. D., et al. 2006, ApJ, 644, 1063

Dessart, L., Hillier, D. J., Waldman, R., Livne, E., & Blondin, S. 2012, Monthly Notices of the Royal Astronomical Society: Letters, 426, L76

Dessart, L., Ott, C. D., Burrows, A., Rosswog, S., & Livne, E. 2009, ApJ, 690, 1681

Dessart, L., Waldman, R., Livne, E., Hillier, D. J., & Blondin, S. 2013, MNRAS, 428, 3227

Dhawan, S., Leibundgut, B., Spyromilio, J., & Maguire, K. 2015, Monthly Notices of the Royal Astronomical Society, 448, 1345

Díaz, M. C., Macri, L. M., Lambas, D. G., et al. 2017, ApJL, 848, L29

Dobie, D., Kaplan, D. L., Murphy, T., et al. 2018, ApJ, 858, L15

Dong, S., Shappee, B. J., Prieto, J. L., et al. 2016, Science, 351, 257

Drake, S., & Ulrich, R. 1980, ApJS, 42, 351

Dressler, A., Hare, T., Bigelow, B. C., & Osip, D. J. 2006, Proc. SPIE, 6269, 62690F

Drout, M. R., Soderberg, A. M., Gal-Yam, A., et al. 2011, The Astrophysical Journal, 741, 97

Drout, M. R., Chornock, R., Soderberg, A. M., et al. 2014, The Astrophysical Journal, 794, 23

Drout, M. R., Piro, A. L., Shappee, B. J., et al. 2017, Sci, 358, 1570

Einstein, A. 1918, Sitzungsber. Preuss. Akad. Wiss. Berlin (Math. Phys.), 1918, 154

Ekstrom, S., Georgy, C., Eggenberger, P., et al. 2012, Astronomy & Astrophysics, 537, A146

Elias-Rosa, N., Mauerhan, J., & Van Dyk, S. 2010, ATel, 2636, 1

Evans, P., Beardmore, A., Page, K., et al. 2009, Monthly Notices of the Royal Astronomical Society, 397, 1177

Evans, P. A., Cenko, S. B., Kennea, J. A., et al. 2017, ArXiv e-prints, arXiv:1710.05437

Fabricant, D., Fata, R., Roll, J., et al. 2005, Publications of the Astronomical Society of the Pacific, 117, 1411

Fazio, G., Hora, J., Allen, L., et al. 2004, The Astrophysical Journal Supplement Series, 154, 10

Fernández, R., & Metzger, B. D. 2013, MNRAS, 435, 502

Ferretti, R., Amanullah, R., Goobar, A., et al. 2016, A&A, 592, A40

Filippenko, A. V. 1997, Annual Review of Astronomy and Astrophysics, 35, 309

Filippenko, A. V., Li, W., Treffers, R., & Modjaz, M. 2001, in International Astronomical Union Colloquium, Vol. 183, Cambridge University Press, 121–130

Firth, R. E., Sullivan, M., Gal-Yam, A., et al. 2015, MNRAS, 446, 3895

Foley, R. J., & Mandel, K. 2013, The Astrophysical Journal, 778, 167

Foley, R. J., Challis, P. J., Chornock, R., et al. 2013, ApJ, 767, 57

Fong, W., Berger, E., Blanchard, P. K., et al. 2017, ApJ, 848, L23

Fong, W.-f., Berger, E., Margutti, R., & Zauderer, B. A. 2015, ApJ, 815, 102

Foreman-Mackey, D. 2015, Astrophysics Source Code Library

Frank, J., & Rees, M. J. 1976, MNRAS, 176, 633

Freedman, W. L., Madore, B. F., Gibson, B. K., et al. 2001, The Astrophysical Journal, 553, 47

Fremling, U., Miller, A., Sharma, Y., et al. 2019, arXiv preprint arXiv:1910.12973

Frontera-Pons, J., Sureau, F., Bobin, J., & Le Floc'h, E. 2017, Astronomy & Astrophysics, 603, A60

Fryer, C., Benz, W., Herant, M., & Colgate, S. A. 1999, ApJ, 516, 892

Gal-Yam, A. 2012, Science, 337, 927

Gal-Yam, A., Mazzali, P., Ofek, E., et al. 2009, Nature, 462, 624

Gall, C., Hjorth, J., Rosswog, S., Tanvir, N. R., & Levan, A. J. 2017, ApJ, 849, L19

Gallagher, J., & Starrfield, S. 1978, ARA&A, 16, 171

Ganeshalingam, M., Li, W., Filippenko, A. V., et al. 2010, ApJS, 190, 418

Gelman, A., Hwang, J., & Vehtari, A. 2014, Statistics and Computing, 24, 997

Gelman, A., & Rubin, D. B. 1992, Statistical science, 457

Gezari, S., Martin, D. C., Milliard, B., et al. 2006, ApJ, 653, L25

Gezari, S., Chornock, R., Rest, A., et al. 2012, Nature, 485, 217

Goldstein, A., Veres, P., Burns, E., et al. 2017, The Astrophysical Journal Letters, 848, L14

Goranskij, V. P., Barsukova, E. A., Spiridonova, O. I., et al. 2016, Astrophysical Bulletin, 71, 82

Gottlieb, O., Nakar, E., Piran, T., & Hotokezaka, K. 2017, ArXiv e-prints, arXiv:1710.05896

Graham, M. L., Connolly, A. J., Ivezić, Ž., et al. 2017, arXiv preprint arXiv:1706.09507

Graur, O., Bianco, F. B., Huang, S., et al. 2017, The Astrophysical Journal, 837, 120

Guidorzi, C., Margutti, R., Brout, D., et al. 2017, ArXiv e-prints, arXiv:1710.06426

Guillochon, J., Manukian, H., & Ramirez-Ruiz, E. 2014, ApJ, 783, 23

Guillochon, J., Nicholl, M., Villar, V. A., et al. 2018, The Astrophysical Journal Supplement Series, 236, 6

Guillochon, J., Nicholl, M., Villar, V. A., et al. 2017a, ArXiv e-prints, arXiv:1710.02145

Guillochon, J., Parrent, J., Kelley, L. Z., & Margutti, R. 2017b, ApJ, 835, 64

Guillochon, J., Parrent, J., Kelley, L. Z., & Margutti, R. 2017, The Astrophysical Journal, 835, 64

Guillochon, J., & Ramirez-Ruiz, E. 2013, ApJ, 767, 25

Guillochon, J., Ramirez-Ruiz, E., Rosswog, S., & Kasen, D. 2009, ApJ, 705, 844

Guy, J., Astier, P., Nobili, S., Regnault, N., & Pain, R. 2005, Astronomy and Astrophysics, 443, 781

Guy, J., Astier, P., Baumont, S., et al. 2007, Astronomy & Astrophysics, 466, 11

Hachisu, I., & Kato, M. 2014, ApJ, 798, 76

Haggard, D., Nynka, M., Ruan, J. J., et al. 2017, ApJ, 848, L25

Hallinan, G., Corsi, A., Mooley, K. P., et al. 2017a, ArXiv e-prints, arXiv:1710.05435

—. 2017b, Science, 358, 1579

Hamuy, M. 2003, ApJ, 582, 905

Heger, A., & Langer, N. 1998, Astronomy and Astrophysics, 334, 210

Hicken, M., Challis, P., Jha, S., et al. 2009, ApJ, 700, 331

Hicken, M., Challis, P., Kirshner, R. P., et al. 2012, ApJS, 200, 12

Hillier, D. 1991, Astronomy and Astrophysics, 247, 455

Hills, J. G. 1988, Nature, 331, 687

Hinshaw, G., Larson, D., Komatsu, E., et al. 2013, The Astrophysical Journal Supplement Series, 208, 19

Hoffman, J. L., Leonard, D. C., Chornock, R., et al. 2008, The Astrophysical Journal, 688, 1186

Holoien, T. W. S., Prieto, J. L., Bersier, D., et al. 2014, MNRAS, 445, 3263

Hotokezaka, K., Kyutoku, K., Tanaka, M., et al. 2013, ApJ, 778, L16

Howell, D., Kasen, D., Lidman, C., et al. 2013, The Astrophysical Journal, 779, 98

Howell, D. A., Sullivan, M., Perrett, K., et al. 2005, The Astrophysical Journal, 634, 1190

Howell, D. A., Kasen, D., Lidman, C., et al. 2013, ApJ, 779, 98

Hoyle, B., Rau, M. M., Bonnett, C., Seitz, S., & Weller, J. 2015, Monthly Notices of the Royal Astronomical Society, 450, 305

Hoyle, F., & Fowler, W. A. 1960, ApJ, 132, 565

Hu, L., Wu, X., Andreoni, I., et al. 2017, SciBu, 62, 1433

Huang, J., Gretton, A., Borgwardt, K. M., Schölkopf, B., & Smola, A. J. 2007, in Advances in neural information processing systems, 601–608

Humphreys, R. M., Bond, H. E., Bedin, L. R., et al. 2011, The Astrophysical Journal, 743, 118

Humphreys, R. M., & Davidson, K. 1994, PASP, 106, 1025

Humphreys, R. M., Davidson, K., Grammer, S., et al. 2013, The Astrophysical Journal, 773, 46

Immler, S., Brown, P., & Russell, B. R. 2010, ATel, 2639, 1

Inserra, C., & Smartt, S. J. 2014, ApJ, 796, 87

Inserra, C., & Smartt, S. J. 2014, The Astrophysical Journal, 796, 87

Inserra, C., Smartt, S. J., Jerkstrand, A., et al. 2013, ApJ, 770, 128

Inserra, C., Smartt, S., Jerkstrand, A., et al. 2013, The Astrophysical Journal, 770, 128

Ishida, E., Beck, R., Gonzalez-Gaitan, S., et al. 2018, arXiv preprint arXiv:1804.03765

Ishida, E. E., & de Souza, R. S. 2013, Monthly Notices of the Royal Astronomical Society, 430, 509

Ivanova, N., Justham, S., Avendano Nandez, J. L., & Lombardi, J. C. 2013, Sci, 339, 433

Ivezic, Z., Nenkova, M., & Elitzur, M. 1999, arXiv e-prints, astro

Ivezic, Z., et al. 2011, Large synoptic survey telescope (lsst) science requirements document

Jedicke, R., Tonry, J., Veres, P., et al. 2012, in AAS/Division for Planetary Sciences Meeting Abstracts# 44, Vol. 44

Jerkstrand, A., Smartt, S., Inserra, C., et al. 2017, The Astrophysical Journal, 835, 13

Jha, S., Kirshner, R. P., Challis, P., et al. 2006, AJ, 131, 527

Jones, D., Scolnic, D., Riess, A., et al. 2017, The Astrophysical Journal, 843, 6

—. 2018, The Astrophysical Journal, 857, 51

Jones, D. H., Read, M. A., Saunders, W., et al. 2009, Monthly Notices of the Royal Astronomical Society, 399, 683

Just, O., Bauswein, A., Pulpillo, R. A., Goriely, S., & Janka, H.-T. 2015, MNRAS, 448, 541

Kaiser, N., Aussel, H., Burke, B. E., et al. 2002, in Survey and Other Telescope Technologies and Discoveries, Vol. 4836, International Society for Optics and Photonics, 154–165

Kaiser, N., Burgett, W., Chambers, K., et al. 2010, in Proc. SPIE, Vol. 7733, Ground-based and Airborne Telescopes III, 77330E

Kangas, T., Blagorodnova, N., Mattila, S., et al. 2017, Monthly Notices of the Royal Astronomical Society, 469, 1246

Kaplan, D., Moon, D.-S., & Reach, W. 2006, ApJL, 649, L107

Karpenka, N. V., Feroz, F., & Hobson, M. 2012, MNRAS, 429, 1278

Karpenka, N. V., Feroz, F., & Hobson, M. P. 2013, MNRAS, 429, 1278

Kasen, D. 2006, The Astrophysical Journal, 649, 939

Kasen, D., Badnell, N., & Barnes, J. 2013, The Astrophysical Journal, 774, 25

Kasen, D., & Bildsten, L. 2010, The Astrophysical Journal, 717, 245

Kasen, D., Fernández, R., & Metzger, B. D. 2015, MNRAS, 450, 1777

Kasen, D., Metzger, B., Barnes, J., Quataert, E., & Ramirez-Ruiz, E. 2017, Nature, 551, 80

Kasen, D., Metzger, B. D., & Bildsten, L. 2016, ApJ, 821, 36

Kasen, D., & Woosley, S. 2009, ApJ, 703, 2205

Kasen, D., Woosley, S., & Heger, A. 2011, ApJ, 734, 102

Kashi, A., Frankowski, A., & Soker, N. 2010, ApJL, 709, L11

Kashi, A., & Soker, N. 2010, arXiv e-prints, arXiv:1011.1222

Kasliwal, M. M. 2011, PhD thesis, California Institute of Technology

—. 2012a, PASA, 29, 482

—. 2012b, Publications of the Astronomical Society of Australia, 29, 482

Kasliwal, M. M., Kulkarni, S. R., Arcavi, I., et al. 2011, ApJ, 730, 134

Kasliwal, M. M., Kulkarni, S. R., Gal-Yam, A., et al. 2012, ApJ, 755, 161

Kasliwal, M. M., Nakar, E., Singer, L. P., et al. 2017, Sci, 358, 1559

Kessler, R., et al., & et al. 2019, in prep.

Kessler, R., Bassett, B., Belov, P., et al. 2010, Publications of the Astronomical Society of the Pacific, 122, 1415

Khan, R., Stanek, K., Kochanek, C., Thompson, T., & Prieto, J. 2010, ATel, 2632, 1

Khokhlov, A. 1991, Astronomy and Astrophysics, 245, 114

Kilpatrick, C. D., Foley, R. J., Kasen, D., et al. 2017a, ArXiv e-prints, arXiv:1710.05434

—. 2017b, Sci, 358, 1583

Kimura, A., Takahashi, I., Tanaka, M., et al. 2017, arXiv preprint arXiv:1711.11526

Kingma, D. P., & Ba, J. 2014, arXiv e-prints, arXiv:1412.6980

Kingma, D. P., & Ba, J. 2014, arXiv preprint arXiv:1412.6980

Kobayashi, H., Kimura, H., Watanabe, S.-i., Yamamoto, T., & Muller, S. 2011, Earth, Plansets and Space, 63, 1067

Kochanek, C., Szczygielstrok, D., & Stanek, K. 2012, ApJ, 758, 142

Kochanek, C. S., Beacom, J. F., Kistler, M. D., et al. 2008, The Astrophysical Journal, 684, 1336

Kochanek, C. S., Shappee, B. J., Stanek, K. Z., et al. 2017, PASP, 129, 104502

Korobkin, O., Rosswog, S., Arcones, A., & Winteler, C. 2012, Monthly Notices of the Royal Astronomical Society, 426, 1940

Kramer, M. A. 1991, AIChE journal, 37, 233

Kulkarni, S. 2018, The Astronomer's Telegram, 11266

Kulkarni, S. R. 2018, The Astronomer's Telegram, 11266

Kulkarni, S. R., Ofek, E. O., Rau, A., et al. 2007, Nature, 447, 458

Lamers, H. J., Zickgraf, F.-J., de Winter, D., Houziaux, L., & Zorec, J. 1998, Astronomy and Astrophysics, 340, 117

Langer, N., & Heger, A. 1998, in Astrophysics and Space Science Library, Vol. 233, B[e] stars, ed. A. M. Hubert & C. Jaschek (Kluwer Academic), 235

Laskar, T., Berger, E., & Chary, R.-R. 2011, ApJ, 739, 1

Laskar, T., Berger, E., & Chornock, R. 2010, ATel, 2648, 1

Lau, R. M., Ofek, E. O., & Kasliwal, M. M. 2017, GRB Coordinates Network, Circular Service, No. 21520, #1 (2017), 21982

Lau, R. M., Kasliwal, M. M., Bond, H. E., et al. 2016, ApJ, 830, 142

Law, N. M., Kulkarni, S. R., Dekany, R. G., et al. 2009, Publications of the Astronomical Society of the Pacific, 121, 1395

Lazzati, D., Perna, R., Morsony, B. J., et al. 2017, ArXiv e-prints, arXiv:1712.03237

Le Fèvre, O., Vettolani, G., Garilli, B., et al. 2005, Astronomy & Astrophysics, 439, 845

Leloudas, G., Chatzopoulos, E., Dilday, B., et al. 2012, Astronomy and Astrophysics, 541, A129

Leloudas, G., Schulze, S., Krühler, T., et al. 2015, Monthly Notices of the Royal Astronomical Society, 449, 917

Leloudas, G., Fraser, M., Stone, N. C., et al. 2016, Nature Astronomy, 1, 0002

Leo, B., Friedman, J. H., Olshen, R. A., & Stone, C. J. 1984, Wadsworth International Group

Levan, A. J., Lyman, J. D., Tanvir, N. R., et al. 2017, ApJ, 848, L28

Lewin, W. H., Lewin, W. H., van Paradijs, J., & van den Heuvel, E. P. 1997, X-ray Binaries, Vol. 26

Li, L.-X., & Paczyński, B. 1998, The Astrophysical Journal Letters, 507, L59

Lilly, S. J., Carollo, C. M., & Stockton, A. N. 2003, The Astrophysical Journal, 597, 730

Lilly, S. J., Le Brun, V., Maier, C., et al. 2009, The Astrophysical Journal Supplement Series, 184, 218

Lippuner, J., Fernández, R., Roberts, L. F., et al. 2017, MNRAS, 472, 904

Lipunov, V., Gorbovskoy, E., Kornilov, V., et al. 2017, The Astrophysical Journal Letters, 850, L1

Liu, L.-D., Wang, S.-Q., Wang, L.-J., et al. 2017, The Astrophysical Journal, 842, 26

Liu, Y.-Q., Modjaz, M., & Bianco, F. B. 2017, ApJ, 845, 85

Lochner, M., McEwen, J. D., Peiris, H. V., Lahav, O., & Winter, M. K. 2016a, ApJS, 225, 31

—. 2016b, The Astrophysical Journal Supplement Series, 225, 31

Lochner, M., McEwen, J. D., Peiris, H. V., Lahav, O., & Winter, M. K. 2016, ApJS, 225, 31

Lodato, G., Saxton, R., & Komossa, S. 2012, EPJ Web of Conf. 39, Tidal Disruption Events and AGN Outbursts, 01001

LSST Science Collaboration, Abell, P. A., Allison, J., et al. 2009, arXiv e-prints, arXiv:0912.0201

LSST Science Collaboration, Marshall, P., Anguita, T., et al. 2017, ArXiv e-prints, arXiv:1708.04058

Lucas, J., Calef, B., & Kyono, T. 2018, in The Advanced Maui Optical and Space Surveillance Technologies Conference

Lunnan, R., Chornock, R., Berger, E., et al. 2013, ApJ, 771, 97

Lunnan, R., Chornock, R., Berger, E., et al. 2013, The Astrophysical Journal, 771, 97

Lunnan, R., Chornock, R., Berger, E., et al. 2014, ApJ, 787, 138

Lunnan, R., Chornock, R., Berger, E., et al. 2014, The Astrophysical Journal, 787, 138

Lunnan, R., Chornock, R., Berger, E., et al. 2016, ApJ, 831, 144

Lunnan, R., Chornock, R., Berger, E., et al. 2016, The Astrophysical Journal, 831, 144

Lunnan, R., Kasliwal, M. M., Cao, Y., et al. 2017, ApJ, 836, 60

Lunnan, R., Chornock, R., Berger, E., et al. 2018, ApJ, 852, 81

Lunnan, R., Chornock, R., Berger, E., et al. 2018, The Astrophysical Journal, 852, 81

Lv, F., Zhao, T., Nevatia, R., et al. 2006, IEEE Transactions on Pattern Analysis and Machine Intelligence, 1513

Lyman, J., Levan, A., Church, R., Davies, M. B., & Tanvir, N. 2014, MNRAS, 444, 2157

Lyman, J. D., Lamb, G. P., Levan, A. J., et al. 2018, ArXiv e-prints, arXiv:1801.02669

Ma, Z., Zhu, J., Li, W., & Xu, H. 2018, in 2018 14th IEEE International Conference on Signal Processing (ICSP), IEEE, 522–526

Madau, P., & Dickinson, M. 2014, ARA&A, 52, 415

Magnier, E., Schlafly, E., Finkbeiner, D. P., et al. 2016a, arXiv preprint arXiv:1612.05242

Magnier, E. A., Chambers, K., Flewelling, H., et al. 2016b, arXiv preprint arXiv:1612.05240

Makovoz, D., & Marleau, F. R. 2005, Publications of the Astronomical Society of the Pacific, 117, 1113

Mandel, K. S., Narayan, G., & Kirshner, R. P. 2011, The Astrophysical Journal, 731, 120

Margalit, B., & Metzger, B. 2017, ArXiv e-prints, arXiv:1710.05938

Margalit, B., & Metzger, B. D. 2016, MNRAS, 461, 1154

Margalit, B., Metzger, B. D., Thompson, T. A., Nicholl, M., & Sukhbold, T. 2018, MNRAS, 475, 2659

Margutti, R., Milisavljevic, D., Soderberg, A. M., et al. 2013, The Astrophysical Journal, 780, 21

Margutti, R., Chornock, R., Metzger, B., et al. 2017, arXiv preprint arXiv:1704.05865

Margutti, R., Berger, E., Fong, W., et al. 2017a, ApJ, 848, L20

Margutti, R., Metzger, B. D., Chornock, R., et al. 2017b, ApJ, 836, 25

Margutti, R., Alexander, K., Xie, X., et al. 2018a, The Astrophysical Journal Letters, 856, L18

Margutti, R., Cowperthwaite, P., Doctor, Z., et al. 2018b, arXiv preprint arXiv:1812.04051

Marshall, J., Burles, S., Thompson, I. B., et al. 2008, in Ground-based and Airborne Instrumentation for Astronomy II, Vol. 7014, International Society for Optics and Photonics, 701454

Martini, P., Wagner, R. M., Tomaney, A., et al. 1999, AJ, 118, 1034

Martins, F., Boissier, S., Buat, V., Cambrésy, L., & Petit, P. 2015, in SF2A-2015: Proceedings of the Annual meeting of the French Society of Astronomy and Astrophysics

Mathew, B., Banerjee, D., Subramaniam, A., & Ashok, N. 2012, ApJ, 753, 13

Matzner, C. D., & McKee, C. F. 1999, ApJ, 510, 379

Mauerhan, J. C., Smith, N., Filippenko, A. V., et al. 2013, Monthly Notices of the Royal Astronomical Society, 430, 1801

Mauerhan, J. C., Van Dyk, S. D., Graham, M. L., et al. 2015, Monthly Notices of the Royal Astronomical Society, 447, 1922

Mauron, N., & Josselin, E. 2011, Astronomy and Astrophysics, 526, A156

Mazzali, P. A., Sullivan, M., Pian, E., Greiner, J., & Kann, D. A. 2016, MNRAS, 458, 3455

McCrum, M., Smartt, S., Kotak, R., et al. 2013, Monthly Notices of the Royal Astronomical Society, 437, 656

McCrum, M., Smartt, S. J., Kotak, R., et al. 2014, MNRAS, 437, 656

McCrum, M., Smartt, S., Rest, A., et al. 2015, Monthly Notices of the Royal Astronomical Society, 448, 1206

McLeod, B., Geary, J., Conroy, M., et al. 2015, Publications of the Astronomical Society of the Pacific, 127, 366

Melandri, A., Covino, S., Rogantini, D., et al. 2014, A&A, 565, A72

Metzger, B., Piro, A., & Quataert, E. 2009, MNRAS, 396, 1659

Metzger, B., Martínez-Pinedo, G., Darbha, S., et al. 2010, Monthly Notices of the Royal Astronomical Society, 406, 2650

Metzger, B. D. 2012, MNRAS, 419, 827

Metzger, B. D. 2017, Living Reviews in Relativity, 20, 3

Metzger, B. D., & Berger, E. 2012, The Astrophysical Journal, 746, 48

Metzger, B. D., & Fernández, R. 2014, MNRAS, 441, 3444

Metzger, B. D., Margalit, B., Kasen, D., & Quataert, E. 2015, Monthly Notices of the Royal Astronomical Society, 454, 3311

Metzger, B. D., & Pejcha, O. 2017, MNRAS, 471, 3200

Metzger, B. D., & Piro, A. L. 2014, MNRAS, 439, 3916

Metzger, B. D., Piro, A. L., & Quataert, E. 2009, MNRAS, 396, 304

Metzger, B. D., Thompson, T. A., & Quataert, E. 2008, ApJ, 676, 1130

Meynet, G., & Maeder, A. 2000, Astronomy and Astrophysics, 361, 101

Miknaitis, G., Pignata, G., Rest, A., et al. 2007, The Astrophysical Journal, 666, 674

Mink, D. J., Wyatt, W. F., Caldwell, N., et al. 2007, in Astronomical Data Analysis Software and Systems XVI, Vol. 376, 249

Minkowski, R. 1941, Publications of the Astronomical Society of the Pacific, 53, 224

Miyaji, S., Nomoto, K., Yokoi, K., & Sugimoto, D. 1980, PASJ, 32, 303

Möller, A., & de Boissière, T. 2019, arXiv preprint arXiv:1901.06384

—. 2020, Monthly Notices of the Royal Astronomical Society, 491, 4277

Möller, A., Ruhlmann-Kleider, V., Leloup, C., et al. 2016, Journal of Cosmology and Astro-Particle Physics, 2016, 008

Möller, A., Ruhlmann-Kleider, V., Leloup, C., et al. 2016, Journal of Cosmology and Astroparticle Physics, 2016, 008

Monard, L. 2010, CBET, 2289, 1

Mooley, K. P., Nakar, E., Hotokezaka, K., et al. 2018, Nature, 554, 207

Moriya, T. J., Blinnikov, S. I., Baklanov, P. V., Sorokina, E. I., & Dolgov, A. D. 2013, MNRAS, 430, 1402

Moriya, T. J., Maeda, K., Taddia, F., et al. 2013, MNRAS, 435, 1520

—. 2014, MNRAS, 439, 2917

Moriya, T. J., Sorokina, E. I., & Chevalier, R. A. 2018, Space Sci. Rev., 214, 59

Moriya, T. J., Mazzali, P. A., Tominaga, N., et al. 2017, MNRAS, 466, 2085

Moss, A. 2018, arXiv preprint arXiv:1810.06441

Müller, T., Prieto, J. L., Pejcha, O., & Clocchiatti, A. 2017, ApJ, 841, 127

Munari, U., Henden, A., Kiyota, S., et al. 2002, A&A, 389, L51

Murguia-Berthier, A., Montes, G., Ramirez-Ruiz, E., De Colle, F., & Lee, W. H. 2014, ApJ, 788, L8

Murguia-Berthier, A., Ramirez-Ruiz, E., Kilpatrick, C. D., et al. 2017, ApJ, 848, L34

Mushtukov, A. A., Suleimanov, V. F., Tsygankov, S. S., & Poutanen, J. 2015, MNRAS, 454, 2539

Muthukrishna, D., Narayan, G., Mandel, K. S., Biswas, R., & Hložek, R. 2019, arXiv e-prints, arXiv:1904.00014

Muthukrishna, D., Narayan, G., Mandel, K. S., Biswas, R., & Hložek, R. 2019a, arXiv preprint arXiv:1904.00014

Muthukrishna, D., Parkinson, D., & Tucker, B. 2019b, arXiv preprint arXiv:1903.02557

Narayan, G., Zaidi, T., Soraisam, M. D., et al. 2018, The Astrophysical Journal Supplement Series, 236, 9

Naul, B., Bloom, J. S., Pérez, F., & van der Walt, S. 2018, Nature Astronomy, 2, 151

Neill, J. D., Sullivan, M., Gal-Yam, A., et al. 2010, The Astrophysical Journal, 727, 15

Newling, J., Varughese, M., Bassett, B., et al. 2011, Monthly Notices of the Royal Astronomical Society, 414, 1987

Newman, J. A., Cooper, M. C., Davis, M., et al. 2013, The Astrophysical Journal Supplement Series, 208, 5

Nicholl, M., Berger, E., Blanchard, P. K., Gomez, S., & Chornock, R. 2018, arXiv preprint arXiv:1808.00510

Nicholl, M., Berger, E., Margutti, R., et al. 2016, arXiv preprint arXiv:1611.06993

—. 2017, The Astrophysical Journal Letters, 835, L8

Nicholl, M., Berger, E., Margutti, R., et al. 2017, ApJ, 835, L8

Nicholl, M., Guillochon, J., & Berger, E. 2017, The Astrophysical Journal, 850, 55

Nicholl, M., Guillochon, J., & Berger, E. 2017a, ApJ, 850, 55

Nicholl, M., & Smartt, S. 2016, Monthly Notices of the Royal Astronomical Society: Letters, 457, L79

Nicholl, M., Smartt, S., Jerkstrand, A., et al. 2013, Nature, 502, 346

Nicholl, M., Smartt, S. J., Jerkstrand, A., et al. 2014, MNRAS, 444, 2096

Nicholl, M., Smartt, S., Jerkstrand, A., et al. 2014, Monthly Notices of the Royal Astronomical Society, 444, 2096

Nicholl, M., Smartt, S. J., Jerkstrand, A., et al. 2015, ApJ, 807, L18

Nicholl, M., Smartt, S., Jerkstrand, A., et al. 2015a, The Astrophysical Journal Letters, 807, L18

Nicholl, M., Smartt, S. J., Jerkstrand, A., et al. 2015b, Monthly Notices of the Royal Astronomical Society, 452, 3869

Nicholl, M., Berger, E., Smartt, S. J., et al. 2016, ApJ, 826, 39

Nicholl, M., Berger, E., Smartt, S., et al. 2016a, The Astrophysical Journal, 826, 39

Nicholl, M., Berger, E., Margutti, R., et al. 2016b, The Astrophysical Journal Letters, 828, L18

Nicholl, M., Berger, E., Kasen, D., et al. 2017b, ApJ, 848, L18

Nomoto, K., & Kondo, Y. 1991, ApJL, 367, L19

Nugent, P., Kim, A., & Perlmutter, S. 2002, PASP, 114, 803

Nynka, M., Ruan, J. J., & Haggard, D. 2018, ArXiv e-prints, arXiv:1805.04093

Oechslin, R., & Janka, H.-T. 2006, MNRAS, 368, 1489

Ofek, E. O., Zoglauer, A., Boggs, S. E., et al. 2014, ApJ, 781, 42

Ohnaka, K., Driebe, T., Hofmann, K.-H., Weigelt, G., & Wittkowski, M. 2008, Astronomy and Astrophysics, 484, 371

Papadopoulos, A., D'Andrea, C. B., Sullivan, M., et al. 2015, MNRAS, 449, 1215

Papadopoulos, A., D'Andrea, C. B., Sullivan, M., et al. 2015, Monthly Notices of the Royal Astronomical Society, 449, 1215

Pasquet, J., Pasquet, J., Chaumont, M., & Fouchez, D. 2019, Astronomy and Astrophysics, 627, A21

Pasquet-Itam, J., & Pasquet, J. 2018, Astronomy & Astrophysics, 611, A97

Pastorello, A., Mazzali, P. A., Pignata, G., et al. 2007, MNRAS, 377, 1531

Pastorello, A., Smartt, S., Mattila, S., et al. 2007, Nature, 447, 829

Pastorello, A., Smartt, S., Botticella, M., et al. 2010, The Astrophysical Journal Letters, 724, L16

Patat, F., Barbon, R., Cappellaro, E., & Turatto, M. 1994, Astronomy and Astrophysics, 282, 731

Patil, A., Huard, D., & Fonnesbeck, C. J. 2010, Journal of statistical software, 35, 1

Perego, A., Rosswog, S., Cabezón, R. M., et al. 2014, MNRAS, 443, 3134

Perley, D. A., Quimby, R. M., Yan, L., et al. 2016, The Astrophysical Journal, 830, 13

Persson, S., Murphy, D., Smee, S., et al. 2013, Publications of the Astronomical Society of the Pacific, 125, 654

Phillips, M. M., Li, W., Frieman, J. A., et al. 2007, PASP, 119, 360

Pian, E., D'Avanzo, P., Benetti, S., et al. 2017, Nature, 551, 67

Planck Collaboration, P., Aghanim, N., Arnaud, M., et al. 2016, Astronomy and Astrophysics, 594, A13

Poelarends, A., Herwig, F., Langer, N., & Heger, A. 2008, ApJ, 675, 614

Pojmanski, G. 2002, arXiv preprint astro-ph/0210283

Polidan, R., & Peters, G. 1976, Spectroscopic Observations of Be Stars in the near Infrared, 59

Popov, D. 1993, ApJ, 414, 712

Portillo, S. K., Parejko, J. K., Vergara, J. R., & Connolly, A. J. 2020, arXiv preprint arXiv:2002.10464

Pozanenko, A., Barkov, M. V., Minaev, P. Y., et al. 2018, The Astrophysical Journal Letters, 852, L30

Prajs, S., Sullivan, M., Smith, M., et al. 2016, Monthly Notices of the Royal Astronomical Society, 464, 3568

Prajs, S., Sullivan, M., Smith, M., et al. 2017, MNRAS, 464, 3568

Prieto, J. L. 2008, ATel, 1550

Prieto, J. L., Bond, H. E., Kochanek, C. S., et al. 2010, The Astronomer's Telegram, 2660, 1

Prieto, J. L., Rest, A., & Suntzeff, N. B. 2006, ApJ, 647, 501

Prieto, J. L., Kistler, M. D., Thompson, T. A., et al. 2008, The Astrophysical Journal Letters, 681, L9

Qian, Y.-Z. 2000, ApJ, 534, L67

Quataert, E., Fernández, R., Kasen, D., Klion, H., & Paxton, B. 2016, Monthly Notices of the Royal Astronomical Society, 458, 1214

Quimby, R., Kulkarni, S., Kasliwal, M., et al. 2011, Nature, 474, 487

Quimby, R. M., Aldering, G., Wheeler, J. C., et al. 2007, The Astrophysical Journal Letters, 668, L99

Quimby, R. M., Yuan, F., Akerlof, C., & Wheeler, J. C. 2013, Monthly Notices of the Royal Astronomical Society, 431, 912

Radice, D., Galeazzi, F., Lippuner, J., et al. 2016, MNRAS, 460, 3255

Ralph, N. O., Norris, R. P., Fang, G., et al. 2019, Publications of the Astronomical Society of the Pacific, 131, 108011

Rau, A., Kulkarni, S., Ofek, E., & Yan, L. 2007, ApJ, 659, 1536

Reig, P. 2011, The Astrophysical Journal Supplement Series, 332, 1

Reig, P., & Fabregat, J. 2015, Astronomy and Astrophysics, 574, A33

Reig, P., & Nespoli, E. 2013, Astronomy and Astrophysics, 551, A1

Rest, A., Stubbs, C., Becker, A. C., et al. 2005, The Astrophysical Journal, 634, 1103

Rest, A., Scolnic, D., Foley, R. J., et al. 2014, ApJ, 795, 44

Retter, A., & Marom, A. 2003, MNRAS, 345, L25

Revsbech, E. A., Trotta, R., & van Dyk, D. A. 2018, MNRAS, 473, 3969

Rhoads, J. E. 1997, ApJL, 487, L1

Richards, J. W., Homrighausen, D., Freeman, P. E., Schafer, C. M., & Poznanski, D. 2012, Monthly Notices of the Royal Astronomical Society, 419, 1121

Richards, J. W., Starr, D. L., Butler, N. R., et al. 2011, ApJ, 733, 10

Richardson, D., Branch, D., Casebeer, D., et al. 2002, The Astronomical Journal, 123, 745

Riess, A. G., Kirshner, R. P., Schmidt, B. P., et al. 1999, AJ, 117, 707

Rizzi, L., Bresolin, F., Kudritzki, R.-P., Gieren, W., & Pietrzynacuterski, G. 2006, ApJ, 638, 766

Roberts, L. F., Kasen, D., Lee, W. H., & Ramirez-Ruiz, E. 2011, The Astrophysical Journal Letters, 736, L21

Rodrigo, C., Solano, E., & Bayo, A. 2012, SVO Filter Profile Service Version 1.0, IVOA Working Draft 15 October 2012

Rossi, E., Lazzati, D., & Rees, M. J. 2002, MNRAS, 332, 945

Rosswog, S., Feindt, U., Korobkin, O., et al. 2017, Classical and Quantum Gravity, 34, 104001

Rosswog, S., Liebendörfer, M., Thielemann, F.-K., et al. 1999, Astronomy and Astrophysics, 341, 499

Rosswog, S., & Ramirez-Ruiz, E. 2002, MNRAS, 336, L7

Ruan, J. J., Nynka, M., Haggard, D., Kalogera, V., & Evans, P. 2018, ApJ, 853, L4

Rubin, A., Gal-Yam, A., De Cia, A., et al. 2016, ApJ, 820, 33

Rumelhart, D. E., Hinton, G. E., Williams, R. J., et al. 1988, Cognitive modeling, 5, 1

Sako, M., Bassett, B., Connolly, B., et al. 2011, The Astrophysical Journal, 738, 162

Sanders, N. E., Soderberg, A. M., Gezari, S., et al. 2015, The Astrophysical Journal, 799, 208

Sari, R., Piran, T., & Narayan, R. 1998, ApJL, 497, L17

Savchenko, V., Ferrigno, C., Kuulkers, E., et al. 2017, ApJ, 848, L15

Schlafly, E. F., & Finkbeiner, D. P. 2011, The Astrophysical Journal, 737, 103

Schlafly, E. F., & Finkbeiner, D. P. 2011, ApJ, 737, 103

Schmidhuber, J. 2015, Neural networks, 61, 85

Schulze, S., Krühler, T., Leloudas, G., et al. 2018, Monthly Notices of the Royal Astronomical Society, 473, 1258

Scodeggio, M., Guzzo, L., Garilli, B., et al. 2018, A&A, 609, A84

Scolnic, D., Rest, A., Riess, A., et al. 2014, The Astrophysical Journal, 795, 45

Scolnic, D., Jones, D., Rest, A., et al. 2017, arXiv preprint arXiv:1710.00845

Scovacricchi, D., Nichol, R. C., Bacon, D., Sullivan, M., & Prajs, S. 2015, Monthly Notices of the Royal Astronomical Society, 456, 1700

Sekiguchi, Y., Kiuchi, K., Kyutoku, K., Shibata, M., & Taniguchi, K. 2016, Phys. Rev. D, 93, 124046

Shappee, B. J., Simon, J. D., Drout, M. R., et al. 2017, ArXiv e-prints, arXiv:1710.05432

Shen, K. J., Kasen, D., Weinberg, N. N., Bildsten, L., & Scannapieco, E. 2010, ApJ, 715, 767

Shen, K. J., Kasen, D., Weinberg, N. N., Bildsten, L., & Scannapieco, E. 2010, ApJ, 715, 767

Shen, S., Cooke, R. J., Ramirez-Ruiz, E., et al. 2015, ApJ, 807, 115

Siegel, D. M., & Ciolfi, R. 2016, ApJ, 819, 14

Siegel, D. M., & Metzger, B. D. 2017, ArXiv e-prints, arXiv:1705.05473

Silverman, J. M., Ganeshalingam, M., Li, W., et al. 2011, MNRAS, 410, 585

Silverman, J. M., Foley, R. J., Filippenko, A. V., et al. 2012, MNRAS, 425, 1789

Sim, S. A., Fink, M., Kromer, M., et al. 2012, MNRAS, 420, 3003

Sim, S. A., Röpke, F. K., Hillebrandt, W., et al. 2010, ApJ, 714, L52

Smartt, S., Eldridge, J., Crockett, R., & Maund, J. R. 2009, MNRAS, 395, 1409

Smartt, S. J., Valenti, S., Fraser, M., et al. 2015, A&A, 579, A40

Smartt, S. J., Chen, T.-W., Jerkstrand, A., et al. 2017, Nature, 551, 75

Smee, S. A., Gunn, J. E., Uomoto, A., et al. 2013, AJ, 146, 32

Smith, J. A., Allam, S. S., Tucker, D. L., & Fornal, B. 2007, in American Astronomical Society Meeting Abstracts, Vol. 211, American Astronomical Society Meeting Abstracts, 132.14

Smith, M., Sullivan, M., D'Andrea, C., et al. 2016a, The Astrophysical Journal Letters, 818, L8

Smith, N. 2013, MNRAS, 429, 2366

—. 2014, ARA&A, 52, 487

Smith, N. 2017, in Handbook of Supernovae, ed. A. W. Alsabti & P. Murdin (Springer), 403

Smith, N., Andrews, J. E., Mauerhan, J. C., et al. 2016b, Monthly Notices of the Royal Astronomical Society, 455, 3546

Smith, N., & Frew, D. J. 2011, MNRAS, 415, 2009

Smith, N., Humphreys, R. M., & Gehrz, R. D. 2001, PASP, 113, 692

Smith, N., Li, W., Silverman, J. M., Ganeshalingam, M., & Filippenko, A. V. 2011, Monthly Notices of the Royal Astronomical Society, 415, 773

Smith, N., Mauerhan, J. C., & Prieto, J. L. 2014, Monthly Notices of the Royal Astronomical Society, 438, 1191

Smith, N., & McCray, R. 2007, ApJL, 671, L17

Smith, N., Silverman, J. M., Chornock, R., et al. 2009, The Astrophysical Journal, 695, 1334

Smith, N., Miller, A., Li, W., et al. 2010, The Astronomical Journal, 139, 1451

Soares-Santos, M., Holz, D., Annis, J., et al. 2017, The Astrophysical Journal Letters, 848, L16

Soares-Santos, M., Holz, D. E., Annis, J., et al. 2017, ArXiv e-prints, arXiv:1710.05459

Soker, N., & Tylenda, R. 2006, MNRAS, 373, 733

Spergel, D., Gehrels, N., Baltay, C., et al. 2015, arXiv e-prints, arXiv:1503.03757

Spergel, D., Gehrels, N., Baltay, C., et al. 2015, arXiv preprint arXiv:1503.03757

Spinelli, J. J., & Stephens, M. A. 1997, Canadian Journal of Statistics, 25, 257

Stone, N. C. 2014, The Tidal Disruption of Stars by Supermassive Black Holes: An Analytic Approach (Springer)

Stritzinger, M., Hamuy, M., Suntzeff, N. B., et al. 2002, AJ, 124, 2100

Stubbs, C. W., Doherty, P., Cramer, C., et al. 2010, ApJS, 191, 376

Stubbs, C. W., Doherty, P., Cramer, C., et al. 2010, The Astrophysical Journal Supplement Series, 191, 376

Sullivan, M., Le Borgne, D., Pritchet, C., et al. 2006, The Astrophysical Journal, 648, 868

Taddia, F., Stritzinger, M., Sollerman, J., et al. 2013, Astronomy and Astrophysics, 555, A10

Taddia, F., Sollerman, J., Leloudas, G., et al. 2015, A&A, 574, A60

Taddia, F., Fremling, C., Sollerman, J., et al. 2016, A&A, 592, A89

Takami, H., Nozawa, T., & Ioka, K. 2014, The Astrophysical Journal Letters, 789, L6

Tanaka, M., & Hotokezaka, K. 2013, The Astrophysical Journal, 775, 113

Tanaka, M., Moriya, T. J., & Yoshida, N. 2013, Monthly Notices of the Royal Astronomical Society, 435, 2483

Tanaka, M., Moriya, T. J., Yoshida, N., & Nomoto, K. 2012, Monthly Notices of the Royal Astronomical Society, 422, 2675

Tanaka, M., Utsumi, Y., Mazzali, P. A., et al. 2017a, ArXiv e-prints, arXiv:1710.05850

—. 2017b, ArXiv e-prints, arXiv:1710.05850

Tanaka, M., Kato, D., Gaigalas, G., et al. 2018, ApJ, 852, 109

Tanvir, N., Levan, A., González-Fernández, C., et al. 2017, The Astrophysical Journal Letters, 848, L27

Tanvir, N. R., Levan, A. J., Fruchter, A. S., et al. 2013, Nature, 500, 547

Tartaglia, L., Pastorello, A., Taubenberger, S., et al. 2015, Monthly Notices of the Royal Astronomical Society, 447, 117

Tartaglia, L., Elias-Rosa, N., Pastorello, A., et al. 2016, The Astrophysical Journal Letters, 823, L23

Tauris, T. M., Langer, N., & Podsiadlowski, P. 2015, MNRAS, 451, 2123

The Dark Energy Survey Collaboration. 2005, ArXiv Astrophysics e-prints, astro-ph/0510346

The LIGO Scientific Collaboration, the Virgo Collaboration, Abbott, B. P., et al. 2017, ArXiv e-prints, arXiv:1710.05836

Thompson, T. A., Prieto, J. L., Stanek, K., et al. 2009, The Astrophysical Journal, 705, 1364

Tominaga, N., Blinnikov, S. I., & Nomoto, K. 2013, ApJL, 771, L12

Tomsick, J. A., Chaty, S., Rodriguez, J., et al. 2006, The Astrophysical Journal, 647, 1309

—. 2009, The Astrophysical Journal, 694, 344

Tonry, J. L., Stubbs, C. W., Lykke, K. R., et al. 2012, ApJ, 750, 99

Tripp, R., & Branch, D. 1999, ApJ, 525, 209

Troja, E., Piro, L., van Eerten, H., et al. 2017, ArXiv e-prints, arXiv:1710.05433

Troja, E., Piro, L., Ryan, G., et al. 2018, MNRAS, L60

Turatto, M., Cappellaro, E., Danziger, I., et al. 1993, Monthly Notices of the Royal Astronomical Society, 262, 128

Utsumi, Y., Tanaka, M., Tominaga, N., et al. 2017, ArXiv e-prints, arXiv:1710.05848

Valenti, S., Taubenberger, S., Pastorello, A., et al. 2012, ApJ, 749, L28

Valenti, S., David, J., Yang, S., et al. 2017, The Astrophysical Journal Letters, 848, L24

Valenti, S., David, Sand, J., et al. 2017, ApJ, 848, L24

Van Dyk, S. D., Filippenko, A. V., Chornock, R., Li, W., & Challis, P. M. 2005, PASP, 117, 553

Van Dyk, S. D., Li, W., Filippenko, A. V., et al. 2006, arXiv e-prints, astro

Van Dyk, S. D., & Matheson, T. 2012, ApJ, 746, 179

Van Dyk, S. D., Peng, C. Y., King, J. Y., et al. 2000, Publications of the Astronomical Society of the Pacific, 112, 1532

van Eerten, H., Zhang, W., & MacFadyen, A. 2010, ApJ, 722, 235

Van Eerten, H. J., & MacFadyen, A. I. 2012, ApJL, 747, L30

van Loon, J. T., Groenewegen, M. A. T., de Koter, A., et al. 1999, A&A, 351, 559

van Velzen, S. 2018, ApJ, 852, 72

Villar, V., Guillochon, J., Berger, E., et al. 2017a, The Astrophysical Journal Letters, 851, L21

Villar, V. A. 2016, Astrobites

Villar, V. A., Berger, E., Metzger, B. D., & Guillochon, J. 2017b, The Astrophysical Journal, 849, 70

Villar, V. A., Berger, E., Metzger, B. D., & Guillochon, J. 2017, ArXiv e-prints, arXiv:1707.08132

Villar, V. A., Nicholl, M., & Berger, E. 2018, The Astrophysical Journal, 869, 166

Villar, V. A., Berger, E., Chornock, R., et al. 2016, ApJ, 830, 11

Villar, V. A., Berger, E., Miller, G., et al. 2019, arXiv e-prints, arXiv:1905.07422

Vinkó, J., Bíró, I. B., Csák, B., et al. 2003, A&A, 397, 115

Vinkó, J., Yuan, F., Quimby, R. M., et al. 2015, ApJ, 798, 12

Vreeswijk, P. M., Savaglio, S., Gal-Yam, A., et al. 2014, The Astrophysical Journal, 797, 24

Vreeswijk, P. M., Savaglio, S., Gal-Yam, A., et al. 2014, ApJ, 797, 24

Vreeswijk, P. M., Leloudas, G., Gal-Yam, A., et al. 2017, The Astrophysical Journal, 835, 58

Walker, E. S., Baltay, C., Campillay, A., et al. 2015, ApJS, 219, 13

Wanderman, D., & Piran, T. 2010, MNRAS, 406, 1944

Wang, W. 2014, MNRAS, 440, 1114

Watanabe, S. 2010, Journal of Machine Learning Research, 11, 3571

Waters, C., Magnier, E., Price, P., et al. 2016, arXiv preprint arXiv:1612.05245

Waxman, E., Ofek, E., Kushnir, D., & Gal-Yam, A. 2017, ArXiv e-prints, arXiv:1711.09638

Weiler, K. 2003, Supernovae and Gamma-Ray Bursters, 598

Werner, M., Roellig, T., Low, F., et al. 2004, The Astrophysical Journal Supplement Series, 154, 1

Wheeler, J. C., Johnson, V., & Clocchiatti, A. 2015, MNRAS, 450, 1295

Williams, S., Darnley, M., Bode, M., & Shafter, A. 2016, ApJ, 817, 143

Wollaeger, R. T., Korobkin, O., Fontes, C. J., et al. 2018, MNRAS, 478, 3298

Wood, P. R., Bessell, M. S., & Fox, M. W. 1983, ApJ, 272, 99

Woosley, S. 1993, ApJ, 405, 273

—. 2010, The Astrophysical Journal Letters, 719, L204

Woosley, S. E., & Kasen, D. 2011, ApJ, 734, 38

Wyrzykowski, Ł., Kostrzewa-Rutkowska, Z., Kozłowski, S., et al. 2014, Acta Astronomica, 64, 197

Xie, X., Zrake, J., & MacFadyen, A. 2018, ArXiv e-prints, arXiv:1804.09345

Yan, L., Perley, D. A., De Cia, A., et al. 2018, ApJ, 858, 91

Yan, L., Quimby, R., Ofek, E., et al. 2015, The Astrophysical Journal, 814, 108

Yan, L., Quimby, R., Gal-Yam, A., et al. 2017a, The Astrophysical Journal, 840, 57

Yan, L., Lunnan, R., Perley, D., et al. 2017b, The Astrophysical Journal, 848, 6

Young, D. R., Smartt, S. J., Valenti, S., et al. 2010, A&A, 512, A70

Yu, Y.-W., Zhang, B., & Gao, H. 2013, ApJL, 776, L40

Yu, Y.-W., Zhu, J.-P., Li, S.-Z., Lü, H.-J., & Zou, Y.-C. 2017, The Astrophysical Journal, 840, 12

Zackay, B., Ofek, E. O., & Gal-Yam, A. 2016, ApJ, 830, 27

Zampieri, L., Pastorello, A., Turatto, M., et al. 2003, Monthly Notices of the Royal Astronomical Society, 338, 711

Zhang, B., & Harding, A. K. 2000, ApJL, 535, L51